Measurement of Detector-Corrected Cross-Sections in Events with Large Missing Transverse Momentum in Association with Jets

Aidan Kelly
of University College London

A dissertation submitted to the University College London
for the degree of Doctor of Philosophy

Abstract

This thesis presents an analysis of events with large transverse missing momentum in association with jets using 139 fb^{-1} of proton-proton collisions at a centre of mass energy of 13 TeV, that was delivered at the Large Hadron Collider and recorded using the ATLAS detector from $2015 - 2018$. The dominant process which contributes to these events is the Z boson decaying to two neutrinos followed closely by the contribution from W bosons decaying leptonically, in which the charged lepton is outside the detector acceptance. The similarity of these processes to Z and W bosons decaying leptonically can be exploited by measuring the one lepton and two lepton regions, and treating the leptons as invisible in order to constrain modelling along with the experimental and theoretical uncertainties. These lepton regions are known as the auxiliary regions.

This analysis was performed using three different phase-spaces that are sensitive to different Dark Matter production channels. These three phase-spaces require the ≥ 1 jet , ≥ 2 jet and VBF topologies. The total yield is measured at the detector level and the differential cross section is measured at the particle level as a function of the missing transverse momentum, the dijet invariant mass and the dijet azimuthal angle. Ratios of these cross sections are also presented at the particle level to facilitate comparisons between regions and minimise the systematic uncertainties.

These results are interpreted using a likelihood fit and the agreement between the modelling and the data is quantified using a χ^2 test and p-value. Constraints are made on the axial-vector and pseudoscalar simplified Dark Matter models and are shown to be com-

petitive with results from the recent dedicated monojet-like search in ATLAS.

Declaration

This dissertation is the result of my own work, except where explicit reference is made to the work of others, and has not been submitted for another qualification to this or any other university.

Aidan Kelly

Acknowledgements

The work presented in this thesis would not have been possible without the support of many people. Regarding the academic aspect, I would like to thank my supervisor, Emily Nurse, who has been very supportive and provided an enormous amount of feedback throughout my doctorate at UCL despite the many obstacles encountered. I would also like to thank Christian Gütschow, who has been extremely important in my education on the technical and computational side of High Energy Physics. I would also like to thank the whole UCL HEP group and the ATLAS $p_{\mathrm{T}}^{\mathrm{miss}}$ analysis group, their feedback has been very useful and informative.

I would like to also thank my family, friends and partner. My Mum and Dad have always stood by me, both financially and emotionally during the highs and the lows. A special mention to my brother, Colin, and sister, Niamh, they have kept me grounded throughout these four years. And finally to my partner, Margarida, she has been extremely supportive during these four years and has helped me greatly, especially through the most difficult moments. Without her, I would not have been able to finish this work and thesis.

Impact Statement

High Energy Physics, or Particle Physics, helps us to understand the biggest mysteries of the Universe and breaks down matter into its fundamental components. This branch of physics allows us comprehend the forces which govern the Universe by observing the interactions of these subatomic particles. This appeals to Humankind's fundamental thirst for exploration and understanding the basic constituents of nature.

The theory which describes how subatomic particles interact and behave is called the Standard Model of particle physics and is one the most successful theories, passing almost every experimental test performed on it and on its predictions. However, there have been astronomical observations of excess matter in the Universe that is currently not explained by the Standard Model and is commonly referred to as Dark Matter.

The work done in this thesis is part of the ongoing effort to perform precision tests of the Standard Model and search for possible Dark Matter production at the Large Hadron Collider. The data for this work are collected from the ATLAS detector and are analysed using detector-correcting techniques, enabling us to compare the data to the current best model predictions without having to perform detector simulations. It will also allow us to easily compare the data to new physics models which predict the existence of Dark Matter.

The research carried out for this thesis – and in the wider experimental particle physics community – is pushing the frontiers of fundamental physics and our understanding of the Universe. The technologies developed to measure these subatomic particles can be used far and wide, with two examples being the development of cancer treatments and the invention of the World Wide Web.

Contents

Chapter 1.

Introduction

"I would rather have questions that can't be answered than answers that can't be questioned."

— Richard P. Feynman, 1918–1988

The Standard Model (SM) of particle physics is a theory that describes three of the four known fundamental forces (the electromagnetic, weak and strong forces with the missing piece being gravity) in the Universe and classifies all known particles into two categories: fermions and bosons. It is able to explain how particles called quarks (which for example make up protons and neutrons) and leptons (this category includes electrons) make up all visible matter, these are fermions. It is also able to explain how gauge bosons, force-carrying particles, interact with quarks and leptons. Electromagnetism is mediated by photons and involves the interaction of the magnetic and electric fields. The strong force, which is mediated by gluons, binds the quarks together to form protons and neutrons. There is also the strong nuclear force (this is distinct from the strong force) which binds protons and neutrons together, through the exchange of pions, to form atoms. The weak force, which is mediated by the $W^{\pm}$ and Z bosons, triggers nuclear reactions which power the Sun and millions of other stars. For gravity, there is no experimental evidence of a mediator particle, the hypothesised graviton, as such it is not described by the SM.

The SM was developed at various stages of the 20th century, by physicists from all over the globe, with the current iteration being concretised in the early 1970s with experimental evidence confirming the existence of quarks [1,2]. After the neutral weak currents caused by Z boson exchange were discovered at CERN in 1973 [3–5], the

electroweak theory became widely accepted. The W and Z bosons were discovered experimentally in 1983 and the ratio of their masses was found to agree with the SM prediction [6]. Quarks and gluons manifest themselves by fragmenting into more quarks and gluons, which hadronize into particles in the form of jets. In 1978, the PLUTO detector at the electron-positron collider DORIS (DESY) produced the first evidence that the hadronic decays of the very narrow resonance $\Upsilon(9.46\ \text{GeV})$ could be interpreted as three-jet event topologies produced by three gluons [7]. The current iteration of the SM has been finalised with evidence for the existence of the top quark in 1995 [8,9], the tau neutrino in 2001 [10] and the Higgs boson in 2012 [11] [12]. The SM has been able to predict various properties of particle physics with great precision. Despite this success and its theoretical self-consistency it leaves some phenomena unexplained and is an incomplete theory of the fundamental interactions. For example, the SM does not fully explain the baryon asymmetry that is seen in our Universe [13], it does not reconcile the theory of general relativity [14] as a quantum field theory, or account for the acceleration of the expansion of the Universe as is potentially done by Dark Energy [15]. A neutrino, which interacts via the weak and gravitational force, is a subatomic particle that is similar to that of an electron except that it has a neutral charge and a very small mass relative to other massive subatomic particles. We know the neutrino is massive due to the observation of its oscillatory behaviour and this is not incorporated within the SM framework.

Along with this, the SM is only able to describe what 15% of the Universe is made of (in terms of matter), whereas the remaining 85% is called Dark Matter (DM) and is not included in the SM. Dark Matter is known to exist from astrophysical observations and this points to a new type of gravity-interacting matter. Dark Matter does not emit or absorb light (i.e., it does not interact electromagnetically), hence why it is called "dark", nor is there evidence that it interacts with any known particle. None of the cosmological observations or simulations so far give a clear indication as to what DM is made of. If it is assumed that DM is a particle, then it must have mass otherwise it would not interact gravitationally.

Producing these DM particles and understanding their fundamental nature under a controlled laboratory environment is highly desirable as there are fewer unknowns than in high energy collisions produced in nature. In a laboratory environment, scientists have control over a number of input parameters that are difficult or impossible to control in high energy collisions in nature. These input parameters include the energy

of the colliding particles, the type of colliding particles and the density of the colliding particles (number of particles per unit volume that are involved in a collision).

The Large Hadron Collider (LHC) is the world's largest and most powerful particle accelerator located at CERN, in Geneva, accelerating protons and colliding them with a centre of mass energy of 13 TeV (corresponding roughly to fourteen thousand times the rest mass of a proton). The hope is that by using the LHC we can produce these DM particles by colliding high energy protons, in the same way the Higgs boson is produced through proton-proton collisions. The advantage of the LHC over particle accelerators found in nature, such as supernovae explosions, is that the initial conditions of the collisions are known, such as the energy and type of particle being collided.

Using the ATLAS detector, one of the four main experiments around the LHC, it is possible to detect many different known particles from collisions in this type of controlled environment. The DM particles are not expected to be detected within ATLAS and this makes it a non-trivial task to potentially observe their signature. Using the detector and some ingenuity it is possible to indirectly detect potential DM particles as a result of a momentum imbalance in the transverse plane of the detector assuming that these exotic particles are produced in association with known SM particles. This momentum imbalance can be as a result of known particles such as neutrinos, which are also invisible to the detector, but in this case the production rate is known from, for example, the precise measurements of the Z boson at LEP [16]. Whilst measuring this momentum imbalance can be difficult as it relies on accurate measurements of all the other particles in the collision, it is a powerful tool for potentially observing DM. Any deviations in the measurements from the SM prediction for the rate of production of invisible particles could indicate the production of DM.

This thesis presents differential cross section measurements of physical processes in regions of phase space which are expected to be sensitive to physics beyond the Standard Model (BSM), and allows us to compare results from the SM and the BSM predictions. A novel approach is taken within this analysis where the final state particles are targeted instead of a particular physical process. These measurements are then corrected for detector inefficiencies and resolution effects so that easy comparisons can be made to new physics models without the need for detector simulation, which can be computationally expensive. This means that these measurements can be used far into the future by physicists and reinterpretation studies on the published data can be easily performed. In this thesis we perform an interpretation of the result, where

we assess how well the SM agrees with the data, look at some new physics models and set exclusion limits using them.

This thesis begins with Chapter 2, where an overview of the Standard Model is given alongside a brief description about the evidence for Dark Matter and an overview potential Dark Matter models.

Chapter 3 describes the Large Hadron Collider, the ATLAS detector along with how physics objects are reconstructed and identified.

The analysis strategy for the measurement of regions sensitive to the production of Dark Matter is described in Chapter 4, along with all the systematic uncertainties and a brief description of the procedure for correcting the measurements for detector-effects. The detector-level and detector-corrected results are presented at the end of this Chapter.

Chapter 5 presents the interpretation performed for this analysis, this includes performing a fit to quantify the agreement between the SM and data along with studying Dark Matter models. A conclusion of the work presented in this thesis is given in Chapter 6.

Contributions

The work presented in this thesis was performed as part of the ATLAS Collaboration, in an analysis team with contributions from many different institutes around Europe. The majority of the author's contribution to this analysis is presented in this thesis and has benefited greatly from the contributions of others. Most notably, the software framework was developed by Christian Gütschow, Vasilis Konstantinides, Louie Corpe and Yoran Yeh. The theory systematics were provided by Christian Gütschow. The QCD multijet background and the fake lepton backgrounds estimates were provided by Sebastian Weber and Matous Vozak respectively. The interpretation framework was developed jointly by the author, Louie Corpe and Martin Habedank. The authors main contributions were towards data quality checks, the development of the interpretation framework, along with performing Standard Model fits and producing the relevant DM samples for the exclusion limits for this analysis.

Chapter 2.

Theoretical Framework

"Like in nature, I like things which are based on a few simple principles, even though their manifestation can be very rich."

— Fabiola Gianotti

2.1. Particles of the Standard Model

The nature, origin and fate of our Universe has been a question that has intrigued humankind since its beginning and to this day we are still trying to answer existential questions such as: How did something come out of nothing? How did the Universe begin and how will it end? What exactly is the Universe made of and what are its basic constituents?

These questions are often framed in a scientific context, and to be more precise they fall into the remit of fundamental physics. One of the branches of fundamental physics is particle physics which deals with the building blocks of matter and how they interact with each other. The topic of particle physics often intersects with astrophysics and cosmology, subjects which describe physics at the largest scales. If we consider that the Universe started a finite time in the past at a singular point, we can rewind the clock to the Big Bang where the Universe gets much smaller and much hotter, and this is where particle interactions become very important.

Many centuries of scientific research have culminated in a framework which describes a Universe made up of matter which interacts via force-carrying mediators.

We are able to see these forces in action all around us, for example the plants we see around us are mainly made up of Carbon, which in itself consists of a nucleus of protons (p^+) and neutrons surrounded by a cloud of electrons (e^-). The negatively charged electrons which surround the nucleus are held there by the electromagnetic attraction to the positively charged protons. This attraction is a manifestation of Quantum Electrodynamics (QED). The nucleus is held together by the strong force, which is just a manifestation of Quantum Chromodynamics (QCD). Plants also use the process of photosynthesis to produce oxygen using carbon dioxide, water, and importantly, sunlight. The Sun is fueled by nuclear fusion reactions which occur in its core, in which the weak force is involved in the dominant fusion process known as the proton-proton chain reaction[1] and this provides the much needed sunlight for plants.

The forces, as are currently known, are completed by the addition of gravity. While this is an extremely weak force, it explains a lot of the large scale structure of the Universe as it is always attractive along with its cumulative effect over vast distances and the fact that it interacts with all forms of matter. All of the common physical processes can be explained by six particles; the proton, the neutron, the electron, the positron, the neutrino[2] and the anti-neutrino– which interact via the electromagnetic, strong and weak forces. These interactions work well at low energies, however, once we get to higher energies, further structure of the proton and neutron appears in the form of quarks. For example, a proton is made up of two up quarks and a down quark whereas a neutron is made up of two down quarks and an up quark. In addition to these up and down quarks, protons and neutrons also contain a "sea" of virtual quark-anti-quark pairs that constantly pop in and out of existence due to fluctuations of energy in the proton's and neutron's internal structure. The strong force which holds the quarks together is mediated by particles called gluons. Gluons are constantly exchanged between quarks, which creates a complex web of interactions that binds the quarks together into a single unit.

The electron, the positron, the neutrino ν_e, and up and down quarks make up what is known as the first generation of fermions. There are also two heavier generations of fermions which become more relevant at higher energies. These particles in the higher generations have exactly the same quantum numbers as those in the first generation

[1] In this process, two protons are fused together into a deuteron (made up of a proton and a neutron). As the protons fuses, one of them undergoes a beta plus decay (mediated by the weak force), converting into a neutron by emitting a positron and an electron neutrino. The positron will annihilate with an electron from the surrounding environment and produce two gamma rays.

[2] Which means the little neutral one in Italian.

with the exception being the mass. Each of these particles have a corresponding anti-particle which will have the same mass but the other quantum numbers (such as the charge) are the opposite. These particles are shown in Figure 2.1.

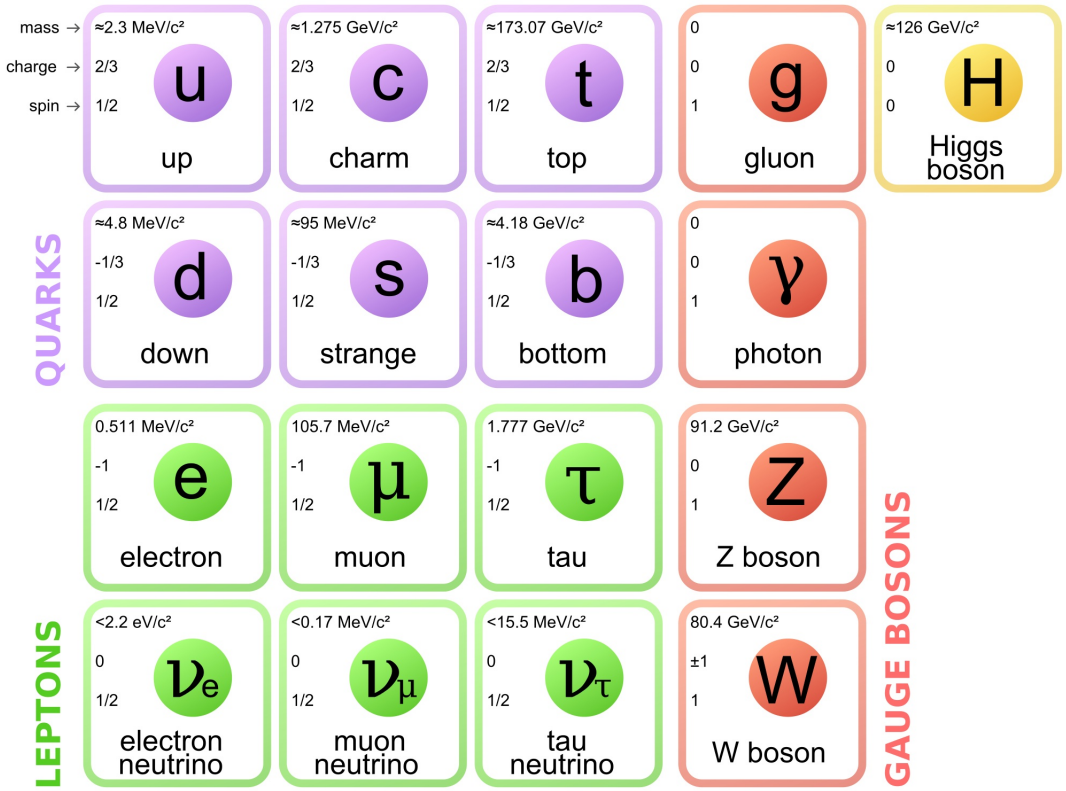

Figure 2.1.: A table of the fundamental particles in the Standard Model [17].

These particles interact via the four fundamental forces: the gravitational force, the strong force, the weak force and the electromagnetic force. The gravitational force is very weak at the subatomic level, therefore it does not need consideration when considering the short scales we are interested in. The interactions of the twelve fermions (spin-1/2), listed in Figure 2.1, are dependent on their properties (i.e., quantum numbers). As already mentioned, these fermions are split into three generations, which can be split up into leptons and quarks as shown in Figure 2.1. These particles interact via the exchange of vector gauge bosons (spin-1 particles). The weak force is mediated between fermions by the $W^{\pm}/Z$ bosons and except for the chargeless neutrinos, the other nine charged fermions interact electromagnetically by exchanging photons.

The quarks possess a quantum number called the colour charge, which is a QCD equivalent of the electric charge, and this means they can feel the strong force and mediate this force via the exchange of gluons. It is important to note that free quarks

cannot be observed[3] as they form bound states called hadrons, either a baryon (made up of three quarks or anti-quarks) or a meson (made up of a quark and anti-quark) such as the proton and pion respectively. These bound states are held together by the strong force, and the baryons or mesons are required to have a net colour charge of zero.

2.2. SM Lagrangian

The SM is a Quantum Field Theory (QFT) which is based on combining quantum mechanics and special relativity. The particles are quantised in fields and interact via mediator particles in which the behaviour and properties of these fields can be described by the Lagrangian density. The Lagrangian density for the SM, which from now will be referred to as the Lagrangian, is given by:

$$\mathcal{L}_{\text{SM}} = \mathcal{L}_{\text{EWK}} + \mathcal{L}_{\text{QCD}} + \mathcal{L}_{\text{Higgs}} + \mathcal{L}_{\text{Yukawa}} \tag{2.1}$$

Here, $\mathcal{L}_{\text{EWK}}$ describes the dynamics and kinematics of the electroweak force, $\mathcal{L}_{\text{QCD}}$ explains the behaviour of the strong force, and the combination of $\mathcal{L}_{\text{Higgs}}$ and $\mathcal{L}_{\text{Yukawa}}$ sets out how fermions and gauge bosons gain mass and how the Higgs interacts with them aswell. The SM Lagrangian is based on a local $\text{SU}(3)\times\text{SU}(2)\times\text{U}(1)_Y$ gauge symmetry, where the $\text{SU}(3)$ is used for the strong force and analogously the $\text{SU}(2)\times\text{U}(1)_Y$ group is used for the electroweak force. We now go on to describe each component of the SM Lagrangian in some detail in sections 2.3, 2.4, 2.5 and 2.6.

2.3. Quantum Electrodynamics

In particle physics, QED is the relativistic QFT of electrodynamics and it explains in essence how matter interacts with light. It was the first theory to combine quantum mechanics with special relativity. It is mathematically represented by the QED Lagrangian, $\mathcal{L}_{\text{QED}}$, in which all phenomena involving electrically charged particles interact by the exchange of photons and represent the quantum equivalent of electromagnetism. We can describe QED through a gauge theory which has the requirement of gauge invariance under a $\text{U}(1)_{EM}$ transformation. The free Lagrangian of the Dirac

[3] Due to a phenomenon known as confinement, more on this later.

spinors [4], Ψ, is given by the Dirac Lagrangian:

$$\mathcal{L}_{\text{Dirac}} = i\overline{\Psi}\gamma^{\mu}\partial_{\mu}\Psi - m\overline{\Psi}\Psi \tag{2.2}$$

where $i\overline{\Psi}\ \gamma^{\mu}\ \partial_{\mu}\Psi$ is the kinetic term, γ^{μ} references the gamma matrices and m is the fermionic mass[5]. We can perform a global phase transformation with the operation $\Psi \rightarrow \Psi = e^{-i\alpha}\Psi$, where α is not dependent on a spacetime coordinate x. It is obvious to see that the global transformation is invariant on the Dirac Lagrangian, $\mathcal{L}_{\text{Dirac}}$. However, if the transformation is local then $\alpha(x)$ is dependent on the spacetime coordinates and it is possible to show that invariance is broken:

$$\partial_{\mu}\Psi \rightarrow \partial_{\mu}\Psi' = e^{-i\alpha(x)}(\partial_{\mu}\Psi - i(\partial_{\mu}\alpha(x)\Psi)) \tag{2.3}$$

and as a consequence of this, a so-called covariant derivative is required and with this we introduce a new field A_{μ} with the corresponding coupling constant e:

$$\partial_{\mu} \rightarrow D_{\mu} = \partial_{\mu} + ieA_{\mu} \tag{2.4}$$

where the A_{μ} transforms as

$$A_{\mu} \rightarrow A_{\mu} - \frac{1}{e}\partial_{\mu}\alpha(x) \tag{2.5}$$

under the local gauge transformation $\alpha(x)$. The covariant derivative has the property that it merely picks up a phase under gauge transformation, with the derivative of $e^{-i\alpha}$ cancelling the transformation of the gauge field. This ensures that the whole Lagrangian is invariant.

In QED, the A_{μ} field can be interpreted as the electromagnetic field and this massless field can be an added as an extra term to the Lagrangian:

$$-\frac{1}{4}F_{\mu\nu}F^{\mu\nu} \tag{2.6}$$

where $F_{\mu\nu}$ is the electromagnetic tensor, $F_{\mu\nu} = \partial_{\mu}A_{\nu} - \partial_{\mu}A_{\mu}$, the variable e is the coupling strength between the fields and this is known as the electric charge. The QED

[4]The Dirac spinor, where the spinors are defined as the elements of a complex vector space associated with Euclidean space, describe all known fermions with the possible exception of neutrinos.

[5]Important to note here that mass terms for (chiral) fermions are forbidden by gauge invariance and this will be shown later.

Lagrangian is therefore given by:

$$\mathcal{L}_{\text{Dirac}} = i\overline{\Psi}\gamma^{\mu}D_{\mu}\Psi - m\overline{\Psi}\Psi - \frac{1}{4}F_{\mu\nu}F^{\mu\nu} \tag{2.7}$$

and this Lagrangian is invariant under the $\mathrm{U}(1)$ local gauge transformation and can be used to derive the Maxwell equations. This Lagrangian describes how charged fermions interact with photons.

2.4. Electroweak Gauge Theory

The electroweak interaction is the unified description of the electromagnetic force and the weak force. Even though these two forces behave very differently at low energies, the electroweak gauge theory models them as two different aspects of the same force. Above the unification energy[6] of around 246 GeV [18], the electromagnetic and weak forces merge. Shortly after the Big Bang, temperatures of approximately 10^{15} K were reached and this is where electroweak unification occurred. Within the SM, the electroweak Lagrangian $\mathcal{L}_{\text{EWK}}$ is invariant under a $\mathrm{SU}(2)\times\mathrm{U}(1)_{Y}$ local gauge transformation. All of the SM particles have a property called the weak isospin, T_3, which is a quantum number that dictates the particle behaviour with regards to the weak force. The weak isospin performs the same function as the electric charge does for electromagnetism.

It is possible to group lepton fields into three generations of isospin, isospin doublets ($T_3 = \pm\frac{1}{2}$) in the left-handed case which is represented by the symbol L_L and isospin singlets ($T_3 = 0$) represented by the field L_R for the right-handed cases. The same can be done for the quarks fields where it is possible to split them into the left-handed doublet and a right-handed singlet.

The electroweak Lagrangian can be written as:

$$\mathcal{L}_{\text{EWK}} = \overline{L}_L\gamma^{\mu}D_{\mu}^{L}L_L + \overline{L}_R D_{\mu}^{R}L_R - \frac{1}{4}\vec{W}_{\mu\nu}\vec{W}^{\mu\nu} - \frac{1}{4}B_{\mu\nu}B^{\mu\nu}, \tag{2.8}$$

where the first two terms represent the interaction between the left-handed and right-handed fields, which is done via the gauge boson fields. We can achieve local gauge

[6] This is the vacuum expectation value $v = \frac{1}{\sqrt{2G_F}}$ of the Higgs field where G_F is the Fermi coupling constant.

invariance with the following covariant derivatives:

$$\begin{aligned} D_\mu^R &= i\partial_\mu + \frac{g'}{2} Y_R B_\mu, \\ D_\mu^L &= i\partial_\mu + \frac{g}{2}\sigma_i W_\mu^i + \frac{g'}{2} Y_L B_\mu. \end{aligned} \tag{2.9}$$

Four gauge fields are introduced $W_\mu^i (i = 1, 2, 3)$ and B_μ with the coupling to the fermion fields given by g and g'. It is possible to group the $\sigma_i/2$ in the D_μ^L term, where σ_i are the Pauli-spin matrices,[7] as three SU(2) generators denoted by $\vec{T}$. The $\vec{T}$ generators are non-commuting and this results in a non-Abelian gauge theory. For the U(1) symmetry, the generator is the weak hypercharge Y and can be related to the electric charge Q and the isospin number T_3 via the relation $Q = Y/2 + T_3$. The weak hypercharge is required to commute with the SU(2) $\vec{T}$ generator. The last two terms in Equation 2.8 are free vector boson fields, in which the assumption is that the gauge bosons are massless and are able to describe the self-interacting bosons. These field tensors can be described as:

$$\begin{aligned} W_{\mu\nu} &= \partial_\mu W_\nu - \partial_\nu W_\mu - g W_\nu \times W_\mu, \\ B_{\mu\nu} &= \partial_\mu B_\nu - \partial_\nu B_\mu \end{aligned} \tag{2.10}$$

where the physical manifestations of the $W^\pm$ bosons, Z bosons and the photon γ can be defined as a mix of the following gauge fields:

$$\begin{aligned} W_\mu^\pm &= (W_\mu^1 \mp i W_\mu^2)/\sqrt{2}, \\ A_\mu &= \cos\theta_w B_\mu + \sin\theta_w W_\mu^3, \\ Z_\mu &= -\sin\theta_w B_\mu + \cos\theta_w W_\mu^3, \end{aligned} \tag{2.11}$$

where θ_w is the Weinberg angle and is related to the coupling constraints by the relation:

$$\tan(\theta_w) = \frac{g'}{g}. \tag{2.12}$$

[7] The Pauli-spin matrices are a set of three 2×2 complex matrices which are Hermitian and unitary.

2.5. Quantum Chromodynamics

The strong force describes how the quarks within protons and neutrons are kept together and is therefore a very important aspect of the SM. The Lagrangian for this fundamental field theory, which is called Quantum Chromodynamics (QCD) is given by:

$$\mathcal{L}_{\text{QCD}} = \overline{\Psi}(i\gamma^{\mu}D_{\mu} - m)\Psi - \frac{1}{4}G^{a}_{\mu\nu}G^{\mu\nu,a}, \tag{2.13}$$

where the covariant derivative is

$$D_{\mu} = \partial_{\mu} + ig_{s}T^{a}G^{a}_{\mu} \tag{2.14}$$

and $G^{a}_{\mu\nu}$ is the gauge invariant gluon field strength tensor defined as:

$$G^{a}_{\mu\nu} = \partial_{\mu}G^{a}_{\nu} - \partial_{v}G^{a}_{\mu} + g_{s}f^{abc}G^{b}_{\mu}G^{c}_{\nu}, \tag{2.15}$$

where $G^{a}_{\mu\nu}$ are the gluon fields, f^{abc} is the structure constants of SU(3) and g_s is the strong coupling constant. The gauge group of QCD is SU(3) and the eight corresponding generators[8] are given by $T^{a} = \lambda^{a}/2$ and this theory also has eight gluons of different colour charges. Out of the fermions, only the quarks interact with the strong force and we write these fermionic fields as spinors. The quarks come in three different colour charges which are labelled as red (R), green (G) and blue (B) and three anti-quarks with the corresponding colour charge of anti-red ($\overline{R}$), anti-green ($\overline{G}$) and anti-blue ($\overline{B}$). The gluons have a combination of one of the green, blue, red colour charges and one of the anti-green, anti-blue and anti-red colour charges. The last terms of Equation 2.13 represents gluon self-interactions, which can be illustrated by Feynman diagrams (see Figure 2.2(a), 2.2(b) and 2.2(c)), in which this self-interaction means the confinement of colour singlet states which results in the free quarks and gluons not being observed. To explain this further, we have to define something called charge screening.

[8] λ^{a} are the Gell–Mann matrices.

Charge Screening

In QED, a charged particle, such as the electron, is surrounded by a cloud of electron-positron pairs and virtual photons coming in and out of existence. Due to the attraction of opposite charges, the virtual positron are close to the electrons and essentially "screens" the electron charge, see Figure 2.3. This gives rise to what is called an effective charge, defined as $e(r)$, that becomes weaker at a larger distance. We can illustrate this using the beta function:

$$\beta(r) = -\frac{de(r)}{d\ln(r)} \tag{2.16}$$

and this is in fact positive for QED.

For QCD, the vacuum consists of virtual quark and anti-quark pairs, and if that was all then the charge screen mechanism would be the same as in QED, with a positive

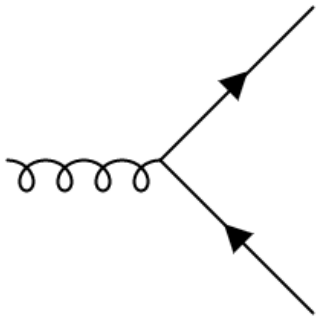

(a) A gluon splitting into two quarks

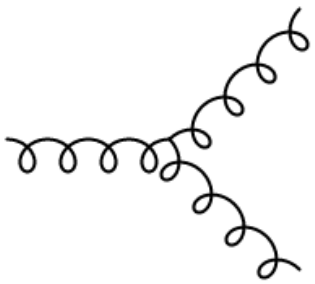

(b) Triple gluon self-interaction

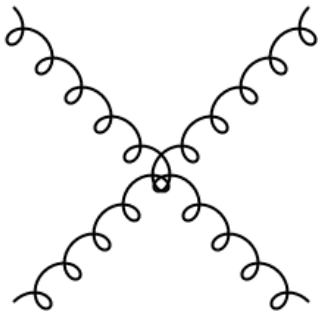

(c) Quartic gluon interaction

Figure 2.2.: Some of the basic QCD interactions along with gluonic self-interactions.

beta function. However, due to the gluon self coupling, the vacuum will also be filled with virtual gluon pairs as can be seen in Figure 2.4. As the gluons carry colour charge, the effective charge becomes bigger with larger distances, this mean the beta function is negative. This effect is what is known as antiscreening.

Charge screening in QED (screening) and QCD (antiscreening) leads to running of the coupling. In QED, the coupling becomes large at (very) short distances but its effect is small. In QCD, the antiscreening effects causes the strong coupling to become small at short distances (large high momentum transfer). This causes the quarks inside the hadrons to act like free quarks at high enough energies. This effect is known as asymptotic freedom and this allows us to use perturbation theory to calculate predictions for hard scattering hadronic cross sections. At increasing distances the coupling becomes so strong that it is impossible to isolate a free quark from a hadron, this is known as confinement. This phenomenon has been confirmed with lattice QCD calculations but cannot be proved mathematically.[9]

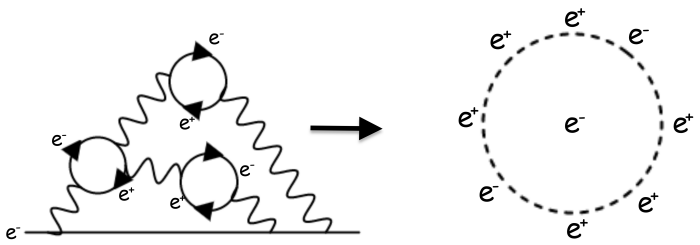

Figure 2.3.: The left figure shows the charged electron being surrounded by a cloud of virtual photons and e^+e^- pairs continuously popping in and out of existence. The right figure shows the e^- surrounded by mostly e^+ which leads to charge screening.

[9] A mathematical proof of confinement will win you a $1M millenium prize from the Clay Mathematics Institute.

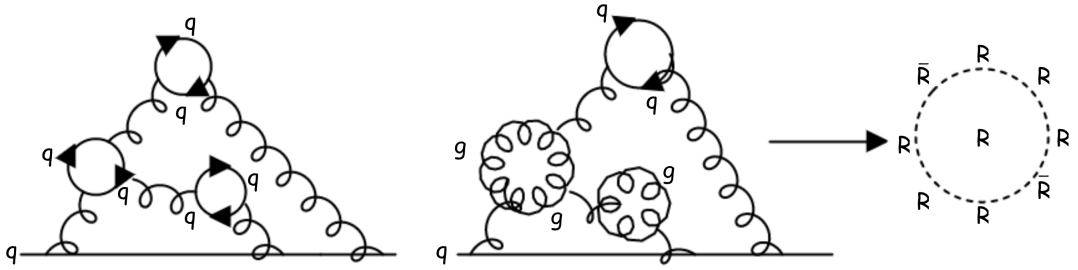

Figure 2.4.: On the left-most figure, the QCD vacuum consist of virtual $q\bar{q}$ pairs, this would lead to an analogous situation to the QED charge screening. However, seen on the middle figure, the vacuum can be filled with virtual gluon pairs, and as they carry colour charge, an anti-screening effect occurs (on the right).

2.6. Higgs Mechanism

2.6.1. Introducing a Mass Term

The local gauge invariance for the electroweak Lagrangian, $\mathcal{L}_{\text{EWK}}$, is broken if mass terms are introduced into $\mathcal{L}_{\text{EWK}}$. The mass terms that come from the Dirac Lagrangian, which describe fermions, are defined as $-m\overline{\Psi}\Psi$ and break invariance under the electroweak symmetry. To explore this in more detail, we can define $\Psi = (\Psi_L + \Psi_R)$ where the left and right-handed chiral projections of Ψ are defined as:

$$\begin{aligned} \Psi_L &= \frac{1}{2}(1-\gamma^5)\Psi, \\ \Psi_R &= \frac{1}{2}(1+\gamma^5)\Psi. \end{aligned} \tag{2.17}$$

With these definitions, it is clear using the identity $(\gamma^5)^2 = \mathbb{1}$ that $-m\overline{\Psi}\Psi = -m(\overline{\Psi}_L\Psi_R + \overline{\Psi}_R\Psi_L)$ where the $\overline{\Psi}_L\Psi_L$ and $\overline{\Psi}_R\Psi_R$ terms go to zero. Such a term in the Lagrangian is not gauge invariant as the left handed fermions form an isospin doublet (e.g. $\binom{\nu}{e}_L$) and the the right-handed fermions form isospin singlets like e_R.

2.6.2. Spontaneous Symmetry Breaking

The problem outlined above regarding mass terms breaking gauge invariance can be solved via a process called spontaneous symmetry breaking. Similar to what is done

with QED, we can use a toy model for this process with a U(1) gauge transformation. Imagine we have a complex scalar field, ϕ, and its corresponding Lagrangian, $\mathcal{L}$:

$$\begin{aligned} \phi &= \frac{1}{\sqrt{2}}(\phi_1 + i\phi_2), \\ \mathcal{L} &= (\partial_\mu \phi)^\dagger (\partial^\mu \phi) - V(\phi), \end{aligned} \tag{2.18}$$

where the potential is defined as

$$V(\phi) = \mu^2(\phi^\dagger \phi) + \lambda(\phi^\dagger \phi)^2. \tag{2.19}$$

This Lagrangian is clearly invariant under the U(1) gauge transformation of $\phi \to \phi = e^{i\alpha}\phi$. If we take a look at Figure 2.5, for parameters of $\mu^2 < 0$ and $\lambda > 0$ potential, at a value of $\phi_1 = \phi_2 = 0$ there is a non-zero value. The minimum of the potential, $V(\phi)$, is

$$\sqrt{\phi_1^2 + \phi_2^2} = \sqrt{-\frac{\mu^2}{\lambda}} = v. \tag{2.20}$$

We can see in Figure 2.5 that this forms a circle of minima in the $\phi_1 - \phi_2$ plane which has infinite possibilities. We choose a minimum, ϕ_0, of $\phi_1 = v$ and $\phi_2 = 0$ and study the behaviour of the Lagrangian under small perturbations around the vacuum and what particles may be present in this model. The perturbations around this minimum are given by the shifted fields of η and ξ. The minimum, ϕ_0, is then defined as

$$\phi_0 = \frac{1}{\sqrt{2}}(\eta + v + i\xi). \tag{2.21}$$

We can substitute this term back into the Lagrangian and, neglecting the constant, this can be written as

$$\mathcal{L}(\eta, \xi) = \frac{1}{2}(\partial_\mu \eta)^2 - (\lambda v^2)\eta^2 + \frac{1}{2}(\partial_\mu \xi)^2 + \text{higher order terms} \tag{2.22}$$

where the massive scalar particle is defined as $m_\eta = \sqrt{2\lambda v^2}$ and a massless particle ξ, called the Goldstone boson appears.[10] This is what happens when you break a continuous global symmetry. However, when the local gauge invariance is broken the Goldstone boson will disappear.

[10] Goldstone bosons are bosons that appear in models which spontaneously break a continuous symmetry.

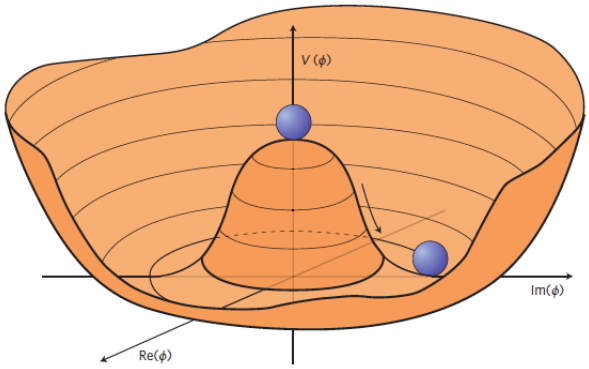

Figure 2.5.: The Higgs potential in the case that $\mu^2 < 0$ and $\lambda > 0$, with the minimum defined as $|\phi|^2 = -\mu^2/(2\lambda)$ [19].

2.6.3. Breaking a Local Gauge Invariant Symmetry: The Higgs Mechanism

Particles in the SM can obtain masses through a mechanism called spontaneous symmetry breaking (SSB). It is possible to obtain a massive W and Z boson whilst maintaining a massless photon with a specific choice of parameters for the Lagrangian. In the electroweak model, there is a Lagrangian which is invariant under $\mathrm{SU}(2)_L \times \mathrm{U}(1)_Y$, undergoes SSB and produces Goldstone bosons. To break the $\mathrm{SU}(2)_L \times \mathrm{U}(1)_Y$ gauge symmetry, we introduce a complex isospin doublet:

$$\begin{pmatrix} \phi^+ \\ \phi^0 \end{pmatrix} = \frac{1}{\sqrt{2}} \begin{pmatrix} \phi_1 + i\phi_2 \\ \phi_3 + i\phi_4 \end{pmatrix}. \tag{2.23}$$

In this instance, we added a left handed doublet (similar to the electron neutrino doublet that was mentioned previously) with a weak isospin of $\frac{1}{2}$. The electric charge of the upper and lower scalar fields are positive and neutral to ensure that the doublet has a hypercharge of $Y_W = +1$, where $Y_W = 2(Q - T_3)$. We then add the potential, $V(\phi)$, which spontaneously breaks the symmetry in the Lagrangian:

$$\mathcal{L}_{\text{scalar}} = (D^\mu \phi)^\dagger (D_\mu \phi) - \mu^2(\phi^\dagger \phi) - \lambda(\phi^\dagger \phi)^2, \text{ with } \mu^2 < 0 \tag{2.24}$$

where D_μ is the covariant derivative associated with the $\mathrm{SU}(2)_L \times \mathrm{U}(1)_Y$ symmetry and is defined as

$$D_\mu = \partial_\mu + ig\frac{1}{2}\vec{\tau}\cdot\vec{W}_\mu + ig\frac{1}{2}YB_\mu. \tag{2.25}$$

We then choose a vacuum which breaks the symmetry and results in massive gauge bosons. The vacuum is chosen to be

$$\text{Vacuum} = \phi_0 = \frac{1}{\sqrt{2}}\begin{pmatrix} 0 \\ v+h \end{pmatrix} \tag{2.26}$$

with h being a scalar field that oscillates around the vacuum perpendicular to the potential. The choice of vacuum breaks the $\mathrm{SU}(2)_L \times \mathrm{U}(1)_Y$ symmetry, but leaves the $\mathrm{U}(1)_{EM}$ invariant which leaves the photon massless. If we substitute the vacuum into the Lagrangian, we get:

$$\mathcal{L}_{\text{scalar}} = \frac{1}{2}\partial_\mu h \partial^\mu h + \mu^2 h^2 + \frac{\lambda}{4}h^4 + \lambda v h^3 + \frac{g^2}{4}(v+h)^2 W_\mu^+ W_\mu^- + \frac{1}{8}(g^2+g'^2)(v+h)^2 Z_\mu Z^\mu \tag{2.27}$$

and the masses of the W, Z bosons and the Higgs boson are given by

$$\begin{aligned} M_W &= \frac{1}{2}gv \\ M_Z &= \frac{1}{2}\sqrt{g^2+g'^2} = \frac{M_W}{\cos\theta_w} \\ M_H &= \sqrt{2}|\mu| = v\sqrt{2\lambda} \end{aligned} \tag{2.28}$$

where the mass of the Higgs is not predicted by theory.

2.6.4. Fermion Masses

As shown before, the fermion masses are not gauge invariant to the different characteristics of the left-handed (LH) and right-handed (RH) fields. For example, with leptons, if we take the mass term, $-m\overline{\Psi}\Psi = -m(\overline{\Psi}_L\Psi_R + \overline{\Psi}_R\Psi_L)$ then this is not gauge invariant since the LH leptons form an isospin doublet, $L_L = \binom{\nu}{e}$ and RH leptons form an isospin singlet like $L_R = e_R$. The fields therefore transform differently under

the $\mathrm{SU}(2)_L \times \mathrm{U}(1)_Y$ gauge symmetry:

$$\begin{aligned} L_L &\to L'_L = e^{i\vec{W}\cdot\vec{\sigma}+i\alpha Y_L} L_L \\ L_R &\to L'_R = e^{i\alpha Y_R} L_R \end{aligned} \tag{2.29}$$

and the $mL\overline{L}$ term is not gauge invariant under these $\mathrm{SU}(2)_L \times \mathrm{U}(1)_Y$ transformations. It is possible to achieve local gauge invariance by introducing a complex doublet, which we defined in the previous section (see Equation 2.26). We can see that the complex doublet has exactly the right quantum numbers to form a $\mathrm{SU}(2)_L \times \mathrm{U}(1)_Y$ singlet as a Lagrangian term, $-\lambda_f \overline{L}_L \phi L_R$, where λ_f is the fermionic coupling or more commonly known as the Yukawa coupling. In summary:

$$\begin{aligned} &\text{a } \mathcal{L} \text{ term} \propto \overline{L}_L L_R \text{ is NOT invariant under } \mathrm{SU}(2)_L \times \mathrm{U}(1)_Y \\ &\text{a } \mathcal{L} \text{ term} \propto \overline{L}_L \phi L_R \text{ is invariant under } \mathrm{SU}(2)_L \times \mathrm{U}(1)_Y \end{aligned} \tag{2.30}$$

and the term which is added to the Lagrangian that couples the Higgs doublet to the fermionic fields is given by

$$\mathcal{L}_{\text{fermion-mass}} = -\lambda_f [\overline{L}_L \phi L_R + \overline{L}_R \overline{\phi} L_L] \tag{2.31}$$

and this describes the interaction between the Higgs field and the leptons. If the Higgs doublet has a non-zero expectation value (see Equation 2.26) then the leptons acquire a finite mass. We can then write the Lagrangian for the electron-neutrino doublet as

$$\begin{aligned} \mathcal{L}_e &= -\lambda_e \frac{1}{2} \left[(\overline{\nu}, \overline{e})_L \begin{pmatrix} 0 \\ v+h \end{pmatrix} e_R + \overline{e}_R (0, v+h) \begin{pmatrix} v \\ e \end{pmatrix}_L \right] \\ &= -\frac{\lambda_e (v+h)}{\sqrt{2}} [\overline{e}_L e_R + \overline{e}_R e_L] \\ &= -\frac{\lambda_e v}{\sqrt{2}} \overline{e} e - \frac{\lambda_e h}{\sqrt{2}} \overline{e} e \end{aligned} \tag{2.32}$$

and in this Lagrangian, the $\frac{\lambda_e v}{\sqrt{2}}$ term is the electron mass and $\frac{\lambda_e h}{\sqrt{2}}$ is the electron-Higgs interaction. The quark masses can be obtained in a similar way, with the Lagrangian, $\mathcal{L}^q_{\text{Yukawa}}$, having a mass term defined as $m_q = \frac{\lambda_f v}{\sqrt{2}}$.

2.7. Physics Beyond the Standard Model

To summarise the previous sections – the SM of particle physics is able to describe three of the four known forces (with the exclusion of gravity), as well as describing the characteristics of the fundamental particles to a high accuracy. The masses of the gauge bosons can be obtained from electroweak symmetry breaking and the masses of the fermions are obtained from Yukawa coupling, resulting in the Higgs bosons and its interactions with massive particles.

Despite being a very successful theory of particle physics, the SM does not explain all observed phenomena, such as gravity, but it can be modified in such a way that it would still be consistent with all the physical phenomena that it explains and yet also address some of the unexplained phenomena we see today. If we take gravity as an example, the approach of simply adding a graviton to the SM does not account for the observed phenomena without having to make other major modifications. It would also be incompatible with General Relativity[11], generally considered the most successful theory of gravity. The SM also does not explain why neutrinos are massive, when in fact it predicts that they are massless. It is possible to add neutrino mass terms to the SM, but this leads to theoretical problems (such as the violation of the conservation of lepton number) which means the masses need to be very small[12]. We also know that the universe is made out of mostly matter. However, the SM predicts that matter and antimatter are (almost) created in equal amounts. As of yet, there is no mechanism in the SM to sufficiently explain this asymmetry.

Another unexplained phenomena in fundamental physics is that 95% of the Universe's energy consists of so-called dark energy and DM (the other 5% is made up of the regular matter). Of this, about $\sim$73% is made up of dark energy. There have

[11] General Relativity is incompatible with the SM as it describes the force of gravity as a curvature of spacetime, while the SM describes the other fundamental forces (electromagnetism, weak force, and strong force) as the exchange of particles. In other words, the SM is based on QFT, which describes the behavior of particles at the subatomic level, while general relativity is a classical theory that describes the behavior of gravity on a large scale.

[12] To avoid these theoretical problems, a mechanism called the seesaw mechanism has been proposed. The seesaw mechanism suggests that there are additional heavy particles, called right-handed neutrinos, that interact with the SM neutrinos and give them mass through a mixing process. The seesaw mechanism predicts that the mass of the SM neutrinos is inversely proportional to the mass of the right-handed neutrinos, which means that the right-handed neutrinos must be very heavy in order to explain the small masses of the SM neutrinos. This is known as the "heavy neutrino problem". Another challenge is that the experimental limits on the masses of neutrinos are very small, which suggest that the right-handed neutrinos must be very heavy, possibly beyond the reach of current experimental capabilities.

been attempts to explain dark energy in terms of vacuum energy of the SM but there is a discrepancy of 120 orders of magnitude between what is found in QFT and that found in general relativity. The other $\sim 27\%$ of this energy is made up of DM, where astrophysical and cosmological observations have provided strong evidence for the existence of this mysterious matter [20–25].

There are two broad categories of potential DM candidates: particle and non-particle candidates. Before going into detail about potential DM particle candidates, we will briefly overview some non-particle candidates. These non-particle candidates include MACHOs (Massive Compact Halo Objects) such as brown dwarfs [26, 27], black holes [28–31] or neutron stars [28, 32] which do not emit light and are difficult to directly detect. Modified Newtonian dynamics (MOND) is also another hypothesis, where Newton's laws of gravity could be modified on very large scales and this would explain the observed behaviour and motion of galaxies without the need for DM [33–35]. In addition, sterile neutrinos which are hypothetical particles that are believed to only interact via gravity could be a DM candidate [36, 37]. It's important to note that although these listed candidates are interesting, none of them have yet proven to be the source of DM or explain the behaviour of all physical systems in the case of MOND [38–42].

In terms of the particle picture, the SM does not provide a viable candidate for a DM particle, and as a consequence BSM physics is required. One of the most popular DM models is the idea of massive neutral particles with a weak interaction, more commonly known as Weakly Interacting Massive Particles (WIMP). Broadly speaking, a WIMP would interact via gravity and a weak force which is at least as weak if not weaker than the weak nuclear force, with WIMP masses ranging from a few MeV to the electroweak scale (energy scale of around 246 GeV, same as the vacuum expectation value).

WIMPs are expected to have been produced in the early universe, in a similar manner to SM particles, according to cosmology and constitute what is known as cold

dark matter.[13] To obtain the correct amount of dark matter present in today's Universe, via thermal production, a new particle in the $m \sim 100$ GeV range would be expected.

Supersymmetry (SUSY) is a theoretical framework which proposes the existence of a new symmetry between fermions (particles with half-integer spin, such as quarks and electrons) and boson (particles with integer, such as photons and W and Z bosons) [43–46]. In SUSY, every fermion has a corresponding bosonic partner (for example, quarks have a squark partner) and vice versa (for example, the gluon has a gluino partner). This framework predicts a new particle with similar properties to what is described as a WIMP. One such candidate is the neutralino [47–49], which is a hypothetically electrically neutral and weakly interacting particle that is predicted by some SUSY models. For example, the Minimal Supersymmetric Standard Model (MSSM) is a commonly used framework for exploring SUSY at low energies. In this model, there exist four electrically neutral fermions known as neutralinos. The neutralino is stable because it is the lightest supersymmetric particle (LSP) and is therefore unable to decay into any lighter particle within the framework of SUSY. This means if neutralinos were produced in the early universe, they would persist to the present day as a form of DM.

Another motivation for WIMPs is the so-called "WIMP miracle" [50, 51], which refers to the fact that the predicted abundance of WIMPs produced in the early universe is consistent with the observed abundance of DM. WIMPs are also predicted by the universal extra dimension (in the form of the lightest Kaluza-Klein particle) and little Higgs theories (lightest T-odd particle). The WIMP is also an experimentally attractive prospect as it is feasible for many experimental setups.

Experimentally there are three approaches to testing the WIMP hypotheses, which include:

- direct production at particle accelerators,
- searching for signals from annihilating particles,

[13] Dark matter can be divided into cold, warm and hot categories. Despite their names, each category refers to the relative velocity not their temperatures, indicating how far the DM candidates moved due to random motion before they were slowed down due to cosmic expansion (this distance is known as the free streaming length (FSL). Primordial density fluctuations which are smaller than this length disperse from high density regions to lower density, while the larger fluctuations stay as is. The FSL therefore sets the minimum scale for later structure formation. The DM candidates are categorised comparing their FSL to the size of a protogalaxy (a cloud of gas which is forming into a galaxy), where if it is much smaller, similar or much larger it corresponds to cold, warm and hot DM respectively.

- direct scattering off nuclei.

These different approaches are illustrated in Figure 2.6, where we see the coupling of the SM to DM particles. Specific to collider physics, which is what we are interested in, the DM particles and their mediator have to be within the energy reach of said collider (in this case the LHC), this is not a constraint in direct and indirect searches. However, direct and indirect searches are less sensitive to low DM masses and are affected by larger experimental uncertainties (those found in cosmology and astrophysics).

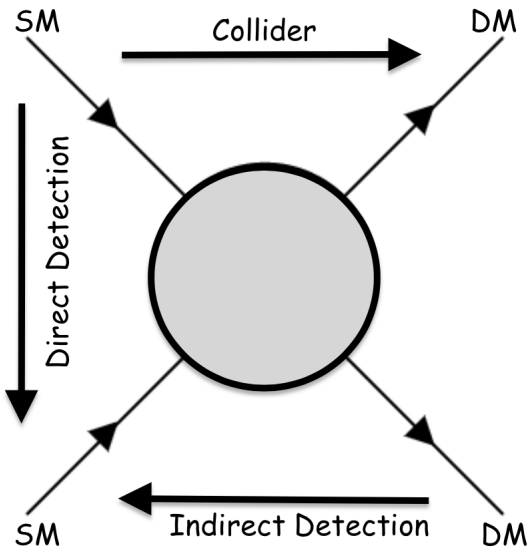

Figure 2.6.: An illustrative Feynman diagram that shows the three possible experimental approaches which include collider production, indirect detection and direct detection of DM.

As has already been discussed, particle physics which includes collider physics does not have a clear picture of a DM particle theory. This means we adopt several different approaches to cover the largest amount of DM parameter space possible. We will outline a few of these approaches and explain their strengths and weaknesses.

One of the approaches that is widely used is Effective Field Theory (EFT). For DM EFT, we assume that the DM particle is the only new particle beyond the SM that is within the energy reach of the LHC. The EFT in this context describes a contact-like interaction between the SM and DM mediated by the particles outside the kinematic reach of the LHC, see Figure 2.7. For DM masses that are smaller than the missing energy requirements (often used for experimental selection), the limits become independent of the DM mass and therefore LHC results can be very sensitive to very low DM masses [52].

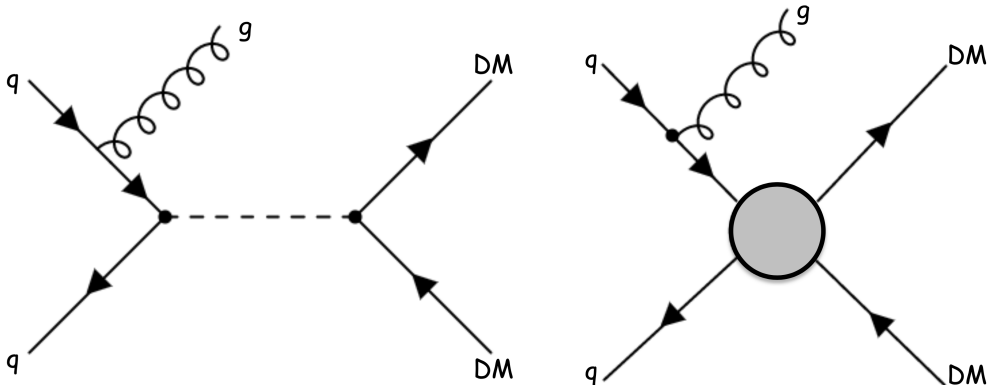

(a) Mediator model of DM production **(b)** EFT model of DM production

Figure 2.7.: The Feynman diagram on the left describes a DM mediator model and the diagram on the right is an EFT model.

The simplicity and model independence of the EFT approach is an attractive proposition, however, many of the interesting models which describe DM production at the LHC are not captured correctly by the EFT approach. These models often give a good picture if the energy scale of the interaction is small in comparison to the energy scale Λ (where Λ is a parameter that sets the energy scale at which new physics beyond the SM becomes important). In this case, we can use an effective operator to describe the effect of the heavy particles (mediator) in a low energy theory in which these particles have been integrated out. However, the LHC delivers very high energy events where a mediator particle could be produced, rendering this low energy approximation inaccurate. Therefore, EFTs have to be used in a careful and consistent way. In the context of the LHC a mediator mass of at least 10 TeV is required for a DM EFT to be considered a valid description of the SM [52]. However, at such large mediator mass scales, putting a constraint on Λ will correspond to large EFT coefficients, to values above the range where perturbative calculations are valid. It is therefore difficult to draw a clear correspondence between constraints from the EFT and to a more detailed model. It is also the case that gauge invariance is often not enforced for EFT operators and this can lead to an artificially inflated cross section due to broken gauge invariance.

On the other extreme, relative to the EFT approaches, are complete models such as Supersymmetry [43–46] or a Higgs-composite model [53, 54]. These models are, by definition, more theoretically sound[14] but crucially rely on many different parameters

[14]This means that the theory is well-motivated and self-consistent. In the specific context of particle physics, a theoretically sound model is one that is consistent with the principles of quantum

and therefore lack a lot of the generality that is obtained with an EFT model or simplified model.

Between these two extremes are the simplified DM models, which are widely used in collider physics literature. In simplified models, the DM particle and the mediator particle are kinematically accessible to the LHC, where an example Feynman diagram can be seen in Figure 2.7. These models essentially resolve the EFT contact operator into an s-channel or t-channel exchange of the mediator, see Figures 2.8 (a) and (b) respectively. Compared to their corresponding EFT models, simplified DM models introduce additional parameters such as the DM mass, mediator mass and the couplings of the mediator the SM and DM particles.

Common benchmark models were agreed within the LHC DM working group[15]. In the approach they undertook, the DM particle is described as a Dirac fermionic particle and the mediators can have scalar, pseudo-scalar, vector or axial-vector couplings. Minimal flavour violation is observed for these models by assuming Higgs-like coupling with the quarks for a scalar or pseudo-scalar mediator model, whilst for a vector or axial-vector mediator model they are assumed to have universal couplings to quarks. A reasonable question to ask is how we have managed to narrow it down to just these models. In a discovery scenario, small kinematic differences which can be found between different models and their corresponding distributions will not matter. Based on a lot of existing theoretical work [55–60], starting off with the assumption that DM is Dirac fermionic is sensible [52]. Different spins of DM particles will lead to, on the whole, similar kinematic results. Therefore, the choice of whether the particle is a Dirac or Majorana[16] fermion will have little effect on the kinematics of the visible particles.

2.7.1. Axial-Vector Mediator

We have motivated the case for simplified models. We will now take a look at our first model in some detail: the axial-vector mediator model for an s-channel exchange.

mechanics, special relativity and other known fundamental interactions. It should also be able to explain existing experimental data and make predictions that can be tested by future experiments.

[15] The LHC DM working group (WG), was established by ATLAS, CMS and the LHC physics centre at CERN in an attempt to standardise which models/parameters should be used in relation to DM.

[16] In simple terms, a Majorona particles is a fermion that is its own anti-particle and was hypothesised by Ettore Majorona in 1937. It is often used in contrast to the Dirac fermion which describes particles which are not their own anti-particle.

This is a simple extension of the SM with an additional U(1) gauge symmetry, where the DM candidate particle only has a charge under this symmetry (similar to the hypercharge). With the assumption that some SM particles are also charged under this new group, a new particle can mediate the interactions between the SM and DM. We can consider the case of a DM particle χ of mass m_χ which is a Dirac fermion, where in this example the production of the DM particle proceeds via the exchange of a spin-1 mediator in the s-channel, see Figure 2.8. This model has axial-vector couplings between the spin-1 mediator Z_A and can be described by the following Lagrangian:

$$\mathcal{L}_{\text{axial-vector}} = g_q \sum_{q=u,d,s,c,b,t} Z'_\mu \bar{q}\gamma^\mu\gamma^5 q + g_\chi Z'_\mu \bar{\chi}\gamma^\mu\gamma^5\chi \tag{2.33}$$

The coupling, g_q, is assumed to be universal to all quarks. Where the minimal set of parameters for this model is:

$$\{g_q, g_\chi, m_\chi, M_{\text{med}}\} \tag{2.34}$$

together with the spin structure of their couplings. The kinematic distributions are shown to be robust to changes in the specific values of coupling, therefore a choice of $g_q = 0.25$ and $g_\chi = 1$ seems reasonable to reduce the parameter space to be scanned [52]. The exclusion limits are therefore set on the mediator mass, M_{med}, and the dark matter mass, m_χ.

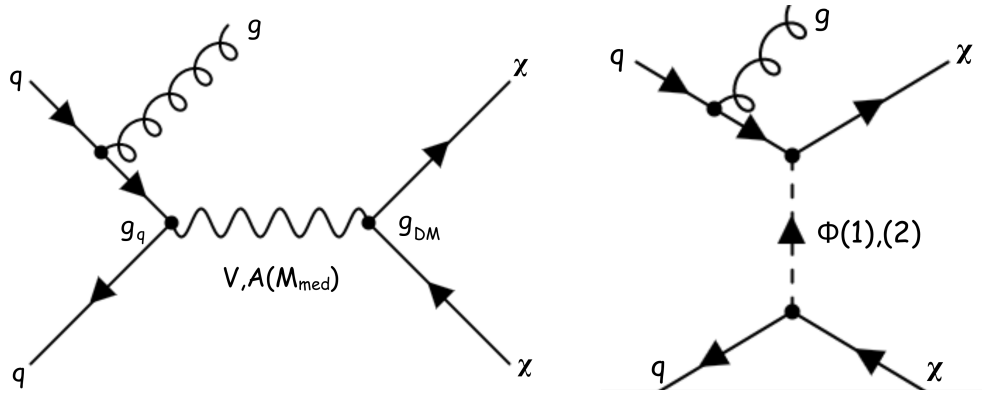

(a) Axial-vector mediator model in the s-channel for a monojet-like event

(b) Scalar model in the t-channel for a monojet-like event

Figure 2.8.: Example Feynman diagrams for the s-channel and t-channel for the simplified DM models.

Figure 2.9 shows the observed and expected 95% CL exclusion limits in the $m_{Z_A} - m_\chi$ parameter plane for the reconstructed monojet-like search in ATLAS. In the region $m_{Z_A} > 2 \times m_\chi$, mediator masses up to about 2.1 TeV are excluded for $m_\chi = 1$ GeV. The masses corresponding to the relic density [61] as determined by the Planck and WMAP satellites [62, 63], within the WIMP DM model and in the absence of any interaction other than the one considered, are shown in this figure as a line that crosses the excluded region at $m_{Z_A} \sim 1500$ GeV and $m_\chi \sim 585$ GeV.

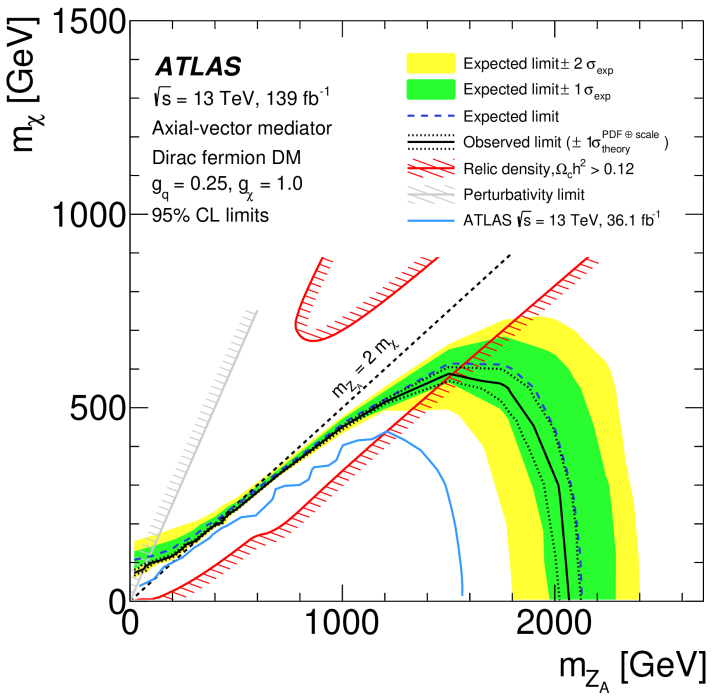

Figure 2.9.: Expected and observed exclusion for the axial-vector mediator model in the $m_\chi - m_{Z_A}$ plane of the recent ATLAS reconstructed monojet-like search [64].

2.7.2. Higgs to Dark Matter Decays

We can extend the SM by simply adding a new DM particle to it, which is also an isosinglet under the electroweak gauge group.[17] This is an iteration of what is known as a Higgs-portal model [65–68], which is essentially an EFT model where the Higgs decays to dark matter particles. One can write the Lagrangian as describing the spin-0,

[17] This approach is taken as it is rather model independent and does not make an assumption on the nature of DM.

spin-1/2 and spin-1 DM particles interacting with the SM Higgs field as:

$$\begin{aligned}
\mathcal{L}_S &= -\frac{1}{2}M_S^2 S^2 - \frac{1}{4}\lambda_S S^4 - \frac{1}{4}\lambda_{HSS}\phi^\dagger\phi S^2, \\
\mathcal{L}_V &= \frac{1}{2}M_V^2 V_\mu V^\mu + \frac{1}{4}\lambda_V (V_\mu V^\mu)^2 + \frac{1}{4}\lambda_{HVV}\phi^\dagger\phi V_\mu V^\mu, \\
\mathcal{L}_\chi &= -\frac{1}{2}M_\chi \overline{\chi}\chi - \frac{1}{4}\frac{\Lambda_{H\chi\chi}}{\Lambda}\phi^\dagger\phi\chi\chi
\end{aligned} \tag{2.35}$$

where $\lambda_{HSS}, \lambda_{HVV}, \lambda_{H\chi\chi}$ are the coupling of the Higgs to the DM particles. The production mechanism which is most sensitive to the Higgs to invisible decay is the Vector Boson Fusion (VBF) Higgs production channel because of its unique jet signature (two jets separated by a large pseudorapidity). We also look at the vector boson Higgs (VH) channel, where the vector boson decays into two hadronic jets and the Higgs itself decays invisibly. These two production mechanisms are shown in Figure 2.10.

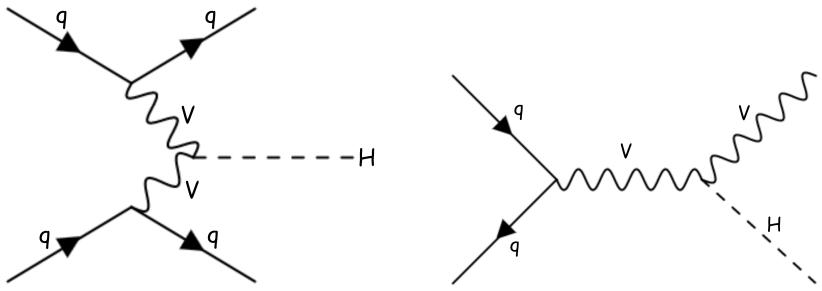

(a) VBF Higgs production mechanism

(b) VH production mechanism

Figure 2.10.: Feynman diagrams of the VBF and vector Higgs (VH) production channels.

A direct search for Higgs bosons produced via vector-boson fusion which decays into invisible particles has been done using 139 fb^{-1} of pp collision data at a centre-of-mass energy of $\sqrt{s} = 13$ TeV recorded with the ATLAS detector at the LHC. The observed number of events were found to be in agreement with the background expectation from SM processes and for a scalar Higgs boson with a mass of 125 GeV an observed upper limit of 0.145 is placed on the branching fraction of its decay into invisible particles at 95% confidence level, with an expected limit of 0.103. These results can be interpreted in the context of Higgs boson DM portal models and limits are set on the scattering cross section of WIMP particles and nucleons as well. These limits are shown in Figure 2.11.

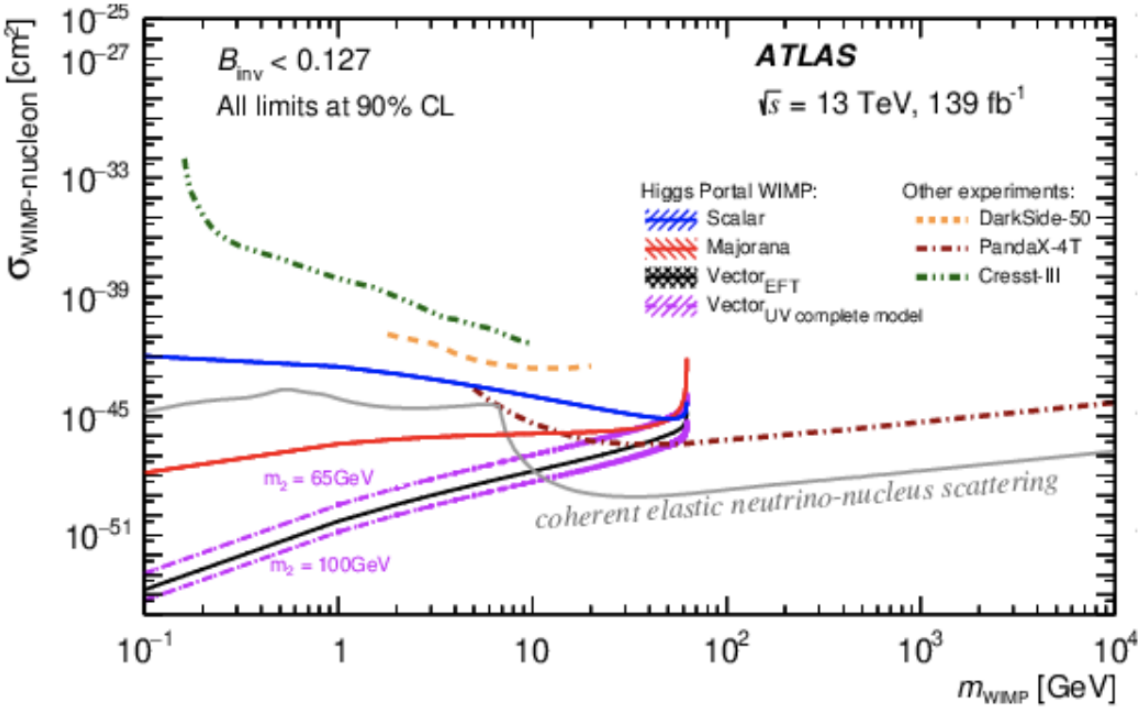

Figure 2.11.: These are the upper limits on the spin-independent WIMP-nucleon cross section using the Higgs portal interpretations of B_{inv} at 90 % CL vs m_{WIMP}. For the vector-like WIMP hypothesis, where the dependence on the mass m_2 of a new scalar particle (often predicted by renormalisable models) is shown for two different values taken from [69]. In comparison to direct searches for DM, this plot also shows the results from [70–72]. The neutrino floor for coherent elastic neutrino-nucleus scattering is taken from [73, 74]. The dependence on the choice of target nucleus is relatively small given the wide range of cross sections which are shown.

Chapter 3.

The ATLAS Experiment

"If science is to progress, what we need is the ability to experiment."
— Richard P. Feynman, 1918–1988

3.1. The LHC

3.1.1. LHC Design

The Large Hadron Collider (LHC) is the world's largest and highest energy particle collider [75]. It is an underground circular collider with a circumference of 26.7 km and a depth ranging from 50 to 175 metres located on the French-Swiss border. This concrete-lined tunnel[1] was built between 1983 and 1989, with it originally being used for the Large Electron-Positron (LEP) collider [76]. The tunnel contains two adjacent beam pipes with particles travelling in opposite directions in each pipe. The beams intersect at four different points around the tunnel, where each of the intersection points are the location of particle collisions. The four main detectors (ATLAS, ALICE, CMS and LHCb) are found at these collision points. There are 1,232 dipole magnets which keep the beam on a circular path and 474 quadropole magnets that focus the beams to maximise the interactions between the two beams of particles, and magnets of higher multipole orders are used to correct for small imperfections in the magnetic

[1] A tunnel was chosen to avoid purchasing expensive land on the surface, which would have an impact on the landscape, with the added benefit of using the Earth's crust for radiation shielding.

field of the dipoles [77,78]. More than 50 types of magnets are required to keep the charged particles on the desired path and the main dipoles are able to generate a powerful 8.3 T magnetic field which is over 100,000 times more powerful than the Earth's magnetic field [78]. In total, there are over 5,000 superconducting magnets and approximately 120 tonnes of super fluid Helium-4 is required to keep them at an operating temperature of 1.9 K ($-271.5\ ^{\circ}$C), this is colder than the average temperature of space [79,80]. The LHC primarily accelerates and collides protons, but it is also able to accelerate lead, xenon and argon ions which results, for the case of lead ions, in to either lead-lead collisions or lead-proton collisions (this happens about one month per year) [81]. The protons between 2015 and 2018 were accelerated to an energy of 6.5 TeV, meaning the total collision energy was 13 TeV. At this time, the protons were travelling at 0.999999990 of the speed of light, this means it took less than 90 µs for a proton to travel around the 26.7 km tunnel. This means the proton was able to circle the tunnel at 11,245 times per second. The proton beams were not continuous but were bunched together into 2,556 bunches where each bunch contained 115 billion protons. This meant that the interactions between the particles occured at discrete intervals, approximately 25 ns apart, and the bunches collided at a rate of 40 MHz [82].

Before the protons are injected into the LHC, they first need to be put into pre-accelerators which successively increased their energies. The first pre-accelerator is the linear particle accelerator LINAC4 [83], which came into operation in 2020, generating 160 MeV negative hydrogen ions (H^- ions) to prepare them for the Proton Synchotron Booster (PSB) [84]. The LINAC4 uses radiofrequency cavities to charge cylindrical conductors and the hydrogen ions pass through conductors which are alternatively positive and negative. This accelerates the particles and the quadrupole magnets focus these ions into a tight hydrogen ion beam. The electrons from the ions are stripped off during their injection into the PSB, leaving only protons. The PSB is the smallest circular proton accelerator and it accelerates the protons to 2 GeV for injection into the Proton Synchotron (PS) [85]. The PS then accelerates the protons to 25 GeV and are injected into the Super Proton Synchotron (SPS) [86], this then increases the particle energy to 450 GeV which are injected over the period of several minutes into the LHC. Figure 3.1 shows the pre-accelerator complex. The proton bunches then accumulate, and are subsequently accelerated over the period of 20 minutes to their collision energy (6.5 TeV for example) and are circulated around the ring for a duration of 5 to 24 hours where the collisions occur at the four collision points.

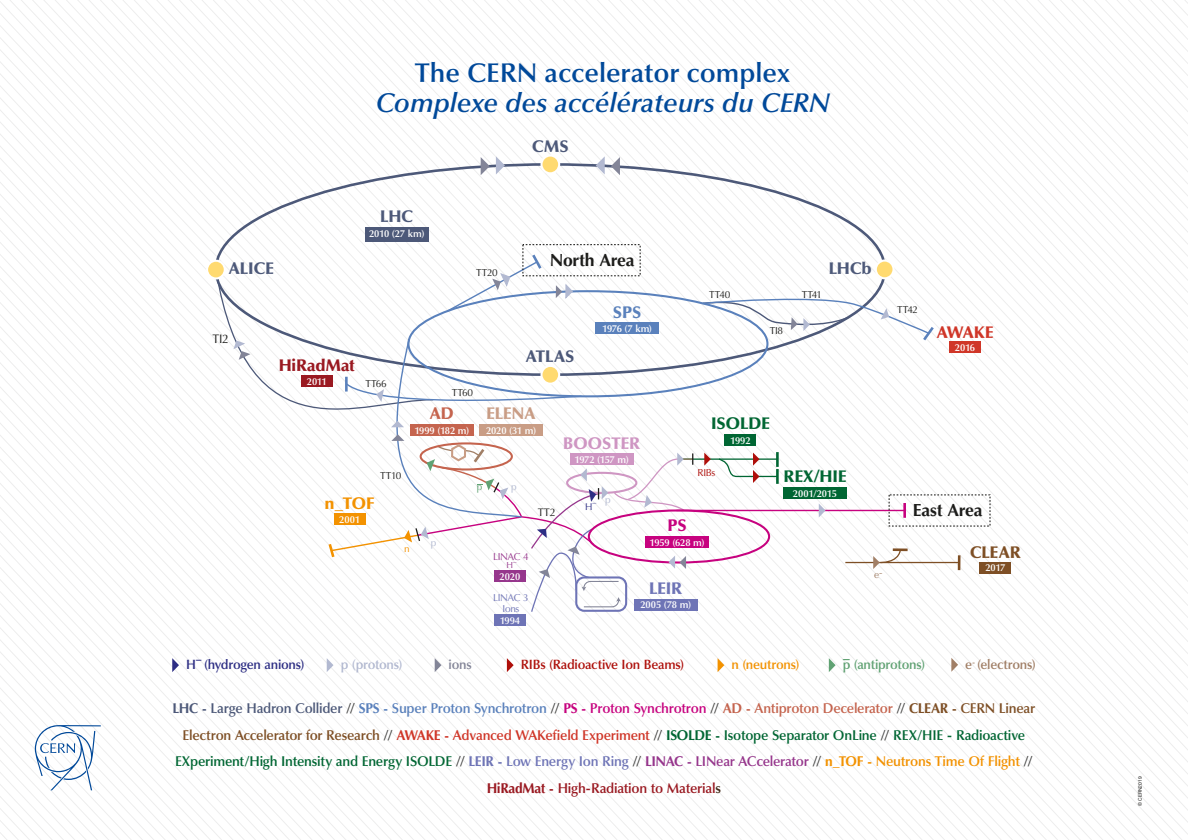

Figure 3.1.: The CERN accelerator complex which contains the pre-accelerators LINAC4, the PSB, the PS, the SPS and the main accelerator LHC [87].

3.1.2. Luminosity and Cross-Section

It is possible to quantify the level of interaction in terms of the cross-section, which can be mathematically defined as the interaction probability per unit flux, i.e.:

$$\sigma = \frac{1}{F} \int |\mathcal{M}_{fi}|^2 \mathrm{d}\phi \tag{3.1}$$

where $|\mathcal{M}_{fi}|^2$ is the Lorentz invariant matrix element and is essentially the probability of transition from one state to another, where the integral is taken over all available phase-space ϕ. The flux factor, F, accounts for the density of incoming states per area. The matrix element $|\mathcal{M}_{fi}|$ contains all the important physics and can be derived from the SM Lagrangian using QFT. The cross-section, σ, of the process is strongly dependent on the energy of the interacting partons and also the luminosity (particle

flux) in which the interaction rate, R, is given by:

$$R = \sigma \mathcal{L} \tag{3.2}$$

to calculate the number of interactions, the luminosity must be integrated over time:

$$N = \sigma \int \mathcal{L} \mathrm{d}t \tag{3.3}$$

where the $\int \mathcal{L} \mathrm{d}t$ is the integrated luminosity. In a proton-proton circular collider, where the beams collide head on, the luminosity is defined as:

$$\mathcal{L} = \frac{N_b^2 n_b f_{rev} \gamma}{4\pi \epsilon_n \beta^*} F_{\text{reduction}} \tag{3.4}$$

where N_b is the number of particles per bunch, n_b is the number of bunches per beam, f_{rev} is the frequency of revolution, γ is the Lorentz factor, [2] ϵ_n is the transverse emittance of the beam,[3] β^* is the beta function of the collision point (related to the transverse size of the beam at a certain point along the nominal beam trajectory) and $F_{\text{reduction}}$ is the reduction factor which is caused by the crossing angle at the interaction point.[4]

The β^* function is a measure of the size of the beams at the interaction point. In a circular collider, such as the LHC, the beam size varies along the trajectory due to the focusing effect of the magnets and this will determine the beam-beam interaction and hence the luminosity of the collider. A smaller β^* corresponds to a smaller beam size at the interaction point and therefore a higher luminosity.

A crossing angle is necessary to avoid unwanted collisions between the proton beams in the event that a particle is deflected from its' intended path due to a mis-alignment in the beam or magnetic fields for example. However having a crossing angle also reduces the probability of a collision between protons and also reduces the luminosity of the collider. Therefore, a balance must be struck between these

[2] The Lorentz factor is defined as $\frac{1}{\sqrt{1-\frac{v^2}{c^2}}}$, where v is the relative velocity between inertial reference frames and c is the speed of light in a vacuum.

[3] In accelerator physics, emittance is the area occupied by the beam in the position-momentum phase-space.

[4] The crossing angle refers to the angle at which the proton beams collide with each other at the interaction point.

two effects, and the crossing angle is optimised to maximise the luminosity while minimising the unwanted beam-beam interactions.

To obtain the highest possible luminosity, the numerator has to be maximised and the denominator minimised. This has been taken into account in the design of the LHC. Despite these efforts, there are inevitably losses from particle and beam scattering.

The High-Luminosity LHC (HL-LHC) is an upgrade of the LHC, which aims to increase the luminosity by a factor of ten compared to the current LHC [88]. To achieve this goal, several improvements have been proposed. One of the improvements is to reduce the crossing angle at the interaction point which will increase the probability of proton-proton collisions and hence increase the luminosity. The β^* function will also be reduced from 30 cm (value at current LHC) to 10 cm at the interaction point, which will further increase the luminosity [89]. These improvements will also increase the number of unwanted collisions and therefore the detector itself must be upgraded to cope with the increased number of events.

3.1.3. Pileup Events

During a collision of interest, there is normally a high energy proton-proton collision that the LHC experiments are interested in studying. There are also a large number of additional proton-proton collisions which will occur during the same bunch crossing and these result in events with low energy jets which are not of interest, these are known as pileup events. The majority of ATLAS analyses are only concerned with high energy collisions and therefore it is of critical importance to distinguish the hard scattering from pileup events, as a result much of the design of the LHC is based upon this aim.

3.1.4. LHC Status

Between 2010 and early 2013, in the data-taking period known as Run 1, the LHC collided protons at a centre of mass energy of $\sqrt{s} = 7$ TeV and $\sqrt{s} = 8$ TeV, collecting $\mathcal{L} = 5.08$ fb^{-1} and $\mathcal{L} = 21.3$ fb^{-1} of data respectively. In early 2013, the LHC was shut down for a two year upgrade and this was known as the Long Shutdown 1 (LS1). This upgrade involved enabling collisions at 14 TeV, upgrading the detectors and pre-accelerator (the PS and SPS) along with the ventilation system and replacing

100 km of damaged cabling.[5] In 2015, the LHC restarted after LS1 and collided protons at a centre of mass energy $\sqrt{s} = 13$ TeV.[6] Between 2015 to 2018, the LHC delivered 156 fb^{-1} and ATLAS recorded 147 fb^{-1} with 139 fb^{-1} of data being good for physics,[7] which is called Run 2. This is illustrated in Figure 3.2. The Long Shutdown 2 (LS2) started at the end of 2018, during which the LHC and the whole CERN accelerator complex was upgraded. These upgrades are devoted to preparations for Run 3 of the LHC, which will have an integrated luminosity equal to the two previous runs combined, and for the HL-LHC, the successor to the LHC. LS2 ended in April 2022. The Long Shutdown 3 (LS3) in the 2020s will take place before the HL-LHC project is operational in 2029. The LHC become operational again at end of April 2022 with a new maximum beam energy of 6.8 TeV (with a total centre of mass energy of 13.6 TeV). This run is expected to continue until 2026, and is known as Run 3.

[5] The cables were damaged by the radiation from the colliders.

[6] It was designed originally to safely handle a centre of mass energy of $\sqrt{s} = 14$ TeV, however, the bending magnets were only able to handle $\sqrt{s} = 13$ TeV due to the delays with the training.

[7] The good for physics criteria requires all reconstructed physics objects to be of high reconstruction efficiency, low misidentification rate and conserve energy.

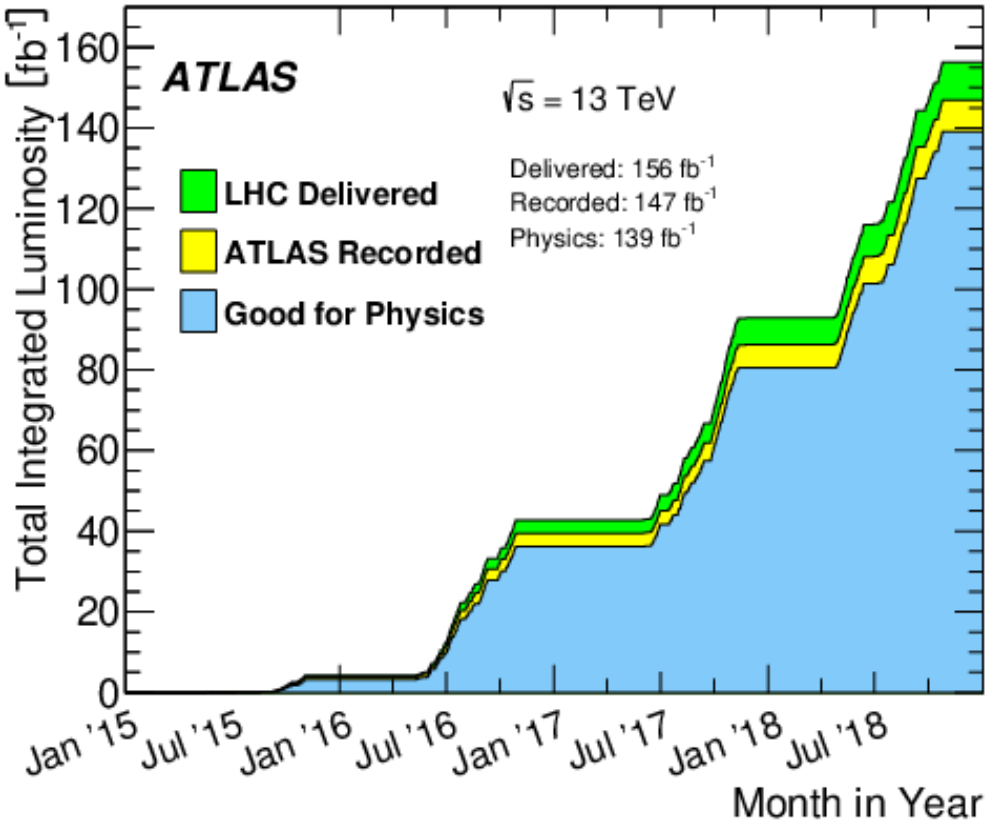

Figure 3.2.: This plot shows the cumulative luminosity versus time delivered to ATLAS (in green), recorded by ATLAS (in yellow) and pass the data quality checks (blue) during stable beams for proton-proton collisions at a 13 TeV centre of mass energy in 2015-2018. This Figure is taken from [90].

3.2. The ATLAS detector

The ATLAS (A Toroidal LHC ApparatuS) detector is one of the four main experiments at the LHC [91]. It is a multipurpose experiment designed to take advantage of the unprecedented energy available at the LHC and help us study phenomena that occur at energies no other collider has produced before. ATLAS was one of two experiments (the other being CMS) to discover the Higgs boson [11, 12] and is now exploring the widest possible range of physics phenomena, from measuring SM physics at high precision to physics beyond the SM, all done at unprecedented collider energies. In terms of analyses, the detector's aim is to gain precision in SM measurements such as vector bosons, jet production, diboson studies and studying the properties of the Higgs and top quark and searching for new physics such as extra dimensions, SUSY-like

particles, micro-blackholes, DM and other exotic particles predicted by various BSM theories.

ATLAS is the largest detector ever (in terms of volume) constructed for a particle collider and is 44 m long and 25 m in diameter. It is a multi-layered detector in which each layer or sub-detector has a specific purpose. It sits in an 100 m deep underground cavern and it weighs 7,000 tonnes [92].[8] The ATLAS detector itself consists of approximately six cylindrical layers around the collision point, and this is divided into four main sections of the detector: the inner detector, the calorimeters, the muon spectrometer and the magnets. Each of the sections have multiple components, where each sub-detector is complementary to each other. The inner detector tracks the particles precisely, the calorimeters measure the energy of the particles and the muon spectrometer helps to measure the muons efficiently.[9] The magnet system bends the charged particles in the inner detector and also the muon spectrometer, this bending allows us to measure the momentum. The ATLAS detector is shown in Figure 3.3, which shows all the individual components.

3.2.1. Coordinate System

The ATLAS collaboration uses a right-handed coordinate system with the collision point being at the centre, where the z-axis is along the beam direction, the x-axis is horizontal to the beam and the y-axis is upwards from the collision point at a slight tilt (in line with the tilt of the collider beam). Due to the cylindrical shape of the collider, it is useful to make use of the spherical coordinate system (r, ϕ, θ). In this system, ϕ, is the azimuthal angle and is defined as the x-y plane transverse to the z-axis, θ, is the angle relative to the z-axis and r is the radial distance from the x-y-z origin.

A variable called the pseudorapidity,[10] η, is defined as:

$$\eta = -\ln\left(\tan\left(\frac{\theta}{2}\right)\right) \tag{3.5}$$

[8] This is the same weight as the Eiffel tower.

[9] The muon is a minimally ionising particle (i.e., it travels far before decaying). Therefore having the additional track from the muon spectrometer, which can be matched with the track from the inner detector, means that muon can be measured more efficiently.

[10] This variable is not Lorentz invariant

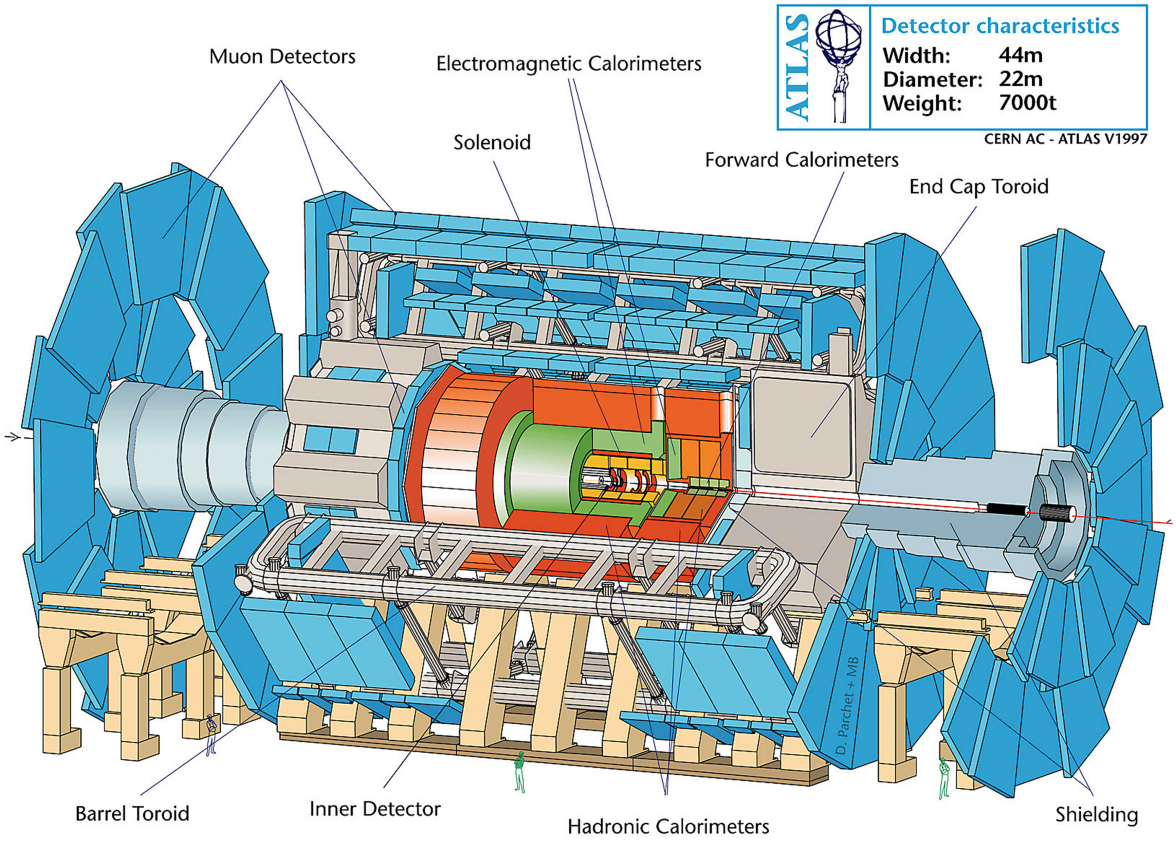

Figure 3.3.: A schematic layout of the ATLAS detector [93].

with values between $(-\infty, \infty)$. In hadron collider physics, the pseudorapidity, η, is preferred over θ because particle production is approximately constant as a function of pseudorapidity.

The rapidity, y, is a Lorentz-invariant quantity that describes the particle's motion in the direction of the beam axis and can be written as a function of the particle energy, E, and the longitudinal momentum, p_l:

$$y = \frac{1}{2} \ln \left(\frac{E + p_l}{E - p_l} \right). \tag{3.6}$$

The rapidity, y, and the pseudorapidity, η, are often used in particle physics as the differences (e.g. $\Delta\eta = \eta_1 - \eta_2$) are Lorentz invariant and these variables are useful for describing the kinematics of the collision.

The angular distance, ΔR, between two different points is therefore defined as:

$$\Delta R = \sqrt{\Delta\phi^2 + \Delta\eta^2}, \tag{3.7}$$

and is often used to describe the radius of jets.

3.2.2. Inner Detector

The Inner Detector (ID) is the innermost layer of ATLAS and is used to measure the charged decay products of high-energy collisions; it is therefore very compact and highly sensitive [94]. It is placed within a 2 T magnetic field, which is generated by a solenoid magnet surrounding the inner detector. The magnetic field bends the charged particles; how much they curve depends on their respective charge and momentum. The ID then tracks the charged particles and is able to measure the momentum and charge from the particles curvature. Using these tracks, it is possible to reconstruct the primary interaction vertex and also the secondary vertices. The tracking resolution and the pseudorapidity range of the ID is shown in Table 3.1. The requirements for the resolution and pseudorapidity of the ID were driven by the need to accurately reconstruct the primary and secondary vertices of the collisions and to identify the decay products of short-lived particles such as b-hadrons. The high resolution in the transverse plane given in Table 3.1 are necessary to achieve the desired precision for tracking and vertex reconstruction, while the coverage up to $|\eta| < 2.5$ was chosen to ensure that the ID covers the central region of the detector, where most of the interesting physics occurs and also due to the high radiation which occurs in the forward region. The ID begins a few centimetres away from the collision point and is 6.2 m in length along the beam pipe (see Figure 3.4). It is made up of four different components:

- the pixel detector,
- the Insertable B-layer (IBL),
- the semiconductor tracker (SCT),
- the transition radiation tracker (TRT).

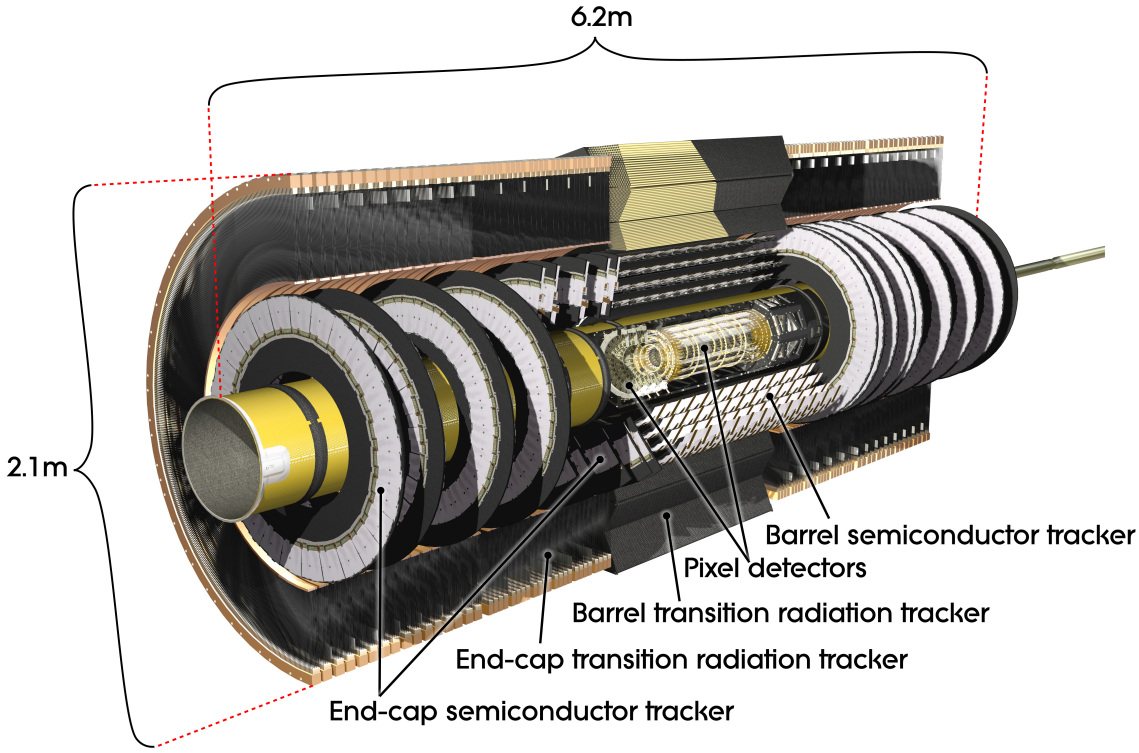

Figure 3.4.: A schematic layout of the Inner detector [95].

Pixel Detector

The pixel detector is located 3.3 cm from the interaction point, which is the first place where particles are detected [94, 96]. It is made up of four layers of silicon pixels, with each pixel being of dimension 50 µm $\times$ 400 µm ($\sim$90% of them) or 50 µm $\times$ 600 µm ($\sim$10% of them), for reference, both of these are smaller than a grain of sand. The microscopic pixel size provides extremely high precision tracking close to the collision point, where the resolution is 10 µm and 115 µm in the transverse and longitudinal directions respectively.[11] In LS1, the ATLAS collaboration constructed and inserted the fourth innermost layer called the Insertable B-Layer (IBL). This is located 3.3 cm from the beam pipe and the main function of this layer was to improve the b-tagging efficiency and reduce the rate of fake tracks. It is a barrel-shaped layer which has smaller size of pixels (50 µm $\times$ 250 µm) than the other layers and incorporates new

[11] The resolution parameters in the ATLAS detector are defined as the uncertainties in the measured quantities such as momentum and energy of the particles passing through the detector. These can be determined with a combination of simulation studies and calibration measurements using known particle tracks.

technology which is more resistant to radiation damage than the rest of the ID.[12] Overall the pixel detector is very compact, it has over 92 million pixels and it has almost 2000 detector elements [94, 96].[13]

Semi-Conductor Tracker

The semi-conductor tracker (SCT) is the middle component of the ID, it has a similar concept to the pixel detector with the exception that, instead of pixels, the SCT consists of long narrow silicon strips [94, 96, 98].[14] Each of these strips has a dimension of 80 µm $\times$ 12 cm, and due to the SCT having a larger area than the pixel detector, it plays a very important role in tracking particles in the plane perpendicular to the beam axis. The SCT is made up of more than 4,000 modules, and each module contains many silicon strips used to track the paths of charged particles. In total, the SCT has around 6 million of these silicon strips arranged perpendicular to the direction of particle motion. The layout is optimised such that each particle crosses at least four layers of silicon and has an area covering 64 m^2. In a typical good quality track, at least three pixel layers and eight SCT layers are crossed by the particle [94, 96, 98].

Transition Radiation Tracker

The third and final layer of the ID is the Transition Radiation Tracker (TRT) and this is the outermost component [94, 96, 99]. The TRT is a combination of a straw tracker and a transition radiation detector. The TRT consist of 370,000 cylindrical drift tubes (or straws). Each straw, which is 4 mm in diameter and consists of polyimide film with a conducting coating, acts as a cathode and is kept at a high voltage (-1500 V). The straws are filled with a gas mixture, the majority of which is xenon (70%) followed by

[12] The new technology used in the IBL is based on the 3D silicon pixel sensor technology, which allows for a higher radiation tolerance and better performance in high-rate environments compared to the planar sensors used in the other layers. The electrodes in the 3D sensors are etched inside the silicon substrate, this reduces the distance that charge carriers need to travel and improves the signal-to-noise ratio. As well as the 3D sensors being made using a new fabrication technique that uses high-purity silicon and a low temperature oxidation process, meaning an enhancement in the radiation hardness of the sensors [97].

[13] This refers to the individual readout chip bonded to a single silicon sensor module. The pixel detector is constructed from many such detector elements arranged in a grid to form a larger module. Each detector element consists of a silicon sensor that is divided into an array of small pixels, and an associated readout chip which amplifies and digitizes the signals from the pixels. The entire assembly (silicon sensor plus readout chip) is typically referred to as a module.

[14] This makes it affordable to cover a large area.

CO_2(27%) and O_2(3%), in which the CO_2 and O_2 increase the electron drift velocity and help to quench photons. The straw tubes have a resolution of 200 µm, whilst not as precise as the pixel or SCT detector, it covers a large volume.

Each of these xenon-based straws become ionised when a charged particle passes through, in which the straws high voltage drives the negative ions towards the 30 µm gold-plated tungsten wire in the centre of the straw. Once the ions hit the wire, they produce an electronic signal and the time delays between the different hits makes it possible to reconstruct the path of the charged particle. The spaces between the straws are filled with polymer fibres and this creates transition radiation. This transition radiation provides information on the particle type that passed through (i.e., whether it was an electron or pion) [94, 96, 99].

3.2.3. Calorimeters

Calorimeters are designed to absorb the energy from the particles (thereby measuring it) until the point where the particles come to a complete stop. The ATLAS calorimeter is shown in Figure 3.5, and consists of two different types of calorimeters: the liquid argon and the tile calorimeter which cover a pseudorapidity range of up to $|\eta| < 4.9$ and are located just outside the solenoidal magnet which surrounds the ID [100, 101]. As illustrated in Figure 3.5, the ATLAS calorimeter consists of layers of high density material, designed to absorb the particles, intertwined with layers of an active medium which measures the energy. The granularity of the EM calorimeter is the same as that of the ID, where the EM calorimeter measures the energy of the photon and the electron. The hadronic calorimeter is dedicated to measuring hadronic particles (which can be conceptualised as jets due to the showering which occurs from them), in which a coarser granularity is sufficient [100, 101].

Electromagnetic (EM) Calorimeter

The EM calorimeter or liquid argon (LAr) calorimeter surrounds the ATLAS ID and is able to measure the energy of electrons, photons and hadrons [100, 101]. The LAr calorimeter is divided into three longitudinal layers: a barrel component ($|\eta| < 1.475$) and two end-caps ($1.375 < |\eta| < 3.2$), as shown in Figure 3.5. The resolution of the electromagnetic calorimeter is shown in Table 3.1. It features layers of metals (tungsten, copper or lead) that absorb incoming particles and then converts them into a shower

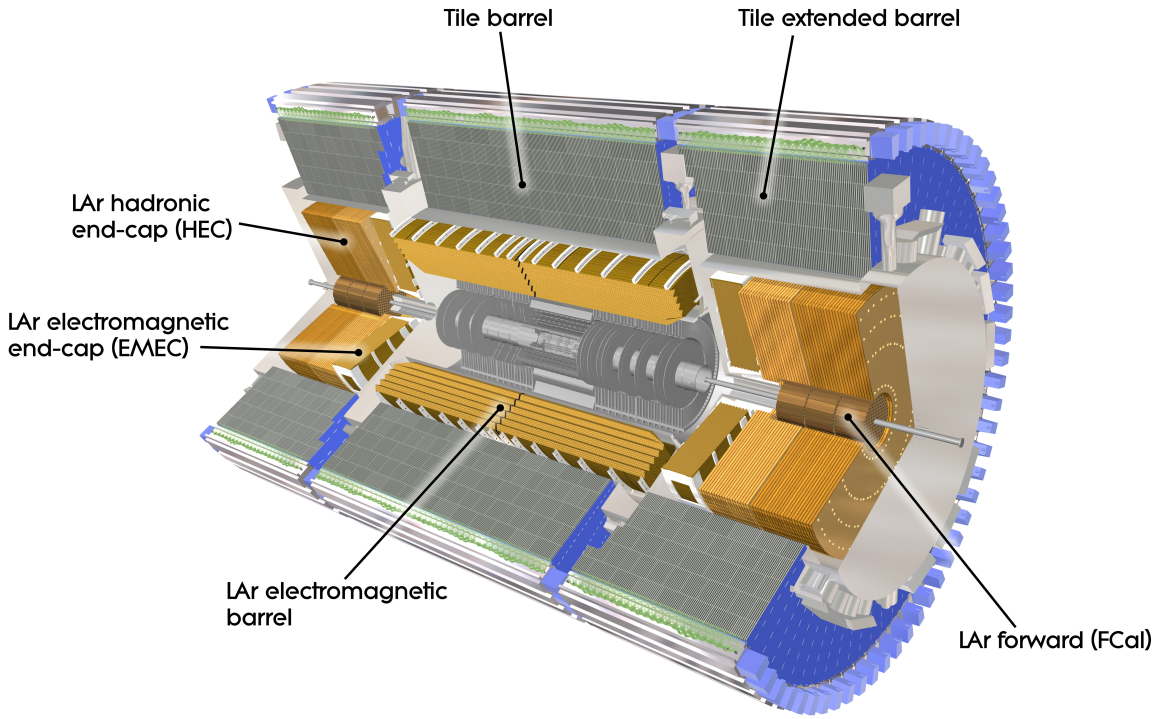

Figure 3.5.: A schematic layout of the electromagnetic and hadronic calorimeter [102].

of new lower energy particles. These lower energy particles ionise the liquid argon that is layered in between the metal components, this in turn produces an electric signal which gives us an output. By combining all these signals, it is possible to infer the energy of the original particle that hit the calorimeter. The middle layer has a granularity of $\Delta\eta \times \Delta\phi = 0.025 \times 0.025$ and most of the transverse energy, E_T, from the electrons and photons are collected here. It has an accordion-like structure, with a honeycomb pattern to make sure that every particle that can be detected, is detected. The first longitudinal layers of the LAr calorimeter is called the strip layer and offers excellent $\gamma - \pi^0$ discrimination. The last longitudinal layer has a coarser granularity and measures the end of the electromagnetic showers. The argon needs to be kept at -184 $^{\circ}$C so as to be in liquid form. There are vacuum-sealed cylinders of cables which carry the signal from the LAr to the warmer area where the readout electronics are located [100, 101]. The requirements for the resolution and pseudorapdity, η, coverage of the EM calorimeter (given in Table 3.1) were driven by the need to accurately measure the energy of electrons and photons, which interact primarily via bremsstrahlung and pair production. Therefore, the EM calorimeter must have excellent energy resolution and good spatial resolution to distinguish closely

spaced electromagnetic showers. The coverage of up to $|\eta| < 3.2$ was chosen to ensure that the EM calorimeter covers the central region of the detector to contain the majority of electromagnetic showers. Electromagnetic showers typically extend over several radiation lengths (where the number of radiation lengths is proportional to energy), hence the relatively wide $|\eta|$ range.

Hadronic Calorimeter

The hadronic calorimeter is made up of three sections. The tile calorimeter, commonly known as TileCal, is located in the central section and covers a pseudorapidity range up to $|\eta| < 1.8$. The hadronic end-caps covers the range $1.5 < |\eta| < 3.2$ and the forward region covers from $3.1 < |\eta| < 4.9$ [100,101]. The resolution of the hadronic calorimeter is shown in Table 3.1. The requirements for the resolution and pseudorapidity coverage were driven by the need to accurately measure the energy of the hadrons in order to reconstruct jets. The coverage of the hadronic calorimeter is large than the EM calorimeter due to the fact that hadrons tend to be produced at larger angles with respect to the beam line than electrons and photons.[15] The hadronic showers energy consists of three components: the electromagnetic fraction, the ionisation energy by charged hadrons and also the invisible fraction of energy. Due to the invisible energy fraction and the large energy fluctuations associated with hadronic showers, the energy resolution is worse compared to the electromagnetic case.

The TileCal is located in the central region of the hadronic calorimeter and consists of layers of steel and plastic scintillating tiles. It is composed of four components, two barrels and two extended barrels, as can be seen in Figure 3.5. The calorimeter consists of about 420,000 scintillator tiles, and they work all in unison to detect hadronic particles. It is also the heaviest part of the ATLAS experiment, weighing almost 2,900 tonnes. The TileCal functions in the following manner: as particles hit the layers of steel they generate a shower of new particles. These new particles interact with the scintillating tiles, which themselves emit photons that are captured by fibres at the

[15] Hadrons are produced larger angles with respect to the beam line than electrons and photons as they are composite particles made up of quarks and gluons. These composite particles undergo multiple interactions before they undergo hadronisations. These interactions cause the initial partons to lose energy, and the hadronisation process also involves the emission of additional particles which carry away energy and momentum. This results in hadrons being produced with a broader distribution of energies and momenta, and therefore at larger angles with respect to the beam line compared to electrons and photons, which are fundamental particles and do not undergo these multiple interactions.

edge of the tiles. These photons are converted to an electric current and their intensity is proportional to the original particle energy [100, 101].

Forward Calorimeter

There are many "low" p_T or "soft" minimum bias collisions that in turn means the detector components measure these types of particles which leads to several problems. In particular, the forward calorimeter (FCal) near the beam direction will have a constant bombardment of particles which create a low level of ionisation in the electrode gaps at every bunch crossing [103]. At high luminosities, these minimum bias particle densities and energies are at their maximum at high pseudorapidities $|\eta|$ (i.e., in the forward and backward directions). Calorimetry is currently the most adept of the detector technologies available for functioning in a harsh environment. The ATLAS forward calorimeter covers the pseudorapidity region $3.1 < |\eta| < 4.9$ and is a liquid argon, ionisation sampling calorimeter. It is located 5 m from the interaction point, where the resolution of this detector is shown in Table 3.1. A major objective of forward calorimetry is to help with reconstructing the p_T^{miss}. High p_T neutrinos and other weakly interacting particles will escape detection but their presence can be inferred from observing events with a large transverse momentum imbalance. Jets often escape detection, frequently down the beam hole or the jets are badly mismeasured. The FCal closes as much of this beam hole as is possible.

3.2.4. Muon Spectrometer

One might ask why is there a need for a muon spectrometer if there is an electromagnetic calorimeter which detects charged particles like the muon. The reason for this is that the muons are not stopped by the calorimeter as they do not experience the same decrease in acceleration (due to them being 200 times heavier than the electron) and therefore do not experience as much bremsstrahlung as the electron [101, 104]. The ID does detect the muons, however the muon spectrometer is used to distinguish the muons from the other charged particles.

The muon spectrometer is an extremely large tracking sub-detector and it consists of three main components:

1. A barrel toroid and two end-cap toroids, which produce a magnetic field of approximately 0.5 T and 1 T respectively,
2. 1,200 chambers which measure muon tracks to a high precision,
3. A set of trigger chambers with excellent time resolution.

The spectrometer starts at a radius of 4.25 m from the collision point and goes out to a radius of 11 m. It is required to have this large radius so it can accurately measure the momentum of muons. It functions in a manner not too dissimilar to the ID, with muons being able to curve in the magnetic field. This allows us to measure the muon momentum with precision.[16] The resolution of the muon spectrometer is shown in Table 3.1.

Within the spectrometer, there are monitored drift tubes (MDTs), see Figure 3.6, and these cover most of the pseudorapidity range of the muon spectrometer. These MDTs are composed of 3 cm wide aluminium tubes which are filled with a Ar:CO_2 (93:7) gas mixture. The muons pass through these tubes knocking electrons out of the gas. The electrons then drift to the centre of the tube where they hit a wire, which is then detected as an electronic signal. There are 380,000 of these aluminium tubes stacked in several layers to precisely track the muons.

Within the spectrometer, there are also fast response detectors which quickly select collision events which are of potential interest for physics analyses (the decision on selection is made within 2.5 µs). The Resistive Plate Chambers (RPCs) surround the middle section of the muon spectrometer. They consist of pairs of parallel plates (made of plastic) with a electric potential differences and between the pair of plates is a $C_2H_2F_4$ (94.7%)–C_4 H_{10} (5%)–SF_6 (0.3%) gas mixture. At the ends of the spectrometers are Thin Gap Chambers (TGCs) which consist of very thin parallel wires (30 µm) in a CO_2(55%)-C_5H_{12}(45%) gas mixture. Both the RPCS and TGCs detect muons when the gas mixture is ionised and the resulting electrons are attracted to the plate and wire respectively to produce an electronic signal. The data from these fast-response detectors gives us a coarse measurements of the muon momentum, it also helps to identify the corresponding ID track and also an insight into whether or not to keep or discard the collision [101,104]. The requirements for the resolution and pseudorapidity coverage of the muon spectrometer, given in Table 3.1, are driven by the need to accurately measure the momentum of muons. The pseudorapidity coverage, $|\eta|$, of

[16] For example, we can measure a muon of momentum 100 GeV with 3% resolution and a 1 TeV muon with 10% resolution.

the muon spectrometer is smaller than the other sub detector since the muons have a tendency to travel in straight lines and are not deflected as much by the magnetic fields as other charged particles. One of the main design features that contributes to the high resolution of the muon spectrometer, is it's size. It is able to make use of the fact that muons are highly penetrating particles which can travel through many layers of material without interaction. This property allows the muon spectrometer to measure the momentum and direction of muons with high precision, since the muons do not lose much energy in changing direction as they travel through the detector.

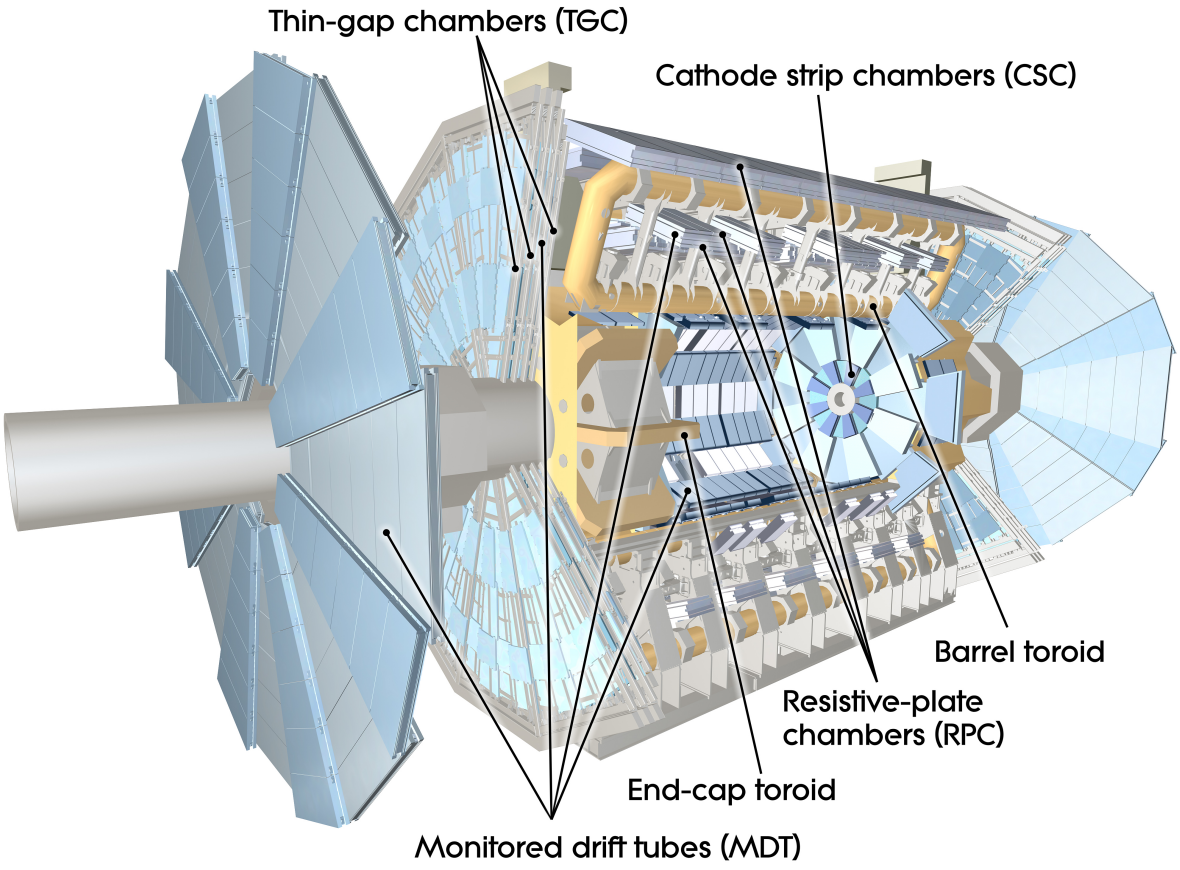

Figure 3.6.: A schematic layout of the muon spectrometer [105].

3.2.5. Trigger and data acquisition

The ATLAS detector sees up to 1.7 billion collisions per second. However, not all of these events are of interest from a physics standpoint [106, 107]. The trigger and data acquisition (DAQ) system is there to ensure optimal data-taking condition and

also selects the most interesting events to study. The trigger system is designed to reduce the 40 MHz rate of proton bunch crossings in the LHC to a rate of 1 kHz for data storage. There are various trigger algorithms which aim to select the interesting physics processes for further offline analyses. The trigger system uses the fact that there are high momentum electrons, photons, jets, muons along with taus decaying hadronically and also missing transverse energy to make split second physics decisions. A schematic of the ATLAS Trigger and DAQ system is shown in Figure 3.7.

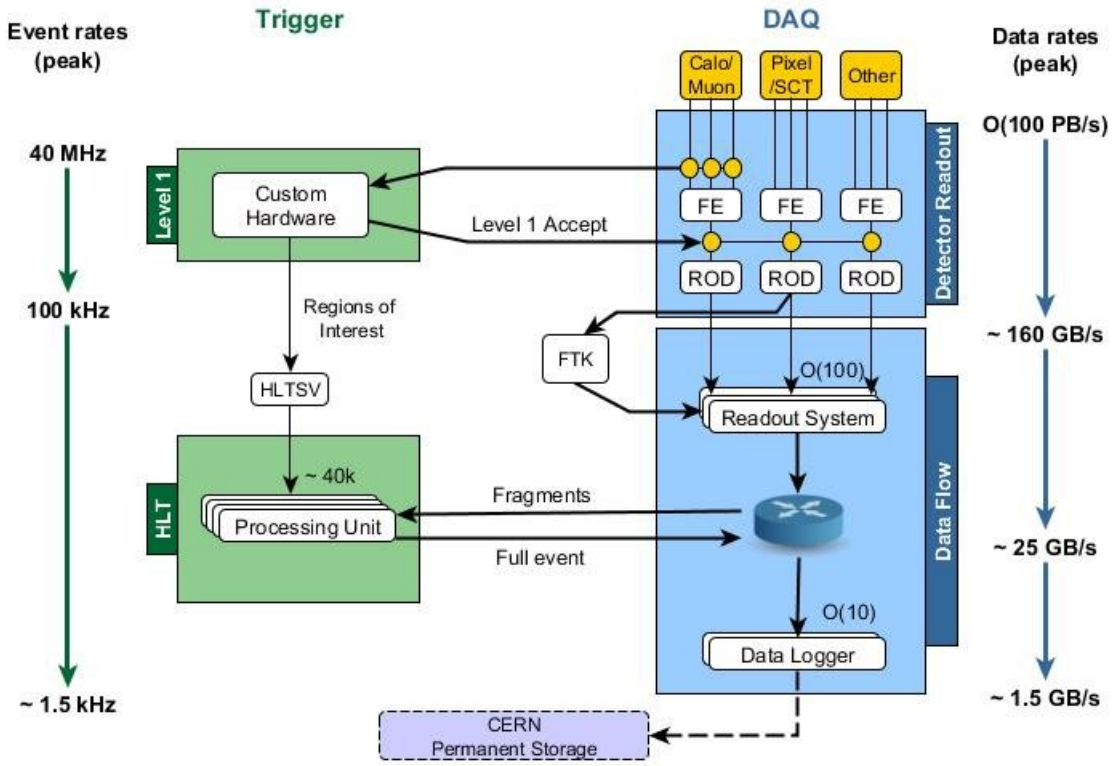

Figure 3.7.: A schematic layout of the ATLAS trigger an DAQ system in LHC Run 2 [108]. Events passing the level 1 hardware trigger are passed to the High Level Trigger (HLT). Simultaneously, event data read from the detector front electronic system are sent to the ReadOut System (ROS) in response to the acceptance of the signal by the level 1 trigger. This event data is buffered in the ROS and is made available to the HLT algorithms. If the HLT accepts the event, it is sent to permanent storage through the data logger.

In Run 2, the trigger system was divided into two levels. The first level of the trigger system is the hardware level trigger and was implemented in dedicated electronics which uses the coarser granularity in the muon spectrometer and the calorimeters

Detector component	Required resolution	η coverage	
		Measurement	Trigger
Tracking	$\sigma_{p_T}/p_T = 0.05\% p_T \oplus 1\%$	± 2.5	± 2.5
Electromagnetic Calorimeter	$\sigma_E/E = 10\%/\sqrt{E} \oplus 0.7\%$	± 3.2	± 2.5
Hadronic Calorimeter (jets)			
barrel and end-cap	$\sigma_E/E = 50\%/\sqrt{E} \oplus 3\%$	± 3.2	± 3.2
forward	$\sigma_E/E = 100\%/\sqrt{E} \oplus 10\%$	$3.1 < \lvert\eta\rvert < 4.9$	$3.1 < \lvert\eta\rvert < 4.9$
Muon spectrometer	$\sigma_{p_T}/p_T = 10\%$ at $p_T = 1$ TeV	± 2.7	± 2.4

Table 3.1.: The resolution of the various subdetectors of ATLAS. The units for E and p_T are in GeV. This table is taken from [101]. The resolution and pseudorapidity coverage requirements for the various subdetectors of ATLAS are primarily driven by the physics goals of the experiment.

to make a decision on whether or not the event is kept and reduces the rate from 40 MHz to 100 kHz. The second level, which is called the High Level Trigger (HLT), is software-based and uses a sequence of algorithms to refine to decision made by the first level trigger. This uses the full detector granularity, including the ID tracker. Depending on the signature, it either reconstructs the region of interest (ROI) around the signature or it can reconstruct the full event. The HLT reduces the input from 100 kHz to 1 kHz, which is then stored. If an event makes it through the trigger system, it is classified based on the fulfilled trigger conditions [106, 108]. There is a dedicated computer farm at Point 1 in CERN that runs the offline reconstruction software on events accepted by the HLT, and this data is then stored at the CERN data centre (commonly known as tier 0). The amount of data collected per event is about 1 MB, and therefore the amount of data collected by ATLAS per year is around 22 PB. The data and luminosity are often used interchangeably in analyses, where the luminosity corresponds to the number of collisions per second and unit area and the data rate is deduced from the events per second.

3.2.6. Particle Identification

The detector is designed to identify and distinguish particles, as discussed in the previous section and this is done using various different subdetectors, see Figure 3.8. For example, electrons and photons deposit their energy in the electromagnetic calorimeter, in addition to this the electron leaves a track in the ID. The muons meanwhile leave a

track in the ID and are also detected by the muon spectrometer. Hadrons are measured in the hadronic calorimeter, and if charged, leave a track in the ID. The hadrons are detected as showers or jets and are normally reconstructed by the anti-k_T clustering algorithm [109].

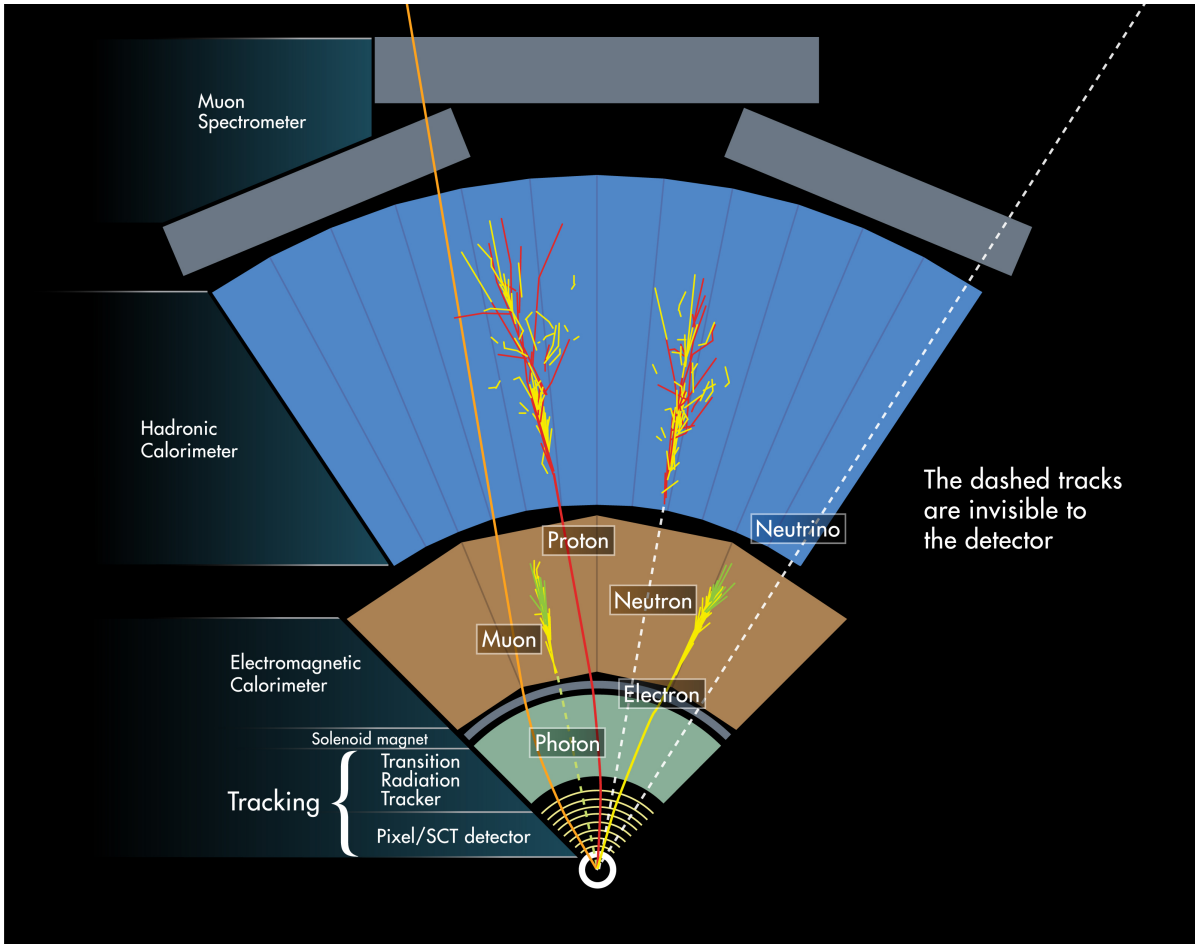

Figure 3.8.: A diagram illustrating how particles are detected by the ATLAS detector [110].

Particle Flow Algorithm

In Run 1 of the LHC, the ATLAS experiment used either the calorimeters only or the ID only to reconstruct hadronic jets or soft particle activity. The vast majority of analyses used jets that were constructed from the topological clusters in the calorimeter cells [111]. These jets were then calibrated to the particle level using a jet energy scale (JES) correction factor [112, 113]. For the final Run 1 jet calibration, the correction factor also took into account the tracks associated with the jet and this greatly improves the jet resolution [112]. The particle flow algorithm introduces an alternative approach,

in which measurements from both the tracker and the calorimeter are combined to form the signals which ideally represent individual particles. All the energy deposited in the calorimeter by the charged particles is removed. The jet reconstruction is then performed on an ensemble of "particle flow objects" consisting of the remaining calorimeter energy and tracks which are matched to the hard interactions, regardless of whether they occurred at a single vertex or multiple vertices in the event, with a focus on the primary interaction. Due to the enhanced performance the particle flow algorithm gives, this is what we use in our analysis. The advantages of integrating the tracking are:

- For low energy charged particles, the momentum resolution of the tracker is significantly better than the energy resolution of the calorimeter. However, at high energies, the calorimeters energy resolution is superior to the momentum resolution for the tracker.
- The acceptance of the detector is extended to softer particles, as tracks are reconstructed for charged particles with a minimum transverse momentum p_T >400 MeV, whose energy deposited often do not pass the noise thresholds required to see the topological clusters.
- Angular resolution of a single charged particle which is reconstructed using the tracker is much better than the calorimeter.
- The capabilities of the tracker in reconstructing charged particles are complemented by the calorimeters ability to reconstruct both the charged and neutral particles.

Therefore a combination of the two sub-detectors is preferred for optimal event reconstruction. Outside the geometrical acceptance of the tracker, only the calorimeter information is available. Hence, in the forward region the topological clusters alone are used as inputs to the particle flow jet reconstruction [114].

3.2.7. Missing Transverse Momentum

The missing transverse momentum ($\not{E}_{\mathrm{T}}$) is an important observable which serves as an experimental proxy for the transverse momentum carried by undetected particles produced in pp collisions measured with the ATLAS detector. It is reconstructed from the signals of the various detected particles in the final state. A non-zero value may

indicate not just the production of SM neutrinos but also the production of new BSM particles which escape the ATLAS detector without being detected. The reconstruction of $\not{E}_{\mathrm{T}}$ is challenging as it involves all sub detectors and requires the most complete representation of the hard interaction of interest by the calorimeters and trackers. The $\not{E}_{\mathrm{T}}$ is limited by detector acceptance, signals and signal remnants from additional pp interactions occurring in the same, previous and subsequent LHC bunch crossings (pileup) relative to the hard interaction. ATLAS has been able to develop successful strategies for a high-quality $\not{E}_{\mathrm{T}}$ reconstruction focusing on minimising the effects of pileup for data recorded between 2010 and 2012 (LHC Run 1) and 2015 (LHC Run 2) [115–117].

In ATLAS, the $\not{E}_{\mathrm{T}}$ is characterised by two contributions. The first contribution is from the hard event signals, which is essentially comprised fully reconstructed particles and jets (essentially hard objects). The reconstructed particles we are referring to are electrons, photons, tau leptons and muons. The second contribution to $\not{E}_{\mathrm{T}}$ is from the soft-event signals consisting of reconstructed charged particle tracks associated with the hard scatter vertex but not with hard objects.[17]

ATLAS carries out a dedicated reconstruction procedure for each of the particles as well as for the jets, casting either a particle or jet hypothesis on the origin of a group of detector signals. These procedures are independent of each other. This means that the same calorimeter signal used to reconstruct an electron is also likely to be used to reconstruct a jet, thus potentially introducing double counting of the same signal when reconstructing $\not{E}_{\mathrm{T}}$. This issue can be addressed by the explicit signal ambiguity resolution in the object-based $\not{E}_{\mathrm{T}}$ reconstruction [115–117].

The missing transverse momentum reconstruction provides a set of observables which are derived from the $p_{x(y)}$ of the transverse momentum vectors (p_{T}) if the various contributions. The missing transverse momentum components, $\not{E}_{\mathrm{T}\,x(y)}$, serve as the basic input for most of these observables. They are given by:

$$\not{E}_{\mathrm{T}x(y)} = -\sum_{i\in\{\text{hard objects}\}} p_{x(y),i} - \sum_{j\in\{\text{soft signals}\}} p_{x(y),j}. \tag{3.8}$$

[17] In this context, the hard objects refer to the electrons, photons, tau leptons and muons.

The set of observables constructed from $\not{E}_{\mathrm{T}\,x(y)}$ is:

$$\begin{aligned} \vec{\not{E}}_{\mathrm{T}} &= (\not{E}_{\mathrm{T}x}, \not{E}_{\mathrm{T}y}), \\ \not{E}_{\mathrm{T}} &= |\vec{\not{E}}_{\mathrm{T}}| = \sqrt{(\not{E}_{\mathrm{T}x})^2 + (\not{E}_{\mathrm{T}y})^2}, \\ \phi^{miss} &= \tan(\not{E}_{\mathrm{T}y}/\not{E}_{\mathrm{T}x}). \end{aligned} \tag{3.9}$$

The vector $\vec{\not{E}}_{\mathrm{T}}$ provides the amount of the missing transverse momentum via its magnitude $|\vec{\not{E}}_{\mathrm{T}}|$, and the direction in of it is given by the azimuthal angle ϕ^{miss}. This means that $|\vec{\not{E}}_{\mathrm{T}}|$ is non-negative by definition. In the calculation of $\not{E}_{\mathrm{T}\,x(y)}$ the contributing objects need to be reconstructed from mutually exclusive detector signals. This means that we avoid multiple inclusions of the same signals in multiple constructed observables. The implementation of this rule in terms of the signal ambiguity requires a definition of a sequence for selected contributions, in addition to a rejection mechanism based on signal overlap between different particles. The most commonly used order for the $\not{E}_{\mathrm{T}}$ reconstruction sequence for hard object contribution starts with electrons (e), followed by photons (γ), then hadronically decaying τ leptons (τ_{had}), and finally jets. Muons are mostly reconstructed from the ID and muon spectrometer tracks alone, this therefore leaves little or no signal overlap with other particles in the calorimeter.

In the sequence discussed, all electrons which pass the selection enter the $\not{E}_{\mathrm{T}}$ reconstruction first. The lower-priority reconstructed particles (γ, τ_{had}) are fully rejected if they share their calorimeter signal with a higher-priority object that has already entered the $\not{E}_{\mathrm{T}}$ reconstruction. Generally, jets are rejected if they overlap with accepted higher-priority particles. To avoid signal losses for $\not{E}_{\mathrm{T}}$ reconstruction in the case of partial or marginal overlap, and to suppress the accidental inclusion of jets reconstructed from calorimeter signals from large muon energy losses or pileup, a more refined overlap resolution strategies can be shown as described in [117]. Any ID tracks which are associated with any of the accepted hard objects contributing to $\not{E}_{\mathrm{T}}$, and ID tracks from the hard scatter collision vertex are used to construct the soft-event signal.

In ATLAS, the flexibility needed to calculate the $\not{E}_{\mathrm{T}}$ under changing analysis requirements for the same event is implemented using dedicated variables corresponding to

specific object contributions. The $\vec{E}_{\mathrm{T}}^{\mathrm{miss}}$ is defined in terms of its contributions as:

$$\vec{E}_{\mathrm{T}}^{\mathrm{miss}} = \underbrace{\underbrace{-\sum_{\text{selected electrons}} \vec{p}_T^{\,e}}_{\vec{E}_{\mathrm{T}}^{\mathrm{miss},e}} \underbrace{-\sum_{\text{selected photons}} \vec{p}_T^{\,\gamma}}_{\vec{E}_{\mathrm{T}}^{\mathrm{miss},\gamma}} \underbrace{-\sum_{\text{accepted } \tau\text{-leptons}} \vec{p}_T^{\,\tau_{\mathrm{had}}}}_{\vec{E}_{\mathrm{T}}^{\mathrm{miss},\tau_{\mathrm{had}}}} \underbrace{-\sum_{\text{selected muons}} \vec{p}_T^{\,\mu}}_{\vec{E}_{\mathrm{T}}^{\mathrm{miss},\mu}} \underbrace{-\sum_{\text{accepted jets}} \vec{p}_T^{\,\mathrm{jet}}}_{\vec{E}_{\mathrm{T}}^{\mathrm{miss,jet}}}}_{\text{hard term}} \underbrace{-\sum_{\text{unused track}} \vec{p}_T^{\,\mathrm{track}}}_{\vec{E}_{\mathrm{T}}^{\mathrm{miss,track}}\ \text{soft term}}}. \tag{3.10}$$

The $E_{\mathrm{T}}^{\mathrm{miss}}$ and ϕ^{miss} observables can be constructed according to Equations 3.9 for the overall missing transverse momentum ($\vec{E}_{\mathrm{T}}^{\mathrm{miss}}$) as well as for each individual term indicated in Equation 3.10. In the priority-ordered reconstruction sequence for $E_{\mathrm{T}}^{\mathrm{miss}}$, contributions are defined by a combination of analysis-dependent selections and a possible rejection due to the applied signal ambiguity resolution. The muon and electron contributions are typically not subjected to the signal overlap resolution mentioned previously and are thus exclusively defined by the selection requirements. The unused tracks in Equation 3.10 refer to the tracks associated with the hard scatter vetex but not any hard object. Neutral particle calorimeter signals suffer from significant contributions from pileup and are not included in the soft term.

We use a variety of techniques to mitigate the effects of pileup on the measurement of missing transverse energy ($E_{\mathrm{T}}^{\mathrm{miss}}$). One of the main approaches used in ATLAS is to exploit the high granularity and precision of the detector to distinguish between particles that originate from the primary hard scatter interaction and those that comes from pileup interactions. This can be achieved through a combination of tracking information, calorimeter measurements and also the timing information. For example, charged particles associated with the primary vertex are identified based on their trajectory in the ID, while neutral particles from pileup interactions are identified based on their characteristic energy deposits in the calorimeters. The timing information can also be used to further differentiate between particles from the primary interaction and those from pileup. In addition, machine learning techniques (such as Boosted Decision Trees [118]) can be used to classify particles based on their properties and identify those that are likely to come from pileup interactions. This allows for more efficient rejection of pileup events and improves the overall performance of the $E_{\mathrm{T}}^{\mathrm{miss}}$ reconstruction. Often the terms missing transverse energy, $E_{\mathrm{T}}^{\mathrm{miss}}$, and missing transverse momentum, $p_{\mathrm{T}}^{\mathrm{miss}}$, are used interchangeably because they represent the same physical quantity.

Chapter 4.

The $p_{\mathrm{T}}^{\mathbf{miss}}$ + Jets Analysis

"Joy in looking and comprehending is nature's most beautiful gift."
— Albert Einstein, 1879–1955

The physics programme at ATLAS involves making measurements of the Standard Model (SM) as well as searching for evidence of new physics. Normally an analysis focuses on one of these two areas, whereas this work straddles these two aims. This analysis performs a measurement of differential cross-sections in regions of phase-space which are populated with many SM processes but are also sensitive to DM processes and other BSM physics. We make a fiducial measurement which restricts itself to the phase-space which is accessible to the detector and does not extrapolate into unknown regions of phase-space (i.e., outside the detector acceptance). In addition to it being a fiducial measurement, it is also defined in terms of the final state particles. This type of measurement has the advantage of the data not being contaminated by the shortcomings of current SM theoretical predictions and therefore any future improvements to these SM theoretical predictions can be used and the data reinterpreted.

In Section 4.1, we outline the analysis, followed by Section 4.2 which describes and motivates the variables. In Section 4.3 and 4.4, we describe the particle-level physics objects and also event selection. In Sections 4.5 and 4.6, we give details of the data-set and MC along with some data quality studies. Following this, we report on both the experimental and theoretical uncertainties for this measurement in Section 4.7. In Sections 4.8 and 4.9, we report on the detector-level and detector-corrected results.

4.1. Analysis Strategy

Dark Matter (DM) particles are not expected to interact with the detector and this therefore makes detection difficult. The aim of this analysis is not necessarily to directly detect DM, but to make full use of the ATLAS detector's ability to measure almost all of the SM particles. As a consequence, it is possible to reconstruct the $p_{\mathrm{T}}^{\mathrm{miss}}$, the missing transverse momentum, of an event and this acts as a proxy for DM particles along with other invisible particles (e.g., neutrinos). As laid out in Section 3.2.7, $p_{\mathrm{T}}^{\mathrm{miss}}$ is defined as the negative sum of all the transverse momenta of the visible particles that are detected. If all the final state particles are detected, then this $p_{\mathrm{T}}^{\mathrm{miss}}$ is close or equal to zero as there is no initial momentum in the transverse plane. The production of invisible particles would result in an energy imbalance in the transverse plane, as long as the invisible particles were produced in association with and also recoiling from other detected objects.

Jets are the most common high p_{T} object that are produced in the LHC and therefore the strategy of this analysis is to search for evidence of DM production and measure the differential cross-section of events with large $p_{\mathrm{T}}^{\mathrm{miss}}$ and jets. An example Feynman diagram involving DM production is shown in Figure 4.1a, which would result in an event with $p_{\mathrm{T}}^{\mathrm{miss}}$ (how large depends on the mediator mass) and jets. The main SM process which contributes to these large $p_{\mathrm{T}}^{\mathrm{miss}}$ + jets events is a Z boson decaying to a pair of neutrinos as seen in Figure 4.1b. In addition to the Z boson decaying invisibly + jets, there is also a large contribution from the process of a W boson decaying to a neutrino and a charged lepton in association with jets, as seen in Figure 4.1c. This said contribution would normally be vetoed from the $p_{\mathrm{T}}^{\mathrm{miss}}$ + jets due to the charged leptons, however leptons can be produced in a phase-space that is outside the detectors acceptance, and hence enter the $p_{\mathrm{T}}^{\mathrm{miss}}$ + jets phase-space. In a more traditional analysis, the contributions such as this would be treated as a background and subtracted from the measured result. In the final state oriented approach that is taken, the contributions from the $Z(\rightarrow \nu\nu)$ + jets and the out of acceptance $W(\rightarrow \ell\nu)$+ jets events are both considered part of the $p_{\mathrm{T}}^{\mathrm{miss}}$ + jets final state. The main reason these irreducible processes are treated as part of the $p_{\mathrm{T}}^{\mathrm{miss}}$ + jets final state is because it disentangles the modelling of the SM processes (which can often be imprecise) from the data. In other words the model-dependent assumptions would have to go into the background subtraction (and therefore the data), which then makes the data much less useful for reinterpretation.

For example, the model-dependent processes, such as the W boson decaying to a lepton and a neutrino (where the lepton is out of acceptance), would have to be subtracted from the $p_{\mathrm{T}}^{\mathrm{miss}}$ + jets phase-space. There are also reducible processes for the $p_{\mathrm{T}}^{\mathrm{miss}}$ + jets state, for example one of these originates from a QCD multijet production, in which the mismeasurement of the jets momentum can lead to an imbalance momentum in the transverse plane which then fakes a $p_{\mathrm{T}}^{\mathrm{miss}}$ + jets event. This fake multijet process is estimated using a data-driven technique as the Monte Carlo simulation poorly models the multijet events and this is treated as a background and subtracted.

In the absence of new physics, the cross-section of events in the $p_{\mathrm{T}}^{\mathrm{miss}}$ + jets region is expected to be similar to that of the SM events in the same region. SM events in this region are primarily composed of Z bosons decaying into neutrinos and W bosons decaying to out of detector acceptance leptons and neutrinos. The contribution from W bosons accounts for approximately half of the events, making background subtraction less desirable.

In addition to measuring the $p_{\mathrm{T}}^{\mathrm{miss}}$ + jets region, four additional auxiliary regions (all of which contain charged leptons), which have similar SM processes to that seen in the $p_{\mathrm{T}}^{\mathrm{miss}}$ + jets region, are measured and unfolded. These additional regions can be used to constrain the systematic uncertainties in $p_{\mathrm{T}}^{\mathrm{miss}}$ + jets region coming from the detector effects and from theoretical modelling. These regions are also useful for setting limits on new physics models which include leptons in their final state. The regions can be grouped in terms of the number of leptons as is outlined in the following subsections.

Auxiliary Regions

2 μ + Jets and 2 e + Jets

These regions predominantly contain a Z boson decaying to two charged electrons or muons. They are very similar to the $Z \to \nu\nu$ process (which is dominant in the $p_{\mathrm{T}}^{\mathrm{miss}}$ + jets region) and are therefore useful for constraining the systematic uncertainties in the $p_{\mathrm{T}}^{\mathrm{miss}}$ + jets region. The $Z \to \ell\ell$ is also a very clean signal, meaning that other processes that contribute to this two lepton region are quite small. However, the branching fraction is a lot smaller for Z to charged leptons and therefore the statistical

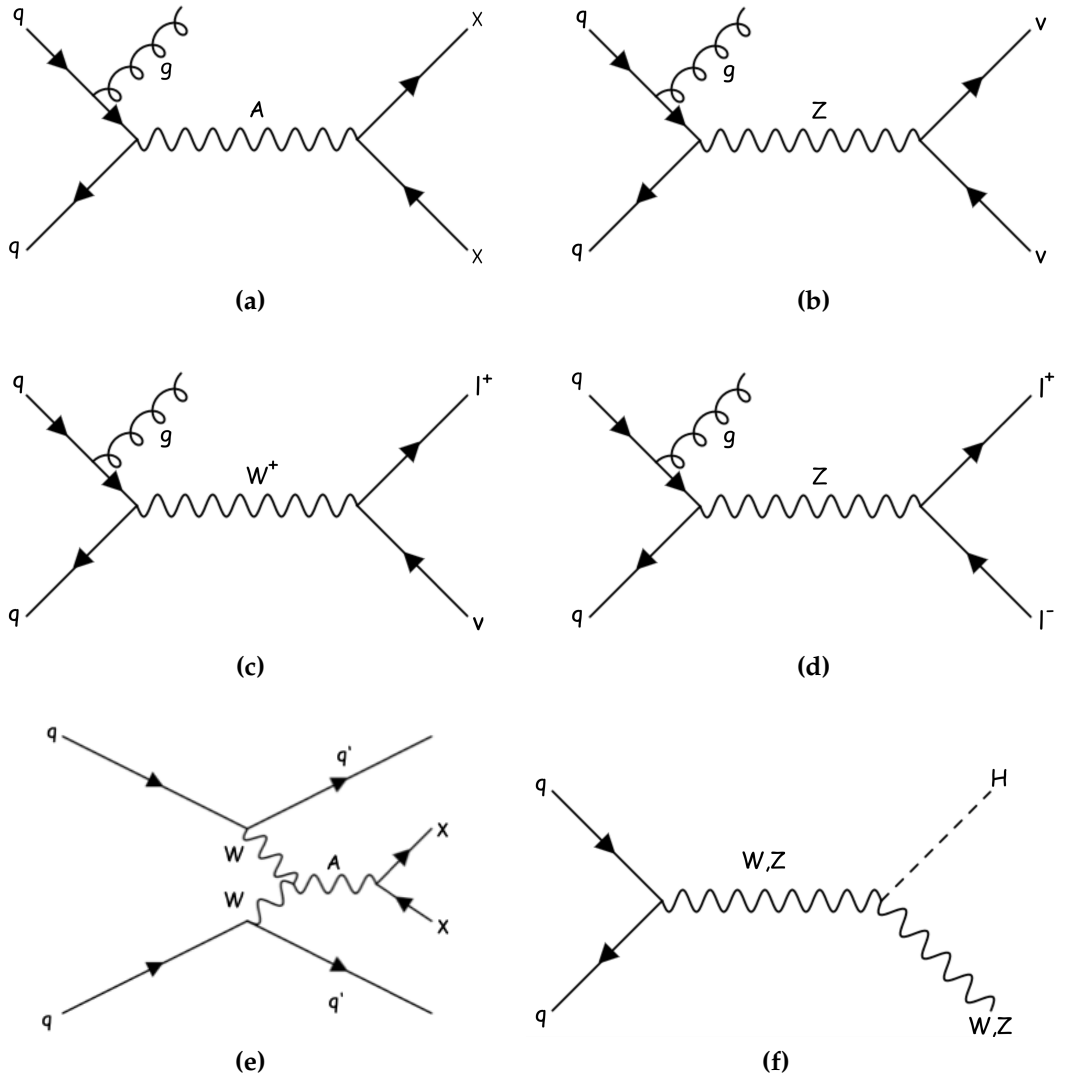

Figure 4.1.: Feynman diagrams for (a) the production of a DM mediator, A, which decay to DM particles, χ, in a monojet event, (b) the decay of a Z boson to two neutrinos, (c) the decay of a W boson to a lepton and neutrino, (d) the decay of a Z boson to two leptons, (e) the production of a DM mediator, A, which decay to DM particles, χ, in a VBF event, (f) the production of a Higgs via the VH channel.

uncertainties will be much larger for the measurements, and so this may effect our sensitivity. An example Feynman diagram is shown here 4.1d.

1 μ + Jets and 1 e + Jets

This region is dominated by $W \to \mu\nu$ and $W \to e\nu$ processes, and is still useful for constraining the systematic uncertainties from the $Z \to \nu\nu$ process as there are

many similarities between the production of W and Z like events at the LHC. These single lepton regions benefit from the fact that the $W \to \mu\nu$ and $W \to e\nu$ processes have a relatively larger cross-section than the $Z \to \nu\nu$ + jets process (almost 10 times larger) which leads to increased statistical precision. There are also reduced systematic uncertainties associated with the lepton efficiencies due to the fact this region only has a single lepton. An example Feynman diagram is shown here 4.1c.

The final state leptons in the above described regions are marked invisible, which means that they are not included in the $p_{\mathrm{T}}^{\mathrm{miss}}$ calculation that is set out in Equation 3.10. This results in an observable called the pseudo-$p_{\mathrm{T}}^{\mathrm{miss}}$, which in the leptonic regions acts as a proxy for the p_{T} of the boson decaying to leptons (in a similar way to the $p_{\mathrm{T}}^{\mathrm{miss}}$ acting as a proxy for the p_{T} of the boson decaying invisibly in the $p_{\mathrm{T}}^{\mathrm{miss}}$ + jets region). This therefore means that all these regions can be compared to each other.

Phase-Spaces

In this analysis, we consider three different phase-spaces. These phase-spaces are meant to be quite general in terms of their event selection yet sensitive to new BSM physics (with a focus on DM production) and are defined by the jet kinematics of the event which are outlined below.

$\geq$ 1 Jet (Monojet-Like)

This ≥ 1 jet phase-space aims to be as inclusive as possible, and requires only the presence of one jet. This is the same as the monojet signature used by other DM searches, where the presence of at least one energetic jet is required. An example Feynman diagram showing the production of DM in association with a gluon is shown in Figure 4.1a. This phase-space takes advantage of the strong coupling of the gluon to the initial state quark.

$\geq$ 2 Jet (Two Jet Inclusive)

The ≥ 2 jet phase-space requires at least two high p_{T} jets and variables which require two jets. This region of phase-space is sensitive to the associated vector boson Higgs

(VH) production, where the Higgs decays invisibly and the vector bosons decays hadronically, see Feynman diagram in Figure 4.1f.

Vector Boson Fusion (VBF)

The VBF phase-space requires the presence of at least two high p_{T} jets and it also has a selection requirement on the jet system (including a third jet veto) to increase the sensitivity to VBF processes. This phase-space aims to be sensitive to DM models where new mediator particles do not directly couple to quarks, as shown in the Feynman diagram in Figure 4.1e. This channel is also sensitive to the VBF Higgs production channel, where the Higgs decays invisibly.

Differential Cross-Section and Ratio

Each region's cross-section is measured differentially with respect to the observable in each phase-space. These observables are discussed in more detail in Section 4.2. Measuring the differential cross-sections means that shape information is garnered for each of these observables, and this increases the sensitivity of the measurement to BSM physics. The differential cross-sections are corrected for detector effects in a procedure known as unfolding. This is done so that it can be directly compared to particle-level calculations, this avoids the need for computationally expensive detector simulation. This also has the advantage that the analysis results can be easily reinterpreted long into the future when better SM predictions as well as new BSM models become available.

This analysis extends work previously done in [119], which had a similar approach and was performed using 3.2 fb^{-1} of 13 TeV data. The previous iteration of this analysis [119] was designed to maximise sensitivity to new physics in events with jets and large missing transverse momentum, while controlling systematic uncertainties to achieve a robust result (similar to what will be done in this analysis). However in that analysis they only consider the 2μ+jets and $2e$+jets regions and as a consequence they suffered from large statistical uncertainties. Another difference is that they measured only the ratio of the $p_{\mathrm{T}}^{\mathrm{miss}}$ + jets to the lepton regions and not the individual cross-sections.

In the new analysis, individual cross-sections are measured for each region as this is useful for constraining new physics models that could be present in the lepton regions as well as the $p_{\mathrm{T}}^{\mathrm{miss}}$ + jets region. The aim is not just to use these regions for searching for BSM physics as these individual measurements can also be a probe for Monte Carlo mismodelling.

The ratio of cross-sections is defined as:

$$R^{\mathrm{miss}} = \frac{\sigma_{\mathrm{fid}}(p_{\mathrm{T}}^{\mathrm{miss}} + \mathrm{jets})}{\sigma_{\mathrm{fid}}(X + \mathrm{jets})} \tag{4.1}$$

where the numerator is the fiducial cross-section of the $p_{\mathrm{T}}^{\mathrm{miss}}$ + jets and the denominator is the fiducial cross-section of the lepton regions ($1e$+jets, 1μ+jets, 2μ+jets, $2e$+jets). The similarity of the processes involved in the numerator and denominator, as previously explained, significantly reduces the experimental and theoretical uncertainties in the ratio as any possible mismodelling will be similar for the numerator and the denominator and therefore some cancellation will occur.

As well as this, the jet systems in both the numerator and denominator are required to satisfy similar selection criteria, and therefore the systematic uncertainties originating from calibration procedures involving the jet system are much reduced. As is done with the cross-section measurements of each region, the ratio is measured differentially with respect to the observables. The presence of new physics in the numerator would lead to a discrepancy between the BSM ratio and the SM ratio.

The limitation of the R^{miss} method is that we assume that there is no new physics in the $1\mu/2\mu$ + jets and $1e/2e$ + jets final states which may not necessarily be the case. It is therefore less useful for constraining BSM models which are present in the $p_{\mathrm{T}}^{\mathrm{miss}}$ region and the $1\mu/2\mu$ + jets / $1e/2e$ + jets regions such as vector-like quarks.

4.2. Measured Variables

As mentioned previously, the various variables that are measured in the ≥ 1 jet, ≥ 2 jet and the VBF phase-spaces are justified in this section, where each variable is measured in all the regions ($p_{\mathrm{T}}^{\mathrm{miss}}$ + jets, $1e$+jets, 1μ+jets, $2e$+jets, 2μ+jets).

$\geq$ 1 Jet (Monojet-Like)

The $p_{\mathrm{T}}^{\mathrm{miss}}$ distribution is measured in the ≥ 1 jet region as BSM models often involve larger particle masses and higher energy scales, which lead to a harder $p_{\mathrm{T}}^{\mathrm{miss}}$ spectrum. Therefore, the cross-section in this phase-space is measured as a function of $p_{\mathrm{T}}^{\mathrm{miss}}$ (or in the lepton regions as a function of the pseudo $p_{\mathrm{T}}^{\mathrm{miss}}$). This means that the $p_{\mathrm{T}}^{\mathrm{miss}}$ distribution is expected to have increased sensitivity to BSM models at the tail of this spectrum. In events where most of the recoil comes from a single jet, the p_{T} of this jet will be very similar to the $p_{\mathrm{T}}^{\mathrm{miss}}$ due to momentum conservation.

$\geq$ 2 Jet

For the same reasons outlined for the ≥ 1 jet phase-space, the cross-sections in the $\geq$ 2 jet phase-space are measured as a function of $p_{\mathrm{T}}^{\mathrm{miss}}$. The requirement of having at least two high p_{T} jets gives us the possibility to probe hadronically decaying vector bosons being produced in association with high $p_{\mathrm{T}}^{\mathrm{miss}}$. One such process could be the VH production mode, in which a Higgs is produced in association with a vector boson decaying to quarks (as jets) and the Higgs decaying invisibly, which has a large $p_{\mathrm{T}}^{\mathrm{miss}}$ signature. The dijet system from the hadronic decay of a vector boson can be used to explore the $V+p_{\mathrm{T}}^{\mathrm{miss}}$ system and for this reason it is interesting to have some dijet variables such as the dijet invariant mass, m_{jj}, and the difference in azimuthal angle between the two jets, $\Delta\phi_{jj}$.

The m_{jj} distribution has bins which are focused on the midpoint between the mass of the W and Z boson, specifically targeting the VH channel and extends to higher m_{jj} bin values in case a DM particle is produced with a high m_{jj} signature.

If the Δy_{jj} is very small, which may happen as no $|\Delta y_{jj}|$ cut is applied in the ≥ 2 jet phase-space, then the rapidity ordering can differ between the truth-level and detector-level. This causes a flip in the sign of $\Delta\phi_{jj}$ and leads to cross-diagonal elements in the response matrix used for the unfolding. For this reason the absolute value of $\Delta\phi_{jj}$ is measured in the unfolded distributions. The correlation between the two leading jets azimuthal angles often depends on the spin of the DM mediator and the $\Delta\phi_{jj}$ distribution can be used to differentiate between different BSM models. For calculating the $\Delta\phi_{jj}$, the two leading jets are ordered in terms rapidity and the azimuthal angle of the least forward jet is subtracted from the most forward jet. This

has the advantage of the $\Delta\phi_{jj}$ observable being sensitive to CP-even and CP-odd models [120].

VBF

As is done in the ≥ 2 jet phase-space, the cross-section is measured differentially with respect to the $p_{\mathrm{T}}^{\mathrm{miss}}$, m_{jj} and $\Delta\phi_{jj}$ variables. This phase-space has overlap in terms of motivation with the ≥ 2 jet phase-space; however it is more focused on its sensitivity to models produced via the VBF mechanism, such as the VBF Higgs production where in this case the Higgs decays invisibly. The main advantage of the VBF phase-space in terms of BSM physics is that the BSM mediator would couple directly to the gauge bosons, whereas in other production modes it would couple to quarks. In general, the VBF production leads to a harder m_{jj} spectrum than is seen in the strong production of jets or a hadronically decaying vector boson. Therefore, we would expect any BSM physics involving VBF-like productions to appear at the tail of the m_{jj} spectrum.

4.3. Particle-Level Object and Event Selection

The particle-level object definitions and event selections define the fiducial space for the ATLAS data to be corrected to.[1] These selections are chosen to be as similar as possible to the reconstruction-level selection so as to avoid unnecessary extrapolations which can be potential sources of uncertainty due to the assumptions that will have to be made during the unfolding process. The kinematic criteria is also defined in more detail for the three phase-spaces as well as the regions.

[1] Particle level refers to the reconstructed particles in a particle physics experiment, where the measured energy and momentum are corrected for detector effects and resolution. The particle-level objects are typically reconstructed using Monte Carlo simulations and represent the final state particles that were produced in the collision.

4.3.1. Particle-Level Object Selection

Jets

Jets are reconstructed using the anti-k_t jet algorithm which clusters the four momenta of the particle-level objects with a radius parameter of $\Delta R = 0.4$ [109].[2] They are required to have p_{T} >30 GeV and also a rapidity of $|y| < 4.4$. Nearly all stable final state particles (has a longer mean lifetime than 10 mm), apart from neutrinos and muons, are captured in the jet clustering algorithm.[3] Neutrinos and muons are not captured in the jet clustering algorithm because they are not efficiently detected by the calorimeters used in the clustering process. Neutrinos are electrically neutral and do not interact with the detector and are typically only detected through their $p_{\mathrm{T}}^{\mathrm{miss}}$. They are therefore not considered as part of the jet clustering algorithm, which relies on energy deposits in the calorimeters. Muons, on the other hand, are relatively heavy and can penetrate through the detector material without losing much energy. As a result, they may not deposit sufficient energy in the calorimeters to be efficiently clustered into a jet.

Electrons and Muons

In this analysis, the electrons and muons are required not to originate from the decay of hadrons, this type of leptons are known as prompt or direct. Electrons are required to have a $p_{\mathrm{T}} > 7$ GeV, to be within a pseudorapidity of $|\eta| < 2.47$ (this the region of the EM calorimeter devoted to precision measurements and excludes the crack region, $1.37 < |\eta| < 1.52$, which is the transition region between the barrel and endcap

[2] The anti-k_t algorithm has several desirable properties. One of these is that it is infrared and collinear (IRC) safety. This means that the algorithm is insensitive to small-angle or soft radiation, which in other jet algorithms [121] can lead to unphysical or unreliable results. This makes the anti-k_t algorithm useful for finding jets in high-multiplicity environments with a large number of overlapping particles, such as those encountered in pp collisions at the LHC. Another advantage of the anti-k_t algorithm is a tendency to cluster particles around a central, high-energy seed. This property makes the algorithm well-suited to identifying the decay products of heavy particles such as top quark or Higgs bosons, which can produce highly collimated jets in their decays. On a computational level, the anti-k_t algorithm has a relatively simple implementation and is computationally efficient, making it suitable for use in large-scale physics analyses such as those done at the LHC.

[3] There is a $|\eta| < 4.9$ restriction on the particles that go into the clustering, which is motivated by the HCAL acceptance.

calorimeter) and to be dressed.[4] Muon candidates are required to have a $p_{\mathrm{T}} > 7$ GeV and to be within a pseudorapidity of $|\eta| < 2.5$. The $p_{\mathrm{T}} > 7$ GeV requirement for electrons and muons is a kinematic cut designed to ensure that the electrons or muons are energetic enough to be reconstructed and identified with high efficiency and quality in the ATLAS detector.

Taus

In this analysis, we only consider hadronically decaying taus as those that decay leptonically are included in the electron and muon categories. The tau candidates, τ, are required to have $p_{\mathrm{T}} > 20$ GeV and a pseudorapidity within $|\eta| < 2.47$ (again excluding the crack region of $1.37 < |\eta| < 1.52$). Any jet which has a hadron that originates from a tau is classified as a hadronically decaying tau. The hadronically decaying taus are identified by checking if any given jet originates from a prompt tau.

Photons

Photons are required to have a $p_{\mathrm{T}} > 7$ GeV, to be within a pseudorapidity of $|\eta| < 2.47$ (again excluding the crack region of $1.37 < |\eta| < 1.52$) and be prompt.

$p_{\mathrm{T}}^{\mathrm{miss}}$ Reconstruction

The particle-level missing transverse momentum ($p_{\mathrm{T}}^{\mathrm{miss}}$) is determined by computing the magnitude of the vectorial sum of the transverse momenta of all visible final-state particles within a specified range of pseudorapidity ($|\eta|$). The contribution of muons with $|\eta| > 2.5$ to the $p_{\mathrm{T}}^{\mathrm{miss}}$ is deemed negligible, as their momentum is taken into account only if recorded in the Inner Detector (ID). In the lepton regions, the contribution of final-state leptons is treated as invisible and therefore excluded from

[4] A dressed lepton refers to a charged lepton (in this case, an electron) that is accompanied by a number of photons within a small distance, typically within a cone around the lepton's direction of motion. The photons are considered part of the final-state object and are included in the calculation of the lepton's momentum. This process is called "dressing" because the photons effectively add energy to the lepton and change its appearance, making it look like a more energetic or "dressed" particle. The use of dressed leptons is particularly important in this analysis because it improves the energy resolution of the reconstructed leptons and reduces the effect of final-state radiation (FSR) from the hard scattering process, which can otherwise lead to a significant loss of information as the photons radiated from leptons and FSR can be indistinguishable.

the vectorial sum that determines the $p_{\mathrm{T}}^{\mathrm{miss}}$. It is also required that events have a missing transverse momentum, $p_{\mathrm{T}}^{\mathrm{miss}}$ >200 GeV.

Overlap Removal Procedure

An overlap removal procedure is applied to particle-level objects to match those applied at the detector-level, see Section 4.4. This procedure can be broken down into four steps:

1. Jets that are within a cone of $\Delta R < 0.2$ around an electron are removed
2. Jets that are within a cone of $\Delta R < 0.2$ around a muon are removed
3. The surviving electrons are then removed if they are within $\Delta R < 0.4$ around a jet
4. The surviving muons are then removed if they are within $\Delta R < 0.4$ around a jet

4.3.2. Event Selection

This analysis considers three different phase-spaces which are defined by the jet kinematics of the event and five different regions which are defined by the number, flavour and kinematics of the leptons. This section outlines the specific kinematic criteria that have been established for the jets and leptons in each respective phase-space and region under consideration.

Phase-Spaces

The event selection is summarised in Table 4.1, where each phase-space has different sensitivity to various BSM models. As can be seen, all three phase-spaces have a $p_{\mathrm{T}}^{\mathrm{miss}} > 200$ GeV requirement. This is motivated by the large $p_{\mathrm{T}}^{\mathrm{miss}}$ characteristic of DM events, increasing the efficiency of the trigger and suppressing the large multijet background for values of $p_{\mathrm{T}}^{\mathrm{miss}} < 200$ GeV. There is also an angular separation requirement between the four leading jets in p_{T}, the $p_{\mathrm{T}}^{\mathrm{miss}}$ vector, $\Delta\phi(\mathrm{jet}_i, p_{\mathrm{T}}^{\mathrm{miss}}) > 0.4$ and is also required to match what is seen at the detector-level. This is motivated to suppress contributions from multijet events where mismeasured jets are mistaken for a large $p_{\mathrm{T}}^{\mathrm{miss}}$ being aligned with one of the jets.

$\geq$ 1 Jet

In events with at least one jet, for example where the Z boson decays to two neutrinos or a DM mediator decaying to two DM particles (a large $p_{\mathrm{T}}^{\mathrm{miss}}$) and is balanced by the leading jet. A kinematic cut is defined for the ≥ 1 jet phase-space in which the high energy jet is required to be in the central pseudorapidity region of the detector ($|\eta| < 2.4$ due to inner detector pseudorapidity constraints) and have a high p_{T} cut of $p_{\mathrm{T}} > 120$ GeV.

$\geq$ 2 Jet

In the ≥ 2 jet phase-space, two jets are required with a minimum p_{T} of 110 GeV for the leading and 50 GeV for the subleading jet. There is an asymmetry in the p_{T} cuts of the leading and subleading jet as we need a high p_{T} requirement for one of the jets so as to suppress the contribution from the QCD backgrounds. In terms of BSM physics, increased sensitivity is gained with this phase-space for models where a hadronically decaying vector boson is back to back with a invisibly decaying system which leads to two or more jets back to back with a large $p_{\mathrm{T}}^{\mathrm{miss}}$.

VBF

This phase-space is targeting the process where quarks from each of the incoming protons radiate a vector boson and fuse together to produce a mediator, such as the Higgs boson. The t-channel exchange of a colour singlet between the incoming quarks means that additional radiation in the rapidity interval between the quarks will be suppressed. As a consequence, they are more likely to continue into the forward region. As stated for the ≥ 2 jet phase-space, the two leading jets balance against the invisibly decaying mediator. Here, the minimum transverse momentum, p_{T}, of the jets are required to be p_{T} >80 GeV and p_{T} >50 GeV of the leading and subleading jets with the asymmetry again being motivated by reducing the QCD background. If the jets are close-by in phase-space then it is possible to run into some issues with jets being misidentified. For example, at the reconstructed level the two close-by truth jets are reconstructed as one big jet, which then means the third jet at truth level becomes the second jet at the detector level. This is why a rapidity cut of $|y| > 1$ between the two jets prevents this type of splitting. To suppress contributions from diboson events,

where one of the bosons decays hadronically and also to be more sensitive to physics at high m_{jj}, there is an invariant mass cut on the dijet system of m_{jj} >200 GeV. There is also a veto on events with additional jets in the rapidity gap. This is done as there are events with two incoming jets which radiate gluons, and are produced back-to-back with a vector boson through QCD, this results in a signature that is very similar to the VBF process. In this scenario, the two outgoing gluon/quark jets are colour-connected and therefore there are additional jets in the gap between the two jets. The central jet veto reduces this V+jets background and enhances the colourless VBF process.

	≥ 1 jet	≥ 2 jet	VBF
$p_{\mathrm{T}}^{\mathrm{miss}}$	> 200 GeV		
$\Delta\phi(\mathrm{jet}_i, p_{\mathrm{T}}^{\mathrm{miss}})$	> 0.4, where $i = 1, ..., 4$ runs over the four highest p_{T} jets		
(Additional) muons	None with $p_{\mathrm{T}} > 7$ GeV, $\lvert\eta\rvert < 2.5$		
(Additional) electrons	None with $p_{\mathrm{T}} > 7$ GeV, $0 < \lvert\eta\rvert < 1.37$ or $1.52 < \lvert\eta\rvert < 2.47$		
Hadronic taus	None with p_{T} >20 GeV, $0 < \lvert\eta\rvert < 1.37$ or $1.52 < \lvert\eta\rvert < 2.47$		
lead jet p_{T}	> 120 GeV	> 110 GeV	> 80 GeV
sub-lead jet p_{T}	N/A	> 50 GeV	> 50 GeV
lead jet $\lvert\eta\rvert$	< 2.4		
m_{jj}	N/A	-	> 200 GeV
$\lvert\Delta y_{jj}\rvert$	N/A	-	> 1
In-gap jets	N/A	-	None with $p_{\mathrm{T}} > 30$ GeV

Table 4.1.: A summary of the selection cuts defining the fiducial regions. These cuts apply to the $p_{\mathrm{T}}^{\mathrm{miss}}$ + jets and the other four regions of phase-space. The in-gap jet veto is applied to jets in-between the two leading jets in rapidity.

Auxiliary Regions

This analysis considers five different auxiliary regions: the $p_{\mathrm{T}}^{\mathrm{miss}}$ +jets, 1e+jets, 1μ+jets, 2e+jets and 2μ+jets regions. The lepton regions are used to constrain theoretical and experimental systematic uncertainties (which originate from the detector) in the $p_{\mathrm{T}}^{\mathrm{miss}}$ +jets region and they also can be used to search for new physics in these regions where BSM particles are produced in association with leptons or a photon. We use these regions also to construct the ratio, R^{miss}. The selection and kinematic criteria for the lepton regions are outlined and summarised in Tables 4.2.

$p_{\mathrm{T}}^{\mathrm{miss}}$ +jets region

The $p_{\mathrm{T}}^{\mathrm{miss}}$ +jets region requires that there are zero leptons in the final state. This essentially means that events containing electrons or muons, or a hadronically decaying tau leptons, are also vetoed.

1e+Jets and 1μ+Jets Regions

The 1e+jets and 1μ+jets regions require exactly one electron (or positron) and one muon (or anti-muon) respectively. However, any events which have an additional lepton or a hadronically decaying tau are rejected. In the 1e+jets lepton region, electrons are required to have a p_{T} >30 GeV and $|\eta| < 2.47$ (excluding the crack region). In the 1μ+jets lepton region, muons are required to have a p_{T} >7 GeV and $|\eta| < 2.5$. The higher lepton p_{T} transverse momentum cut in the 1e+jets region is motivated by the fact that the trigger scale factors are only available for electrons with p_{T} >30 GeV. This region has an additional real $p_{\mathrm{T}}^{\mathrm{miss}} > 60$ GeV cut which suppresses the contributions from multijet events.[5]

2e+Jets and 2μ+Jets Regions

The 2e+jets and 2μ+jets lepton regions require a pair of opposite charge leptons (an electron-positron pair or a muon-anti-muon) respectively. Any additional leptons or hadronically decaying tau leptons are rejected, where the leading and subleading lepton have transverse momentum cuts of p_{T} >80 GeV and p_{T} >7 GeV respectively. The leading lepton p_{T} cut is motivated by the need to suppress the contribution from top quark pair decays but still less than half the p_{T} of the Z boson (which has a p_{T} of at least 200 GeV). There is also a dilepton invariant mass requirement of 66 GeV $< m_{\ell\ell} <$ 116 GeV imposed around the Z boson mass, this suppresses contributions from the $\gamma^* \to \ell\ell$ and the associated interference terms.

[5] The real $p_{\mathrm{T}}^{\mathrm{miss}}$ calculation treats leptons as *visible* particles and represents the p_{T} of actual invisible particles.

	1ℓ+jets	2ℓ+jets
lepton $\|\eta\|$ (muons)	$\|\eta\| < 2.5$	
lepton $\|\eta\|$ (electrons)	$0 < \|\eta\| < 1.37$ or $1.52 < \|\eta\| < 2.47$	
leading lepton p_{T}	> 30 GeV for e, > 7 GeV for μ	> 80 GeV
sub-leading lepton p_{T}	N/A	> 7 GeV
di-lepton mass	N/A	$66 < m_{\ell\ell} < 116$ GeV
transverse mass	$30 < m_T < 100$ GeV for e only	N/A
real $p_{\mathrm{T}}^{\mathrm{miss}}$	> 60 GeV for e only	N/A

Table 4.2.: A summary of the lepton selection cuts defining the lepton-based auxiliary regions. These cuts apply to the ≥ 1 jet , ≥ 2 jet , and VBF regions.

4.4. Detector-Level Object and Event Selection

The object definition and event selection at detector-level is outlined here, details about the object reconstruction are then provided along with their identification and calibration methods.

4.4.1. Detector-Level Object Selection

The objects at the detector-level have to satisfy the same kinematic requirements as those for the particle-level. The additional requirements for the detector-level objects are detailed in this section.

Electrons

The electrons have to have good object quality.[6] For this to happen, rejecting fake electrons is desirable. Fake electrons originating from hadronic showers in the calorimeter can be suppressed using likelihood identification algorithms. These type of algorithms use shape information from the electromagnetic showers and on the electron track quality to discriminate between the real and fake electrons. Three likelihood identification working points can be defined with increasing fake rejection and decreasing real electron acceptance: *Loose*, *Medium* and *Tight* [122].

[6] All instruments in the electromagnetic calorimeters involved in the electron reconstruction were fully functional.

1. Veto electrons (i.e., electrons used for the additional lepton veto) are required to pass the loose ID likelihood selection criteria; however, no isolation requirements are applied. The veto electron must pass overlap removal. As the E_T increases, the identification efficiency increases from 86% at $E_T = 20$ GeV to 95% at $E_T = 100$ GeV for the *Loose* operating point [122].

2. Selected electrons in the 1e+jets region are required to pass additional criteria, for instance they are required to pass a *Tight* selection, this is to reduce contributions from multijet events. With increasing E_T, the identification efficiency varies from 58% at $E_T = 4.5$ GeV to 88% at $E_T = 100$ GeV for the *Tight* operating point [122]. To make sure that electrons originate from the primary vertex, we make the following cuts $|z_0 \times \sin(\theta)|$ <0.5 mm and $|d_0|/\sigma(d_0) < 5$, where $|z_0 \times \sin(\theta)|$ and $|d_0|$ are the distances of closest approach to the primary vertex in the longitudinal and transverse planes respectively.

3. Similar to the case of electrons in the 1e+jets region, electrons in the 2e+jets are required to pass additional criteria on top of the veto electron requirements. These electrons are required to pass a *Medium* identification along with a close-by correction being applied on electrons to increase the efficiency. As the E_T increases, the identification efficiency increases from 80% at $E_T = 20$ GeV to 93% at $E_T = 100$ GeV for the *Medium* operating point [122].

For both electrons in the 1e+jets and 2e+jet regions, they need to satisfy the isolation criteria *FCHighPtCaloOnly*, which performs better than other isolation criteria in terms of reducing multijet background. This working point (WP) requires that the sum of the p_{T} of energy clusters in the EM calorimeter within $\Delta R < 0.2$ of the electron candidate is either less than 3.5 GeV or $0.015 \times p_T$. This WP has good background rejection in the high electron p_{T} region with a prompt electron selection efficiency over 90% [122].

Muons

In this analysis, there are two different types of muon requirements:

1. Veto muons are required to pass the *Loose* identification working point. The *Loose* identification working point has a prompt muon selection efficiency of 99% (20<p_{T} [GeV]<100, see [123] for other p_{T} ranges) and also follows the overlap removal procedure but there are no isolation requirements. These muons are also required to pass a list of track quality requirements to suppress backgrounds from

false tracks and muons coming from hadron decays. These veto muons can be classified as either combined or segment-tagged. Combined muons are identified by matching muon spectrometer tracks to inner detector tracks and performing a combined track fit based on the hits in those detectors (taking into account the energy loss in the calorimeters). The segment-tagged muons are identified by requiring that an inner detector track extrapolated to the muon spectrometer satisfies tight angular matching requirements to at least one reconstructed muon spectrometer segment [124]. An inner detector track which is successfully matched is then a muon candidate, and the muon parameters are extracted from the inner detector track fit.

2. Selected muons in 1μ+jets and 2μ+jets regions have to pass the *Medium* identification working point and also the *FCLoose* isolation working point. The *Medium* identification working point has a prompt muon selection efficiency of 97% ($20 < p_{\mathrm{T}}[GeV] < 100$, see [123] for other p_{T} ranges). The *FCLoose* isolation working point has a fixed muon selection efficiency of 99%. This is achieved using a cut on the sum of the p_{T} of tracks within a varying radius around the muon (dependent on the muons momentum) [123]. As for the selected electrons, we make sure that they associate to a primary vetex by making cuts of $|z_0 \times \sin(\theta)| < 0.5$ mm and $|d_0|/\sigma(d_0) < 3$ on the longitudinal and transverse impact parameters.

Photon Identification

Similar to electrons, photons are reconstructed from energy clusters in the electromagnetic calorimeter. As photons are neutral particles, they leave no tracks in the inner detector, and therefore it is possible to distinguish them from electrons. However it is possible for electrons to produce photons through bremsstrahlung and for photons to convert to an electron-positron pair through photon conversion. The information from the electromagnetic calorimeter and the inner detector tracks is used to disentangle these processes and reconstruct the correct final state particles. In this analysis, the energy deposits for the photons are included in the reconstruction of the jets and no further photon selection is needed.

Tau Identification

The tau (τ) is the heaviest lepton and the only lepton heavy enough to decay to hadrons. Taus possess the capability to decay off shell, giving rise to a decay product containing a W boson and a neutrino. The W boson, in turn, can undergo decay either into a lepton-neutrino pair or hadronically. The taus which decay leptonically are reconstructed as electrons or muons in this analysis. Taus which are matched to an electron within a cone of $\Delta R < 0.4$ and have a large electron likelihood will be discarded. The hadronically decaying taus must have one or three associated tracks which correspond to a one or three-prong tau decay mode respectively and also an absolute charge of one. The hadronically decaying taus are required to have $p_{\mathrm{T}} > 20$ GeV and $|\eta| < 2.47$, excluding the crack region of $1.37 < |\eta| < 1.52$. The reconstruction of hadronic tau decays is seeded by the reconstructed anti-k_t jets (with $\Delta R = 0.4$). The first step is that the centre of the clusters (a jet consists of several clusters, where each cluster is a set of calorimeter cells) is identified and all the clusters which are within $\Delta R = 0.2$ are included in the calculation. The relative position of the clusters is calculated with respect to the tau vertex and from this it is possible to obtain the tau axis. Another cone of $\Delta R = 0.2$ is constructed around this tau axis and the tracks within said cone are considered to be associated to the tau decay. An isolation cone with $\Delta R = 0.4$ is constructed and this is done as to collect tracks within the $0.2 < \Delta R < 0.4$ range and this helps to evaluate the isolation of the tau candidate. They also must satisfy the *JETIDRNNLOOSE* selection criteria, which is a RNN *Loose* working point with an ID efficiency of 85% for the one prong decay mode and an ID efficiency of 75% for the three prong decay mode.[7] This WP uses a novel τ_{had} identification algorithm which separates the truth τ_{had} from the misidentified τ_{had} originating from quark and gluon-initiated jets. This algorithm is based on a RNN and uses information from reconstructed charged-particle tracks and clusters of energy in the calorimeter associated to τ_{had} as well as high-level discriminating variables to separate the truth τ_{had} from the misidentified τ_{had}.

Jet Identification

Jets are reconstructed using the anti-k_T jet algorithm with a radius parameter of 0.4 and using particle flow objects as input to the clustering, see Section 3.2.6. The jets are

[7] RNN stands for recurrent neural network, which is a class of artificial neural networks which recognises the data's sequential characteristics and uses patterns to predict the next likely scenario.

required to have p_{T} >30 GeV and a rapidity $|y| < 4.4$. The jet vertex fraction (JVF) is a variable used in ATLAS to identify the primary vertex from which the jet originated. A cut on the JVF variable can help to remove jets which are not associated with the hard scatter primary vertex. Unfortunately the JVF has some pileup dependence, which can be remedied by correcting with the corrJVF variable (a pileup corrected JVF variable) and also introducing a new variable defined from hard scatter observables ($R_{p_{\mathrm{T}}}$). The variable $R_{p_{\mathrm{T}}}$ is defined as the scalar sum of the p_{T} of the tracks that are associated with the jet and originate from the hard scatter vertex divided by the fully calibrated jet p_{T}, which includes the pileup subtraction. The jet-vertex-tagger (JVT) discriminant is constructed using $R_{p_{\mathrm{T}}}$ and corrJVF as a two-dimensional likelihood derived using simulated dijet events and based on a k-nearest neighbour (kNN) algorithm. This discriminant has the advantage of not having the pileup dependence of the JVF variable [125].

All jets are required to satisfy a set of *Medium* JVT criteria, corresponding to a JVT>0.64 cut. The *Medium* JVT working point is found to be 92% efficient at selecting jets which originate from the primary vertex with a 2% fake rate from pileup jets. Jets with a pseudorapidity of $|\eta| > 2.5$ are also required to pass the fJVT criteria with a required *Tight* working point.[8] The *Tight* operating point of the fJVT algorithm, which is designed to select jets originating from the primary vertex, has an efficiency of 79.9% for jets with 20 GeV$< p_T <$30 GeV and an efficiency of 94.6% for jets with 40 GeV$< p_T <$50 GeV.

$\boldsymbol{p_{\mathrm{T}}^{\mathrm{miss}}}$

At the detector-level the $p_{\mathrm{T}}^{\mathrm{miss}}$ is calculated following the same method as for the particle-level, such as in Section 3.2.7, and using the Equation 3.10. In this analysis, photons are treated as jets in the $p_{\mathrm{T}}^{\mathrm{miss}}$ calculation. As done for particle-level $p_{\mathrm{T}}^{\mathrm{miss}}$, the leptons in the regions are treated as invisible and are excluded from the reconstruction level $p_{\mathrm{T}}^{\mathrm{miss}}$. Jets which overlap with a muon, have a low track number and a low p_{T} track are assumed to originate from muon bremsstrahlung and are marked as invisible. This step is equivalent to using dressed leptons in the particle-level $p_{\mathrm{T}}^{\mathrm{miss}}$ calculation [126].

[8] The topological correlation among particles originating from a pileup interaction is exploited to extrapolate the forward jet vertex tagger (fJVT), using track and vertex information, which goes beyond the tracking coverage of the inner detector to identify and reject pileup jets at high pseudorapidities.

4.4.2. Fake Estimates

Fake $p_{\mathrm{T}}^{\mathrm{miss}}$ in the $p_{\mathrm{T}}^{\mathrm{miss}}$+jets Region

Multijet events can enter the $p_{\mathrm{T}}^{\mathrm{miss}}$+jets region due to neutrinos from heavy flavour decays or fake $p_{\mathrm{T}}^{\mathrm{miss}}$ from detector effects. To estimate the contribution of multijet events, the jet smearing method is used, where the momenta of jets in well-measured multijet seed events are smeared multiple times with data-constrained jet response functions. A large pseudo-data sample is created from the smeared events, and the shape of the multijet background and its relative normalization with respect to a multijet-enriched control region is predicted. The control region is used to normalize the background, and the shape agreement of the pseudo-data is checked in the control and validation regions. The background contributes about 1% to the total yield at low $p_{\mathrm{T}}^{\mathrm{miss}}$. The impact of this uncertainty on the final cross-section measurement is expected to be 0.8% in the lowest $p_{\mathrm{T}}^{\mathrm{miss}}$ bin, where the relative background contribution is largest and well below that in all higher bins. Figures and details on this study can be found in [126].

Fake Lepton Backgrounds

The background in the 1ℓ+jets and 2ℓ+jets regions arise from the jets mis-identified as leptons and leptons from heavy flavour decays. This section describes the data-driven procedures, which are used to estimate this background in the $1e$+jets region (matrix method) and 1μ+jets and 2ℓ+jets regions (fake factor method). Both of these procedures are briefly discussed below and summarised in [127].

The Matrix Method (MM)

In the case of the $1e$+jets region, the dominant background arises from jets misidentified as electrons. This background is difficult to estimate accurately using a fake factor method due to the large uncertainties on the electron identification efficiency and the misidentification rate. Therefore, the matrix method is used to estimate this background by measuring the rate at which jets are misidentified as electrons in a control sample with looser electron identification requirements, and then extrapolating this rate to the "real" $1e$+jets region with tighter electron identification requirements.

The matrix method allows us to estimate the number of fake lepton which pass the selected lepton selection of the auxiliary regions. For a fake lepton study, it is useful to define the *loose* lepton selection, which enhances the fake contribution and this definition is taken from [122].

The matrix method relates the number of *loose* real (N_r^l) and fake (N_f^l) leptons to the number of *loose* leptons which pass the "selected electron" criteria (N^S) and those that do not ($N^{!S}$). The criteria for the "selected electron" are given in Subsection 4.4.1. This can be done via a matrix, which consists of the efficiencies of a real and fake *loose* lepton being reconstructed as a selected lepton, which are represented as r and f respectively:

$$\begin{pmatrix} N^S \\ N^{!S} \end{pmatrix} = \begin{pmatrix} r & f \\ 1-r & 1-f \end{pmatrix} \begin{pmatrix} N_r^l \\ N_f^l \end{pmatrix} \tag{4.2}$$

Both r and f are defined as

$$r = \frac{N_r^S}{N_r^l}, \quad f = \frac{N_f^S}{N_f^l}. \tag{4.3}$$

Once the quantities N^S, $N^{!S}$, r and f are determined, the Equation 4.2 can be inverted to obtain the number of real and fake leptons. The fake lepton contributions to the lepton regions are then given by:

$$N_f^S = f N_f^l = \frac{f}{r-f}\left(r\left(N^{!S}l + N^S l\right) - N^S\right). \tag{4.4}$$

For the 1e+jets region, the *loose* electrons are required to pass the *loose* electron identification working point, whereas the selected electrons have to pass the “selected electron” criteria defined in Subsection 4.4.1. The systematic uncertainty for the fake background estimate in the 1e+jets auxiliary region was determined based on the variation of the fake lepton efficiency, which depends on the choice of the fake-

enriched control region. The uncertainty was varied according to specific criteria and the relative uncertainty on the background estimates for different phase-spaces was calculated with statistical fluctuations accounted for by rebinning and symmetrising the uncertainty. A more detailed description of this systematic uncertainty is given here [126].

The Fake Factor Method (FFM)

The 1μ+jets and 2ℓ+jets regions have a significant contribution from heavy flavour decays, which can be estimated using the fake factor method. This method involves measuring the rate at which muons (or electrons in the two electron region) are produced in a control sample enriched in heavy flavour events, and then applying this rate to the desired region to estimate the background. The uncertainties on the muon identification and misidentification rates are typically smaller than those for electrons, making the fake factor method more reliable in these regions.

The fake factor method starts from the same assumption as in Equation 4.2 to derive the non-prompt contribution in Equation 4.4.

The final non-prompt background is then given by:

$$N_f^S = \frac{f}{1-f}(N^{!S} - N_r^{!S}) = F(N^{!S} - N_r^{!S}), \tag{4.5}$$

Where $F = \frac{f}{1-f}$ is the fake factor, $N^{!S}$ is the yield with *loose* and "non-selected" leptons measured in the data and $N_r^{!S}$ is the yield with real *loose* "non-selected" leptons from the simulation.

In the case of determining the fake lepton estimate for multiple leptons, the final non-prompt prediction is given by all the possible combinations of the prompt and non-prompt leptons, which each non-prompt lepton is multiplied by the respective fake factor. In contrast to the matrix method, only fake lepton efficiencies are needed. The uncertainty on these fake lepton predictions in various regions was calculated by considering several sources such as fake efficiencies, data statistics in the fake control region, and determining the resulting relative systematic uncertainty on the fake background estimate for each source.

4.4.3. Detector-Level Event Selection

The event selection for leptons and jets is the same for the detector-level as it is for the particle-level. This is by design, as we want the two event selections to be as similar to each other as possible to avoid extrapolation issues in the unfolding procedure. The detector-level event selection for the lepton regions are given by Tables 4.2. The same is true for the detector-level event selection for ≥ 1 jet , ≥ 2 jet and VBF phase-spaces, which are defined in Table 4.1. There are additional criteria (relative to particle-level) applied to the detector-level events.

Event and Jet Cleaning

The reconstructed events are required to have a primary vertex with at least two associated tracks, where these associated tracks need to satisfy certain criteria. These events are required to be on the Good-Runs List (GRL), this means that all parts of the detector were working properly and that the events happened during good quality beam conditions. The luminosity blocks that meet these criteria have all data quality flags set to good. "Jet cleaning" is when bad quality jets are rejected, these are generally expected to originate from non-collision backgrounds or calorimeter noise. We are able to reduce the number of bad jets using the *LooseBad* and also *TightBad* working point. The *LooseBad* selection is designed to provide an efficiency of selecting jets from pp collisions above 99.5% (99.9%) for $p_{\mathrm{T}} > 20(100)$ GeV (this is considered the default) whereas the *TightBad* is designed to further reject background jets especially in regions sensitive to non-collision backgrounds with an efficiency of selecting jets from proton-proton collisions above 95% (99.5%) for $p_{\mathrm{T}} > 20(100)$ GeV.

Trigger Selection

We use two types of trigger to select events for this analysis. The main feature of this analysis is to study the $p_{\mathrm{T}}^{\mathrm{miss}}$ +jets final state with its large amount of missing transverse energy. Events in this region are selected using the lowest unprescaled $p_{\mathrm{T}}^{\mathrm{miss}}$ trigger for events from 2015 to 2018. The high level trigger (second level trigger) does not use information from the muon systems in the calculation of the $p_{\mathrm{T}}^{\mathrm{miss}}$ for the trigger. Muons are therefore invisible to the trigger algorithm and the events containing muons can be triggered on with the $p_{\mathrm{T}}^{\mathrm{miss}}$ trigger. For this reason, the events

in the 1μ+jets and 2μ+jets region are selected using the $p_{\mathrm{T}}^{\mathrm{miss}}$ +jets region triggers. Events in the $1e$+jets and $2e$+jets regions are selected using the lowest unprescaled single electron trigger in every run period (2015 to 2018). The triggers used for each region are summarised in Table 4.3.

Region	Trigger requirement
$p_{\mathrm{T}}^{\mathrm{miss}}$+jets, 1$\mu$+jets & 2$\mu$+jets	2015:
	HLT_xe70
	2016:
	HLT_xe90_mht_L1XE50
	HLT_xe110_mht_L1XE50
	2017:
	HLT_xe110_pufit_L1XE55
	2018:
	HLT_xe110_pufit_xe70_L1XE50
	HLT_xe120_pufit_L1XE50
	HLT_xe110_pufit_xe65_L1XE50
1e+jets & 2e+jets	2015:
	HLT_e24_lhmedium_L1EM20VH
	HLT_e60_lhmedium
	HLT_e120_lhloose
	2016:
	HLT_ e24_lhmedium_nod0_L1EM20VH
	HLT_e60_lhmedium
	HLT_e26_lhtight_nod0_ivarloose
	HLT_e60_lhmedium_nod0
	HLT_e140_lhloose_nod0
	HLT_e300_etcut
	2017:
	HLT_e26_lhtight_no d0_ivarloose
	HLT_e60_lhmedium_nod0
	HLT_e140_lhloose_nod0
	HLT_e300_etcut
	2018:
	HLT_e26_lhtight_nod0_ivarloose
	HLT_e60_lhmedium_nod0
	HLT_e140_lhloose_nod0
	HLT_e300_etcut

Table 4.3.: A summary of the trigger requirements applied to the $p_{\mathrm{T}}^{\mathrm{miss}}$+jets region and the four lepton-based regions. HLT stands for high level trigger, L1 stands for Level 1, the xe stands for the $p_{\mathrm{T}}^{\mathrm{miss}}$, i is for the isolation requirements, e stands for the electron, lh stands for likelihood, pufit corrects for pileup effects, nod0 indicates that no transverse impact parameter cuts are required and ivarloose indicates a variable sized cone isolation requirement, etcut stands for transverse energy cut and EM stands for electromagnetic.

4.5. Datasets and Monte Carlo Simulation

4.5.1. Data

The data in this analysis were collected by the ATLAS experiment during Run 2 in the years 2015–2018. This dataset amounts to an integrated total luminosity of 139 fb^{-1} of proton-proton collisions at a centre of mass energy of $\sqrt{s} = 13$ TeV as shown in Figure 3.2. The uncertainty for the integrated luminosity is 1.7 % [128], which is obtained using the LUCID-2 detector for the primary luminosity measurements.[9] The average number of collisions per bunch crossing (pileup) was around 34 over the whole 2015–2018 data taking period [129].

4.5.2. Modelling High Energy Collisions Using Monte Carlo

Typically there are hundreds of particles which are produced in high energy particle collisions at the LHC and understanding these collisions is an extremely challenging theoretical problem. The matrix elements (ME) for the relevant processes become difficult to calculate beyond the first few orders and in the case of QCD they involve processes which are inherently non-perturbative with the additional issue of confinement. When these matrix elements have been calculated with an approximation scheme, there are still many divergences and/or near-divergences which cannot be resolved. These matrix elements need to be integrated over the final-state phase-space to obtain predictions for the experimental observables that we are interested in. Over many years, physicists have been developing many tools to deal with what on the surface appear to be irresolvable problems. One of the most important of these tools is factorisation. This method allows for many of the processes of interest to be split up into different regimes based on their scale of transfer momentum. At the highest transfer momentum scale, the partons which constituent the incoming particles interact to produce a relatively small number of the energetic outgoing partons, leptons or gauge bosons. The matrix elements of these hard processes can be computed via perturbation theory. At the lowest scales, $\mathcal{O}(1\text{ GeV})$, the incoming partons are confined to the particle beams and the outgoing partons interact non-perturbatively to form the final-state hadrons. This change in parton behaviour is due to the running of the strong

[9] The ATLAS luminosity monitor, LUCID-2 (LUminosity Cherenkov Integrating Detector), which was upgraded from LUCID in 2015 to account for the increased luminosity.

coupling α_s as a function of the energy scale, where it can be seen that α_s becomes large around 1 GeV but the Taylor expansion used in perturbation theory requires α_s to be small. Hence the confinement of partons into hadrons. These so-called "soft" processes cannot be calculated perturbatively but instead have to be modelled.

These hard and soft regimes are distinct but are connected by a progressive process which itself (the progressive process that is) can be calculated using QCD via perturbation theory. This progressive process refers to the intermediate scale regime between the hard and soft processes, where the outgoing partons from the hard process are transformed into a spray of collimated particles (otherwise known as a jet), which eventually hadronises into a collection of final-state hadrons. This process is also known as parton showering. The parton showering process can be described using perturbative QCD calculations, but the resulting jet formation and hadronisation cannot, and must be modeled using phenomenological models or Monte Carlo (MC) simulations. The process of matching the hard and soft regimes is referred to as matching, and is used to ensure that the predictions from the perturbative QCD calculations and the hadronisation models are consistent with each other. This scale evolution results in many additional partons which comes in the form of initial-state and final-state radiation, which eventually evolves down to the low-scale processes of hadron formation.

These three different transfer momentum schemes (the soft, the progressive process and the hard) form a highly successful picture of hard collisions which can be simulated using the MC method. The final state is integrated in a dimension of phase-space given by $3n - 4$ along with the flavour and spin for the n-particle final state.[10] This makes the MC a suitable method of choice for the integration over the phase-space. The numerical accuracy of this method increases as the inverse square root of the number of integration points. The evolution of the scales which leads to parton showering can in fact be simulated efficiently and the hadronisation can be simulated via MC as well. The fact that the event generation is factorised means that this evolution can be improved systematically as more precise QCD perturbative calculations or better hadronisation models are computed. Using this evolution scale, it is possible to obtain a MC event generator which can simulate a wide range of the most interesting particle processes at the LHC. Comparison of these MC predictions to data is very useful to constrain SM parameters.

[10] It is $3n - 4$ as there are three components of momentum for every produced particle, minus the four constraints of overall energy-momentum conservations.

Historically, the event generators came shortly after the discovery of the partonic structure of hadrons along with QCD being the theory of strong interactions. Deep inelastic scattering and hadronic production of jets and leptons can be understood via partonic interactions.

To describe the final states in more detail, phenomenological models are used to fragment the partons directly into hadrons. However this does not account for the broadening of the jets and lepton distributions with increasing energy. On the other hand the initial-state partons are coloured and therefore emit gluons or quark-pairs in the same way scattered charge particles emit photons, where these gluons, as opposed to the photons, can also radiate and this leads to parton showering accounting for the broadening distributions.

Two important methods which are used for these type of calculations are called matching and merging. A matching scheme defines on an event-by-event basis which of the paths should be followed (that of a "hard" or "soft" process). The primary goal of a matching scheme is to avoid double counting (prevent events going through both paths). Furthermore, a good matching scheme will optimise the choice of the path and choose the path that describes the process best given certain kinematics. Merging is when one performs tree-level calculations for each parton of interest, in which the soft and collinear divergences of the hard matrix elements can be regulated. These calculations are then "merged" with the relevant parton shower, and double counting is removed by vetoing certain parton shower branches.

There are various matching and merging schemes which exist to improve the approximations of these parton showers by combining the parton shower modelling with the matrix element calculations at a suitable scale [130–133]. The endpoint of the parton showering is hadron formation, where the scale of momentum transfers is low and the strong coupling constant is large (due to QCD running, as mentioned earlier). This means that the hadronisation process is non-perturbative and these models were developed with tunable parameters to describe the properties of the hadronic final states. Popular choices include the cluster model [134] as well as the Lund string model [135]. The partons from the parton shower will be combined according to their colour charge which leads to resonances (e.g., excited kaons) that will then decay into a hadronic final state. The collimated parton shower (can be seen as a QCD particle cascade) can also be considered a jet, the precise definition of the jet depends on the choice of the jet reconstruction algorithm [136–138].

Most of the signal processes that are of interest at the LHC are from hard interactions, however the vast majority of collisions are soft which leads to diffractive scattering along with multiparton production at low transverse momenta. The non-perturbative nature of soft collisions means that they are simulated with models with tunable parameters to describe the data. There is also a related phenomenon which is a component of the final state in hard interactions which is not associated with the primary hard process — this is called the "underlying event". The remnants of these hard interactions are described by pertubative QCD but again the soft components have to be modelled. It is possible to use the same multiple-parton interactions to model these collision remnants, as long as there aren't conflicts between the parameter values needed for the two regimes.

Although the factorisation of the hard scattering process in the calculation of the cross-section has not been proven, there are strong arguments that this factorisation method holds for many of the processes of interest [139, 140].

4.5.3. Monte Carlo Samples for SM processes

The SM processes which contribute to the fiducial phase-space are simulated using MC models and have been propagated through to GEANT4 [141, 142] for a full simulation of the ATLAS detector and are reconstructed using the same analysis chain as for data. Additional pileup collisions are overlaid (based on soft QCD processes) which are simulated by PYTHIA 8.186 [143] using the NNPDF2.3LO PDF set [144] and the A3 set of tuned parameters [145] over the original hard scattering event. A summary of the main SM MC samples used in this analysis are listed in Table 4.4.

V+Jets

The events containing single W or Z/γ^* bosons in association with jets are generated with the SHERPA v2.2.1 [146] parton shower MC generator. These events are calculated to an accuracy of NLO matrix elements for up to two jets, and LO matrix elements for up to four jets using the COMIX [147] and OPENLOOPS [148, 149] libraries.

For the parton showering, the default SHERPA setting is used [150] which is based on the Catani-Seymour dipoles[11] and the cluster hadronisation model[12] [151]. The parton showering makes use of the dedicated set of tuned parameters by the SHERPA authors for this version based on the NNPDF3.0NNLO set [152]. The NLO matrix elements of a given jet multiplicity are matched to the parton shower through a colour-exact invariant of the MC@NLO algorithm [153]. Different jet multiplicities are merged into an inclusive sample using the improved CKKW matching procedure [154] and is then extended to the NLO accuracy using the MEPS@NLO method [131], where the merging cut is $Q_{cut} = 20$ GeV. The V+jets samples are normalised to NNLO prediction [155]. Details for the full process configuration for V+jets are given in [156].

The electroweak production of the W or Z/γ in association with two jets and up to one additional parton emission at LO accuracy is generated using SHERPA 2.2.11. Again for the parton showering, this is based on the Catani Seymour dipole [150], the cluster hadronisation model [151] and matched with the Matrix Elements using the MEPS@LO prescription.

The SHERPA V+jets samples are generated in slices of a kinematic variable (such as boson p_{T}) and need to be combined according to their relative cross-sections. This ensures that there are sufficient statistics in the tails of the distributions. For the W and Z bosons decaying into charged leptons, the slicing is done in terms of the maximum boson p_{T} and H_T in the event.[13] For the $Z \to \nu\nu$ samples, the slicing is done in terms of the Z boson p_{T} and the dijet invariant mass in events with at least two jets. The

[11] The Catani-Seymour dipoles are a method for describing the real emission contributions to the parton shower in perturbative QCD calculations. They provide a way of factorizing the QCD amplitudes for real emissions into a color structure times a kinematic factor, which is proportional to the tree-level matrix element for the associated process. This factorization allows for the implementation of the parton shower in a way that is both systematic and gauge invariant. The Catani-Seymour dipole method is commonly used in Monte Carlo event generators, such as SHERPA, to describe the showering of partons and the production of hadrons.

[12] In this model, partons produced in the hard interaction are evolved using the parton shower algorithm, which generates additional partons and gluons via branching processes. These partons are then grouped together into colour-neutral clusters, which subsequently fragment and hadronise to form observable hadrons. The cluster hadronisation model differs from other hadronisation models, such as the string fragmentation model, in that it does not rely on a string-like structure between partons. Instead, it is based on the idea that the hadronisation process is dominated by the softest partons in the shower, which form clusters that subsequently hadronise.

[13] H_T is defined as the sum of the transverse momenta of all jets in the event, represented by $p_{\mathrm{T}_{j'}}^{\mathrm{jet}}$. Here, j' refers to the different ordered jets, such as leading jet (j^1), sub-leading jet(j^2), and third-order jet (j^3).

Physics Process	Generator	Parton Shower	Accuracy of cross-section	Tune	PDF Set
QCD V+jets	SHERPA v2.2.1	SHERPA v2.2.1	NNLO	SHERPA default	NNPDF3.0NNLO
EWK V+jets	SHERPA v2.2.11	SHERPA v2.2.11	LO	SHERPA default	NNPDF3.0NNLO
VV(semileptonic)	SHERPA v2.2.1	SHERPA v2.2.2	NLO	SHERPA default	NNPDF3.0NNLO
VV(fully leptonic)	SHERPA v2.2.2	SHERPA v2.2.2	NLO	SHERPA default	NNPDF3.0NNLO
VVV	SHERPA v2.2.2	SHERPA v2.2.2	NLO	SHERPA default	NNPDF3.0NNLO
$t\bar{t}$	POWHEG-BOXv2	PYTHIA v8.230	NNLO+NNLL	A14	NNPDF3.0NLO
Single top (Wt)	POWHEG-BOXv2	PYTHIA v8.230	NLO	A14	NNPDF3.0NLO
Single top (t-channel)	POWHEG-BOXv2	PYTHIA v8.230	NLO	A14	NNPDF3.0NLOnf4
Single top (s-channel)	POWHEG-BOXv2	PYTHIA v8.230	NLO	A14	NNPDF3.0NLO

Table 4.4.: Simulated event samples used in this analysis with their corresponding matrix element and their parton shower generators, accuracy of the cross-section, the event tuning parameters and the PDF set used.

change in phase-space biasing strategy for this channel was motivated by trigger considerations.

Dibosons

Samples containing a pair of vector bosons, which both decay to leptons, were generated with SHERPA v2.2.2 [146]. In this setup, the matrix elements are matched with parton showering (from SHERPA) based on Catani-Seymour dipole factorisation [150] using the MEPS@NLO method [131, 153, 154]. There are virtual NLO QCD corrections for the Matrix Elements which are provided by the OPENLOOPS library [148, 149]. The jet multiplicities for the fully leptonic samples are $0, 1j@NLO + 2, 3j@LO$ (calculated the samples with zero and one jet to NLO accuracy and those with two and three jets to LO accuracy). The samples are generated using the NNPDF3.0NNLO set [152], along with the set of tuned parton shower parameters developed by the SHERPA authors. The semileptonically decaying diboson samples are simulated with an almost identical setup to the fully leptonic decays, except the SHERPA v2.2.1 [146] generator is used.

Triboson

The triboson samples are also generated with SHERPA v2.2.2 [146]. In this setup, multiple matrix elements are matched and merged with the SHERPA parton showering based on the Catani-Seymour dipole factorisation [147, 150] using the MEPS@NLO prescription [131, 153, 154]. The virtual QCD corrections for matrix elements at NLO

accuracy are provided by the OPENLOOPS library for the inclusive process and up to two additional jets at LO. These samples are produced using the NNPDF3.0NNLO PDF set [152] with a dedicated set of tuned PDF parameters.

Top Events

On-shell $t\bar{t}$ events are produced using POWHEG-BOX v2 [157–160] at NLO based on the NNPDF3.0NLO [152] PDF, where the h_{damp} [14] is set to 1.5 m_t [161]. The $t\bar{t}$ events are interfaced with PYTHIA 8.230 [162] using the A14 tune [163] and the NNPDF2.3LO PDF set. The NLO $t\bar{t}$ inclusive production cross-section is corrected to NNLO in QCD, including the resummation of next-to-next-to-leading logarithmic (NNLL) soft-gluon terms which is calculated using TOP++2.0 [164–170].

Single-top tW associated production is generated using POWHEG-BOX v2 [158–160, 171] at NLO in QCD using the NNPDF3.0NLO [152] PDF set. For these samples, a diagram subtraction scheme [172] is used to deal with $t\bar{t}$ production [161]. For parton showering, these events use PYTHIA 8.230 [162], a dedicated A14 tune [163] and the NNPDF2.3LO PDF set. The inclusive cross-section is corrected to the theory prediction calculated at NLO in QCD with NNLL soft gluon corrections [173, 174].

Single top t-channel production uses POWHEG-BOX v2 generator [158–160, 175] at NLO QCD in the four flavour scheme with the NNPDF3.0NLOnf4 [152] PDF set. Again, the events require parton showering and this is managed using PYTHIA 8.230 [162] with the A14 tune [163] and the NNPDF2.3LO PDF set. The inclusive cross-section is corrected to the theory prediction at NLO in QCD using HATHOR v2.1 [173, 174].

Single top s-channel production uses POWHEG-BOX v2 generator [158–160, 176] at NLO QCD in the five flavour scheme with the NNPDF3.0NLO PDF set. Again, the events require parton showering and this is managed using PYTHIA 8.230 [162] with the A14 tune [163] and the NNPDF2.3LO PDF set. The inclusive cross-section is corrected to the theory prediction at NLO in QCD using HATHOR v2.1 [173, 174].

[14] The h_{damp} parameter controls the transverse momentum p_{T} of the first additional emission which is beyond the leading order diagram in the parton shower, and as a result this parameter which can control the high-p_{T} emission against which the $t\bar{t}$ system recoils.

4.5.4. Monte Carlo Event Reweighting

The simulated events are often reweighted such that the MC, used for the unfolding, better matches the data that is also being unfolded. All MC events are reweighted using scale factors for the leptons and photons, accounting for efficiency differences between the data and simulation. The level of pileup in each event are quantified by the average number of inelastic interactions per bunch crossing, $\langle\mu\rangle$. This can be estimated using the instantaneous luminosity, the inelastic proton-proton cross-section and the corresponding beam parameters for the relevant luminosity blocks. The MC events are weighted to reproduce the pileup distribution of the average pileup per bunch crossing which is observed in data, this is known as pileup reweighting. During the pileup reweighting, the $\langle\mu\rangle$ value from the data is divided by a factor[15] of 1.03 ± 0.04. This rescaling makes the number of reconstructed primary vertices agree better between data and simulation and this is able to reproduce the cross-section of inelastic proton-proton collisions as seen in data.

The central SHERPA 2.2.1 samples exhibit a difference in the boson p_{T} spectrum for the electron and muon channels.[16] The region that is mostly relevant to this analysis is p_{T} >200 GeV,where the difference between the two lepton channels is at a 5-10% level and for the one lepton channel is a couple of %. Lepton universality is restored for the two lepton regions in the bug fix for the SHERPA 2.2.2. Comparing the two SHERPA versions for the same $Z \to \ell\ell$ channel, it can be seen that the $Z \to \mu\mu$ channel is consistent between the versions while the $Z \to ee$ channel is not. From this it is possible to conclude that the centrally produced $Z \to ee$ samples are affected by the bug. Therefore a reweighting function derived from the ratio of the centrally produced $Z \to ee$ to $Z \to \mu\mu$ is used for the central SHERPA $Z \to ee$ sample.

The SHERPA V+jets samples have been reweighted to approximately account for higher-order electroweak effects. The electroweak corrections are based on a fixed-order calculation at NLO accuracy in the electroweak coupling, performed in [177]. The numerical values from the paper have been made publicly available by the authors and are used in this analysis to reweight the SHERPA V+jets samples as a function of the inclusive boson p_{T}.

[15] This is calculated using the pileup reweighting tool https://gitlab.cern.ch/atlas/athena/tree/master/PhysicsAnalysis/AnalysisCommon/PileupReweighting.

[16] Central refers to samples produced by the Physics Modelling Group (PMG) who are responsible for the development and validation of MC generators and samples for analyses for the experiments at the LHC.

4.5.5. Monte Carlo Samples for BSM Processes

We generate a number of BSM samples in order to set confidence limits.

Dark Matter *s*-Channel Interactions

We produce Weakly Interacting Massive Particle (WIMP) signals of the type $\chi\bar{\chi}$+jet where χ is the DM candidate. These samples are generated by using POWHEG-BOX [158–160, 176] using the following two models:

1. $\chi\bar{\chi}$ production with a spin-1 axial-vector mediator exchange at NLO precision [52]
2. $\chi\bar{\chi}$ production with a spin-0 pseudoscalar mediator exchange with a quark loop at LO precision [52]

The renormalisation and factorisation are set to $H_T/2$ on an event-by-event basis, where $H_T = \sqrt{m_{\chi\bar{\chi}}^2 + p_{\mathrm{T},j1}^2} + p_{\mathrm{T},j1}$. The events are generated using POWHEG generator (v3359) [178] interfaced to PYTHIA 8.205 with A14 tuning [163]. The couplings of the mediator to DM particles and SM quarks are set to $g_\chi = 1$ and $g_q = 1/4$ for the axial-vector mediator model and $g_\chi = 1$ and $g_q = 1$ for the pseudoscalar model. A grid is produced of samples of DM masses ranging from 1 GeV to 1 TeV and the mediator masses between 10 GeV and 10 TeV.

Invisible Decays of Higgs

The Higgs samples are generated with the decay of the Higgs to two Z bosons and subsequently to four neutrinos ($H \to ZZ^* \to \nu\nu\nu\nu$) and a branching ratio of 100% is used to provide a simulation of the Higgs to invisible decay, see the Feynman diagram in Figure 4.1f. These are generated at a mass of 125 GeV for VBF production and VH production. These samples were generated at NLO in QCD using POWHEG-BOX [179]. The generated events were interfaced with PYTHIA 8 [143] for hadronisation and showering, using the AZNLO tune [180] and the NNPDF3.0NNLO PDF set [152]. The VH samples are produced with POWHEG-BOX v2 [160] + GoSam[17] [181] + MiNLO

[17] Automated one-loop calculations with GoSam is a program package which is designed for the automated calculation of one loop amplitudes for multi-particle processes in renormalisable quantum field theories.

(multiscale improved NLO)[18] [182, 183] procedure applied and are interfaced with PYTHIA 8 [143] for the showering and hadronisation using the AZNLO tune [180] and the NNPDF3.0NLO PDF set [152].

4.6. Data Quality

This section discusses possible pileup dependence of the reconstructed variables that are being measured in each region and each phase-space. This is done for the Run 1 dataset ($\mathcal{L} = 36.2$ fb^{-1}) and its corresponding MC campaigns. Pileup means that there are additional particles produced in the detector that are not associated with the hard scattering process of interest. These additional particles can interfere with the measurement of the final-state objects, such as jets (which are reconstructed using a clustering algorithm) and $p_{\mathrm{T}}^{\mathrm{miss}}$ that use the energy deposits in the detector. The energy from pileup can be misattributed to the hard scattering process, leading to a degradation of the energy resolution and biases in the reconstructed kinematic variables. For these reasons, data quality checks on the pileup dependence are important. If the pileup conditions in the data and simulation are different, the observed discrepancies between them could be due to pileup effects rather than true physics effects. Therefore, it is crucial to ensure that the simulation accurately reproduces the pileup conditions in the data and that any pileup effects on the reconstructed objects are properly accounted for in the analysis.

The average pileup, $\langle\mu\rangle$, is shown in the ≥ 1 jet phase-space, in Figure 4.2a, and there is adequate agreement between MC and data with a slight shift in the tails of the distribution. The same conclusions can be taken for the VBF phase-space, see Figure 4.2b, and the ≥ 2 jet phase-space, see Figure 4.2c. These figures do not include any pileup-related uncertainties (e.g., due to the pileup reweighting (PRW) shifts). The same MC/Data agreement was seen in the lepton regions for the VBF , ≥ 1 jet and ≥ 2 jet $\langle\mu\rangle$ distributions. The agreement between the MC and data is generally good for these pileup distributions, nevertheless, a correction could be made for the MC $\langle\mu\rangle$ to adjust for the difference in the tails that are seen throughout all the distributions. However for the purposes of this analysis this correction is deemed unnecessary as the agreement between MC and Data are deemed adequate.

[18] A method that chooses scales and includes Sudakov form factors in NLO calculations of processes involving jet production.

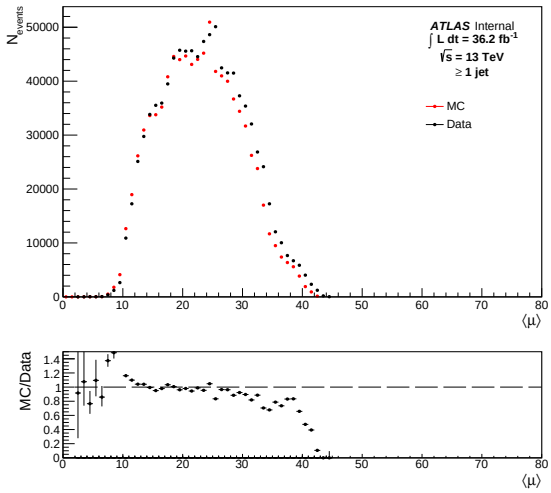

(a) $p_{\mathrm{T}}^{\mathrm{miss}}$+jets region in the ≥ 1 jet phase-space

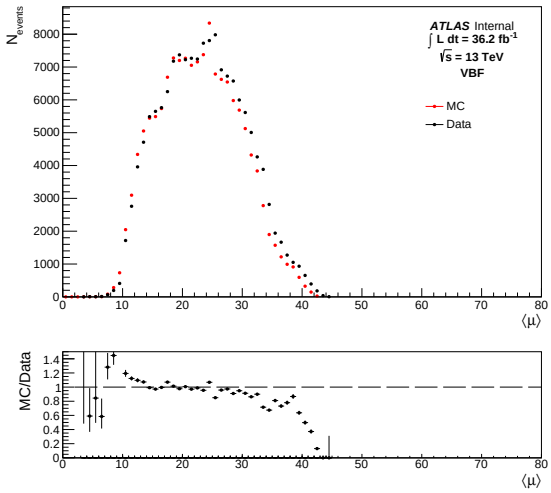

(b) $p_{\mathrm{T}}^{\mathrm{miss}}$+jets region in the VBF phase-space

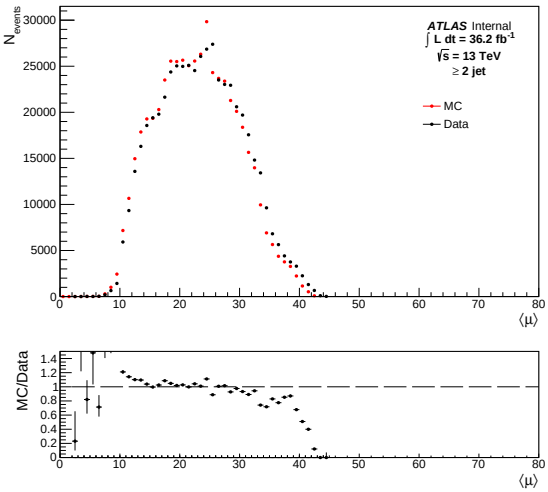

(c) $p_{\mathrm{T}}^{\mathrm{miss}}$+jets region in the ≥ 2 jet phase-space

Figure 4.2.: The average pileup, $\langle\mu\rangle$, distribution for the $p_{\mathrm{T}}^{\mathrm{miss}}$+jets region.

In the following plots, the ratio of the $p_{\mathrm{T}}^{\mathrm{miss}}$, m_{jj} and $\Delta\phi_{jj}$ distributions in different $\langle\mu\rangle$ regions are shown for all the regions. Three different $\langle\mu\rangle$ regions are chosen so as to split the available data statistics evenly across $\langle\mu\rangle$. These are: $0 \leq \langle\mu_{\mathrm{low}}\rangle \leq 22$, $22 \leq \langle\mu_{\mathrm{med}}\rangle \leq 40$ and $40 \leq \langle\mu_{\mathrm{high}}\rangle \leq 80$. After selecting the different core variables into $\langle\mu_{\mathrm{low}}\rangle$, $\langle\mu_{\mathrm{med}}\rangle$ and $\langle\mu_{\mathrm{high}}\rangle$, the ratios of $\langle\mu_{\mathrm{med}}\rangle/\langle\mu_{\mathrm{low}}\rangle$ and $\langle\mu_{\mathrm{high}}\rangle/\langle\mu_{\mathrm{med}}\rangle$ are then taken. This is shown for both data and MC. The ratios of higher to lower pileup

bins are a way of quantifying pileup effects. As long as any pileup effects are well modelled by the MC then they should be accounted for in the detector-corrections.

4.6.1. $p_{\mathrm{T}}^{\mathrm{miss}}$ Distributions

Figures 4.3–4.5 show the $\langle\mu_{\mathrm{med}}\rangle/\langle\mu_{\mathrm{low}}\rangle$ and $\langle\mu_{\mathrm{high}}\rangle/\langle\mu_{\mathrm{med}}\rangle$ ratios for the $p_{\mathrm{T}}^{\mathrm{miss}}$ distribution in the $p_{\mathrm{T}}^{\mathrm{miss}}$+jets region for the ≥ 1 jet , VBF and ≥ 2 jet phase-spaces respectively. For all figures the MC is mostly in agreement with data (within the statistical errors).

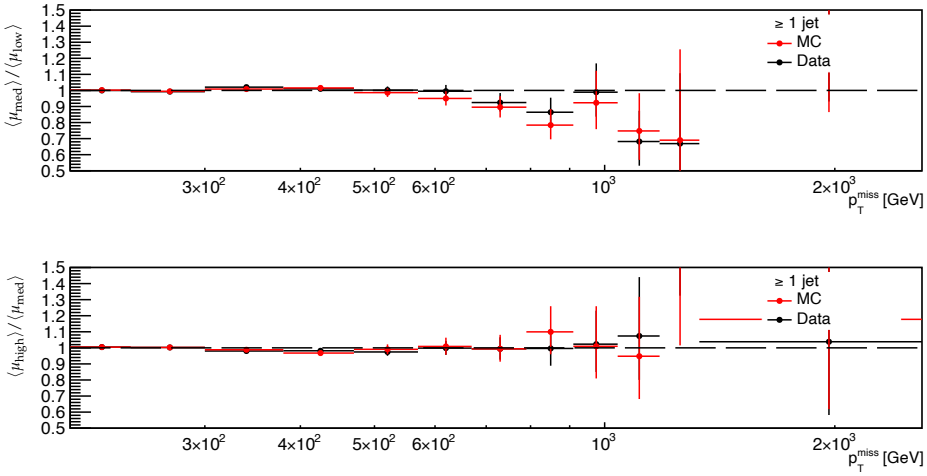

Figure 4.3.: The $\langle\mu\rangle$ dependence for the $p_{\mathrm{T}}^{\mathrm{miss}}$ in the $p_{\mathrm{T}}^{\mathrm{miss}}$+jets region for the ≥ 1 jet phase-space. Both the MC and Data are normalised to unity to help make shape comparisons, this is done for all $\langle\mu\rangle$ dependence figures. The error is calculated using the ratio of the two quantities (e.g., $\langle\mu_{\mathrm{med}}\rangle$ and $\langle\mu_{\mathrm{low}}\rangle$) using the equation $\sigma_{\mathrm{R}}^2 = \left(\frac{\partial R}{\partial X}\right)^2\sigma_{\mathrm{X}}^2 + \left(\frac{\partial R}{\partial Y}\right)^2\sigma_{\mathrm{Y}}^2 - 2\frac{\partial R}{\partial X}\frac{\partial R}{\partial Y}\mathrm{cov}(X,Y)$. Here, R is the ratio of two quantities X and Y with uncertainties σ_{X} and σ_{Y}, respectively. $\mathrm{cov}(X,Y)$ is the covariance between X and Y. The partial derivatives are evaluated at the central values of X and Y. In this case $X = \langle\mu_{\mathrm{med}}\rangle, \langle\mu_{\mathrm{high}}\rangle$ and $Y = \langle\mu_{\mathrm{low}}\rangle, \langle\mu_{\mathrm{med}}\rangle$. The same error propagation is used for the rest of these $\langle\mu\rangle$ dependence figures.

4.6.2. m_{jj} Distributions

The invariant mass of the two leading jets, m_{jj}, is only determined for the VBF and ≥ 2 jet phase-space region as these phase-spaces require two jets, whereas in a ≥ 1 jet event only one energetic jet coming from the event of interest is required. Figures

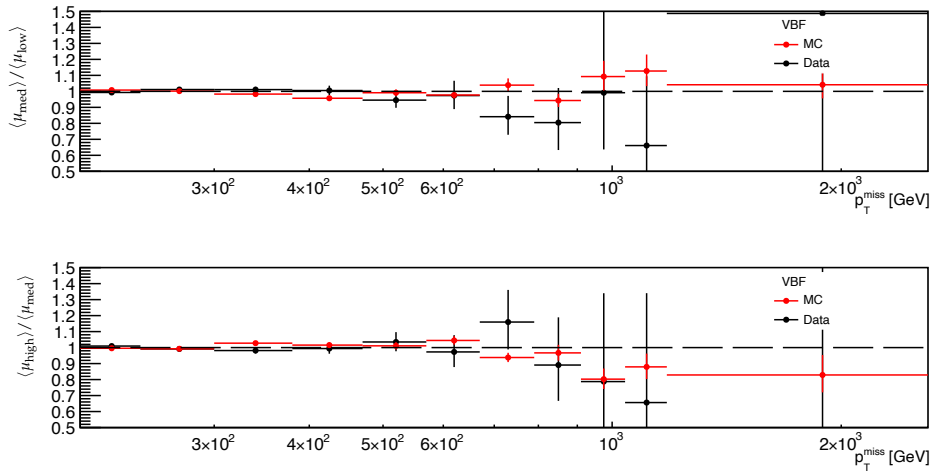

Figure 4.4.: The $\langle\mu\rangle$ dependence for the $p_{\mathrm{T}}^{\mathrm{miss}}$ in the $p_{\mathrm{T}}^{\mathrm{miss}}$+jets region for the VBF phase-space.

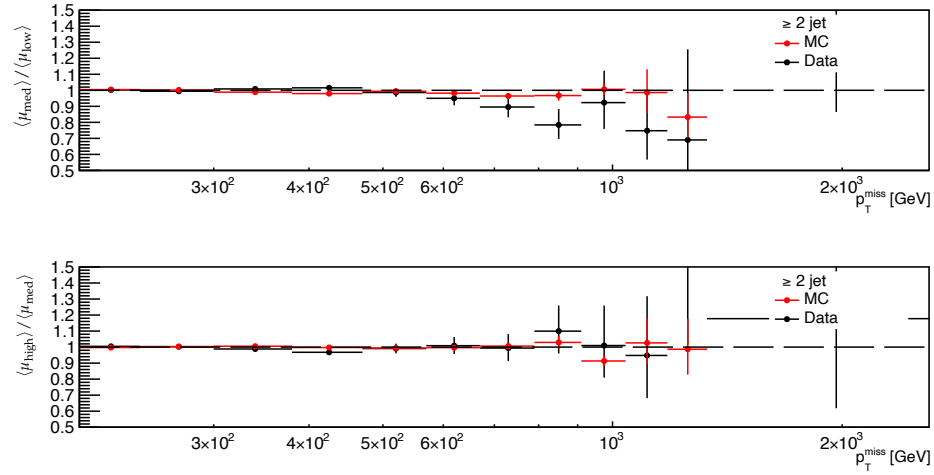

Figure 4.5.: The $\langle\mu\rangle$ dependence for the $p_{\mathrm{T}}^{\mathrm{miss}}$ in the $p_{\mathrm{T}}^{\mathrm{miss}}$+jets region for the ≥ 2 jet phase-space. Both the MC and Data are normalised to unity to help make shape comparisons, this is done for all $\langle\mu\rangle$ dependence Figures.

4.6 and 4.7 show the ratios of $\langle\mu_{\mathrm{med}}\rangle/\langle\mu_{\mathrm{low}}\rangle$ and $\langle\mu_{\mathrm{high}}\rangle/\langle\mu_{\mathrm{med}}\rangle$ for the m_{jj} variable in the $p_{\mathrm{T}}^{\mathrm{miss}}$+jets region for the VBF and ≥ 2 jet phase-space. The ratios for the MC and the data are mostly in agreement (within the statistical errors).

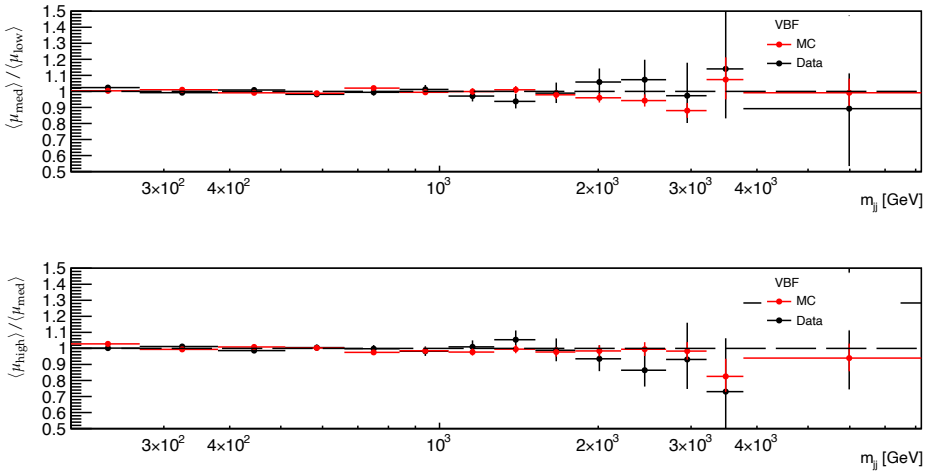

Figure 4.6.: The $\langle\mu\rangle$ dependence for the m_{jj} in the $p_{\mathrm{T}}^{\mathrm{miss}}$+jets region for the VBF phase-space.

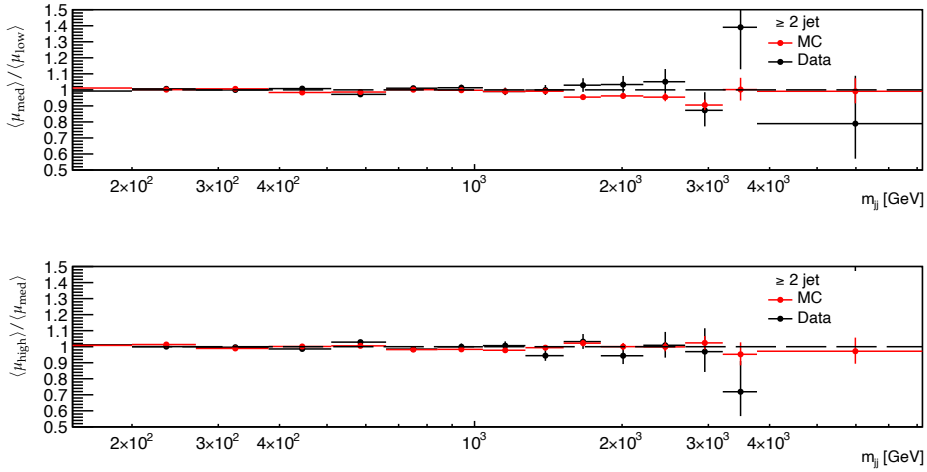

Figure 4.7.: The $\langle\mu\rangle$ dependence for the m_{jj} in the $p_{\mathrm{T}}^{\mathrm{miss}}$+jets region for the ≥ 2 jet phase-space.

4.6.3. $\Delta\phi_{jj}$ Distributions

For the same reasoning as for the m_{jj} distributions we only consider the VBF and ≥ 2 jet phase-space for the $\Delta\phi_{jj}$ distribution. Figures 4.8 and 4.9 show the ratios of $\langle\mu_{\mathrm{med}}\rangle/\langle\mu_{\mathrm{low}}\rangle$ and $\langle\mu_{\mathrm{high}}\rangle/\langle\mu_{\mathrm{med}}\rangle$ for the $\Delta\phi_{jj}$ variable in the $p_{\mathrm{T}}^{\mathrm{miss}}$+jets region. The ratios for the MC and the data are mostly in agreement (within the statistical errors).

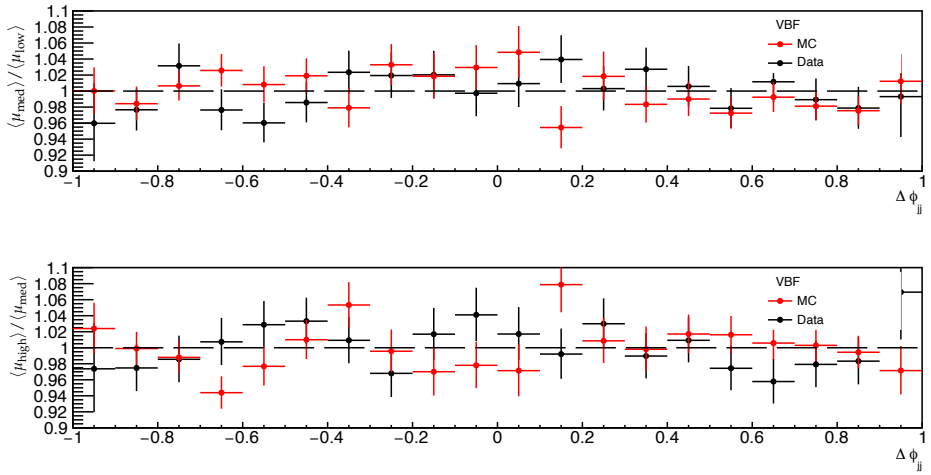

Figure 4.8.: The $\langle\mu\rangle$ dependence for the $\Delta\phi_{jj}$ in the $p_{\mathrm{T}}^{\mathrm{miss}}$+jets region for the VBF phase-space.

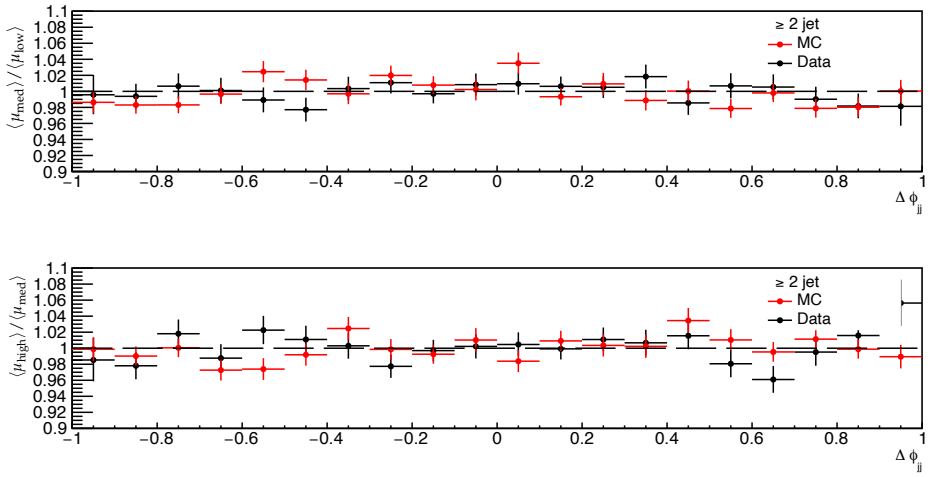

Figure 4.9.: The $\langle\mu\rangle$ dependence for the $\Delta\phi_{jj}$ in the $p_{\mathrm{T}}^{\mathrm{miss}}$+jets region for the ≥ 2 jet phase-space.

4.6.4. Conclusions on Pileup Studies

No pileup dependence has been observed in the shape studies, where both the $\langle\mu_{\mathrm{med}}\rangle/\langle\mu_{\mathrm{low}}\rangle$ and $\langle\mu_{\mathrm{high}}\rangle/\langle\mu_{\mathrm{med}}\rangle$ distributions are in general flat for both the data and the MC. This suggests no strong pileup dependence and that the MC models the data well (within statistical errors) for the $p_{\mathrm{T}}^{\mathrm{miss}}$ (≥ 1 jet , VBF and ≥ 2 jet phase-space), m_{jj} (VBF and ≥ 2 jet phase-space) and $\Delta\phi_{jj}$ (VBF and ≥ 2 jet phase-space) variables. In the $\langle\mu\rangle$ distributions shown in Figures 4.2a, 4.2b and 4.2c, there is a shift between the MC and data which could be quantified by performing a fit of $\langle\mu\rangle$. However, after

seeing the agreement between MC and data for the pileup dependency distributions this is deemed unnecessary.

4.7. Systematic Uncertainties

There are various systematic uncertainties which are associated with methods such as the calibration, energy scale and energy resolutions of physics objects and also the uncertainties which affect the SM theoretical particle predictions and also the BSM predictions which are used for the fits. This section describes these uncertainties.

4.7.1. Experimental Uncertainties

Each of the methods that were discussed in the previous section which involve the calibration, energy scale and energy resolution of physics objects have an associated experimental systematic uncertainty. To propagate such uncertainties to the final measurement, each calibration method has a list of nuisance parameters.[19] Each of these nuisance parameters are varied by one standard deviation around its nominal value and this then corresponds to the calibration method uncertainty. It is possible to quantify the effect of an uncertainty on the detector-level result by varying one nuisance parameter at a time, recalibrate the physics object to take into account this variation and repeating the simulation. The resulting relative shift in the final distribution from this nuisance parameter variation compared to the nominal distribution is taken as the systematic uncertainty associated with, for example, the calibration method. The dominant systematic uncertainties arising from the jet calibration procedure come from the localised corrections used to correct for differences between the MC and data and the modelling of the events used in the calibration. Together with the systematic uncertainties coming from the jet flavour composition, the jet energy scale calibration and the treatment of pileup jets, these are then grouped into a jet energy scale (JES) systematic uncertainty. There are additional systematics which come from the jet energy resolution (JER) method, the contribution of soft terms to the calculation of $p_{\mathrm{T}}^{\mathrm{miss}}$ and also pileup reweighting. The JES and the JER uncertainties are derived using dijet samples following [184]. The "CategoryReduction" scheme was chosen for the

[19] Nuisance parameters are introduced as free parameters, and their values are determined by fitting the data to the simulation or control regions. The uncertainties in these parameters are then propagated to the final measurement as systematic uncertainties.

JES systematic uncertainties, and the "ALLJERNP" scheme was chosen for the JER systematics. These are different decorrelation schemes which have varying granularity and these schemes are chosen as they are suitable for high-precision measurements (finest granularity). Both the "CategoryReduction" and "ALLJERNP" schemes contain roughly 30 nuisance parameters each, with up and down variations.

There are additional experimental systematic uncertainties which arise from the treatment and reconstruction of leptons, and the differences between these methods in the data and the MC. These differences can be accounted for by applying a scale factor uncertainty on the event weight for each selected lepton. These scale factor uncertainties can be estimated from well known SM processes. As for the calibration method, each of these scale factor uncertainties are varied by one standard deviation around its nominal value and the uncertainty extracted is propagated to the final result.

For instance, the electron uncertainties related to the electron efficiency measurements and calibration are obtained from tag and probe measurements of J/ψ and $Z \to \ell\ell$ events [185]. The tag and probe method is a procedure where say the $Z \to \ell\ell$ events are "tagged" (tight selection of a lepton to give a high purity sample) and a sample of probes (very loose selection) are obtained with which it is possible to calculate efficiency.

This method is applied for both data and MC, where the scale factors are the ratios of these efficiencies. The trigger, isolation, identification and reconstruction efficiencies and their uncertainties are provided in these lepton scale factors (which are parameterised as lepton kinematics).

The muon uncertainties are dealt with in a similar fashion to the electron uncertainties. The efficiencies and calibration uncertainties are again obtained from the tag and probe measurements such as J/ψ and $Z \to \ell\ell$ as described in [186]. There are 8 nuisance parameters which are associated with the muon p_{T} reconstruction, isolation and also track to vertex association efficiencies and 5 nuisance parameters related to the scale, inner detector, muon spectrometer and sagitta corrections. All of these nuisance parameters again have up and down variations. The uncertainties on the tau calibration can be accounted for with four nuisance parameters, which are documented in [187].

The performance of photon reconstruction and the photon efficiencies with their respective systematic uncertainties are studied using the measurement of $Z \to (\ell\ell)\gamma$

events [188]. Two nuisance parameters are incorporated for photon identification, isolation and also energy scale calibration respectively. The uncertainty of the $p_{\mathrm{T}}^{\mathrm{miss}}$ are given by a Track Soft Terms (TST) and are represented by three nuisance parameters [117].

The experimental uncertainties are mainly sourced by various combined performance (CP) groups, and the experimental systematic uncertainties from the analysis are shown in Table 4.5 (JES, JER, $p_{\mathrm{T}}^{\mathrm{miss}}$ and pileup) with their respective nuisance parameters and in Table 4.6 (lepton energy scale, resolution and the efficiencies). The impact of each systematic uncertainty on the measurement is evaluated by using modified Monte Carlo (MC) simulations. The simulation is changed for each systematic variation to construct a new simulated response of the detector. The unfolding procedure is then performed with each modified detector response as input to produce a separate unfolded result. The difference between the unfolded result obtained with the modified detector response and the nominal one is considered as the unfolded systematic uncertainty.

In Figures 4.10 and 4.11 the systematic breakdown is shown for the $p_{\mathrm{T}}^{\mathrm{miss}}$ observable in the ≥ 1 jet phase-space at the reconstruction level. The dominant systematic in all regions is coming from the JES systematic uncertainty. This uncertainty is expected to be considerably reduced in the construction of R^{miss} as it is highly correlated between regions. In regions containing leptons, we see that the systematics associated with the fake leptons and lepton efficiencies tend to contribute significantly. It is interesting to note that the single top quark (singleTopDR) systematic uncertainty contributes significantly in the tails of the $p_{\mathrm{T}}^{\mathrm{miss}}$ distribution, and this is likely due to the fact that top quarks are very heavy particles ($m_t \sim 173$ GeV) and therefore are likely to be produced in events with large $p_{\mathrm{T}}^{\mathrm{miss}}$.

4.7.2. Theoretical Uncertainties

The theoretical uncertainties affect the particle-level predictions (as well as at the reconstructed level) which are subsequently compared to the unfolded data.

The uncertainties on the top, diboson and triboson samples come from the PDFs, the renormalisation and factorisation scale choices (in which the variations of scales give an estimate of the potential size of the missing higher order QCD effects, but with

Experimental Systematic Uncertainty	Nuisance Parameter
Jet Energy Scale (JES)	JET_BJES_Response JET_Effective_NP_Detector (2) JET_EffectiveNP_Mixed (3) JET_EffectiveNP_Modelling (4) JET_EffectiveNP_Statistical (6) JET_EtaIntercalibration_Modelling JET_EtaIntercalibration_NonClosure_highE JET_EtaIntercalibration_NonClosure_negEta JET_EtaIntercalibration_NonClosure_posEta JET_EtaIntercalibration_TotalStat JET_Flavor_Composition JET_Flavor_Response JET_Pileup_OffsetNPV JET_Pileup_PtTerm JET_Pileup_RhoTopology JET_PunchThrough_MC16 JET_RelativeNonClosure_MC16 JET_SingleParticle_HighPt
Jet Energy Resolution (JER)	JET_JER_DataVsMC_MC16 JET_JER_EffectiveNP (12)
$p_{\mathrm{T}}^{\mathrm{miss}}$ soft term scale and resolution	MET_SoftTrk_Scale MET_SoftTrk_ResoPara MET_SoftTrk_ResoPerp
Pileup Reweighting	PRW_DATASF

Table 4.5.: Jet and $p_{\mathrm{T}}^{\mathrm{miss}}$ experimental systematic uncertainties with their associated nuisance parameters.

Experimental Systematic Uncertainty	Nuisance Parameter
electron energy resolution	EG_RESOLUTION_ALL
electron energy scale	EG_SCALE_ALL
electron identification efficiency	EL_EFF_ID_CorrUncertaintyNP (15) EL_EFF_ID_SIMPLIFIED_UncorrUncertaintyNP (17) EL_EFF_ID_TOTAL_1NPCOR_PLUS_UNCOR
electron isolation efficiency	EL_EFF_Iso_CorrUncertaintyNP (10) EL_EFF_RECO_SIMPLIFIED_UncorrUncertaintyNP (17) EL_EFF_Iso_TOTAL_1NPCOR_PLUS_UNCOR
electron reconstruction efficiency	EL_EFF_RECO_CorrUncertaintyNP (6) EL_EFF_RECO_SIMPLIFIED_UncorrUncertaintyNP (17) EL_EFF_Iso_TOTAL_1NPCOR_PLUS_UNCOR
electron trigger efficiency	EL_EFF_TriggerEFF_CorrUncertaintyNP (10) EL_EFF_TriggerEFF__SIMPLIFIED_UncorrUncertaintyNP (17) EL_EFF_Trigger_SIMPLFIED_UncorrUncertaintyNP (17) EL_EFF_Trigger_TOTAL_1NPCOR_PLUS_UNCOR EL_EFF_Trigger_CorrUncertaintyNP (10)
muon track resolution	MUON_ID MUON_MS
muon energy scale	MUON_SAGITTA_RESBIAS MUON_SAGITTA_RHO MUON_SCALE
muon isolation efficiency	MUON_EFF_ISO_STAT MUON_EFF_ISO_SYS
muon reconstruction efficiency	MUON_EFF_RECO_STAT MUON_EFF_RECO_STAT_LOWPT MUON_EFF_RECO_SYS MUON_EFF_RECO_SYS_LOWPT
muon track-to-vertex association efficiency	MUON_EFF_TTVA_STAT MUON_EFF_TTVA_SYS

Table 4.6.: Lepton experimental systematic uncertainties with their associated nuisance parameters.

no shape or correlation information). In each PDF uncertainty, the standard deviation of the 100 MC replicas of the (default) NNPDF3.0NNLO set, as well using the central values for the alternative CT14 NNLO [189] and MMHT NNLO [190] PDF sets is taken, and therefore the envelope of these individual PDFs as a combined PDF uncertainty can be calculated. In the case of top quark pair production, the NNLO versions of the PDF sets are used to match the PDF used for the nominal. An uncertainty from the strong coupling constant $\alpha_S(m_Z)$ is derived using up and down variations to 0.117 and 0.119 (where the nominal value is 0.118) and then add this contribution in quadrature with the combined PDF uncertainty.

The scale uncertainties are estimated using a set of seven values of the renormalisation and the factorisation scales which are obtained by varying each value by one half, one or two times the nominal value (using the multiweight functionality available for these MC samples). This can be formalised in a list [μ_R, μ_F], [$2\mu_R$, $2\mu_F$], [$0.5\mu_R$, $0.5\mu_F$], [$2\mu_R$, μ_F], [$1\mu_R$, $2\mu_F$], [μ_R,$0.5\mu_F$],[$0.5\mu_R$,μ_F], where μ_R is the renormalisation scale and μ_F is the factorisation scale. The renormalisation scale sets a cut-off for the loop corrections to ensure convergence of the perturbative calculations and the factorisation scale determines the cut off which separates hard interactions from softer interactions (this could be for example because of parton distribution functions). The envelope of these variations is taken as the systematic uncertainty on the particle-level prediction. For top quark pair production, the factorisation scale in the parton shower is varied up and down by a factor of two for Initial State Radiation (ISR) and Final State Radiation (FSR) separately. These two uncertainties are added in quadrature to the other uncertainties. There is an additional uncertainty on the top sample which comes from the treatment of the overlap of the $t\bar{t}$ and Wt samples. This uncertainty comes from the subtraction of the nominal diagram (as opposed to the usual diagram removal) [191].

For the dominant V+jets samples, a more sophisticated uncertainty treatment is done, these are based on the recommendations from [177]. For V+jets, this includes the PDF uncertainty (the PDF uncertainties are based on the LUXqed_plus_PDF4LHC15_nnlo_100 set and these are split into 107 independent Hessian PDF eigenvectors and are fully correlated) and the standard seven-point scale variations (as discussed above), including correlated variations of the QCD scales. In addition, there is a shape uncertainty for the boson p_{T} as well as the m_{jj} variable caused by the scale variations, the parameterisation of this is given in [177]. This is because scale variations mainly affect the overall normalisation of p_{T} distribution and tend to underestimate the shape uncertainties,

this plays an important role in the extrapolation from a low p_{T} measurement to high p_{T}. The scale variations were shown to be well correlated as a function of boson p_{T} in event topologies with large $p_{\mathrm{T}}^{\mathrm{miss}}$ balanced by at least one energetic jet [177]. As a result, QCD K-factors $K(V)$ $N^kLO(x)$[20] and their uncertainties depend only very weakly on the vector boson, V, at high p_{T}, and in this situation the small process-dependent part of QCD K-factors can be used as an estimator of the degree of correlation across processes. To quantify the amount of non-correlation between the different processes, a comparison of the differential NLO K (which are specific to each process) with respect to the LO K-factor for the Z boson channel (which is a common process) has been made. The impact of parton showering on the jet balancing cuts as well as the central jet veto in the VBF region can be estimated by varying the resummation scale by factor of two and a factor of a half.[21]

[20] The N^kLO K-factor of a process is defined as the ratio of cross-sections at N^KLO and $N^{K-1}LO$ for that process.

[21] Many applications in QCD require precision calculations for high energy collider physics which involve the perturbative solution of Renormalisation Group Equations (RGE). These equations describe the behavior of the coupling constants in a quantum field theory, such as QCD, as the energy scale of the process changes. There are various RGE solutions obtained by different methods and this is a significant source of theoretical uncertainty on the predictions for the physical observables. In QCD resummation, these uncertainties can be commonly taken into account by a variety of different techniques, which appeal to the principle of introducing so-called resummation scales (on the order of the hard momentum-transfer scale of the process, but otherwise arbitrary) and setting criteria to let them vary and evaluate the corresponding variation in the theoretical prediction.

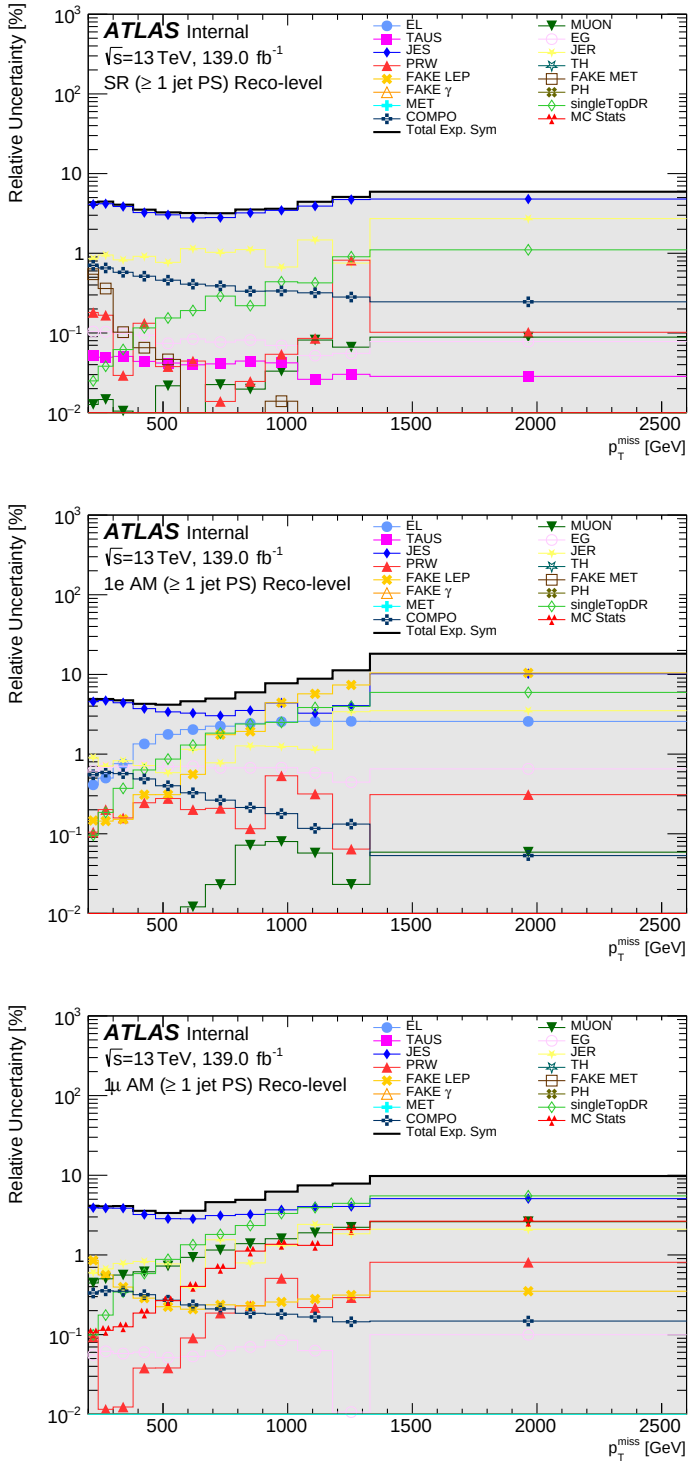

Figure 4.10.: Systematic breakdown for the $p_{\mathrm{T}}^{\mathrm{miss}}$ observable in the ≥ 1 jet phase-space at reconstruction-level for the $p_{\mathrm{T}}^{\mathrm{miss}}$+jets and one lepton regions. In addition to the systematics discussed above, the FAKE LEP, FAKE γ and FAKE MET are experimental systematic uncertainties which account for the data to MC discrepancy for the fake lepton and $p_{\mathrm{T}}^{\mathrm{miss}}$ estimates.

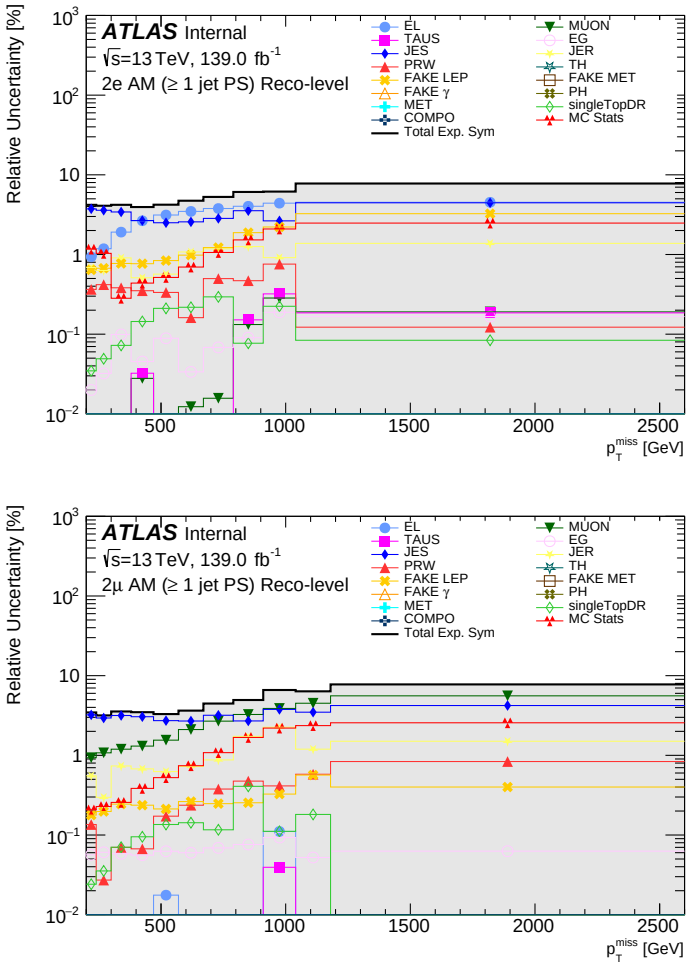

Figure 4.11.: Systematic breakdown for the $p_{\mathrm{T}}^{\mathrm{miss}}$ observable in the ≥ 1 jet phase-space at reconstruction-level for the two lepton regions. In addition to the systematics discussed above, the FAKE LEP, FAKE γ and FAKE MET are experimental systematic uncertainties which account for the data to MC discrepancy for the fake lepton and $p_{\mathrm{T}}^{\mathrm{miss}}$ estimates.

4.8. Detector-Level Results

In this section, comparisons between the detector-level data and the SM prediction are made, this is shown for all regions separately. In these distributions, each of the contributions to the SM prediction are shown as stacked histograms, including the QCD multijet process and this is included in the "Fakes" contribution. This process is mainly present in the low $p_{\mathrm{T}}^{\mathrm{miss}}$ and high $\Delta\phi_{jj}$ bins at a $1-2\%$ level and mostly consists of neutrinos from heavy-flavour decays or fake $p_{\mathrm{T}}^{\mathrm{miss}}$ due to detector effects in the jet measurement. The fake background in the lepton regions essentially arises from jets being mis-identified as leptons and also leptons from heavy flavour decays. These appear at the $\mathcal{O}(1\%)$ level in the lepton regions. In the panels underneath the distributions are the ratios of the data to the SM prediction, where the statistical uncertainties of the data are shown in the error bars and the blue bars represents the statistical uncertainty on the MC. The detector systematic uncertainties added in quadrature to the statistical uncertainties are also shown in the ratio panel with the blue hatched lines. These plots show a comparison between the detector-level data and the MC for the full Run 2 dataset of $\mathcal{L} = 139$ fb^{-1}. Figure 4.12 shows a comparison between the data and MC in the ≥ 1 jet phase-space for all the regions. There is a 10%–20% discrepancy between the MC and data (more events in data than in MC) in the $p_{\mathrm{T}}^{\mathrm{miss}}$ distributions. The shape is reasonably well-modelled.

Figures 4.13, 4.14 and 4.15 show comparisons between the detector-level data and the MC for $p_{\mathrm{T}}^{\mathrm{miss}}$, m_{jj}, and $\Delta\phi_{jj}$ for all the regions in the VBF phase-space. The agreement between the data and MC in these $p_{\mathrm{T}}^{\mathrm{miss}}$ distributions follow a similar pattern to that found in the ≥ 1 jet phase-space. The m_{jj} is badly mismodelled by the MC in all of the regions, where the m_{jj} shows a much harder spectrum for the SM prediction than the data. This is a well-known feature of Sherpa 2.2.1 and has been shown before in [192]. The mismodelling is similar for all regions and therefore it may be possible to use the lepton regions, where the modelling could be better, to constrain the experimental and theoretical uncertainties in the $p_{\mathrm{T}}^{\mathrm{miss}}$+jets region. This can be achieved by incorporating information from the lepton regions in a global fit to extract the relevant parameters of the physical process, while taking into account the uncertainties associated with the modeling. To account for this mismodelling, m_{jj} reweighting (MJJRW) factors are derived from these data/MC reconstruction level distributions and these factors applied to the MC that is used for the unfolding. Unfortunately this MJJRW reweighting is not available for this thesis due to time constraints. In the

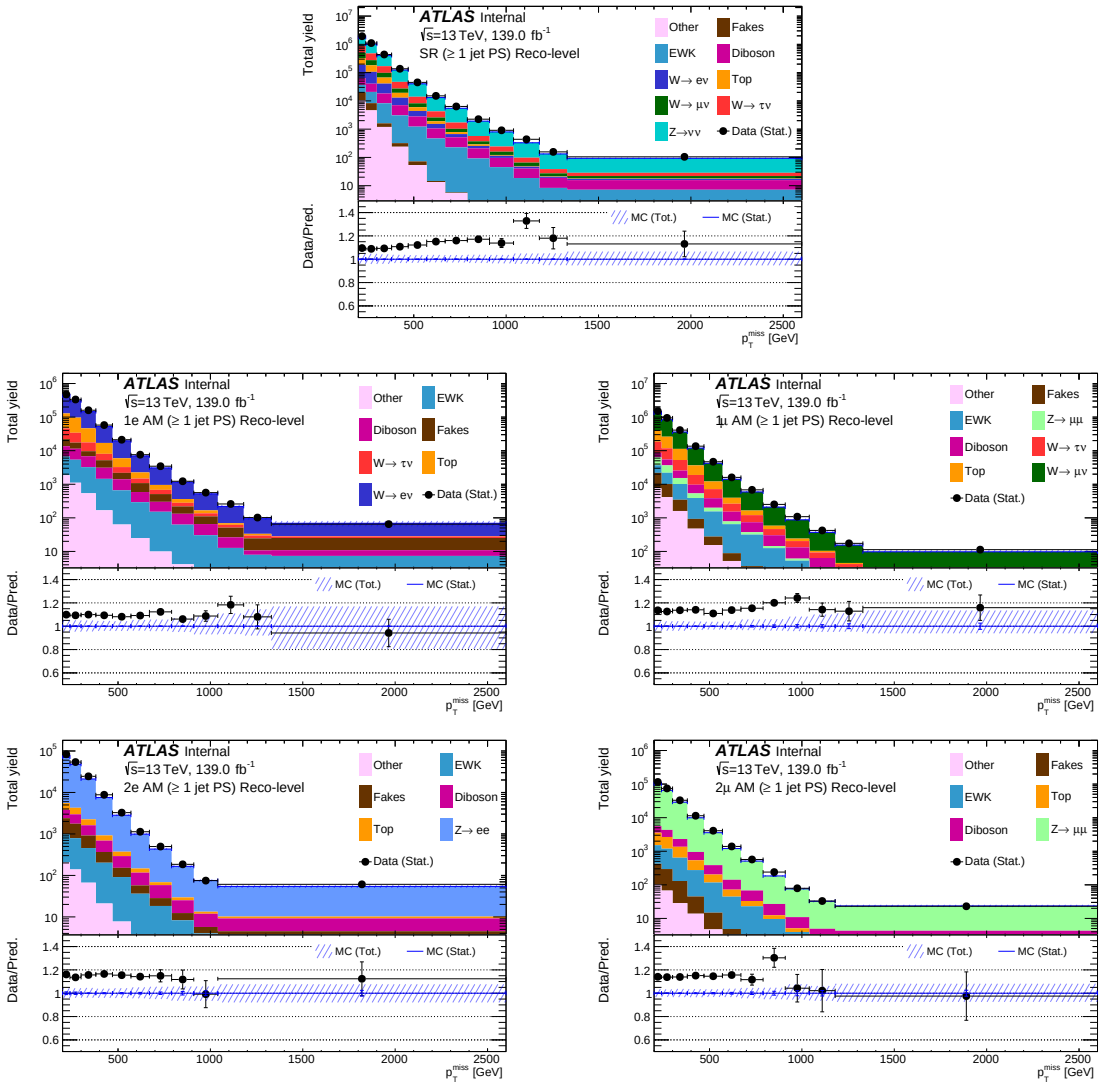

Figure 4.12.: MC/Data comparisons for $p_{\mathrm{T}}^{\mathrm{miss}}$ in the ≥ 1 jet phase-space for the five regions (the $p_{\mathrm{T}}^{\mathrm{miss}}$+jets, the $1e$+jets, the 1μ+jets, the $2e$+jets and the 2μ+jets region). The shaded band shows the combination of the systematic and statistical uncertainty on the MC. The black dots indicate the data with its bars being the statistical uncertainty. Each of the stacked contributions are ordered in terms of their contribution, this is done for all the detector-level Figures.

VBF phase-space there is a much larger contribution of the electroweak production of $V + jj$ events compared to the ≥ 2 jet phase-space, and this in turn appears to be better modelled than the other SM contributions. The reconstruction-level plots show the signed $\Delta\phi_{jj}$ distributions rather than the $|\Delta\phi_{jj}|$ distributions because the absolute values of $\Delta\phi_{jj}$ is only applied after the unfolding as explained previously. The $\Delta\phi_{jj}$ distribution peaks towards values between $0.4 < \Delta\phi_{jj} < 0.6$, for all regions. The $\Delta\phi_{jj}$

distribution dip towards the centre (this is in part due to the high m_{jj} cut of 200 GeV and the fact that they cannot be exactly next to each other) and the higher (and lower) values of $\Delta\phi_{jj}$. The data is seen to have a slightly more peaked structure.

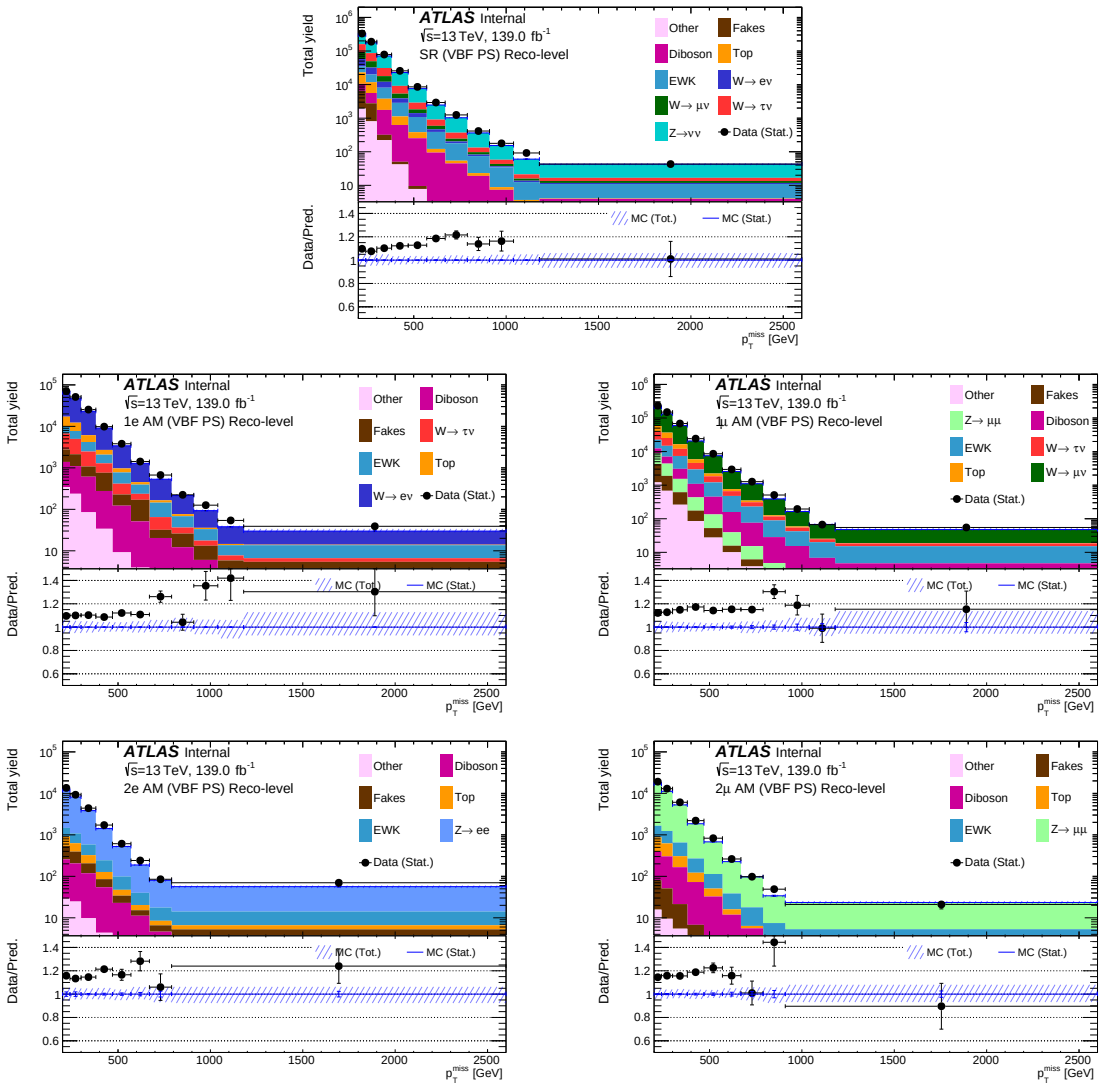

Figure 4.13.: MC/Data comparisons for $p_{\mathrm{T}}^{\mathrm{miss}}$ in the phase-space for the five regions (the $p_{\mathrm{T}}^{\mathrm{miss}}$+jets, the $1e$+jets, the 1μ+jets, the $2e$+jets and the 2μ+jets region). The shaded band shows the combination of the systematic and statistical uncertainty on the MC. The black dots indicate the data with its bars being the statistical uncertainty.

Figures 4.16, 4.17 and 4.18 shows the comparisons between the detector-level data and MC for $p_{\mathrm{T}}^{\mathrm{miss}}$, m_{jj} and $\Delta\phi_{jj}$ for all regions in the ≥ 2 jet phase-space. The same type of discrepancy (in terms of shape and magnitude) between the data and the MC for the $p_{\mathrm{T}}^{\mathrm{miss}}$ observable in the ≥ 1 jet is also seen for the ≥ 2 jet phase-space. The m_{jj} distribution is again badly modelled for the MC in the ≥ 2 jet phase-space. This is

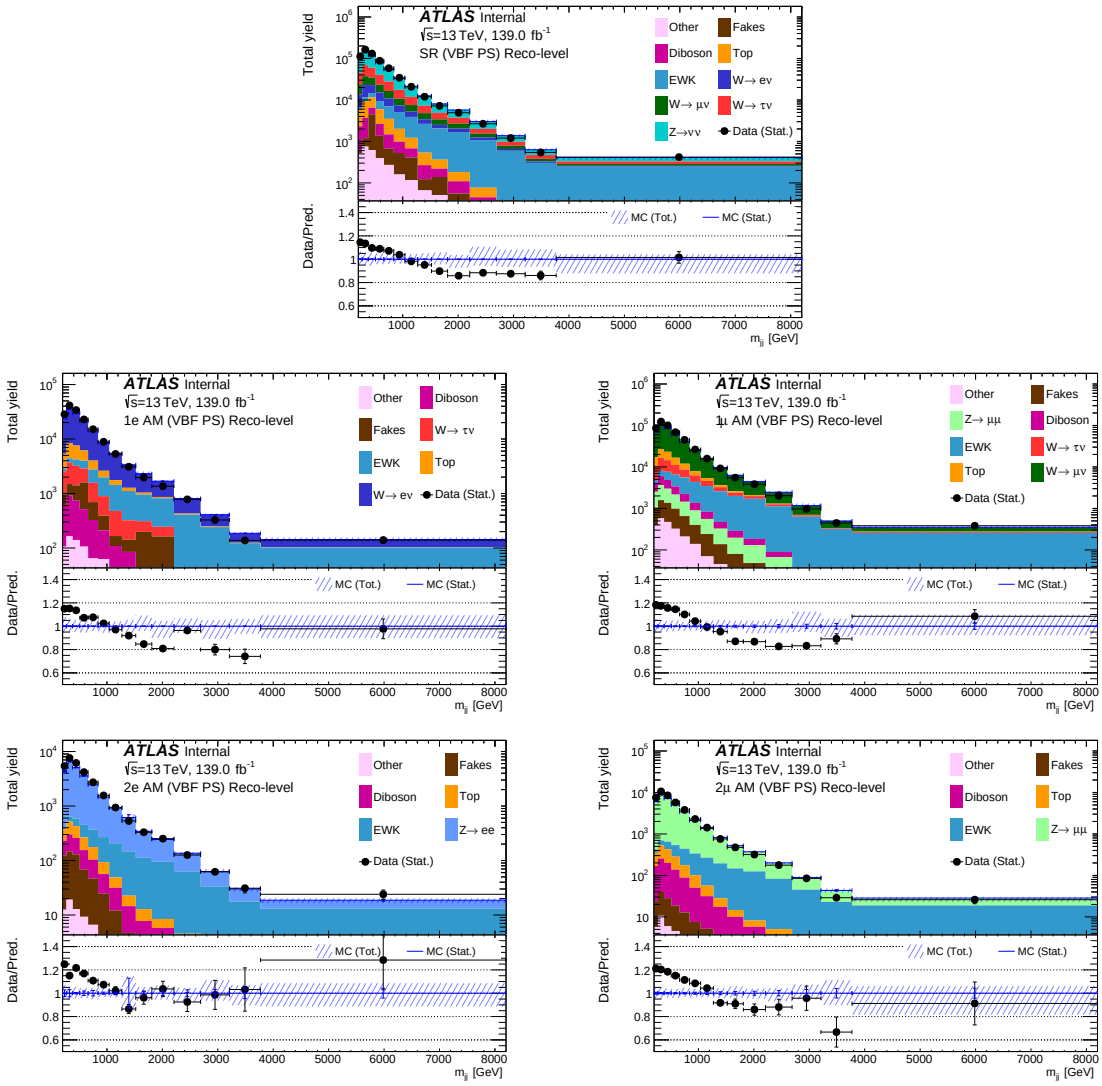

Figure 4.14.: MC/Data comparisons for m_{jj} in the phase-space for the five regions (the $p_{\mathrm{T}}^{\mathrm{miss}}$+jets, the 1$e$+jets, the 1$\mu$+jets, the 2$e$+jets and the 2$\mu$+jets region). The shaded band shows the combination of the systematic and statistical uncertainty on the MC. The black dots indicate the data with its bars being the statistical uncertainty.

worse than for the VBF phase-space as the relative contribution of the electroweak $V + jj$ (which is modelled better by the MC than the other contributions) is smaller. The $\Delta\phi_{jj}$ distribution peaks toward smaller values, which are jets produced close to each other and a dip at very small values (near zero) as the jets cannot exactly be on top of each other. The data has a slightly more peaked structure than the MC which can be seen in the ratio of the data to the SM prediction.

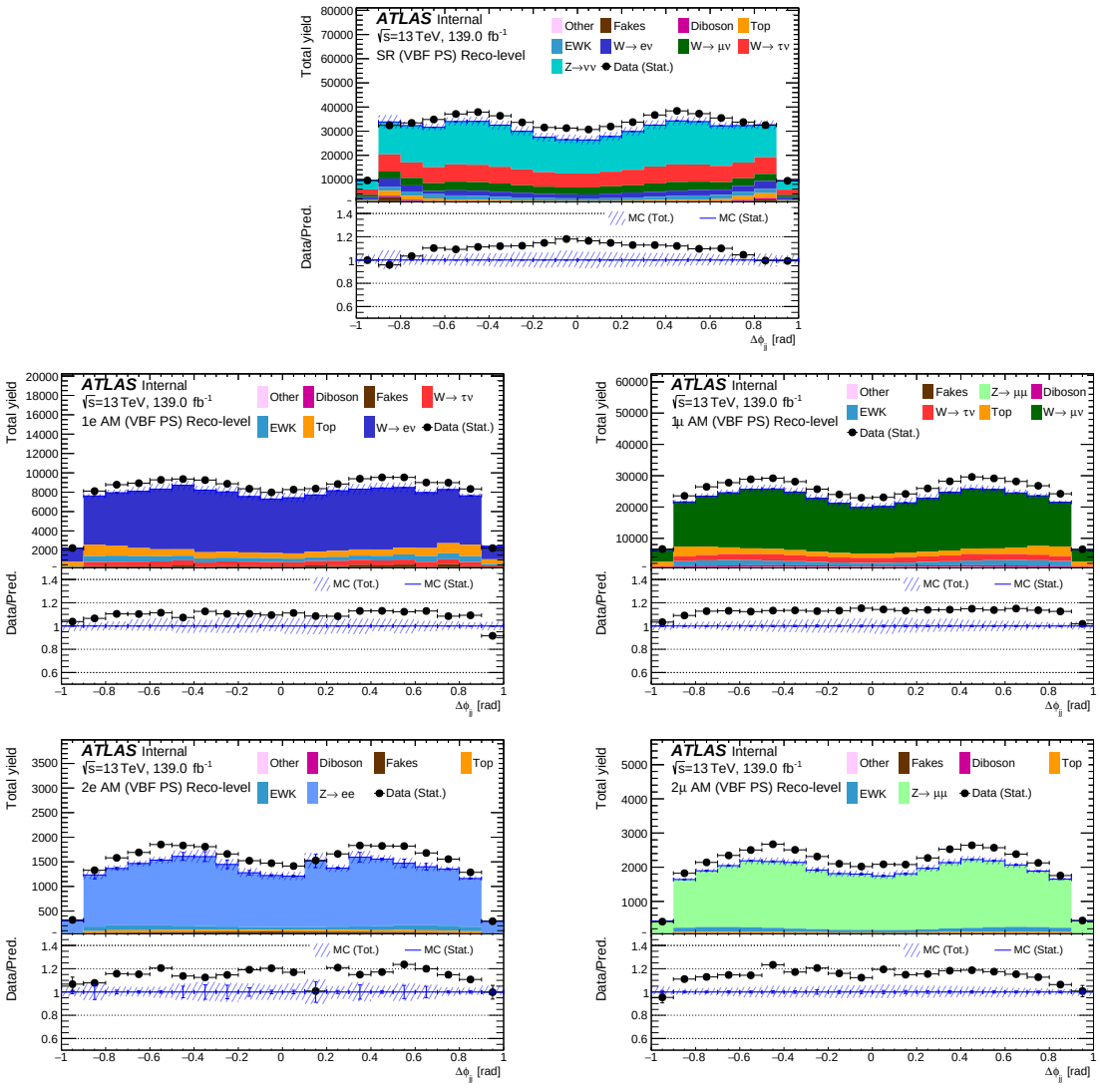

Figure 4.15.: MC/Data comparisons for $\Delta\phi_{jj}$ in the phase-space for the five regions (the $p_{\mathrm{T}}^{\mathrm{miss}}$+jets, the $1e$+jets, the 1μ+jets, the $2e$+jets and the 2μ+jets region). The shaded band shows the combination of the systematic and statistical uncertainty on the MC. The black dots indicate the data with its bars being the statistical uncertainty.

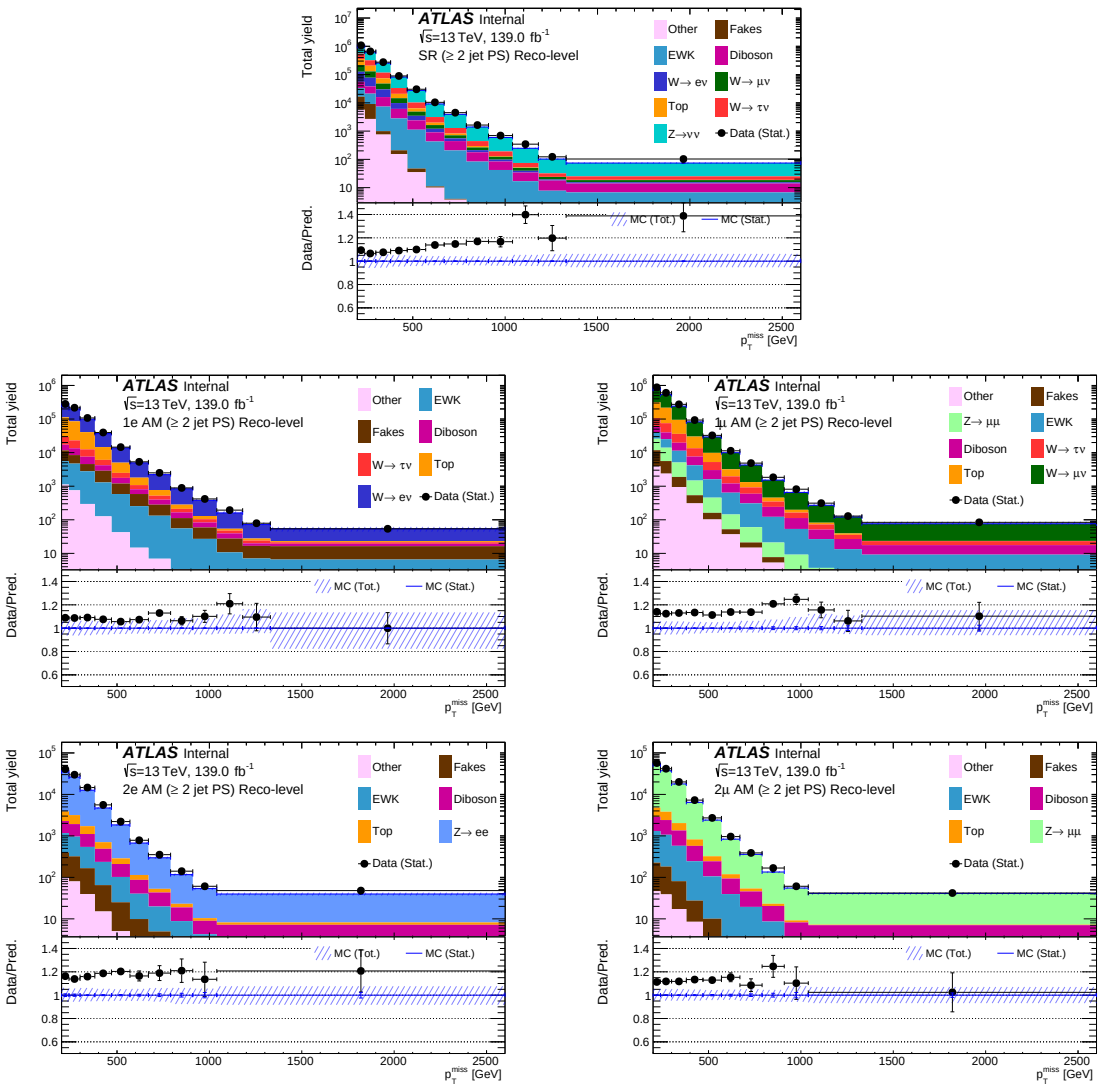

Figure 4.16.: MC/Data comparisons for $p_{\mathrm{T}}^{\mathrm{miss}}$ in the ≥ 2 jet phase-space for the five regions (the $p_{\mathrm{T}}^{\mathrm{miss}}$+jets, the $1e$+jets, the 1μ+jets, the $2e$+jets and the 2μ+jets region). The shaded band shows the combination of the systematic and statistical uncertainty on the MC. The black dots indicate the data with its bars being the statistical uncertainty.

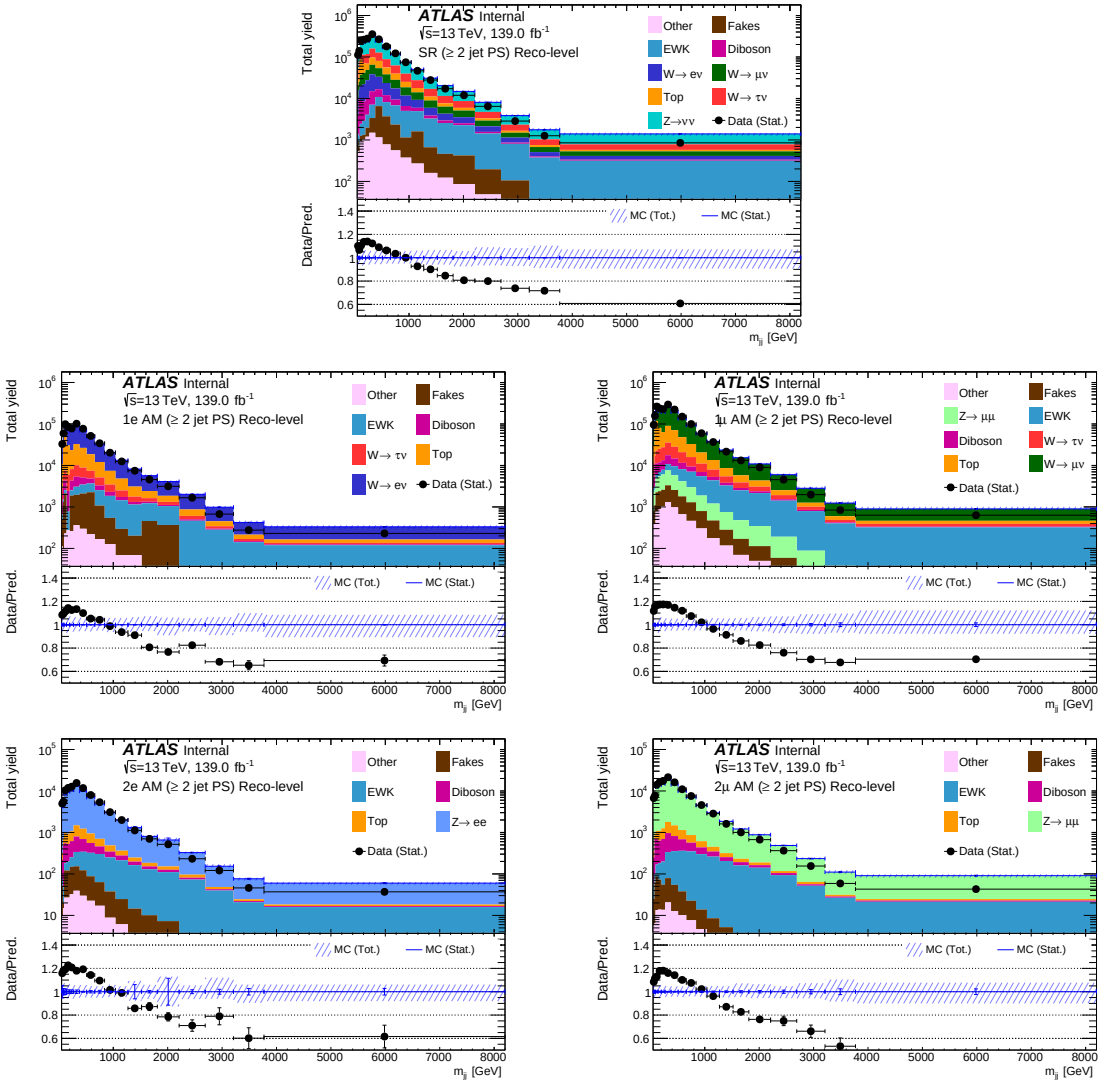

Figure 4.17.: MC/Data comparisons for m_{jj} in the ≥ 2 jet phase-space for the five regions (the $p_{\mathrm{T}}^{\mathrm{miss}}$+jets, the $1e$+jets, the 1μ+jets, the $2e$+jets and the 2μ+jets region). The shaded band shows the combination of the systematic and statistical uncertainty on the MC. The black dots indicate the data with its bars being the statistical uncertainty.

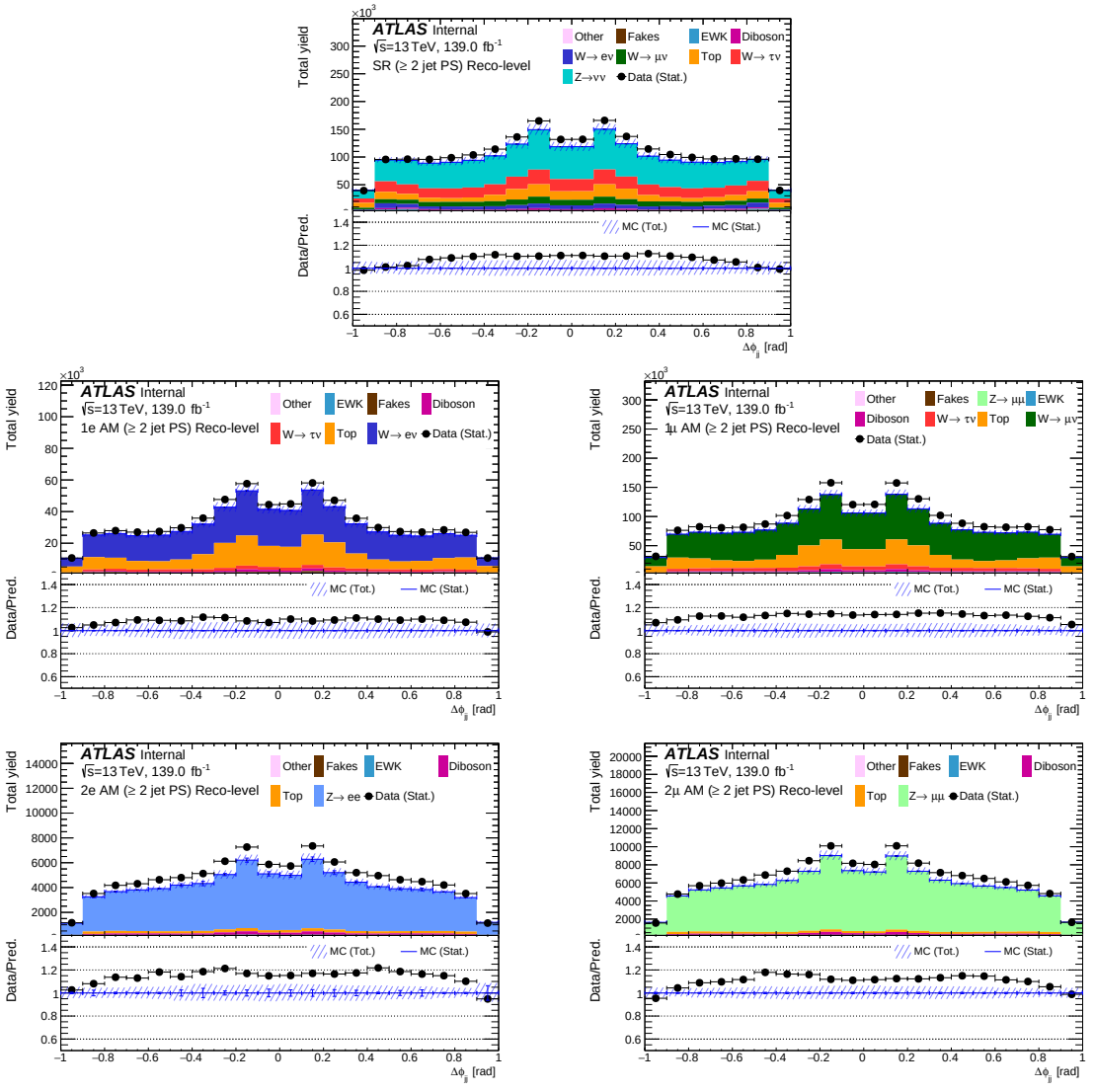

Figure 4.18.: MC/Data comparisons for $\Delta\phi_{jj}$ in the ≥ 2 jet phase-space for the five regions (the $p_{\mathrm{T}}^{\mathrm{miss}}$+jets, the $1e$+jets, the 1μ+jets, the $2e$+jets and the 2μ+jets region). The shaded band shows the combination of the systematic and statistical uncertainty on the MC. The black dots indicate the data with its bars being the statistical uncertainty.

4.9. Detector-Corrected Results

4.9.1. Unfolding Technique

The measurements are then corrected for detector effects so that they can be defined in terms of particle-level objects. This can be done by different methods which follow different approaches. There are in general two different classes of strategies for correcting detector effects. In the first approach, a mathematical function for the particle-level distribution can be assumed (together with other functions to model the noise) and the task becomes about estimating the free parameters of the function(s). This is the domain of *parametric inference* ('fits') which is associated with statistical fits such as 'least-squares' or 'maximum likelihood'. In this type of parametric inference, all the information contained in the observed spectrum is distilled into the model parameters. Parametric inference is often the best and fastest way to proceed, if there is confidence in the hypothesised family of functions.

However, sometimes, as is the case in the analysis, one wishes to interpret the data as little as possible and calculate an equivalent experimental distribution, in which the bin contents fluctuate according to an underlying multinomial distribution, having corrected for detector effects. This second approach goes under the name of *unfolding*. Iterative Bayesian unfolding is a popular choice because it provides a flexible framework for data analysis that can handle complex situations where the signal and background are difficult to separate [193, 194]. This method involves using a Bayesian approach to iteratively estimate the true distribution of events from the measured distribution, based on a prior knowledge of the expected distribution of events. There are other methods such as matrix inversion, singular value decomposition and Bayesian with regularisation [195]. Each having their relative strengths and weaknesses. For instance, in matrix inversion, it is assumed that the response matrix is well understood and that the signal and background are comparable, which for our purposes is not the case. Bayesian with regularisation is not as flexible as iterative Bayesian unfolding in handling complex situations involving signal and background contamination or the issue with the singular value decomposition technique using the matrix inversion method and therefore inheriting it's relative weaknesses. For the reasons listed, this analysis uses the iterative Bayesian unfolding technique to correct the data for detector inefficiencies and resolutions [193, 194]. These detector effects include the acceptance, efficiency, resolution and calibration of the detectors. All these

can be used to define a response matrix $R_{i,j}$ along with the detector-level distribution of the reducible background, b_i, to establish a relation between the reconstructed-level measured distribution, r_i, and the particle-level distribution:

$$r_i = R_{i,j} t_j + b_i. \tag{4.6}$$

Where i and j indicate the bin indices for the reconstructed and particle-level distributions respectively. In the same manner, an unfolded distribution, u_j, can be related to the reconstructed-level measured distribution by inverting the same response matrix and using the background subtracted measured distribution:

$$u_j = R_{ji}^{-1}(r_i - b_i). \tag{4.7}$$

At this step, unfolding by matrix inversion becomes non-trivial. Even if the response matrix is invertible, solutions to the above equation can be unstable due to the nature of the measured values r_i which are random variables which follow Poisson distributions. This instability is dealt with by adding a regularisation process in the unfolding procedure. Using the *Iterative Bayesian Unfolding* method along with Bayesian theorem it is possible to invert the response matrix and add a regularisation step. This technique is able to account for the underlying shape of the distribution by iterating the unfolding after reweighting the input distribution to the corrected data from the previous iteration. In this study two iterations are used following studies done on the optimal number of iterations such that the regularisation bias introduced from a prior truth distribution in the unfolding is minimised.[22] The binning of a distribution is usually preferred to be kept as fine as possible so that we are able to garner highly granular shape information about the distribution. This is not always possible as extremely fine binning can lead to large migrations of events across neigbouring bins. This would then result in a low purity and large off-diagonal elements in the response matrix which in turn leads to large statistical uncertainties in the unfolded result. The binning of the distributions is therefore defined so that each bin contains at least 20 reconstructed events and has a purity of at least 60%. The statistical uncertainty on the unfolded data is calculated using the bootstrap method [196, 197] where a detector-level data distribution is Poisson fluctuated, producing 2000 replicas. Each replica is then unfolded using the nominal detector-response and this results in 2000

[22] Fewer iterations result in a higher regularisation bias and a larger dependence on the input, this can be treated as a systematic uncertainty. However, increasing the number of iterations reduces the bias but it increases the statistical uncertainty, so it is a balance between these two factors.

unfolded distributions. The root mean square (RMS) of the results per bin is taken as the statistical uncertainty in that bin. The bootstrap method allows for statistical correlations between bins, introduced in the iterative part of the unfolding, to be properly propagated to the unfolded result. Unfortunately there was not enough time to have the bootstrapped inputs for this work, but they are currently being produced and iterated upon.

4.9.2. Differential Cross-Sections

In this section, the unfolded data is compared to the particle-level SM predictions and these are shown for all the regions. Backgrounds from the QCD multijet events in the all the regions are subtracted from the data before unfolding. The contributions to the SM predictions are shown in stacked histograms (similar to those shown for the detector-level results). In the bottom panel is the ratio of the unfolded data over the particle-level SM prediction where the statistical uncertainties are shown as error bars. The systematic uncertainties (detector and theoretical) are added in quadrature to the statistical uncertainties and are shown in the ratio panel as a band with red hatched lines. The figures shown here only show the $p_{\mathrm{T}}^{\mathrm{miss}}$+jets region for the unfolded 2015, 2016, 2017 and 2018 datasets and the corresponding MC campaigns.

Figure 4.19 shows a comparison between the unfolded data and the particle-level SM prediction for the $p_{\mathrm{T}}^{\mathrm{miss}}$ variable in the ≥ 1 jet phase-space for all the regions. Similar to the detector-level distributions, there is a 10%–20% discrepancy between the particle-level SM prediction and the unfolded data in the $p_{\mathrm{T}}^{\mathrm{miss}}$ distribution for all regions. It is important to note that in the detector-level ratio distributions they are calculated as the data over the prediction and not prediction over the data as in the unfolded distributions. This is a really important point when comparing the different ratios, where an excess of data over the prediction (ratio above one) will translate to a ratio under one for the unfolded distributions (note of caution that, for example, a 10% excess in the detector-level ratio will not directly translate to a 10% deficit in the particle-level ratio, it will actually translate to a 9% deficit). The shape of the distribution is well modelled and is covered by the total error (the systematic and statistical uncertainty added in quadrature).

The MC total error is relatively large compared to the detector-level figures (this is seen through all of the particle-level differential cross-section figures) and this is due

to the effects of propagating the uncertainties through the response matrix used for the unfolding as well as the fact that the theoretical systematic uncertainties are not included for the detector-level plots. It is important to note here that it seems for the nominal values of MC, there is an underestimation of the data for the $p_{\mathrm{T}}^{\mathrm{miss}}$+jets and the two lepton auxiliary regions. The level of agreement between the model and data is quantified using a p-value in the next chapter.

In the one lepton regions of Figure 4.12, there is a $\sim$15% difference between the nominals of the data and the prediction, which is not apparent in the one lepton regions of Figure 4.19 which agree well. When we compare Figure 4.12 to the unfolded distribution in Figure 4.19 for the 2ℓ+jets, there is this $\sim$20% difference between the nominal MC and data for the detector-level distributions, whereas this difference is only $\sim$5% in the unfolded distribution.

Figures 4.20, 4.21 and 4.22 show the comparison between the unfolded data and particle-level SM predictions for $p_{\mathrm{T}}^{\mathrm{miss}}$, m_{jj} and $\Delta\phi_{jj}$ for all the regions in the VBF phase-space. The agreement between the unfolded data and SM prediction show similar discrepancy to that shown in the ≥ 1 jet for the $p_{\mathrm{T}}^{\mathrm{miss}}$ distribution. It is important to note again that for the nominal MC, it appears that there is a slight underestimation of the data for the $p_{\mathrm{T}}^{\mathrm{miss}}$+jets and two lepton auxiliary regions but it is covered by the respective uncertainties. When comparing the $p_{\mathrm{T}}^{\mathrm{miss}}$ in the VBF phase-space for the $p_{\mathrm{T}}^{\mathrm{miss}}$+jets region shown in Figure 4.13, we see that the shapes and agreement between the nominal data and prediction are similar to what is shown in the equivalent distribution in Figure 4.20. In the one lepton regions of Figure 4.13, there is a $\sim 10\% - 20\%$ difference between the nominal of the data and prediction in the low $p_{\mathrm{T}}^{\mathrm{miss}}$ bins, where this difference is only $\sim 3\% - 15\%$ in the equivalent bins of the one lepton regions of Figure 4.20. In the two lepton regions of Figure 4.13 there is an almost flat $\sim$20% difference between MC/Data for the low $p_{\mathrm{T}}^{\mathrm{miss}}$ bins, whereas in the unfolded distribution it goes from a $\sim$10% discrepancy in the first $p_{\mathrm{T}}^{\mathrm{miss}}$ bin and gradually falls to a $\geq \sim$30% difference in the tail of the distribution (this could be due to fluctuations due to the lower sample size).

The m_{jj} is badly mismodelled by the MC in all the regions, with the MC showing a much harder m_{jj} spectrum than the data as was seen for the detector-level comparisons. The shape is quite distinct, it goes from an MC underestimation in the first few m_{jj} bins to overestimating in the region 1000 GeV $< m_{jj} <$ 3000 GeV. These discrepancies are mostly covered by the systematic uncertainties.

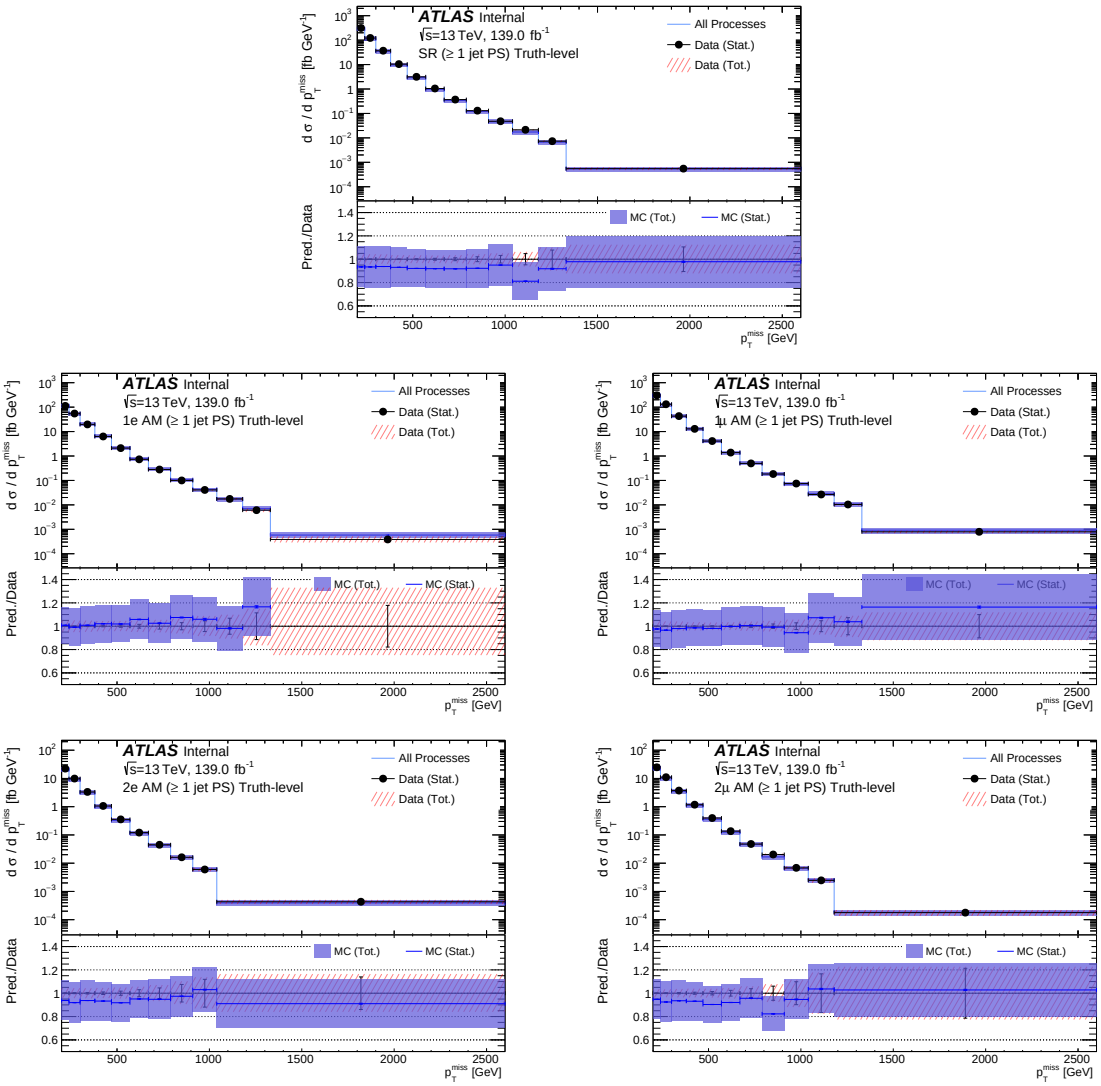

Figure 4.19.: Particle-level MC/Data comparisons for $p_{\mathrm{T}}^{\mathrm{miss}}$ in the ≥ 1 jet phase-space for the five regions (the $p_{\mathrm{T}}^{\mathrm{miss}}$+jets, the $1e$+jets, the 1μ+jets, the $2e$+jets and the 2μ+jets region). The blue band shows the combination of the systematic and statistical uncertainty on the MC. The black dots with the bars shows the data with the statistical uncertainties and the hatched red line represents the total error on the data (statistical + systematic uncertainties).

For the $\Delta\phi_{jj}$ distributions, a similar pattern is seen to that of the detector-level results where the distribution peaks towards values between $0.4 < |\Delta\phi_{jj}| < 0.6$, for all the regions. The $\Delta\phi_{jj}$ distribution dips towards the centre and the higher absolute values of $\Delta\phi_{jj}$. However in the 1ℓ+jets in Figure 4.15, the $\Delta\phi_{jj}$ distribution has an almost flat excess of data over MC of about $\sim 15\%$. In the equivalent unfolded

distribution, shown in Figure 4.22, the nominal $\Delta\phi_{jj}$ distribution has an almost flat $\sim$10% discrepancy in terms of the MC/data agreement.

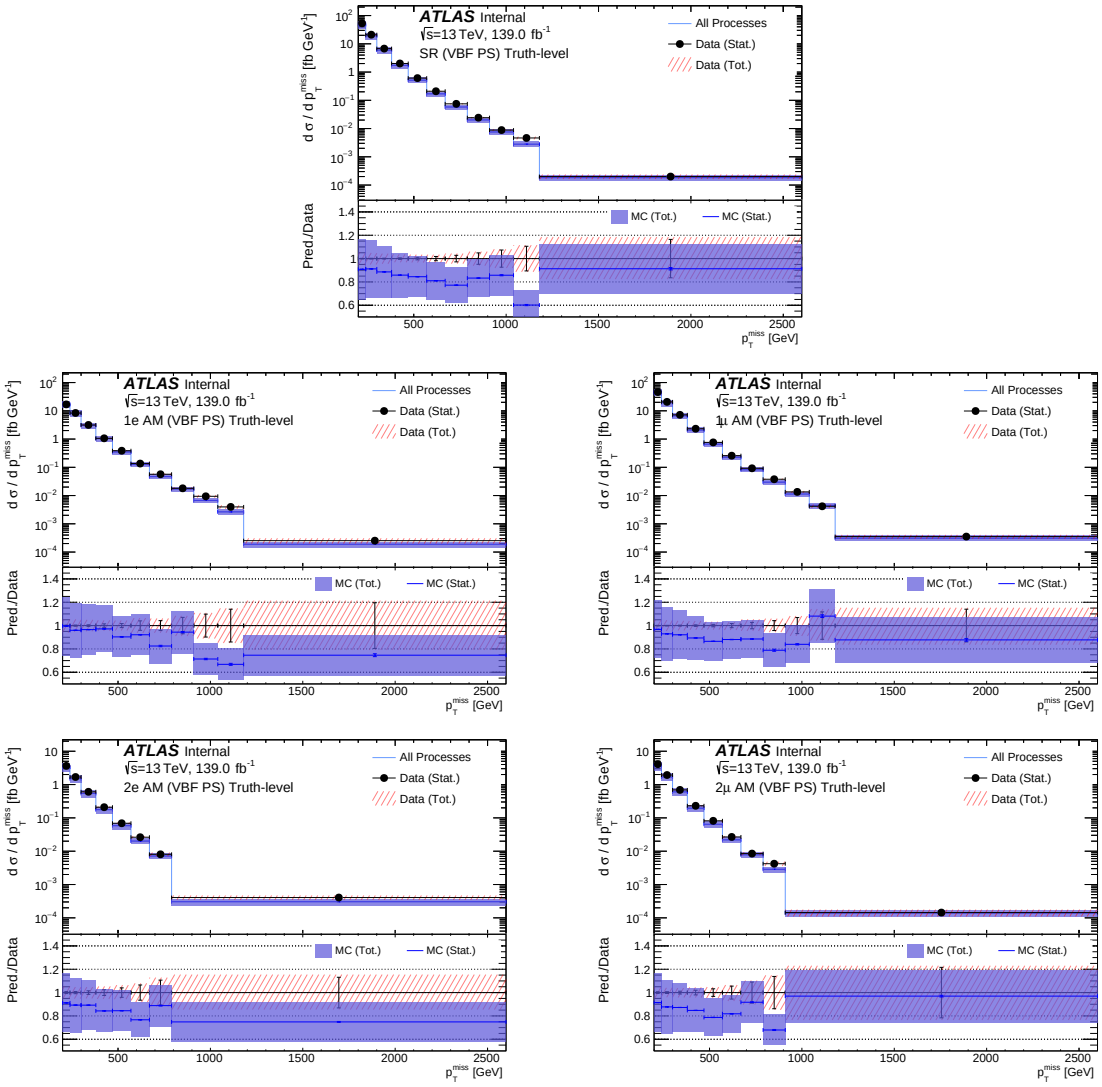

Figure 4.20.: MC/Data comparisons for $p_{\mathrm{T}}^{\mathrm{miss}}$ in the VBF phase-space. The shaded band shows the combination of the systematic uncertainty on the MC and the statistical uncertainty on the data.

Figures 4.23, 4.24 and 4.25 show comparisons between unfolded data and the particle-level SM predictions for the $p_{\mathrm{T}}^{\mathrm{miss}}$, m_{jj} and $\Delta\phi_{jj}$ for all regions in the ≥ 2 jet phase-space. For $p_{\mathrm{T}}^{\mathrm{miss}}$, the discrepancy between the unfolded data and MC is similar to that seen for the ≥ 1 jet phase-space. When we compare the $p_{\mathrm{T}}^{\mathrm{miss}}$ distribution in the ≥ 2 jet phase-space for the $p_{\mathrm{T}}^{\mathrm{miss}}$+jets and 1ℓ+jets region shown in Figure 4.16, to the equivalent unfolded distribution shown in Figure 4.23, the shapes and agreement between the nominal data and prediction are similar. Looking at the $p_{\mathrm{T}}^{\mathrm{miss}}$+jets region

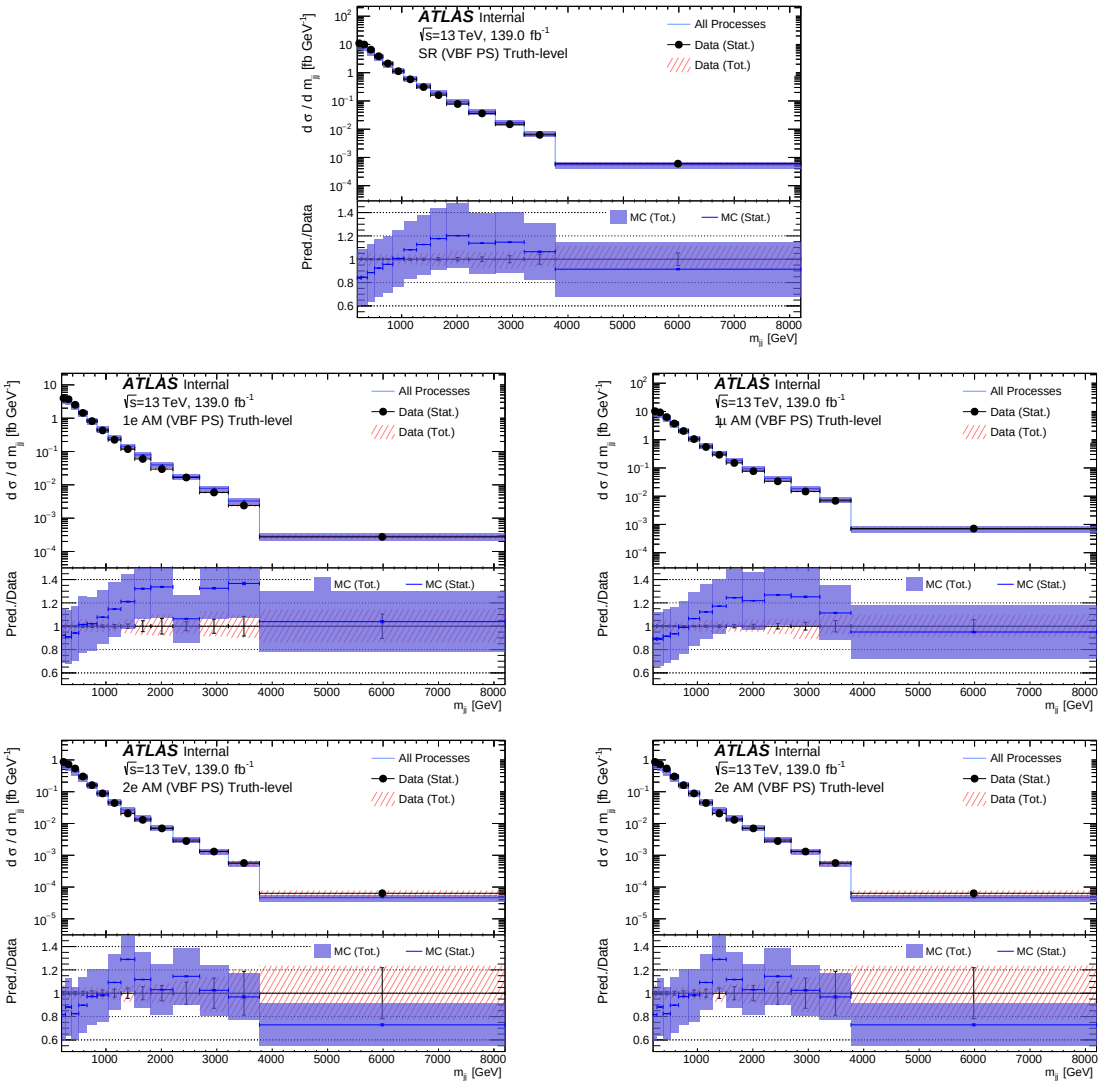

Figure 4.21.: MC/Data comparisons for m_{jj} in the VBF phase-space. The shaded band shows the combination of the systematic uncertainty on the MC and the statistical uncertainty on the data.

(specifically the pred/data figure) along with the $2e$+jets and 2μ+jets regions, there is a slight negative gradient reading from left to right on the $p_{\mathrm{T}}^{\mathrm{miss}}$ x-axis. This does not seem to be the case for the $1e$+jets and 1μ+jets regions for $p_{\mathrm{T}}^{\mathrm{miss}}$, although they do have similar shapes to each other. The detector-level $p_{\mathrm{T}}^{\mathrm{miss}}$ distribution in the 2ℓ+jets region, shown in Figure 4.16, has an almost flat $\sim$20% excess of data over the MC. For the equivalent unfolded distribution shown in Figure 4.23, the discrepancy's shape is slightly different in terms of having a steeper gradient and it ranges from a $\sim$10% to $\sim$30% deficit in the prediction over data ratio.

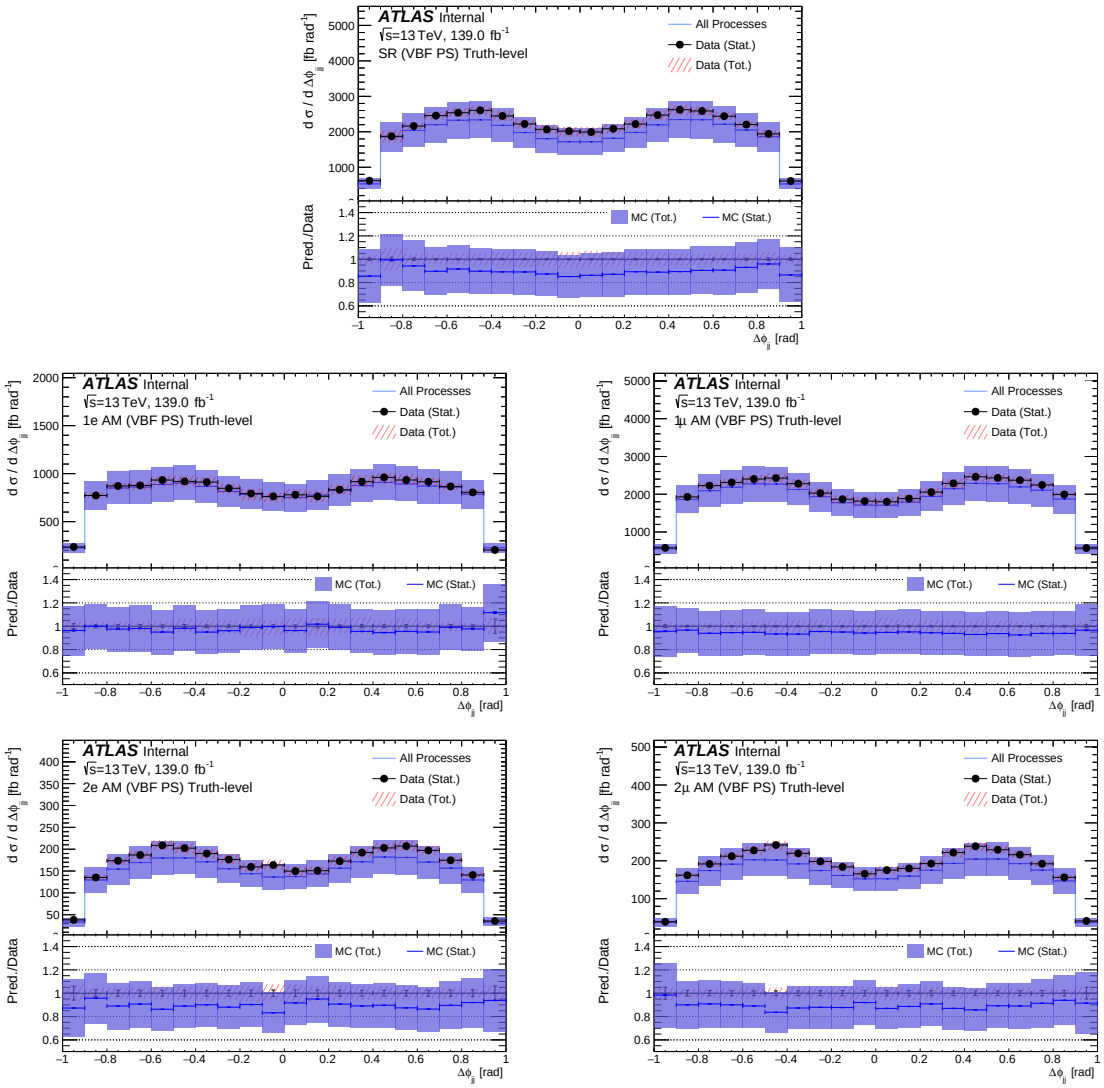

Figure 4.22.: MC/Data comparisons for $\Delta\phi_{jj}$ in the VBF phase-space. The shaded band shows the combination of the systematic uncertainty on the MC and the statistical uncertainty on the data.

The m_{jj} distribution is badly mismodelled as in the VBF phase-space and the equivalent detector-level distribution, where the discrepancies are covered by the total uncertainty.

The $\Delta\phi_{jj}$ distribution peaks at small $\Delta\phi_{jj}$ values, due to close together jets, with a dip at values close to zero as the jets cannot be exactly on top of each other. The unfolded data has slightly higher peaks than the MC in all regions. When comparing the unfolded $\Delta\phi_{jj}$ distributions to the detector-level $|\Delta\phi_{jj}|$ distribution, the clear distinction between them is that they are different distributions (compare Figures 4.18 to 4.25). The

absolute value for $\Delta\phi_{jj}$ was taken in ≥ 2 jet phase space for the unfolded distribution due to jet mismatching (see Section 4.2, in the ≥ 2 jet heading). This makes it slightly harder to make comparisons, yet for both Figures 4.18 and 4.25, the discrepancies look quite similar in terms of their magnitude for all regions ($p_{\mathrm{T}}^{\mathrm{miss}}$+jets, 1ℓ+jets, 2ℓ+jets).

The differences between the detector-level and particle-level distributions that are seen can be caused by a combination of factors. For instance, the detector resolution affects the measurement of the kinematic variables ($p_{\mathrm{T}}^{\mathrm{miss}}$, m_{jj}, $\Delta\phi_{jj}$) leading to smearing and migration effects across bins. We attempt to correct for these resolution effects by applying the unfolding procedure. Also another contribution could be the fake lepton background which is estimated using data-driven methods such as the matrix method and the fake factor method, and the accuracy of these methods can introduce additional uncertainties in the measurement of the kinematic variables when the fake background is subtracted.

4.9.3. Ratio, R^{miss}

A ratio, R^{miss}, is defined as the fiducial cross-section for $p_{\mathrm{T}}^{\mathrm{miss}}$+jets events divided by the fiducial cross-section for events in any of the $1e$+jets, 1μ+jets, $2e$+jets and 2μ+jets regions as defined in Section 4.1. The error for R^{miss} is calculated using the ratio of the two cross-sections using the equation $\sigma_{\mathrm{R}}^2 = \left(\frac{\partial R}{\partial X}\right)^2 \sigma_{\mathrm{X}}^2 + \left(\frac{\partial R}{\partial Y}\right)^2 \sigma_{\mathrm{Y}}^2 - 2\frac{\partial R}{\partial X}\frac{\partial R}{\partial Y}\mathrm{cov}(X,Y)$. Here, R is the ratio of two quantities X and Y with uncertainties σ_{X} and σ_{Y}, respectively. $\mathrm{cov}(X,Y)$ is the covariance between X and Y. The partial derivatives are evaluated at the central values of X and Y. In this case X could be seen as the fiducial cross-section for $p_{\mathrm{T}}^{\mathrm{miss}}$+jets and Y as the fiducial cross-section for events in any of the $1e$+jets, 1μ+jets, $2e$+jets and 2μ+jets regions.

Figures 4.26–4.32 show the R^{miss} for the various observables, regions, and phase-spaces considered in the measurement, for the final-state unfolding strategy. The modelling of the data in each region can be easily compared to each other by constructing a double ratio, defined as R^{miss} as measured in the data divided by R^{miss} as predicted by the MC and is shown in the bottom panel of each figure. The error bars on the double ratio show the statistical uncertainty combined with the systematic uncertainties.

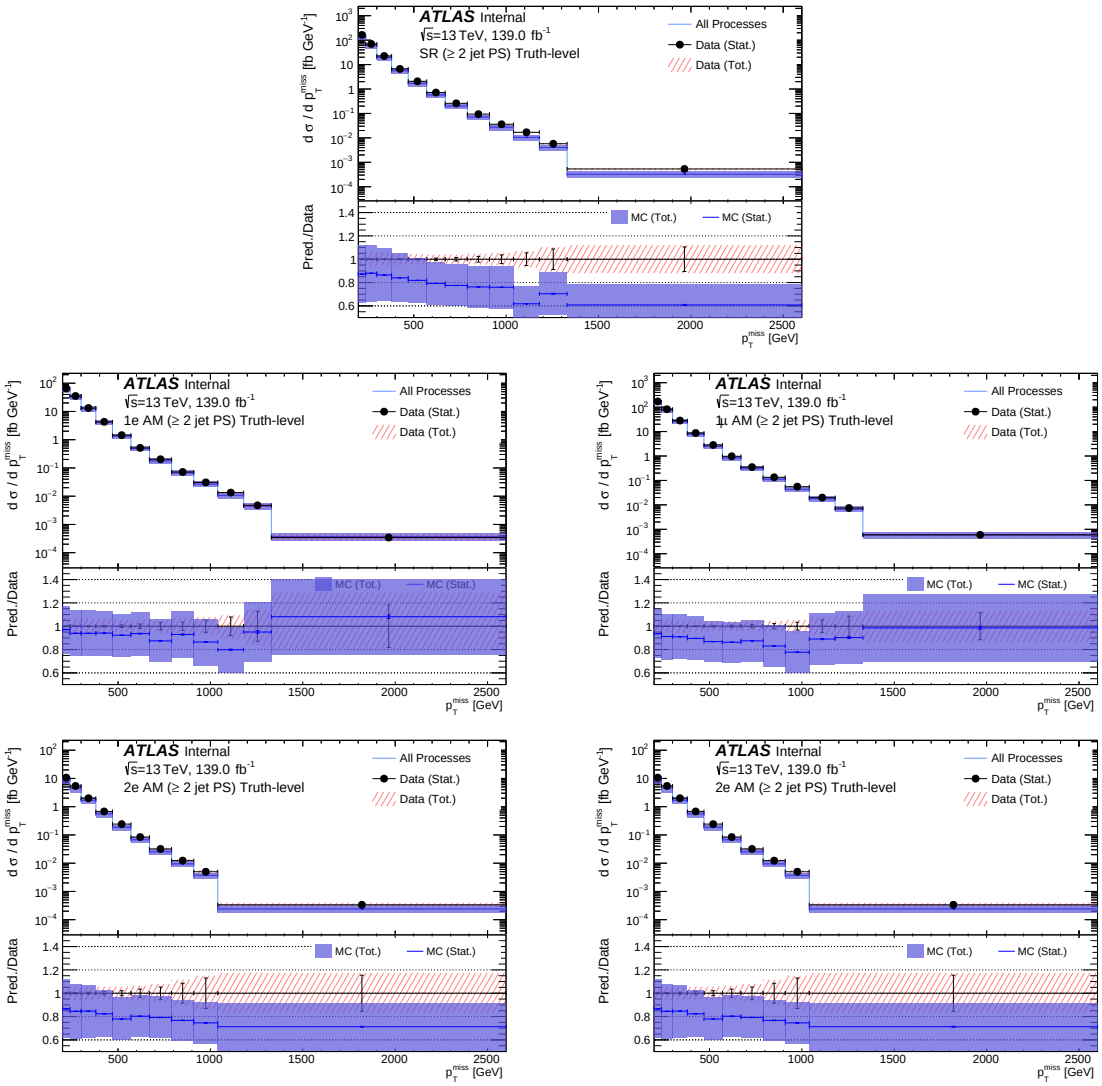

Figure 4.23.: MC/Data comparisons for $p_{\mathrm{T}}^{\mathrm{miss}}$ in the ≥ 2 jet phase-space. The shaded band shows the combination of the systematic uncertainty on the MC and the statistical uncertainty on the data.

The experimental systematic uncertainties which originate from the jet calibration procedure are significantly reduced in the ratio due to the similarity of the jet systems in the $p_{\mathrm{T}}^{\mathrm{miss}}$ regions in the numerator of R^{miss} and the lepton regions in the denominator.

The lepton efficiency systematics are uncorrelated between the numerator and denominators and are therefore the dominant experimental systematic uncertainties on the R^{miss} ratio. Theoretical systematic uncertainties on the particle-level SM predictions are shown as a blue band. These are significantly reduced in the ratio because of the similarity of the processes in the numerator and the denominator.

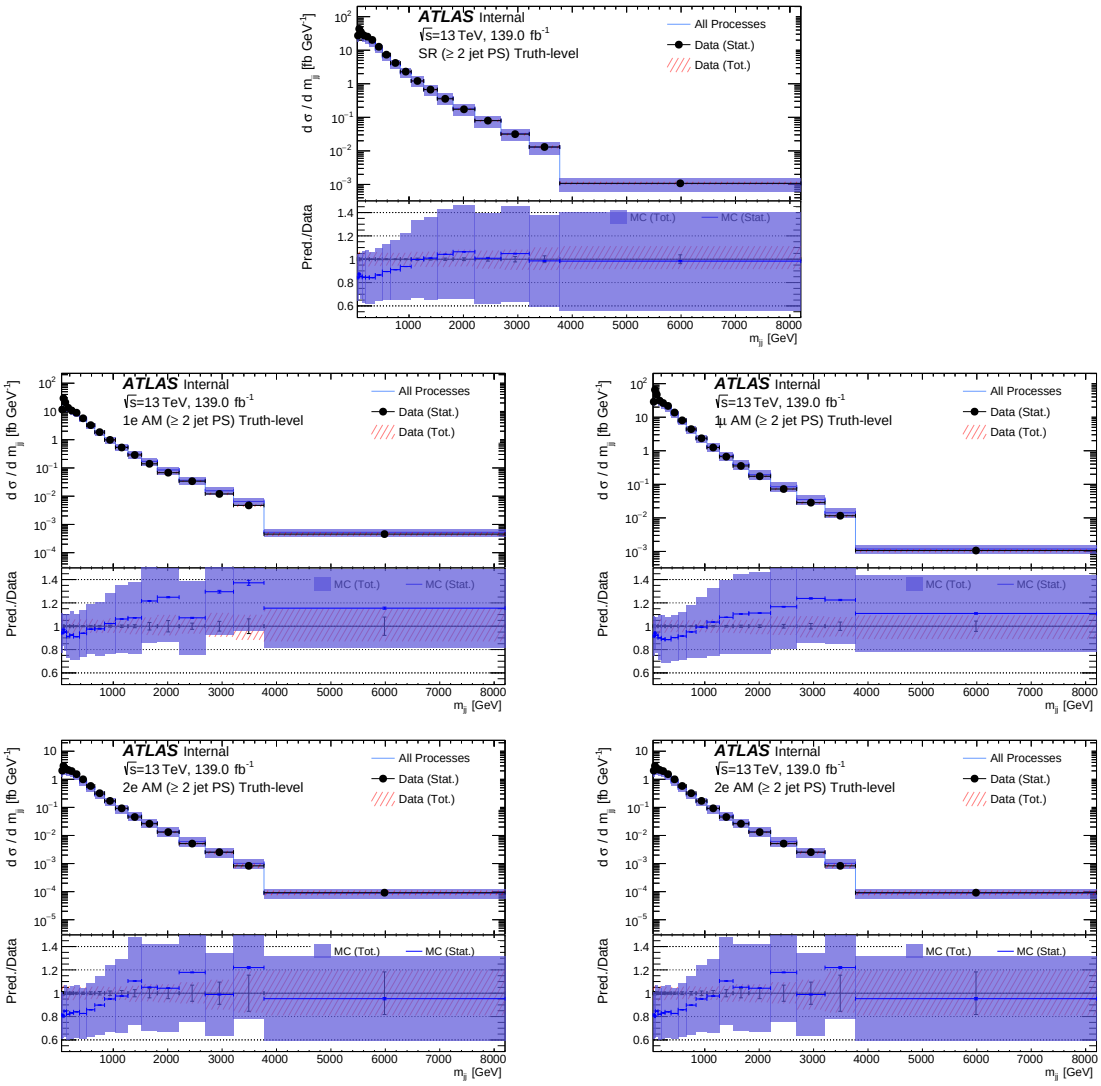

Figure 4.24.: MC/Data comparisons for m_{jj} in the ≥ 2 jet phase-space. The shaded band shows the combination of the systematic uncertainty on the MC and the statistical uncertainty on the data.

A slightly weaker cancellation of theoretical uncertainties is observed here compared to the previous measurement of R^{miss} published in [119]. This is to be expected since all the regions in this thesis are defined in terms of the final-state particles instead of a particular processes, which results in the $p_{\mathrm{T}}^{\mathrm{miss}}$ regions being populated by both the Z+jets and W+jets events. Both of these processes introduce theoretical uncertainties which have uncorrelated components between the $p_{\mathrm{T}}^{\mathrm{miss}}$ regions and and the 1ℓ + jets (mainly populated by W+jets events) or the 2ℓ + jets (mainly populated by Z+jets events).

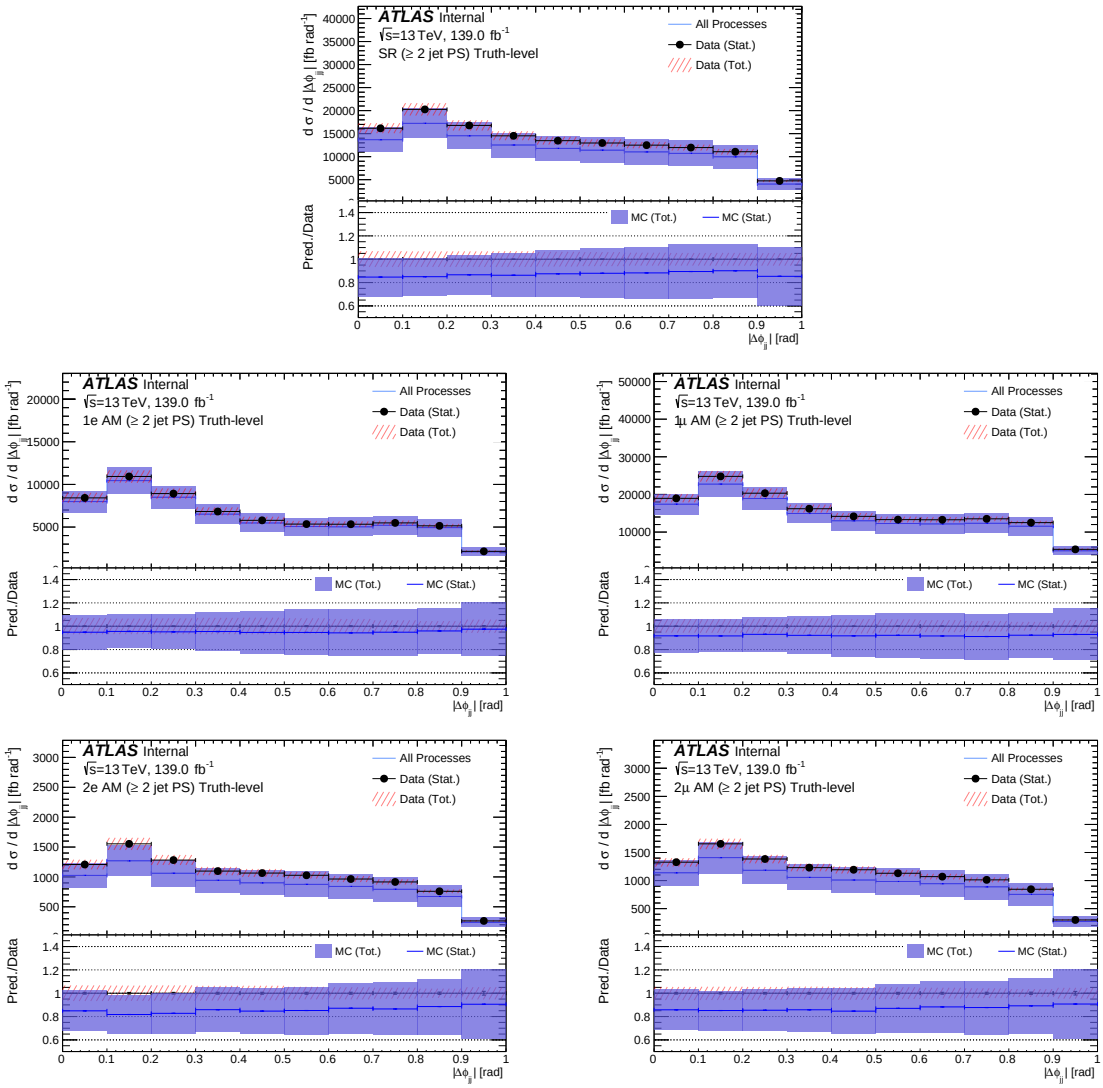

Figure 4.25.: MC/Data comparisons for $\Delta\phi_{jj}$ in the ≥ 2 jet phase-space. The shaded band shows the combination of the systematic uncertainty on the MC and the statistical uncertainty on the data.

Figure 4.26 show the comparisons between the R^{miss} as measured for data and for the SM prediction, as a function of $p_{\mathrm{T}}^{\mathrm{miss}}$ in the ≥ 1 jet phase-space. For the one electron and one muon regions in Figures 4.26(a) and 4.26(b), these Figures have values of $R^{\mathrm{miss}} \sim 1.5 - 2.5$ and $R^{\mathrm{miss}} \sim 0.8 - 1.2$ for low $p_{\mathrm{T}}^{\mathrm{miss}}$ bins which then decreases to $R^{\mathrm{miss}} \sim 1.5$ and $R^{\mathrm{miss}} \sim 0.8$ for high $p_{\mathrm{T}}^{\mathrm{miss}}$ bins respectively for the SM prediction. The shape of R^{miss} is not very well modelled (with a slope for the MC/Data double ratio as one gets to higher $p_{\mathrm{T}}^{\mathrm{miss}}$, especially for the one electron plot), with some discrepancies between the SM prediction and data, most of the differences are covered by the theory and experimental uncertainties. The ratio is shown to be higher when looking at the

one electron region, this is due to the additional real $p_{\mathrm{T}}^{\mathrm{miss}} > 60$ GeV requirement for this region which results in a small cross-section.

For the two electron and two muon region R^{miss} in Figures 4.26 (c) and 4.26 (d), there are large values of R^{miss} at low $p_{\mathrm{T}}^{\mathrm{miss}}$ for both regions at a value of approximately of 14 and 12 respectively which decreases to 7 at higher $p_{\mathrm{T}}^{\mathrm{miss}}$.

The higher values of R^{miss} is due to the contributions of W+jets to the $p_{\mathrm{T}}^{\mathrm{miss}}$ + jets region, which are much larger at values of low $p_{\mathrm{T}}^{\mathrm{miss}}$. The shape is also affected by the fiducial requirements on the charged leptons in the denominator. For example, at higher $p_{\mathrm{T}}^{\mathrm{miss}}$, the leptons have larger p_{T} and tend to be more central, this makes them more likely to pass the selection criteria of the 2ℓ + jets regions, and therefore increasing the fiducial cross-sections of the denominators.

The shape of the measured R^{miss} (data) is, as can be seen, very well modelled by the SM prediction for 2ℓ + jets with the MC in general very slightly underestimating the value of R^{miss}. The discrepancy is covered by the uncertainties save a couple of bins (at $\sim$800 GeV and $\sim$1000 GeV) for the 2ℓ + jets regions. The theoretical uncertainties on R^{miss} are expected to be of the order of a percent in all bins and they are shown to be of sub-percent level and this has been demonstrated before in studies in [177].

Figure 4.27 show the comparisons between R^{miss} for the SM prediction and the data as a function of $p_{\mathrm{T}}^{\mathrm{miss}}$ in the VBF phase-space. The shape of R^{miss} is similar to what is seen for the ≥ 1 jet phase-space, where the discrepancies seen for the normalisation and shape are similar again to ≥ 1 jet except in 4.27 (a) where in low $p_{\mathrm{T}}^{\mathrm{miss}}$ the MC does not agree well with the unfolded data.

Figure 4.28 show the comparisons between R^{miss} for the SM prediction and the data as a function of m_{jj} in the VBF phase-space. The SM prediction shows a relatively (compared to $p_{\mathrm{T}}^{\mathrm{miss}}$ distributions) flat shape for the m_{jj} distribution, which the data shows as well. In the VBF phase space region, which is characterized by two high-energy jets with a large invariant mass and a large separation in azimuthal angle, Figure 4.28 is flat for the m_{jj} variable. This is because the VBF process is dominated by the exchange of two virtual W or Z bosons, which leads to a distinctive topology of the two high-energy jets with a large invariant mass and a large separation in azimuthal angle. In this process, the production of missing transverse momentum is associated with the recoil of the two jets, which are typically back-to-back in azimuthal angle. Since the VBF process is characterized by a distinctive topology, this results in a flat R^{miss} distribution for m_{jj} in the VBF phase space region.

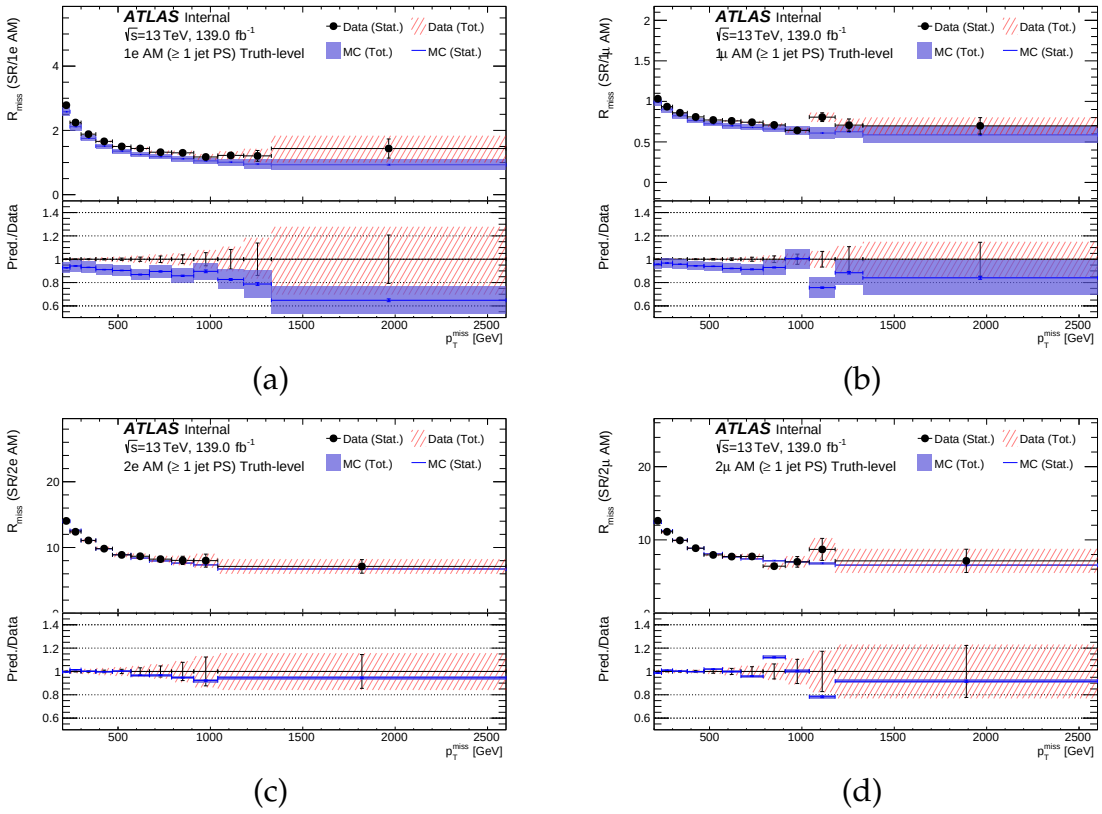

Figure 4.26.: R^{miss} for $p_{\mathrm{T}}^{\mathrm{miss}}$ in the ≥ 1 jet phase-space. The red hashed band shows the combination of the statistical and systematic uncertainty on the data and the blue band is the statistical and systematic uncertainty on the MC. The black dot with the bar represents the data and its respective statistical uncertainty.

Figure 4.29 show the comparisons between R^{miss} for the SM prediction and the data as a function of $\Delta\phi_{jj}$ in the VBF phase-space. Figures 4.29 (a) and 4.29 (b) show R^{miss} for the $1e$ + jets or 1μ + jets lepton regions in the denominator. The R^{miss} has a relatively flat SM prediction. The same can be said for 4.29 (c) and 4.29 (d) for the two lepton regions. The only difference is that the one lepton region has smaller values of R^{miss} than the two lepton regions due to large contributions from top-pair events which results in a increased cross-section in the denominator of R^{miss} and therefore a smaller ratio. The data agrees within the uncertainties with the SM predictions for the two lepton regions but not the one lepton regions.

Figures 4.30, 4.31 and 4.32 show comparisons between R^{miss} as measured in the data as well as the SM predictions, using the lepton regions in the denominator, as a function of $p_{\mathrm{T}}^{\mathrm{miss}}$, m_{jj} and $|\Delta\phi_{jj}|$ in the ≥ 2 jet phase-space. In Figures 4.30 (a) and (b), the MC does not agree well with the data whereas in Figures 4.30 (c) and (d)

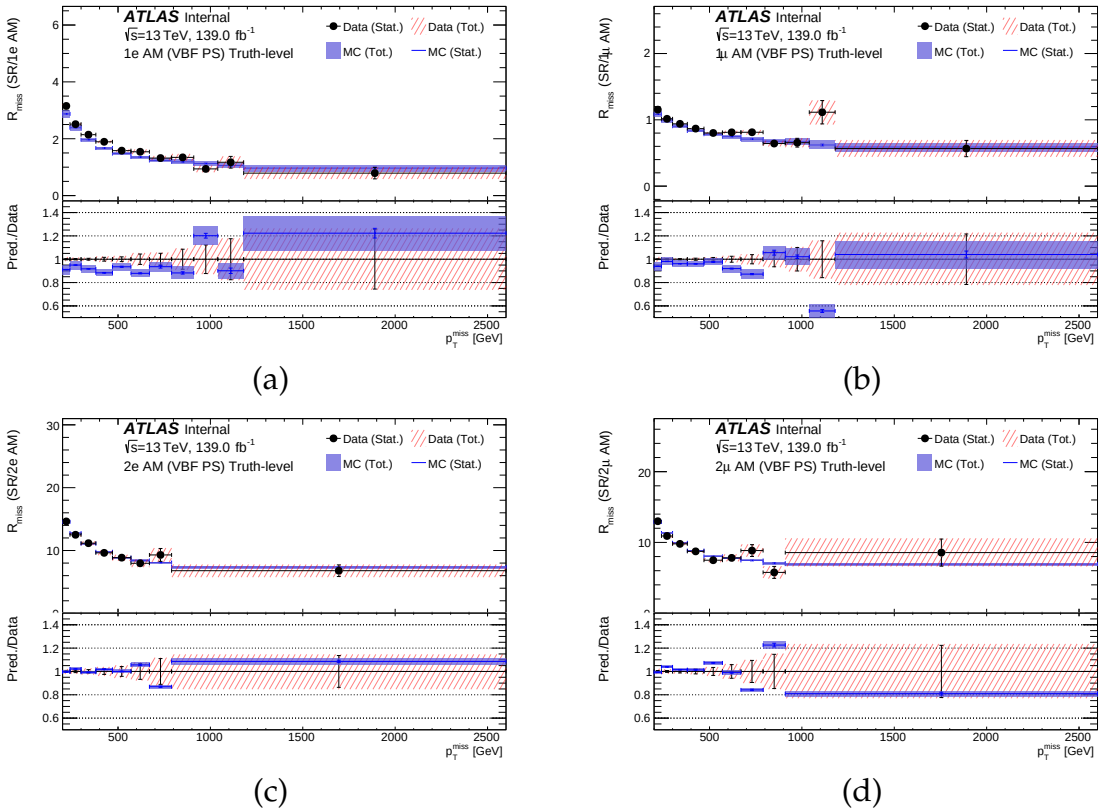

Figure 4.27.: R^{miss} for $p_{\mathrm{T}}^{\mathrm{miss}}$ in the VBF phase-space. The red hashed band shows the combination of the statistical and systematic uncertainty on the data and the blue band is the statistical and systematic uncertainty on the MC. The black dot with the bar represents the data and its respective statistical uncertainty.

it does. In Figures 4.31 (a) and (b), there is an interesting excess (about three σ) at around $m_{jj} = 3500$ GeV. This excess could be due to the mismodelling of m_{jj} being distinct across different regions. In this instance, the m_{jj} mismodelling has a slightly different shape and normalisation in $p_{\mathrm{T}}^{\mathrm{miss}}$+jets region (see Figure 4.17) than the $1e$+jets region (see Figure 4.17). For the $p_{\mathrm{T}}^{\mathrm{miss}}$+jets region in Figure 4.17, the nominal MC is in agreement with the data around this excess, whereas for the $1e$+jets region in Figure 4.17 the nominal MC is well above the nominal data. Due to the nominal MC being in excess of the data at $m_{jj} = 3500$ GeV in the denominator (i.e., $1e$+jets region in Figure 4.17) of R_{1e}^{miss}, this causes the MC R_{1e}^{miss} to be smaller than the data R_{1e}^{miss} at $m_{jj} = 3500$ GeV. Further investigation into this excess is required which unfortunately due to time constraints could not be done for this thesis. In Figure 4.32, the data is found to be in agreement with the SM predictions apart from a few fluctuations.

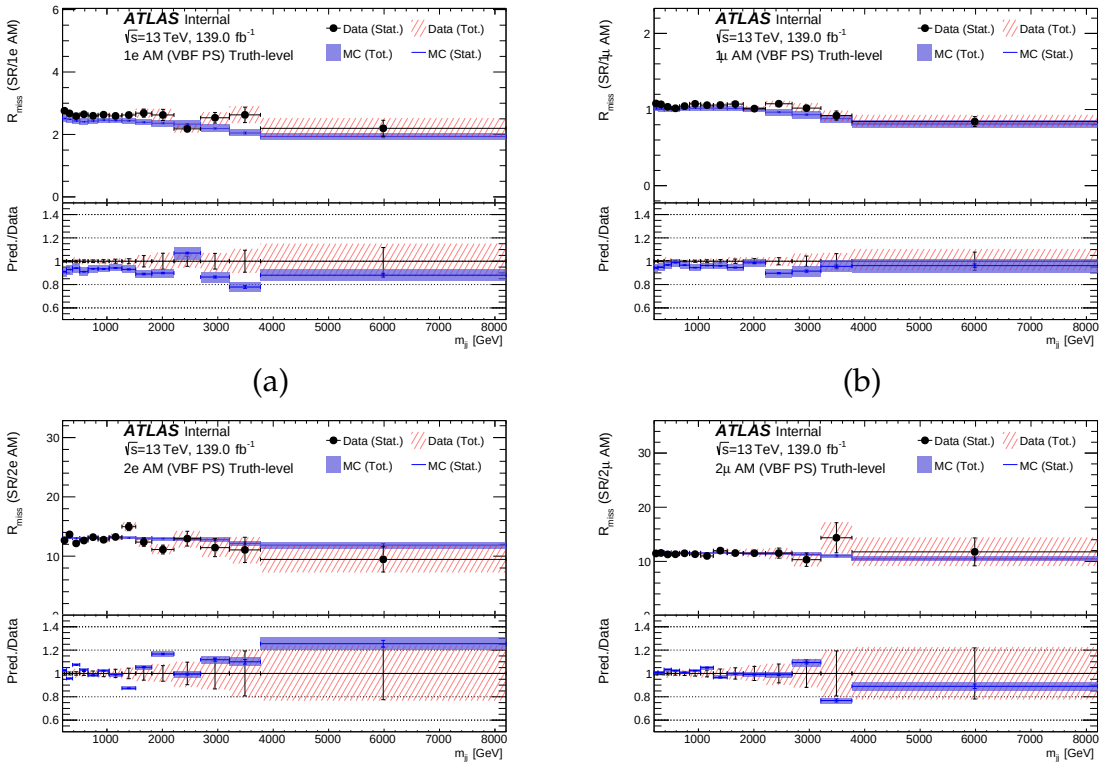

Figure 4.28.: R^{miss} for m_{jj} in the VBF phase-space. The red hashed band shows the combination of the statistical and systematic uncertainty on the data and the blue band is the statistical and systematic uncertainty on the MC. The black dot with the bar represents the data and its respective statistical uncertainty.

Apart from these noted differences, the discrepancies for Figures 4.30, 4.31 and 4.32 in terms of the normalisation and the shape are similar to what is observed in the ≥ 1 jet and VBF phase-space. The data is mostly found to be in agreement with the SM prediction within the uncertainties.

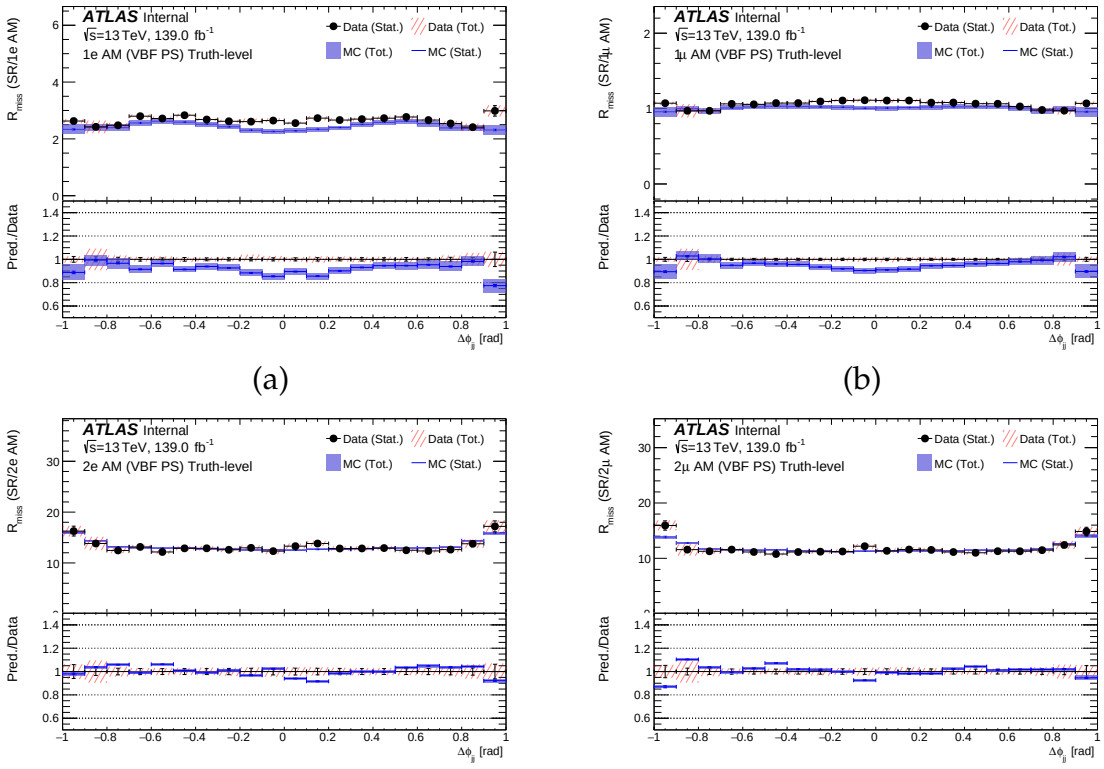

Figure 4.29.: R^{miss} for $\Delta\phi_{jj}$ in the VBF phase-space. The red hashed band shows the combination of the statistical and systematic uncertainty on the data and the blue band is the statistical and systematic uncertainty on the MC. The black dot with the bar represents the data and its respective statistical uncertainty.

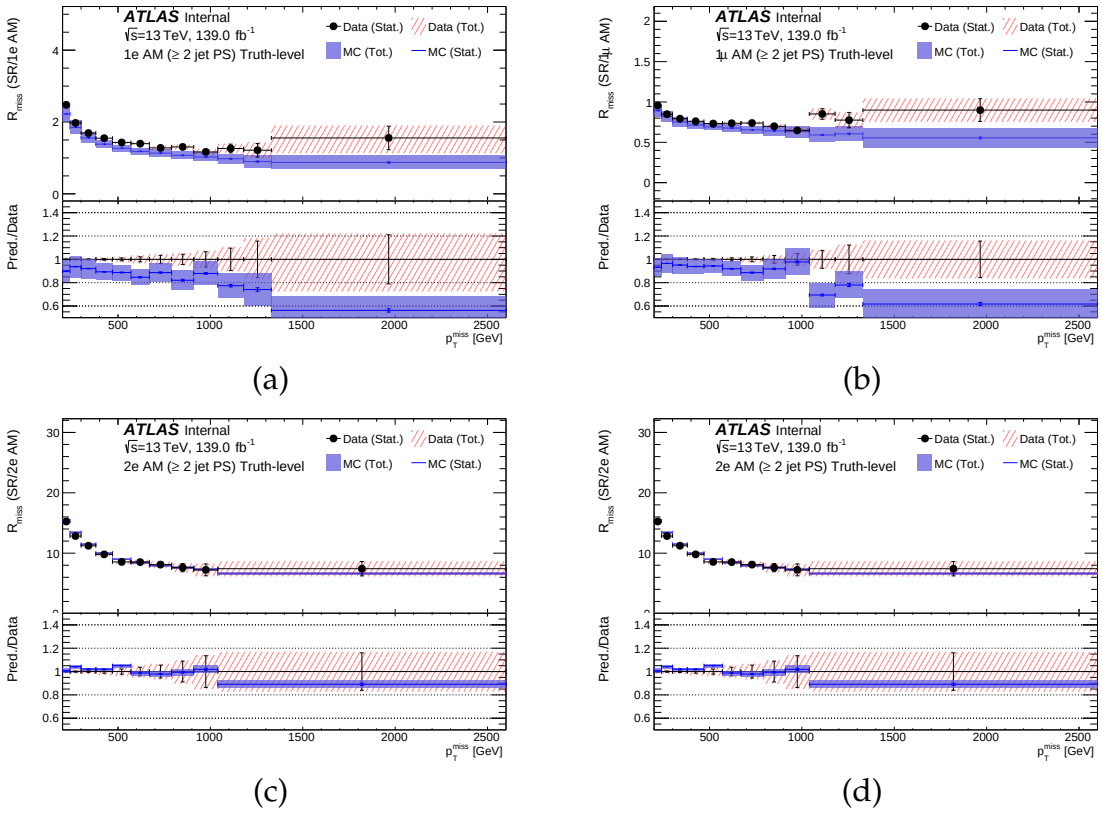

Figure 4.30.: R^{miss} for $p_{\mathrm{T}}^{\mathrm{miss}}$ in the ≥ 2 jet phase-space. The red hashed band shows the combination of the statistical and systematic uncertainty on the data and the blue band is the statistical and systematic uncertainty on the MC. The black dot with the bar represents the data and its respective statistical uncertainty.

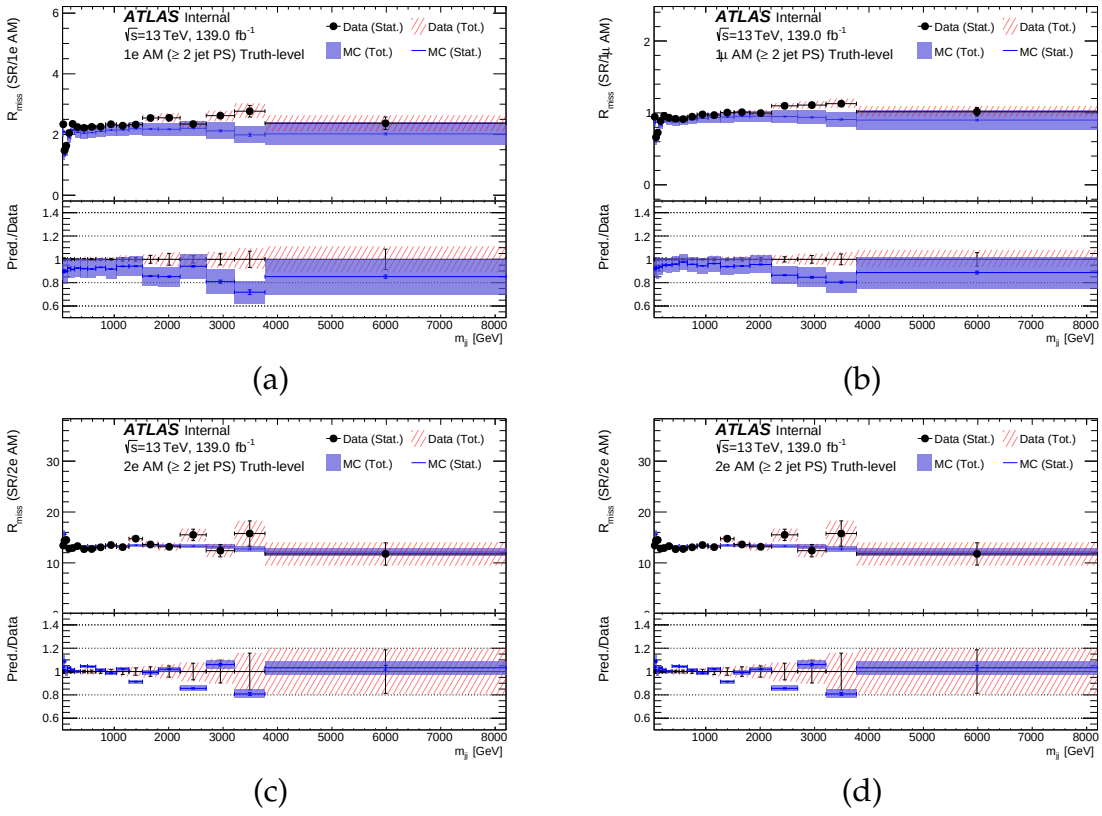

Figure 4.31.: R^{miss} for m_{jj} in the ≥ 2 jet phase-space. The red hashed band shows the combination of the statistical and systematic uncertainty on the data and the blue band is the statistical and systematic uncertainty on the MC. The black dot with the bar represents the data and its respective statistical uncertainty.

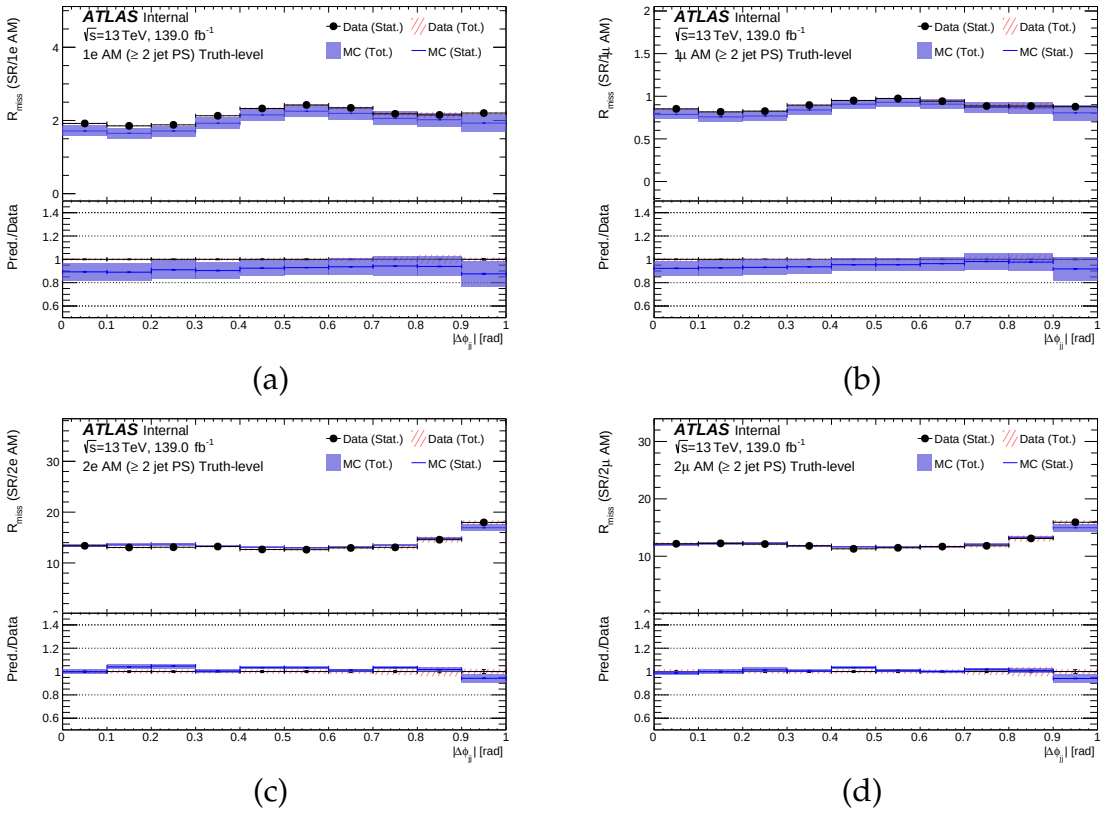

Figure 4.32.: R^{miss} for $|\Delta\phi_{jj}|$ in the ≥ 2 jet phase-space. The red hashed band shows the combination of the statistical and systematic uncertainty on the data and the blue band is the statistical and syst uncertainty on the MC. The black dot with the bar represents the data and its respective statistical uncertainty.

Chapter 5.

Interpretation

"It is necessary to look at the results of observation objectively, because you, the experimenter, might like one result better than another."

— Richard P. Feynman, 1918–1988

5.1. Introduction

Finding the significance for a specific data set and the expected sensitivity, which may involve many MC calculations, can be computationally expensive. The results by Wilks [198] and Wald [199] provide a way to approximate the probability density function (pdf) of the test statistic under certain assumptions, without the need to generate a large number of MC simulated data sets. In hypothesis testing, the test statistic is a quantity calculated from the data that is used to decided whether or not to accept or reject a specific hypothesis. The pdf of the test statistic is important as it allows one to determine the probability of observing a given test statistic under the hypothesis being tested (i.e., the null hypothesis) which in this case is the SM prediction which in turn allows us to calculate the $p-$value (the probability of obtaining a result as extreme or more than the observed result, assuming the null hypothesis to be true).

Wilks and Wald showed that, under certain conditions, the pdf of the test statistic can be approximated by an asymptotic formula. The conditions include the assumption that the sample size is large, the test statistic is a continuous function of the data and

that the null hypothesis is well behaved (i.e., the maximum likelihood estimate of the parameters is well-defined and unique).

The asymptotic formula can be used to find the expected sensitivity of a specific data set, as well as the full sampling distribution under different signal hypotheses, without having to generate a lot of MC distributions. This is done by using a single representative data set, known as the "Asimov" data set, which is constructed to have the same expected distribution as the real data under a specific hypothesis. The "Asimov" data set is then used to calculate the test statistic and approximate its pdf using the asymptotic formula. This avoids the need to generate multiple MC data sets, which can be computationally expensive, especially when testing many different BSM signal models.

This section discusses the procedures that are used to set limits on various DM signal models. Two distinct (but complementary) techniques are used: a **goodness-of-fit** test which uses a ***p*-value** to quantify "is the measured data consistent with SM hypothesis", and a **hypothesis test** which uses a **confidence level (CL)** to quantify "is the data significantly more consistent with the signal hypothesis than the SM hypothesis". Both of these quantities are important, because a hypothesis test may significantly favour the signal hypothesis compared with the SM (based on a **confidence level** test), despite neither being compatible with the data (based on ***p*-value** tests). In this case, potential mismodelling may be a worry, rather than claiming evidence for the signal hypothesis. It is possible for the data to be consistent with the SM hypothesis (have a reasonable p-value), but still significantly favour a signal hypothesis (the degree to which the signal hypothesis improves the agreement is statistically significant). For this reason, the methodology used is as follows:

1. Use fits to an Asimov data-set (i.e., a data-set in which all measurements are fixed to their SM values) to quantify how much each independent source of systematic uncertainty is constrained, when both the main signal and auxiliary measurements are considered.

2. Use **goodness-of-fit tests** to quantify data/MC agreement in the auxiliary regions, and in the unblinded $p_{\mathrm{T}}^{\mathrm{miss}}$+jets region. These will demonstrate whether systematic uncertainties on SM processes are being well modelled. Once the modelling is considered adequate, it is then possible to progress to setting limits on DM hypotheses.

3. Use **hypothesis tests** to set limits on DM hypotheses, using both the Asimov data-set (expected) and measured data-set (observed).

In this analysis the unfolded differential measurements of m_{jj}, $\Delta\phi_{jj}$ and $p_{\mathrm{T}}^{\mathrm{miss}}$ in the $p_{\mathrm{T}}^{\mathrm{miss}}$+jets and auxiliary regions are considered. The measurements in each bin of each differential distribution are treated as random variables. The likelihood function is written assuming that these measurements are Gaussian distributed within the associated statistical[1] and systematic uncertainties, where (i) the significant statistical correlations which exist between bins of different observables (these are significant as they are measured using the same data-set) are taken into account and (ii) a fully decorrelated set of systematic uncertainties in order to correctly account for their correlations between bins and fiducial phase-space regions are considered. The auxiliary regions will be used to constrain systematic uncertainties for which the transfer into the $p_{\mathrm{T}}^{\mathrm{miss}}$+jets is considered to be well-understood. There are various uncertainties which are considered such as those from the unfolded measurements, both from experimental sources and the modelling of the response matrix used in the unfolding. There are also theoretical uncertainties on the SM and also the BSM signal.

The interpretation is performed using the following method:

1. Construct the likelihood function, $\mathcal{L}\left(\vec{x}|\vec{p}\right)$. This is a model-dependent parameterisation of the probability density of obtaining data-set $\vec{x}$ if the model is true, where $\vec{p}$ are tunable model parameters. Such model parameters include the *parameters of interest* (PoIs), $\vec{\mu}$, and *nuisance parameters* (NP), $\vec{\theta}$. In a simple case, $\vec{\mu}$ could be a one-dimensional vector whose only component is the signal-strength for some BSM model, in which case $\vec{\mu}^{\mathrm{SM}} = \{0\}$. For almost all cases considered below, $\vec{\theta}$ will be a vector of NPs describing pulls on systematic uncertainties.

2. Construct the test statistic, $t_{\vec{\mu}}$. Calculated by optimising the likelihood function at each point in $\vec{\mu}$-space, this number quantifies the consistency between the model hypothesis and the measured data-set.

3. Based on the value of $t_{\vec{\mu}}$ at each hypothesised value of $\vec{\mu}$, the *confidence level* $CL\left(\vec{\mu}\right)$ are then calculated. This represents the frequency with which a randomly generated data-set would be judged to be 'less consistent' with the model than the one which was generated. Within a purely frequentist framework, the hy-

[1] In particle physics, the statistical uncertainties are often assumed to be Gaussian because they arise from counting statistics and can be modeled by Poisson distributions in the limit of large sample sizes.

pothesis $\vec{\mu}$ with confidence $1-\alpha$ can be excluded when $CL(\vec{\mu}) < \alpha$. Typically the value of α considered is $\alpha = 0.05$, and therefore models are excluded when $CL(\vec{\mu}) < 0.05$. The $CL(\vec{\mu})$ method doesn't take into account the possibility of downward fluctuations in the SM, which can mimic the expected signal and lead to overestimating the significance of the observed excess. This can be problematic in cases where the sensitivity is limited by the uncertainty in the SM prediction.

4. Confidence intervals are set using the CL_s method. This method deliberately overcovers (i.e., has a frequentist coverage not equal to $= 1-\alpha$ but $\geq 1-\alpha$).[2] This compromise is accepted because the CL_s method reduces the chance of excluding a BSM model which has a similar inconsistency with the measured data-set as that of the SM.

5.2. The Likelihood Function

When setting limits on new physics, the alternative hypothesis (H_1) represents the combination of BSM signal and the SM, whereas the null hypothesis (H_0) is that the measurements can be explained using only SM processes. A **goodness-of-fit** is performed by constructing a test statistic which quantifies the level of agreement between the data and the hypothesis. The observed value of this test statistic is then compared with the expected distribution, assuming the hypothesis to be true, to derive a p-value quantifying the observed compatibility. A **hypothesis** test is performed by constructing a test statistic which quantifies how much more/less consistent the data is with H_1 compared with H_0. This is used to extract a confidence level, in a similar manner.

Assuming that all systematic uncertainties treated in the covariance matrix and all statistical uncertainties can be modelled as Gaussian, the likelihood (derived in appendix C) is given by:

$$\mathcal{L}\left(\vec{x} \mid \vec{\mu}, \vec{\theta}\right) = \frac{1}{\left(\sqrt{2\pi}\right)^{k} |\mathrm{Cov}|} \cdot e^{-\frac{1}{2}\chi^2\left(\vec{x},\vec{\mu},\vec{\theta}\right)} \cdot \prod_i \mathcal{G}\left(\theta^{(i)}\right) \tag{5.1}$$

[2] In statistics, the term "overcover" refers to the situation where the interval is wider than it needs to be to achieve the desired level of confidence, resulting in the inclusion of more values than strictly necessary.

where k is the number of Parameters of Interest (PoI) and

$$\chi^2\left(\vec{x},\vec{\mu},\vec{\theta}\right) = \left(\vec{x}-\vec{p}^{\,\mathrm{mod}}\left(\vec{\mu}\right)+\sum_i \theta^{(i)}\cdot\vec{\epsilon}^{(i)}\right)^{\mathrm{T}} \mathrm{Cov}^{-1} \left(\vec{x}-\vec{p}^{\,\mathrm{mod}}\left(\vec{\mu}\right)+\sum_i \theta^{(i)}\cdot\vec{\epsilon}^{(i)}\right) \tag{5.2}$$

is the χ^2 test statistic, Cov is the covariance matrix which describes the statistical uncertainties and correlations, and any symmetric systematic uncertainties and correlations which are not profiled as NP. The SM + BSM model prediction at a particular hypothesis $\vec{\mu}$ is denoted by $\vec{p}^{\,\mathrm{mod}}\left(\vec{\mu}\right)$ and $\epsilon^{(i)}$ is the absolute uncertainty amplitude associated with a nuisance parameter $\theta^{(i)}$. The standard normal constraint term, $\mathcal{G}\left(\theta^{(i)}\right)$, represents the prior probability distribution of $\theta^{(i)}$.[3]

The impact of systematic uncertainties can be implemented in two equivalent ways [200]. Firstly, they can be included in the covariance matrix, allowing implicit profiling. In this case, $\mathrm{Cov} = \mathrm{Cov}^{\mathrm{stat}} + \sum_{\mathrm{source}} \mathrm{Cov}^{\mathrm{syst,source}}$, and $\mathrm{Cov}_{ij}^{\mathrm{syst,source}} = \epsilon_i^{\mathrm{source}}\epsilon_j^{\mathrm{source}}\ \forall\ i,j$. Here, $\epsilon_{i,j}^{\mathrm{source}}$ are signed uncertainties, and so measurement correlations and anti-correlations are taken into account. Alternatively, Gaussian uncertainties can be included as NP shifts on either $\vec{x}$ or $\vec{p}$ (c.f. θ above). In this case, the external constraint term describes the Gaussian nature of the uncertainty. Profiling systematic uncertainties as NPs allows us to (i) implement asymmetric or one-sided uncertainty amplitudes, (ii) investigate the post-fit NP values and uncertainties, alerting us to possible mismodelling effects and demonstrating how each systematic uncertainty is being constrained by the data, and (iii) plot the post-fit agreement between a model and the data-set. The downside of using NPs is that it increases the complexity of the likelihood function, thus it becomes computationally expensive to perform fits to thousands of toy data-sets or with hundreds of observed measurements. The following approach is taken:

- Use NPs when performing individual goodness-of-fit tests, since these aim to quantify and understand the modelling and constraint of systematic uncertainties.
- Do not use NPs when deriving observed distributions using thousands of toys.

[3]Note that if the uncertainty $\epsilon^{(i)}$ was constrained using a prior fit to auxiliary measurements, then $\mathcal{G}\left(\theta^{(i)}\right)$ approximately represents the likelihood contour resulting from these measurements, and is not a Bayesian prior.

5.3. Test Statistic and Confidence Levels

The hypothesised value of μ was tested by taking the ratio between the likelihoods of the signal and the SM hypotheses:

$$\lambda(\vec{\mu}) = \frac{\text{argmax}_{\vec{\theta}}\mathcal{L}(\vec{x} \mid \vec{\mu}, \vec{\theta})}{\text{argmax}_{\vec{\theta}}\mathcal{L}(\vec{x} \mid \vec{\mu}_{SM}, \vec{\theta})} \tag{5.3}$$

where the likelihoods of the μ and μ_{SM} hypotheses are evaluated by marginalising the NPs $\vec{\theta}$ and argmax$\vec{\theta}$ represents the value of the parameter vector $\vec{\theta}$ that maximizes the likelihood function. This can re-parameterised to write the test statistic as

$$t_{\vec{\mu}} = -2\ln\lambda(\vec{\mu}) \; = \; \chi^2_{\mu} - \chi^2_{SM} \tag{5.4}$$

which is equal to the $\Delta\chi^2$ between the two hypotheses assuming that all statistical and systematic uncertainties are modelled as Gaussian. This number will be negative when the data has better compatibility with the signal hypothesis than the SM hypothesis, and positive when the SM hypothesis is more compatible. The observed value of $t_{\vec{\mu}}$ will be a random number drawn from whatever distribution is expected based on the "true" hypothesis. The confidence level is defined as the probability of $t_{\vec{\mu}}$ being higher than what was observed, assuming the signal model to be true:

$$CL(\vec{\mu}) = \int_{t_{\vec{\mu},obs}}^{\infty} f(t_{\vec{\mu}}|\vec{\mu})dt_{\vec{\mu}} \tag{5.5}$$

where $t_{\vec{\mu},obs}$ is the value of the statistic observed from the data and $f(t_{\vec{\mu}}|\vec{\mu})$ denotes the pdf of $t_{\vec{\mu}}$ under the assumption of a fixed signal of $\vec{\mu}$.

The Neyman-Pearson lemma states that the likelihood ratio is the most powerful test at some significance threshold α. The hypothesis can be excluded if the observed confidence level is below α. To extract the CL, the $t_{\vec{\mu}}$ distribution under the signal hypothesis, $f(t_{\vec{\mu}}|\vec{\mu})$, must be known. If the profile-likelihood-ratio (PLR) test statistic is being used, then Wilks' theorem can be used to assume that $f(t_{\vec{\mu}}|\vec{\mu})$ follows a χ^2 distribution. However, since this was not the case, the only generally correct way to obtain $f(t_{\vec{\mu}}|\vec{\mu})$ is by generating pseudo-experiments according to the expected statistical and systematic covariances. There are several reasons why this method is chosen:

- The PLR test statistic requires the PoIs to be profiled every time it is evaluated. However, typically parameter grids are explored and it is not easy to interpolate predictions without a complicated morphing scheme. It is easier to perform a hypothesis test at each gridpoint, using the above method, and interpolate the results.
- The likelihood ratio is strictly the most powerful test statistic, whereas the PLR is only an approximation to this.
- In order to implement the CL_s method, one must use pseudo-experiments to evaluate the expected distribution of the test statistic when calculating the CL of the signal hypothesis, assuming the SM to be true. This is true, whether the LR or PLR is used. Since avoiding the use of pseudo-experiments is the main reason to use the PLR, this is no longer applicable.

This is a widely used procedure to establish discovery or exclusion in particle physics and is based on a frequentist significance test which use the likelihood as the test statistic. In addition to the parameters of interest such as the cross-section of the BSM signal process, both the BSM signal and the SM processes will contain general nuisance parameters whose values are not assumed but must be fitted from data.

In the likelihood ratio, $\lambda(\vec{\mu})$, it is defined such that $0 \leq \lambda \leq 1$, where λ near one implies good agreement between data and the hypothesized value of $\vec{\mu}$. The test statistic is defined as

$$t_{\vec{\mu}} = -2\ln\lambda(\vec{\mu}) \ = \ \chi^2_{\mu} - \chi^2_{SM} \tag{5.6}$$

and this means that larger values of $t_{\vec{\mu}}$ correspond to increasing incompatibility between the data and $\vec{\mu}$. To quantify the level of disagreement the p-value can be computed:

$$p_{\vec{\mu}} = \int_{t_{\vec{\mu},obs}}^{\infty} f(t_{\vec{\mu}}|\vec{\mu}) dt_{\vec{\mu}} \tag{5.7}$$

where $t_{\vec{\mu},obs}$ is the value of the statistic observed from the data and $f(t_{\vec{\mu}}|\vec{\mu})$ denotes the pdf of $t_{\vec{\mu}}$ under the assumption of a fixed signal of $\vec{\mu}$.

Suppose that the hypothesised $\vec{\mu}$, along with some combination of NP values randomly chosen from their standard normal prior distributions, is the true underlying model. In this case, the likelihood function profiled in the denominator of $\lambda(\vec{\mu})$ nests

the *true* model. However, the denominator contains a number of extra degrees of freedom as it floats $\vec{\mu}'$ for a given data-set (which is randomly sampled from the ensemble of possible data-sets). In the asymptotic limit, and under certainly regularity conditions, Wilks' theorem states that the measured $t_{\vec{\mu},obs}$ is randomly distributed according to a χ^2 distribution with number of degress of freedom equal to the number of parameters contained within $\vec{\mu}$, which are called k.

At each point in $\vec{\mu}$-space, the model is hypothesised as correct. The $t_{\vec{\mu},obs}$ is then calculated for the measured data-set. Under this hypothesis, $t_{\vec{\mu},obs}$ is expected to be randomly drawn from a χ^2 distribution, and $CL\left(\vec{\mu}\right)$ is evaluated by integrating this χ^2 distribution between $t_{\vec{\mu},obs}$ and $+\infty$:

$$CL\left(\vec{\mu}\right) \;=\; \int_{t_{\vec{\mu},obs}}^{\infty} \chi^2\left(\text{d.o.f.} = k\right) dt_{\vec{\mu}} \tag{5.8}$$

5.4. The CL_s Method

It is possible for large fluctuations around the SM to result in a data-set which is very inconsistent with the SM+BSM hypothesis, but also rather inconsistent with the SM itself, and this may not be considered as evidence against the BSM component. Furthermore, using a pure frequentist method will always exclude a "correct" hypothesis in a fraction α of cases. However, this is not desirable if the data-set did not contain much expected sensitivity to the BSM model. These problems can be mitigated by using the CL_s method. Whereas CL was defined by testing the signal hypothesis against the SM, assuming the signal hypothesis is true, CL_b is defined by using *the same LR* to test the signal hypothesis, assuming the SM is true. The *modified frequentist confidence level* is then defined as:

$$CL_s\left(\vec{\mu}\right) = \frac{CL\left(\vec{\mu}\right)}{CL_b} \tag{5.9}$$

Limits are set by excluding regions for which $CL_s < \alpha$. This can only occur when the signal and SM hypotheses were actually separable using the data. Since $CL_b \leq 1$, this means that $CL_s \;\geq\; CL \;\forall\; \vec{\mu}$ by construction. Setting limits using the CL_s method therefore overcovers, and sets more conservative limits. This is the method used to set exclusion limits for this analysis.

5.5. SM Modelling Goodness-of-Fit Tests

In this section, the goodness-of-fit is investigated between the data and the SM hypothesis given the theoretical uncertainties, considering also the statistical and systematic uncertainties on the unfolded measurements. This step is important, because it demonstrates whether or not the systematic uncertainties are well-understood or if there is a potential deviation from the SM (e.g., by investigating the MC/Data agreement in the auxiliary regions, where one expects the signal to be in the $p_{\mathrm{T}}^{\mathrm{miss}}$+jets region or potentially seeing a signal in one of the auxiliary regions). Only then can one use the data to constrain new physics contributions. We will perform a fit of the likelihood function (see Equation 5.1) to the data, this means estimating the values of the parameters of a model which maximises the probability of the observed data, given the assumptions of the model (i.e., extra information about the parameters which describe the underlying physics process by comparing the model predictions to the observed data). This process is commonly known as the maximum likelihood fit.

In this section, the $p_{\mathrm{T}}^{\mathrm{miss}}$ distribution is studied in the ≥ 1 jet phase-space for all the regions ($p_{\mathrm{T}}^{\mathrm{miss}}$+jets + auxiliary regions), as well as just the two lepton regions ($p_{\mathrm{T}}^{\mathrm{miss}}$+jets + 2ℓ+jets), because this is important when it comes to finding or constraining DM models. It is important to note that other phase-spaces are not included in the likelihood fit as the statistical correlations (calculated via the bootstrap method [196]) across phase-spaces were not available at the time. The m_{jj} distribution is then studied in the VBF phase-space, due to the fact that the kinematics of the two high energy jets are of interest and could be produced in association with a DM particle that only interacts with gauge bosons. Finally the $\Delta\phi_{jj}$ variable is looked at in the ≥ 2 jet phase-space as it could be sensitive to DM models as shown in [201]. The correlation matrices for these distributions are shown and discussed in Appendix D.

Figure 5.1 (top) shows the comparison between the data and the SM prediction for the pre-fit particle-level differential cross-section as a function of $p_{\mathrm{T}}^{\mathrm{miss}}$ in all the regions ($p_{\mathrm{T}}^{\mathrm{miss}}$+jets region and the auxiliary regions) of the ≥ 1 jet phase-space. The differences between data and the SM prediction can be seen quite clearly by eye, and the overall agreement is inadequate as shown by a huge χ^2/NDF. Although the data/MC differences appear by eye to be covered by the uncertainty, the χ^2/NDF sum accounts for the systematic uncertainties being strongly correlated between bins. This in turn reduces the level of agreement that is seen with χ^2/NDF and the p-value. Figure 5.1 (bottom) shows the post-fit distribution after performing a maximum

likelihood fit using Equation 5.1. In this instance, no signal model is assumed, i.e., a SM fit is done where the NPs are the best-fit parameters. The post-fit agreement is much better between the SM and data than for the pre-fit as is seen with $\chi^2/NDF \sim 3.4$. No NPs are pulled significantly. In the post-fit figure, we see that in the $p_{\mathrm{T}}^{\mathrm{miss}}$+jets region that the data point in the tenth bin is in excess of the SM prediction and it is not within the uncertainty. This is what causes the relatively large χ^2/NDF value.

The post-fit NP values are shown in Figure 5.2 (in this case, only NPs which have an amplitude > 2 % anywhere in the spectrum are plotted). Some of the NPs which represent the QCD scale uncertainties and their shapes are constrained by construction, i.e., these uncertainties are fully correlated between boson channels and regions of phase-space. This allows the data from the auxiliary regions to constrain the data in the $p_{\mathrm{T}}^{\mathrm{miss}}$ region. This follows the approach of an aggressive correlation model developed and validated using state of the art calculations done at NNLO QCD and NLO EW [177]. Additional NPs for the QCD scale uncertainties are introduced to allow for moderate shape variations within the band but also to provide an uncorrelated uncertainty component for the channels, based on the differences between the higher-order K-factors.

Specific to Figure 5.2, we see that the SM_syst_TH_STACK_VJETS_d1K_NLO and SM_syst_TH_STACK_VJETS_d2K_NLO are very well constrained within the one σ yellow band. SM_syst_TH_STACK_VJETS_d1K_NLO (d1K is the usual 7-point envelope of the scale variations for V+jets, taken to be fully correlated between the boson channels). These constant scale variations mainly affect the overall normalisation of the boson p_{T} distributions (a proxy for $p_{\mathrm{T}}^{\mathrm{miss}}$) and tend to underestimate the shape uncertainties, which play an important role in the extrapolation of low p_{T} measurements to high p_{T}. Thus a reasonably conservative estimate of the shape uncertainties is introduced, SM_syst_TH_STACK_VJETS_d2K_NLO, where the standard scale uncertainty, SM_syst_TH_STACK_VJETS_d1K_NLO, is multiplied by a shape distortion factor, see more on this [177]. These NP are very well constrained due to the fact that the V+jets are the main processes that contribute to these regions ($p_{\mathrm{T}}^{\mathrm{miss}}$+jets, 1ℓ+jets and 2ℓ+jets) and the fact that they are fully correlated across the boson channels. The SM_syst_TH_STACK_VJETS_d1K_NLO is able to account for the normalisation differences across the regions, whereas the SM_syst_TH_STACK_VJETS_d2K_NLO is able to account for any potential shape differences across the regions. It is also noticeable the large maximum impact postfit (8.4%) of the fake one electron systematic uncertainty, which has a NP value near zero but is quite well constrained (within one

σ). This means that the variation of this parameter within its allowed range has a significant effect on the final fit and it is related to the fact that the overall SM pre-fit prediction in the one electron region is considerably pulled as can be seen in Figure 5.1 (bottom). Since the fake one electron systematic is specific to that region, it being pulled up or down can cause a big impact on that region and effect all the other NPs in that region. These other NPs are however heavily correlated across the different regions and therefore any pull on the fake one electron systematic uncertainty will therefore have a significant impact across all the regions.

The pre- and post-fit R^{miss} for the $p_{\text{T}}^{\text{miss}}$ region in the ≥ 1 jet phase-space for all regions is shown in Figure 5.3, along with its respective NP ranking in Figure 5.4. As mentioned in section 4.9.3, the definition of R^{miss} means that effects due to modelling, jet energy scales and resolution, common to all regions, are expected to cancel. In a similar manner, a lot of the theory and jet-related uncertainties mostly cancel in the ratio. This can be seen with a χ^2/NDF value of ~ 1.95 in Figure 5.3 (bottom), which is already much improved with respect to the differential cross-section measurement post-fit seen in Figure 5.3, with no significant pulls or constraints. Also notice that in Figure 5.3, the jet-related uncertainties do indeed drop out in comparison to Figure 5.1. It is also noticeable in Figure 5.3 post-fit plot that the one lepton regions SM prediction is being pulled upwards. This could suggest mismodelling in the one lepton region, in which the dominant process is the W boson leptonic decay, or mismodelling in the $p_{\text{T}}^{\text{miss}}$+jets and two lepton region, in which the dominant processes are the $Z \to \ell\ell$ and $Z \to \nu\nu$ decays respectively.

In this case, it could be of interest to study the $p_{\text{T}}^{\text{miss}}$ observable in the ≥ 1 jet phase-space for the $p_{\text{T}}^{\text{miss}}$+jets region along with the two lepton auxiliary regions. Figure 5.5 (top) shows the comparison between the data and the SM prediction for the pre-fit particle-level differential cross-section as a function of $p_{\text{T}}^{\text{miss}}$ in the $p_{\text{T}}^{\text{miss}}$+jets region and the two lepton regions of the ≥ 1 jet phase-space. The differences between data and the SM prediction can still be seen quite clearly by eye, however the overall agreement is much better compared to the pre-fit including all regions as is shown by an improved χ^2/NDF. Figure 5.5 (bottom) shows the post-fit plot, in which the SM prediction is pulled slightly up however there are no significant shape differences. This results in a χ^2/NDF of ~ 1.73 which is significantly improved compared to the all region fit of $\chi^2/NDF \sim 3.4$. No significant pulls on the nuisance parameters can be seen in Figure 5.6, where similar conclusions can be taken out for the well constrained SM_syst_TH_STACK_VJETS_d1K_NLO and SM_syst_TH_STACK_VJETS_d2K_NLO.

The pre- and post-fit R^{miss} for the $p_{\text{T}}^{\text{miss}}$ region in the ≥ 1 jet phase-space for the $p_{\text{T}}^{\text{miss}}$ region and the two lepton regions is shown in Figure 5.7, along with its respective NP ranking in Figure 5.8. The post-fit χ^2/NDF R^{miss} value of ~ 1.75 shows a better agreement than for the equivalent differential cross-section χ^2/NDF of ~ 1.92. Figure 5.8 shows the pulls on the nuisance parameters for an amplitude of $> 1\%$, in which the jet related uncertainties have dropped out.

The pre-fit and post-fit m_{jj} distributions, along with the NP rankings for both the differential cross-section distributions and the R^{miss} are shown in Figures 5.9, 5.11, 5.10 and 5.12 for the VBF phase-space. It is also important to note the large fluctuation in the one electron region of Figure 5.9 in the fourth from last bin. For the case of the m_{jj} differential cross-section distribution, which is shown in Figure 5.9, both the pre-fit and the post-fit have poor agreement between the data and SM prediction and this is likely due to bad m_{jj} modelling. This can be seen in Figure 5.10 with the huge pulls on the $V + jj$ scale uncertainties. The SM_syst_TH_STACK_VJJ_d1K_NLO (d1K is the usual 7-point envelope of the scale variations, taken to be fully correlated between the boson channels) and SM_syst_TH_STACK_VJJ_d4K_NLO (d4K is allowing for a smooth shape variation within that scale variation band) theory systematic uncertainties are pulling 6σ in opposite directions. This is a contentious finding as the VBF $Z + jj$ process has been measured with full Run-2 data, in which the data and SM prediction agree very well [202]. Again, this is unlikely evidence for new physics in $V + jj$ but a sign of the mismodelling of the SM prediction in SHERPA. The m_{jj} R^{miss} pre-fit and post-fit in Figure 5.11 shows better data/MC agreement as expected with a post-fit $\chi^2/NDF \sim 2.1$. This does indicate that the modelling effects are cancelled out in R^{miss} as expected, and without having significant pulls or constraints on the NPs, as shown in Figure 5.12. A more robust correlation scheme for the theory NPs is required for the m_{jj} observable, which will likely resolve some of these differences. There are also missing parton shower uncertainties affecting the m_{jj} which may improve the agreement slightly. These m_{jj} distributions will not be used for the limit setting exclusion.

The pre-fit and post-fit differential cross-section and the R^{miss} distribution for the $\Delta\phi_{jj}$ observable are shown in the ≥ 2 jet phase-spaces for all regions in Figures 5.13 and 5.15 respectively. The NP ranking Figures for these distributions are shown in Figures 5.14 and 5.16.

For both the $\Delta\phi_{jj}$ cross-section and R^{miss} distribution, the post-fit agreement between the data and the SM prediction is quantified by the respective values of

$\chi^2/NDF \sim 6.5$ and $\chi^2/NDF \sim 5.7$. It is interesting to note that in the R^{miss} distributions, the last bin is higher compared to the rest of the bins for both the pre-fit and post-fit distributions. This is likely causing the apparent normalisation issues shown in Figure 5.13. Compared to the previous $p_{\text{T}}^{\text{miss}}$ and m_{jj} distributions (and their respective NPs) there are fewer systematics which play a significant role in $\Delta\phi_{jj}$ (as shown by Figures 5.14 and 5.16, in which a 0.5% threshold is imposed as opposed to $> 1\%$). In Figure 5.14, there is quite a spread in terms of the jet calibration systematic uncertainties, with some having a pull of four σ (given by names of data_syst_JET_JER_EffectiveNP_1 and data_syst_JET_JER_EffectiveNP_2 in Figure 5.14). This is unlikely due these systematic uncertainties being incorrect, but rather a consequence of SHERPA mismodelling in the dijet systems . There are no significant pulls observed for Figure 5.16 and only some minor constraints are seen.

Globally, the post-fit $p-$values calculated (shown in Figures 5.1 – 5.15) suggest that the SM prediction does not agree with the data. There is no consistent pattern across the distributions to suggest that this is due to BSM physics but it is much more likely due to mismodelling (known to be the case in the SHERPA MC for m_{jj}) , lack of an adequate correlation scheme across uncertainties (e.g., a more robust correlation scheme required across the theory NPs for m_{jj}), and some missing systematic uncertainties (e.g., missing parton shower uncertainties) which were not ready in time for this analysis along with the fact that no statistical correlations across phase-space regions were available. It is important to state, that this fit involves hundreds of NPs and is very complicated in terms of its scope and ambition. The analysis itself is still a work in progress and that these fits are still being understood and iterated upon with new inputs.

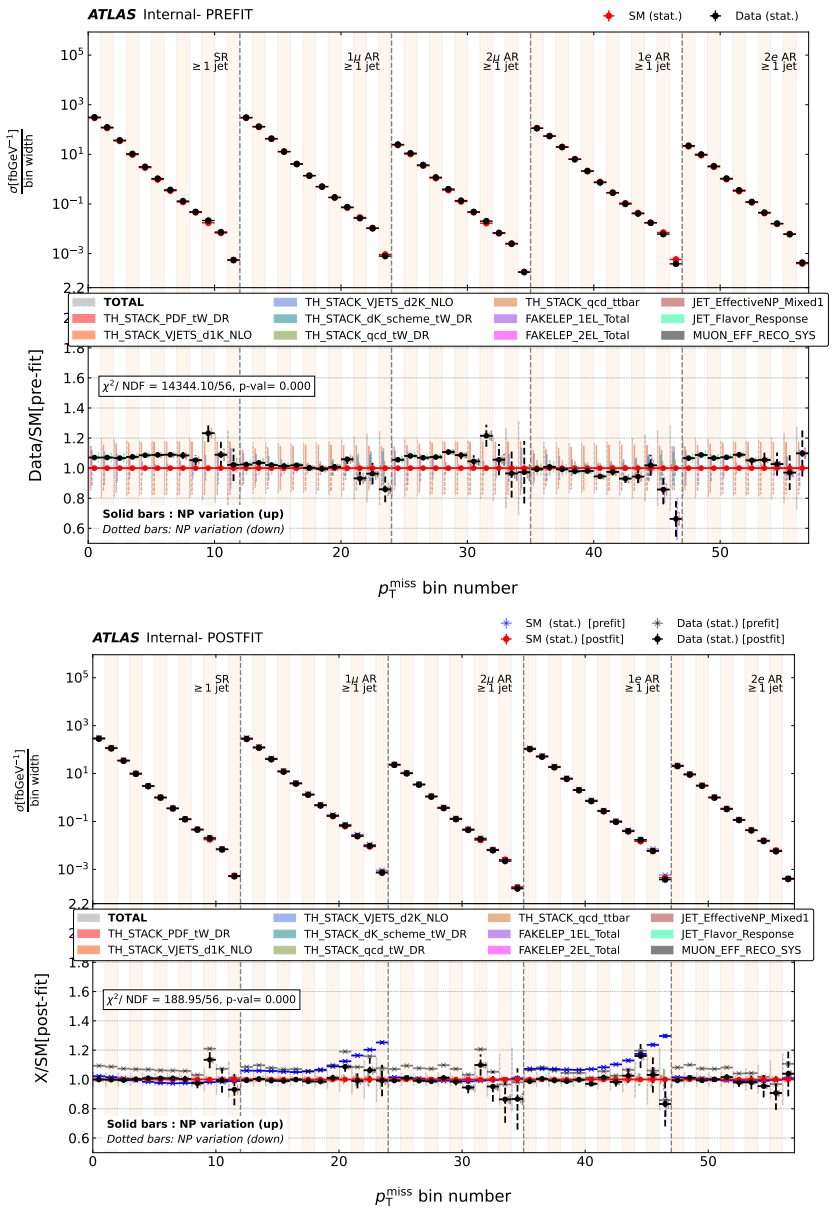

Figure 5.1.: Differential cross-section as a function of $p_{\mathrm{T}}^{\mathrm{miss}}$ for data (black) and SM prediction (red), for all regions of the ≥ 1 jet phase-space. This comparison uses 139 fb^{-1} of data. The ratio panel demonstrates the impact of different systematic uncertainty pulls. Data points show statistical uncertainties, coloured full (hollow) bars represent the impact of $+1\sigma$ (-1σ) variations on the dominant systematic uncertainties, which are labelled. Uncertainties on the measurement are shown as bars connected to the data points, whereas uncertainties on the SM are connected to the SM points. The bottom plot shows the effect of fitting all systematic NPs. The quadrature combination of all statistical and systematic uncertainties, on both the data and SM, is shown in grey.

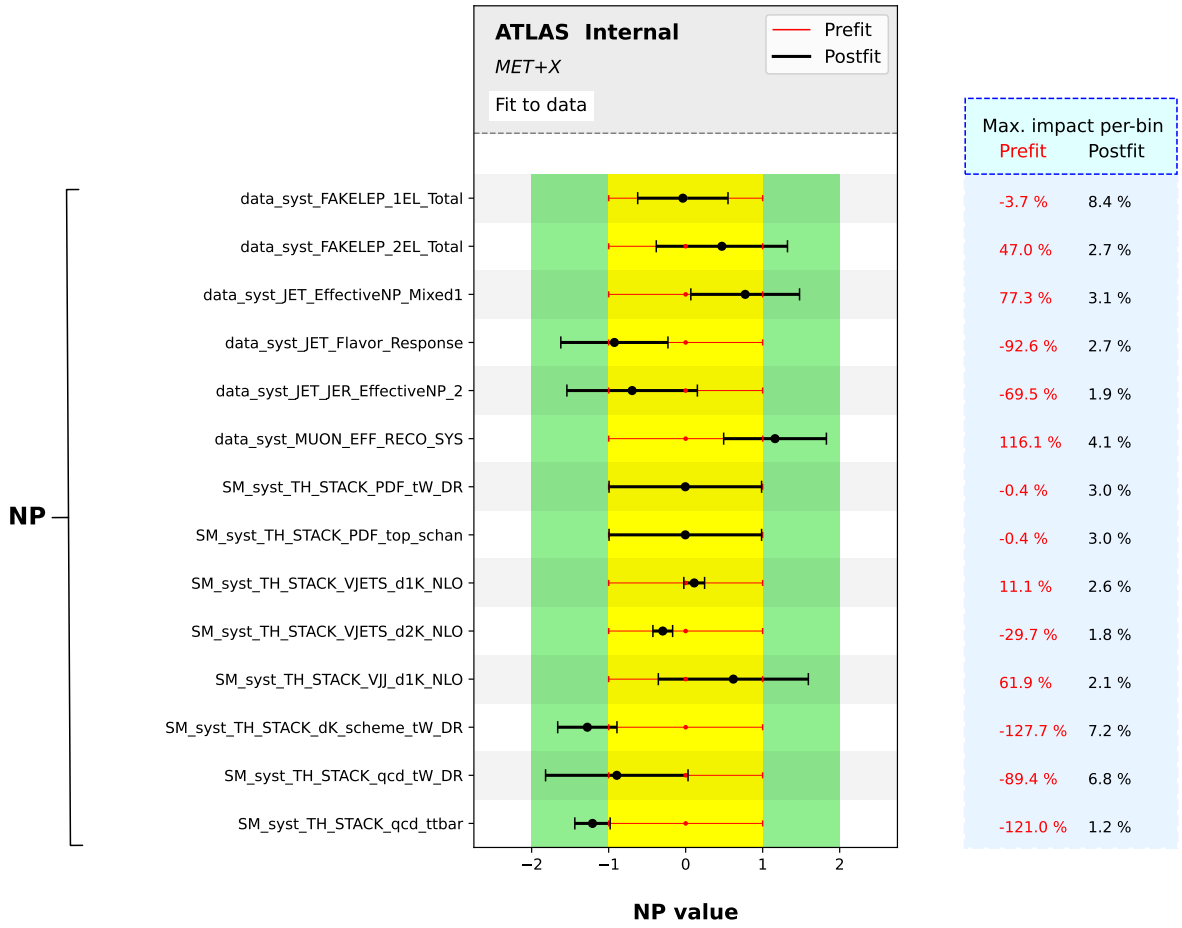

Figure 5.2.: The nuisance parameter ranking plot for the differential cross-section as a function of $p_{\mathrm{T}}^{\mathrm{miss}}$ in the $p_{\mathrm{T}}^{\mathrm{miss}}$ + jets region and auxiliary regions for the ≥ 1 jet . Only NPs with amplitude $> 2\%$ anywhere in the spectrum are plotted.

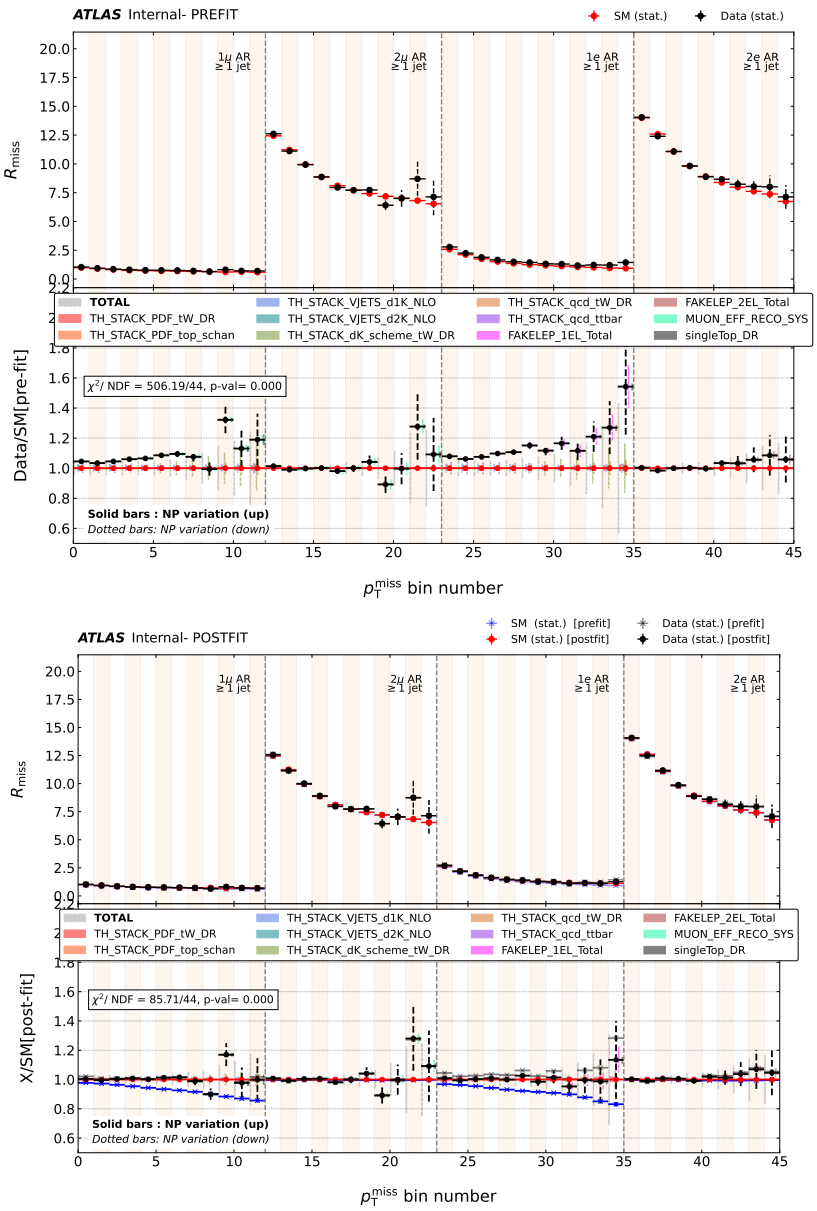

Figure 5.3.: R^{miss} as a function of $p_{\text{T}}^{\text{miss}}$ for data (black) and SM prediction (red), for all regions of the ≥ 1 jet phase-space. This comparison uses 139 fb^{-1} of data. The ratio panel demonstrates the impact of different systematic uncertainty pulls. Data points show statistical uncertainties, coloured full (hollow) bars represent the impact of $+1\sigma$ (-1σ) variations on the dominant systematic uncertainties, which are labelled. Uncertainties on the measurement are shown as bars connected to the data points, whereas uncertainties on the SM are connected to the SM points. The bottom plot shows the effect of fitting all systematic NPs. The quadrature combination of all statistical and systematic uncertainties, on both the data and SM, is shown in grey.

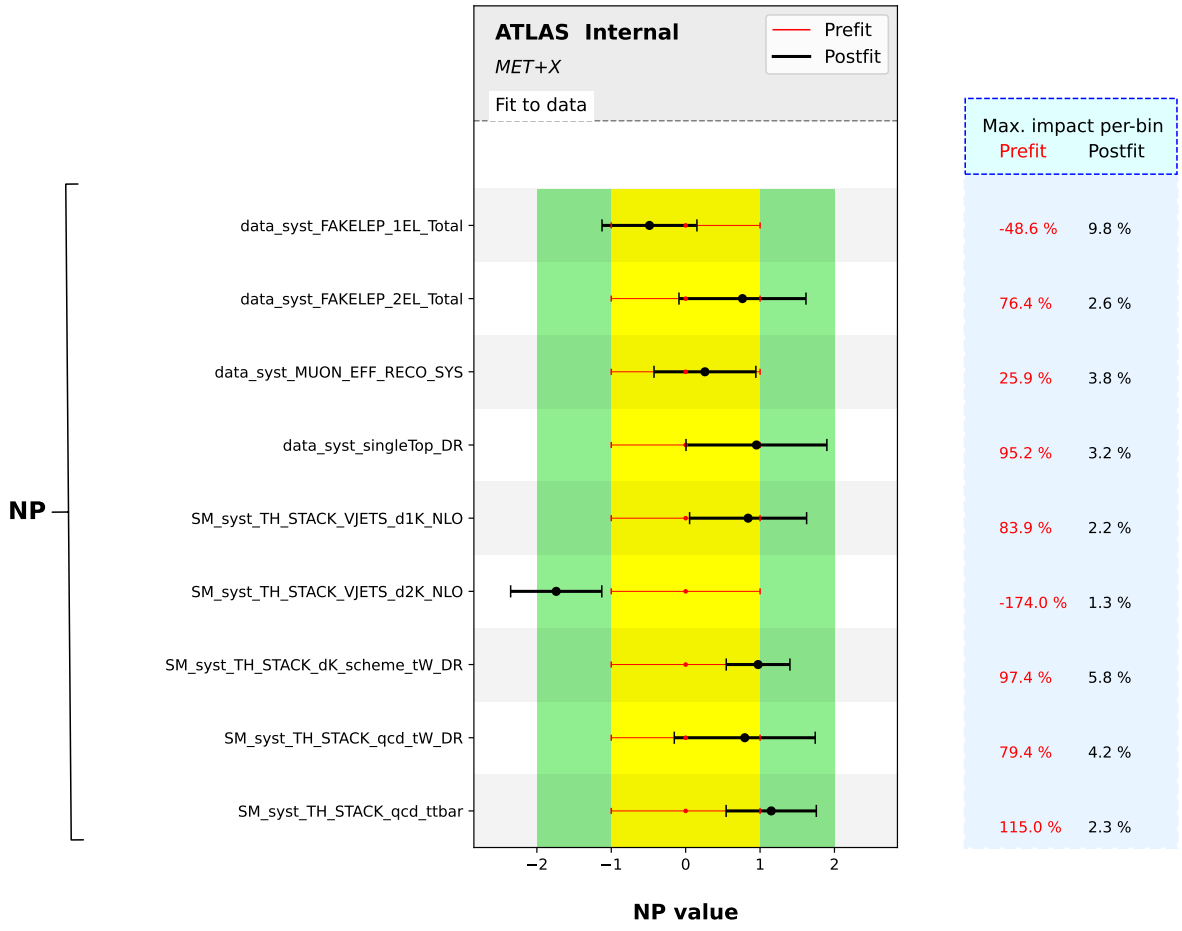

Figure 5.4.: The nuisance parameter ranking plot for the R^{miss} as a function of $p_{\text{T}}^{\text{miss}}$ in the $p_{\text{T}}^{\text{miss}}$ + jets region and auxiliary regions for the ≥ 1 jet phase-space. The yellow band represents a 1σ variation and the green band represents a 2σ variation (the same is true for the rest of the nuisane paramterer ranking plots). Only NPs with amplitude $> 2\%$ anywhere in the spectrum are plotted.

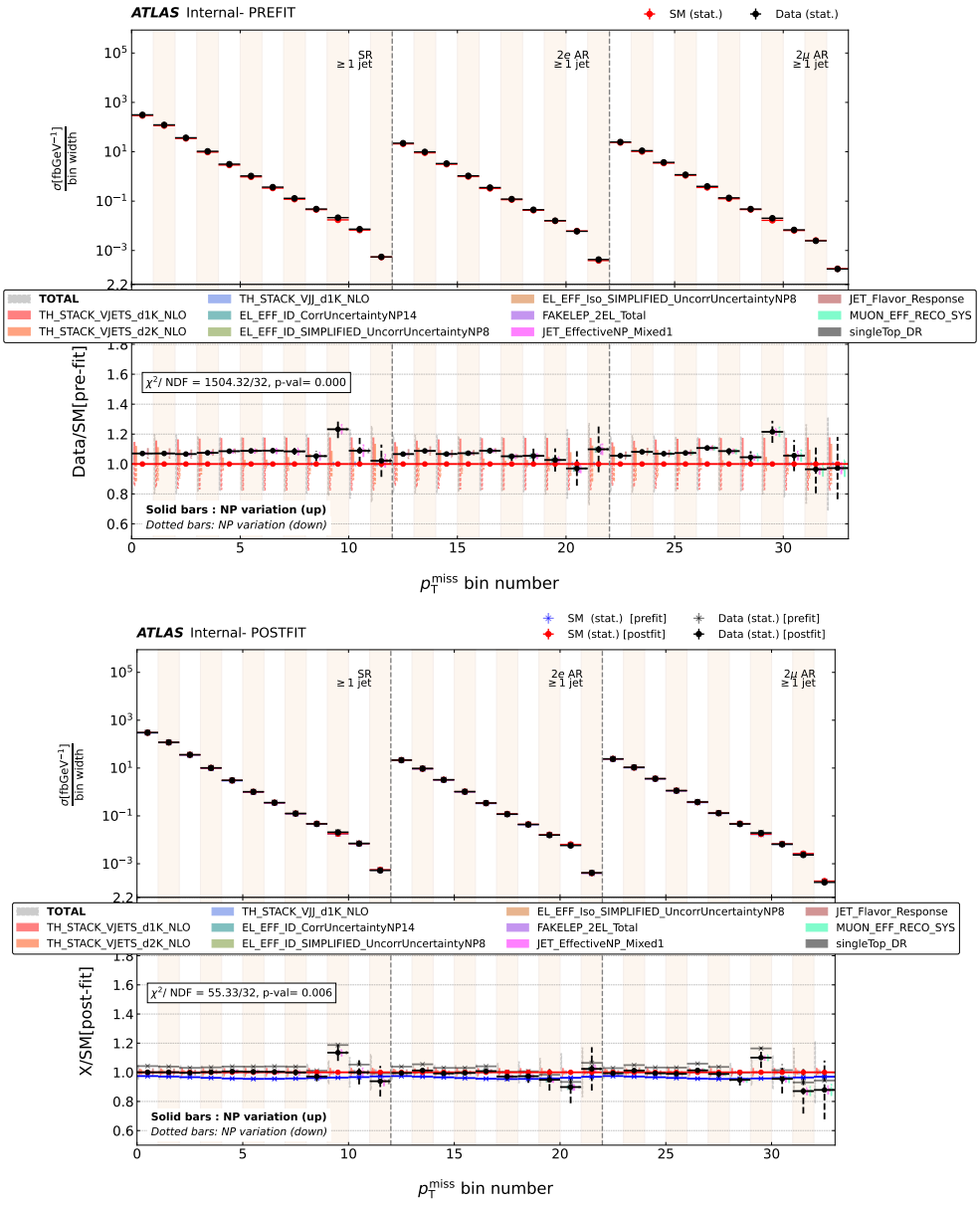

Figure 5.5.: Differential cross-section as a function of $p_{\mathrm{T}}^{\mathrm{miss}}$ for data (black) and SM prediction (red), for the $p_{\mathrm{T}}^{\mathrm{miss}}$ and 2ℓ+jets regions of the ≥ 1 jet phase-space. This comparison uses 139 fb^{-1} of data. The ratio panel demonstrates the impact of different systematic uncertainty pulls. Data points show statistical uncertainties, coloured full (hollow) bars represent the impact of $+1\sigma$ (-1σ) variations on the dominant systematic uncertainties, which are labelled. Uncertainties on the measurement are shown as bars connected to the data points, whereas uncertainties on the SM are connected to the SM points. The bottom plot shows the effect of fitting all systematic NPs. The quadrature combination of all statistical and systematic uncertainties, on both the data and SM, is shown in grey.

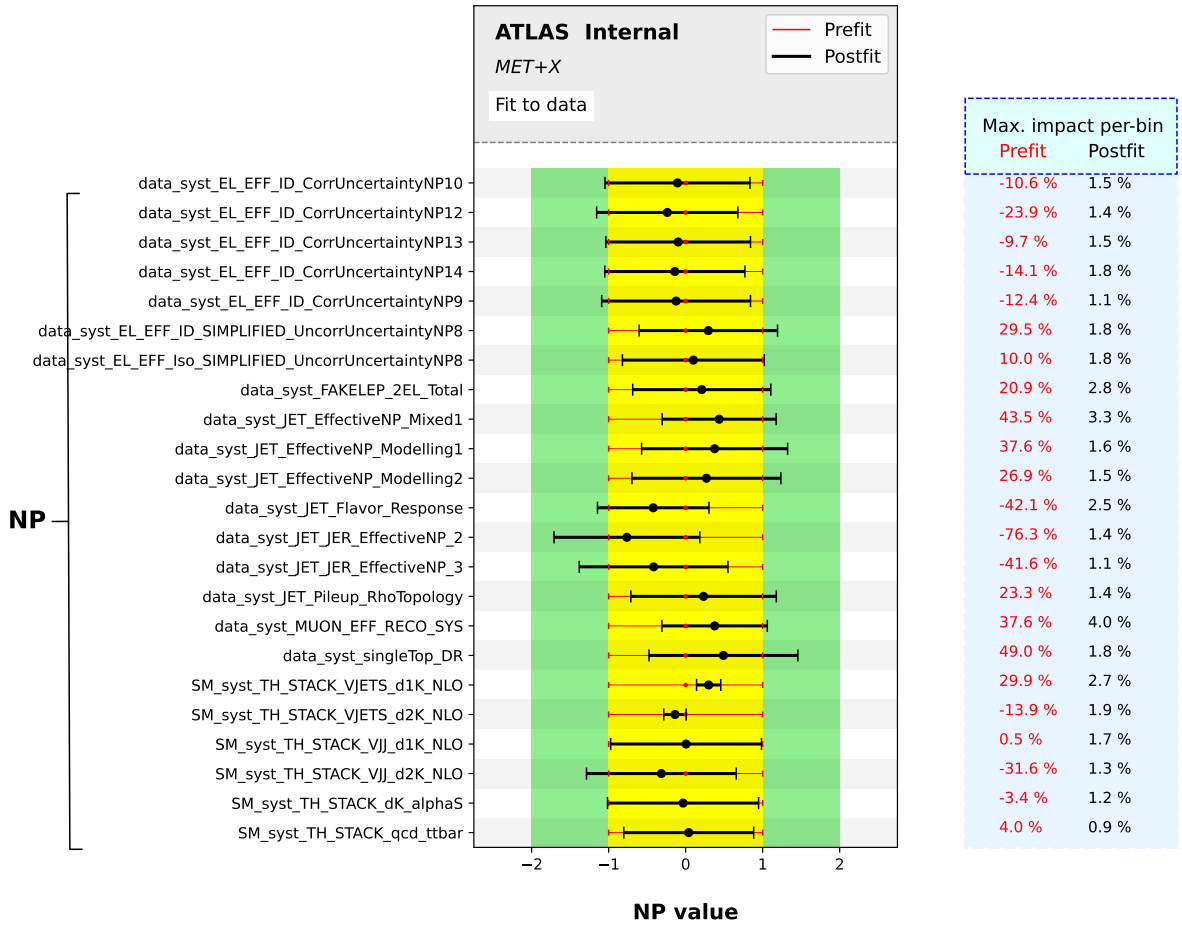

Figure 5.6.: The nuisance parameter ranking plot for the differential cross-section as a function of $p_{\mathrm{T}}^{\mathrm{miss}}$ in the $p_{\mathrm{T}}^{\mathrm{miss}}$ + jets region and two lepton auxiliary regions for the ≥ 1 jet phase-space. Only NPs with amplitude $> 2\%$ anywhere in the spectrum are plotted.

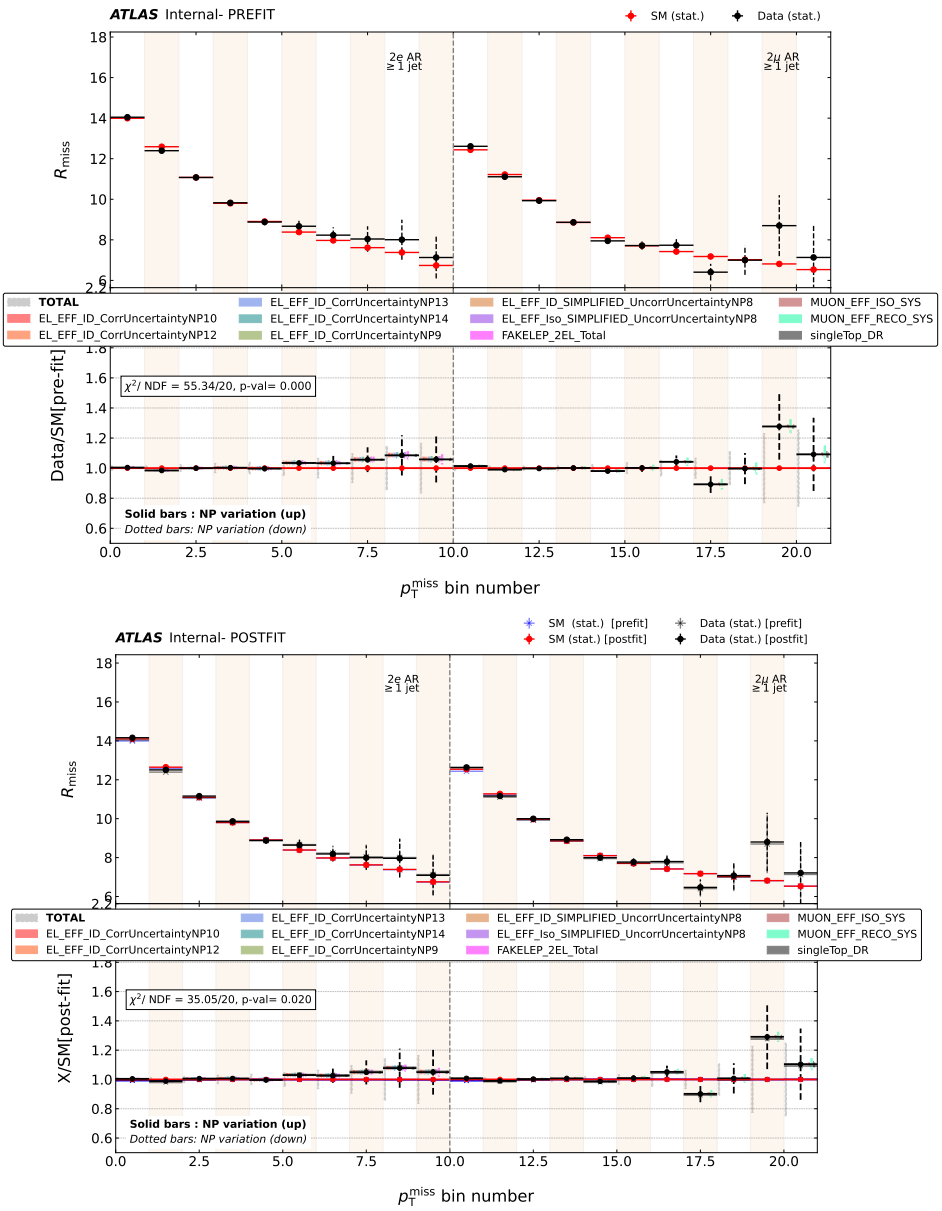

Figure 5.7.: R^{miss} as a function of $p_{\text{T}}^{\text{miss}}$ for data (black) and SM prediction (red), for the $p_{\text{T}}^{\text{miss}}$ and two lepton regions of the ≥ 1 jet phase-space. This comparison uses 139 fb^{-1} of data. The ratio panel demonstrates the impact of different systematic uncertainty pulls. Data points show statistical uncertainties, coloured full (hollow) bars represent the impact of $+1\sigma$ (-1σ) variations on the dominant systematic uncertainties, which are labelled. Uncertainties on the measurement are shown as bars connected to the data points, whereas uncertainties on the SM are connected to the SM points. The bottom plot shows the effect of fitting all systematic NPs. The quadrature combination of all statistical and systematic uncertainties, on both the data and SM, is shown in grey.

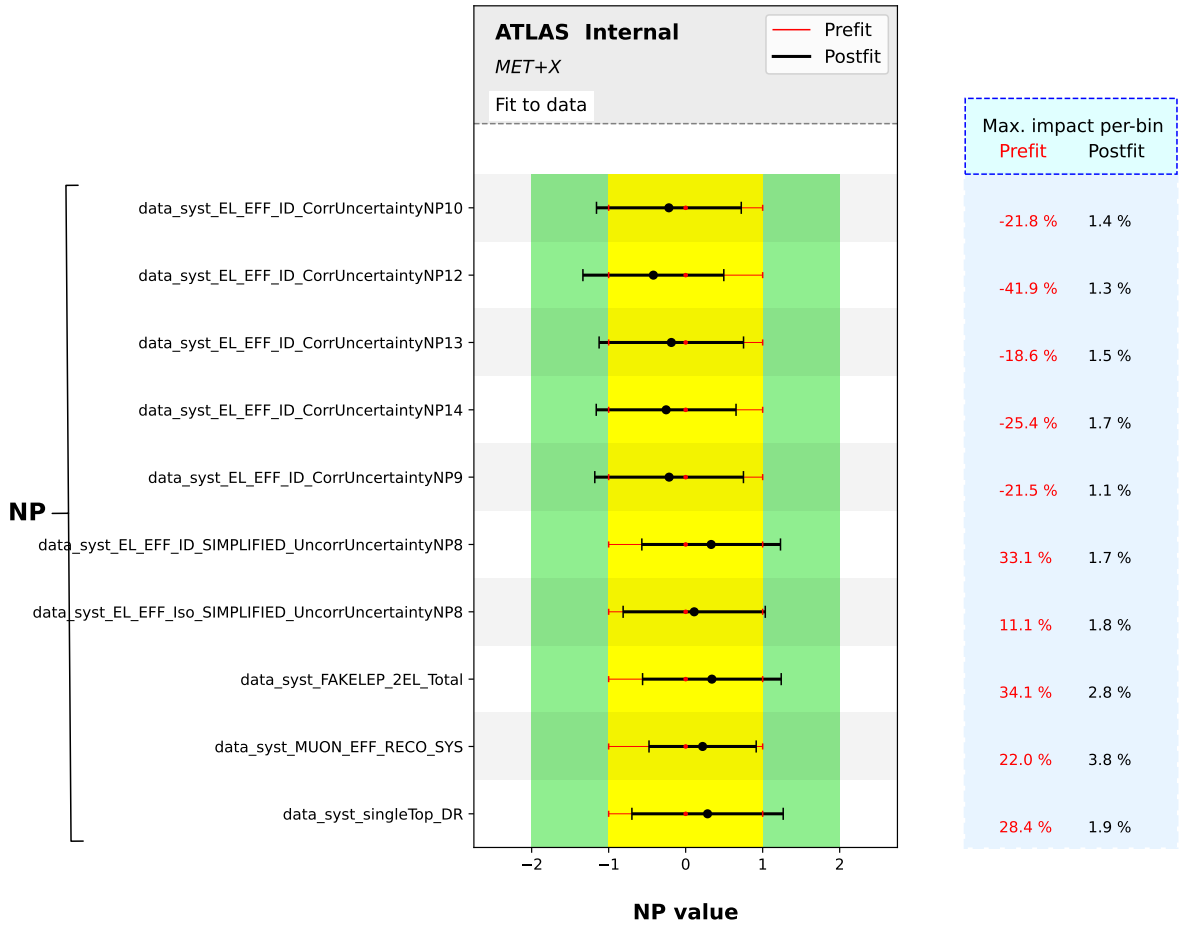

Figure 5.8.: The nuisance parameter ranking plot for the R^{miss} as a function of $p_{\text{T}}^{\text{miss}}$ in the $p_{\text{T}}^{\text{miss}}$ + jets region and the two lepton auxiliary regions for the ≥ 1 jet phase-space. Only NPs with amplitude $> 1\%$ anywhere in the spectrum are plotted.

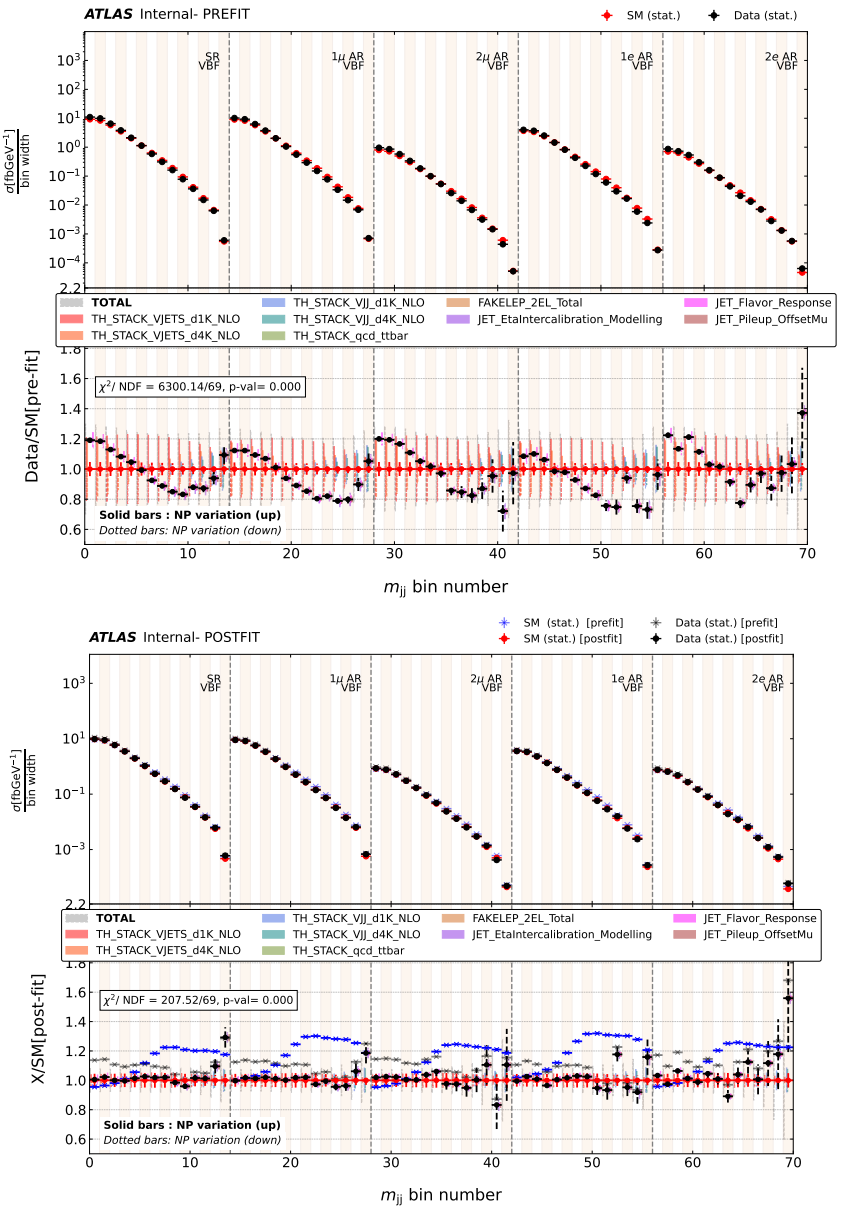

Figure 5.9.: Differential cross-section as a function of m_{jj} for data (black) and SM prediction (red), for all regions of the VBF phase-space. This comparison uses 139 fb^{-1} of data. The ratio panel demonstrates the impact of different systematic uncertainty pulls. Data points show statistical uncertainties, coloured full (hollow) bars represent the impact of $+1\sigma$ (-1σ) variations on the dominant systematic uncertainties, which are labelled. Uncertainties on the measurement are shown as bars connected to the data points, whereas uncertainties on the SM are connected to the SM points. The bottom plot shows the effect of fitting all systematic NPs. The quadrature combination of all statistical and systematic uncertainties, on both the data and SM, is shown in grey.

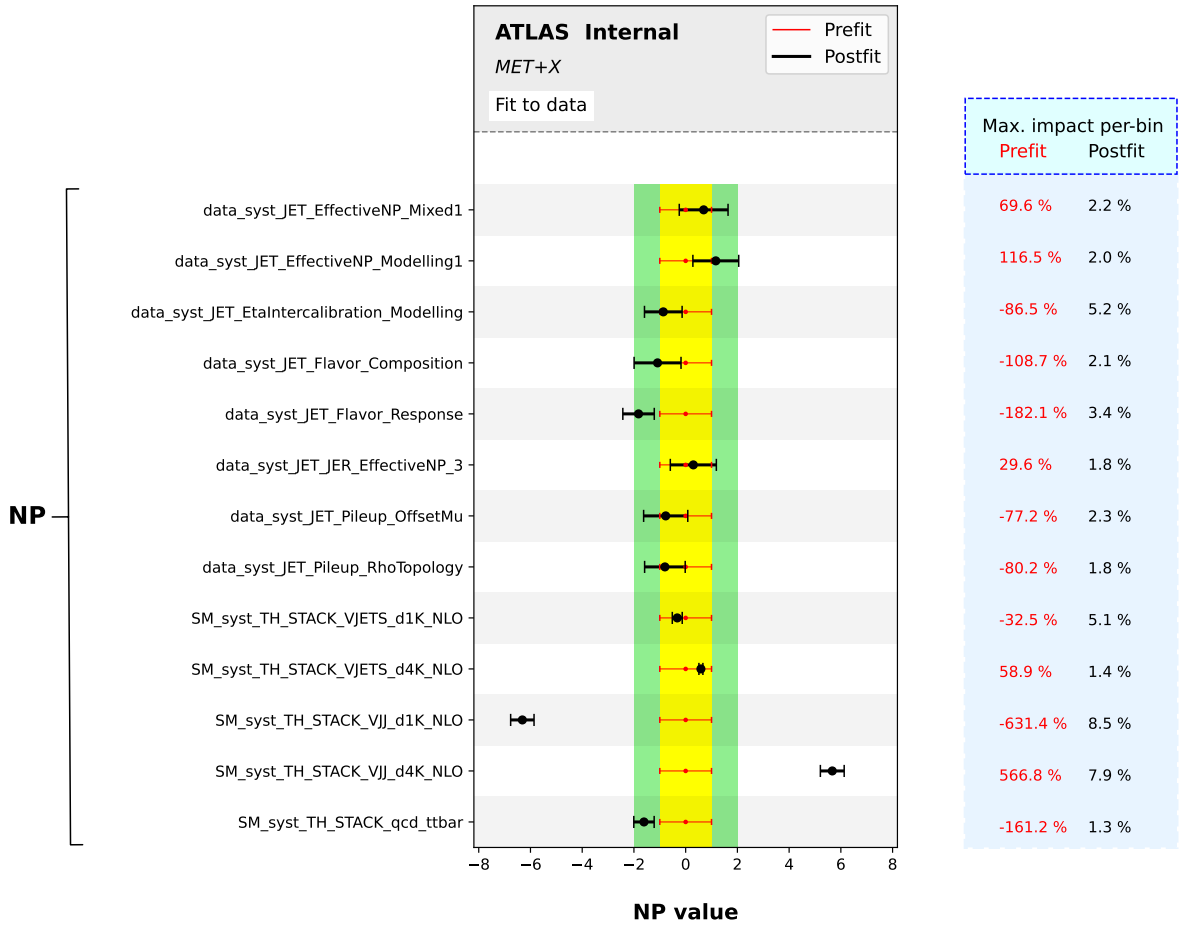

Figure 5.10.: The nuisance parameter ranking plot for the differential cross-section as a function of m_{jj} in the $p_{\mathrm{T}}^{\mathrm{miss}}$ + jets region and auxiliary regions for the VBF phase-space. Only NPs with amplitude $> 2\%$ anywhere in the spectrum are plotted.

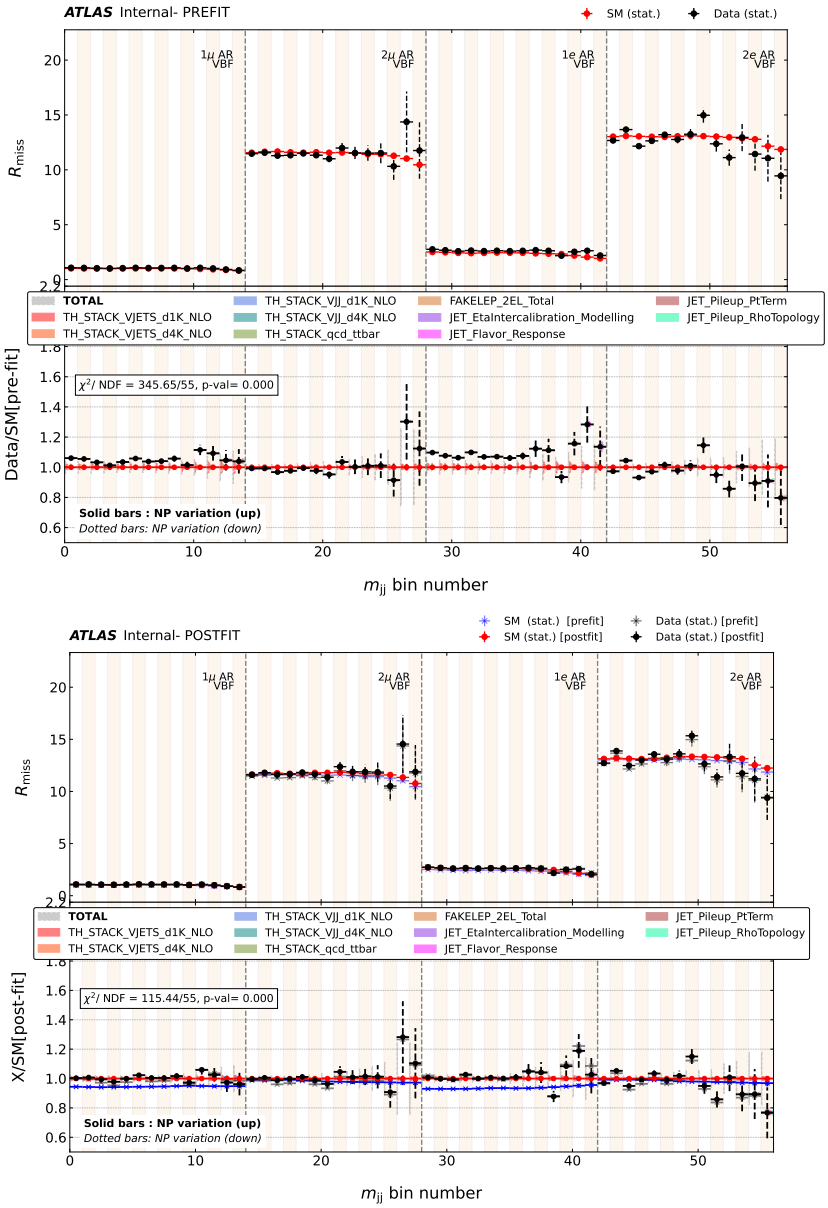

Figure 5.11.: R^{miss} as a function of m_{jj} for data (black) and SM prediction (red), for all regions of the VBF phase-spaces. This comparison uses 139 fb^{-1} of data. The ratio panel demonstrates the impact of different systematic uncertainty pulls. Data points show statistical uncertainties, coloured full (hollow) bars represent the impact of $+1\sigma$ (-1σ) variations on the dominant systematic uncertainties, which are labelled. Uncertainties on the measurement are shown as bars connected to the data points, whereas uncertainties on the SM are connected to the SM points. The bottom plot shows the effect of fitting all systematic NPs. The quadrature combination of all statistical and systematic uncertainties, on both the data and SM, is shown in grey.

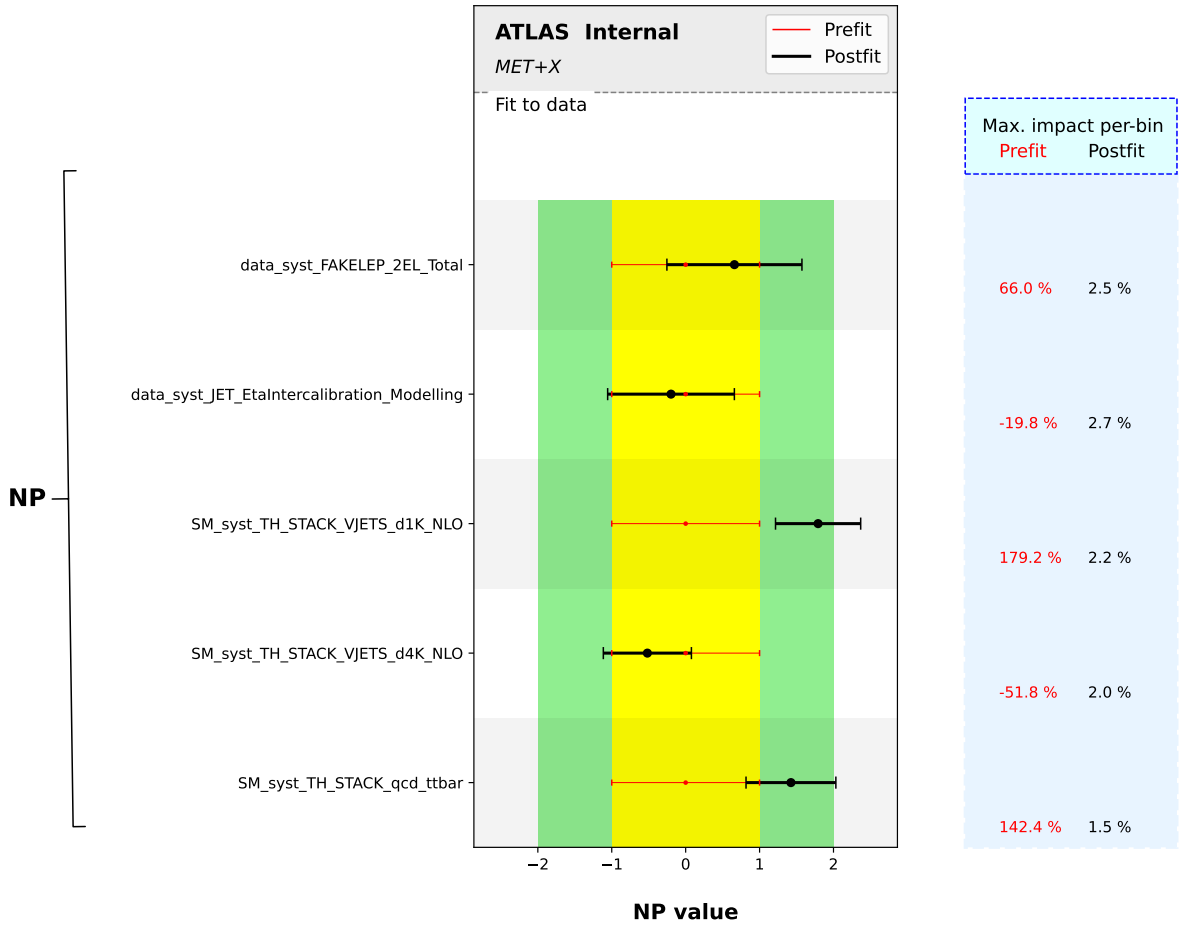

Figure 5.12.: The nuisance parameter ranking plot for the R^{miss} as a function of m_{jj} in the $p_{\text{T}}^{\text{miss}}$ + jets region and auxiliary regions for the VBF phase-space. Only NPs with amplitude $> 2\%$ anywhere in the spectrum are plotted.

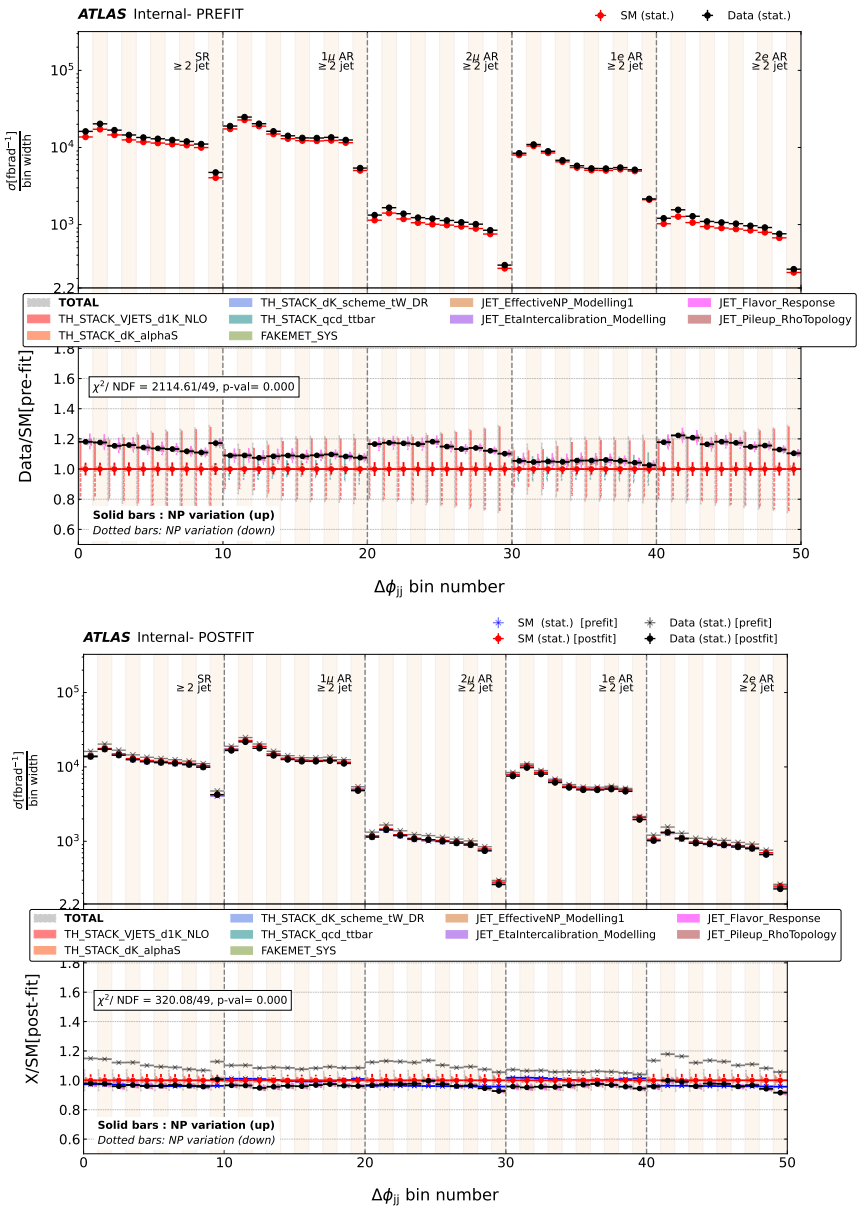

Figure 5.13.: Differential cross-section as a function of $\Delta\phi_{jj}$ for data (black) and SM prediction (red), for all regions of the ≥ 2 jet phase-space. This comparison uses 139 fb^{-1} of data. The ratio panel demonstrates the impact of different systematic uncertainty pulls. Data points show statistical uncertainties, coloured full (hollow) bars represent the impact of $+1\sigma$ (-1σ) variations on the dominant systematic uncertainties, which are labelled. Uncertainties on the measurement are shown as bars connected to the data points, whereas uncertainties on the SM are connected to the SM points. The bottom plot shows the effect of fitting all systematic NPs. The quadrature combination of all statistical and systematic uncertainties, on both the data and SM, is shown in grey.

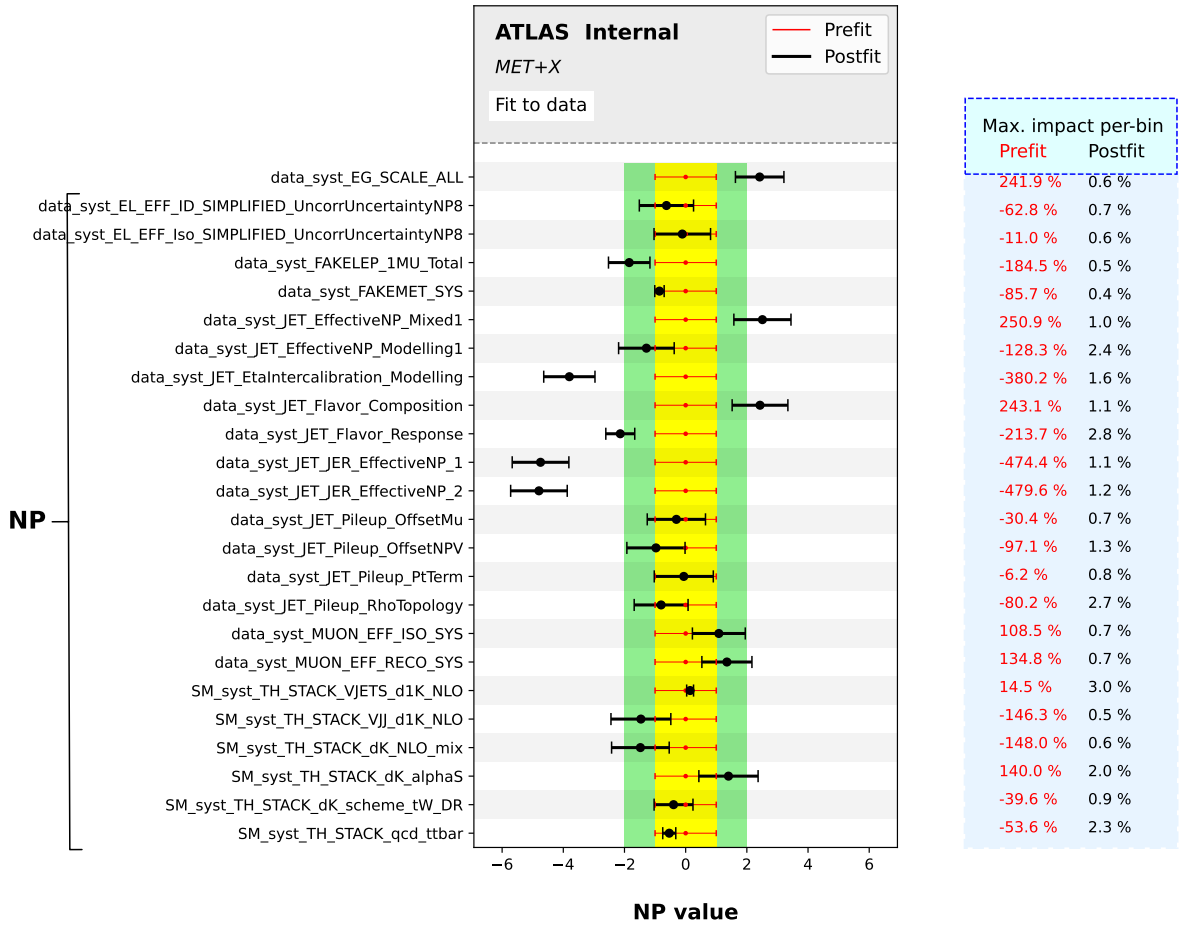

Figure 5.14.: The nuisance parameter ranking plot for the differential cross-section as a function of $\Delta\phi_{jj}$ in the $p_{\mathrm{T}}^{\mathrm{miss}}$ + jets region and auxiliary regions for the ≥ 2 jet phase-space. Only NPs with amplitude $> 0.5\%$ anywhere in the spectrum are plotted.

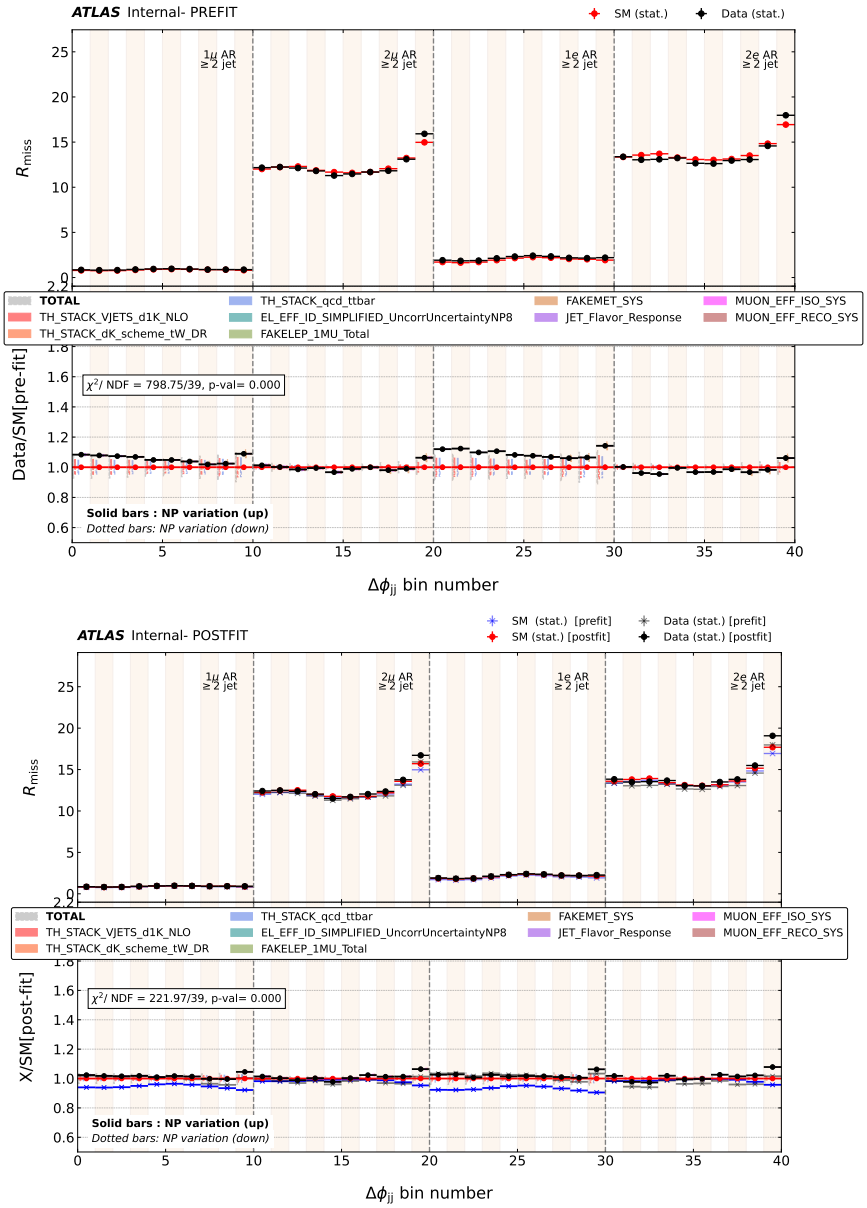

Figure 5.15.: R^{miss} as a function of $\Delta\phi_{jj}$ for data (black) and SM prediction (red), for all regions of the ≥ 2 jet phase spac. This comparison uses 139 fb^{-1} of data. The ratio panel demonstrates the impact of different systematic uncertainty pulls. Data points show statistical uncertainties, coloured full (hollow) bars represent the impact of $+1\sigma$ (-1σ) variations on the dominant systematic uncertainties, which are labelled. Uncertainties on the measurement are shown as bars connected to the data points, whereas uncertainties on the SM are connected to the SM points. The bottom plot shows the effect of fitting all systematic NPs. The quadrature combination of all statistical and systematic uncertainties, on both the data and SM, is shown in grey.

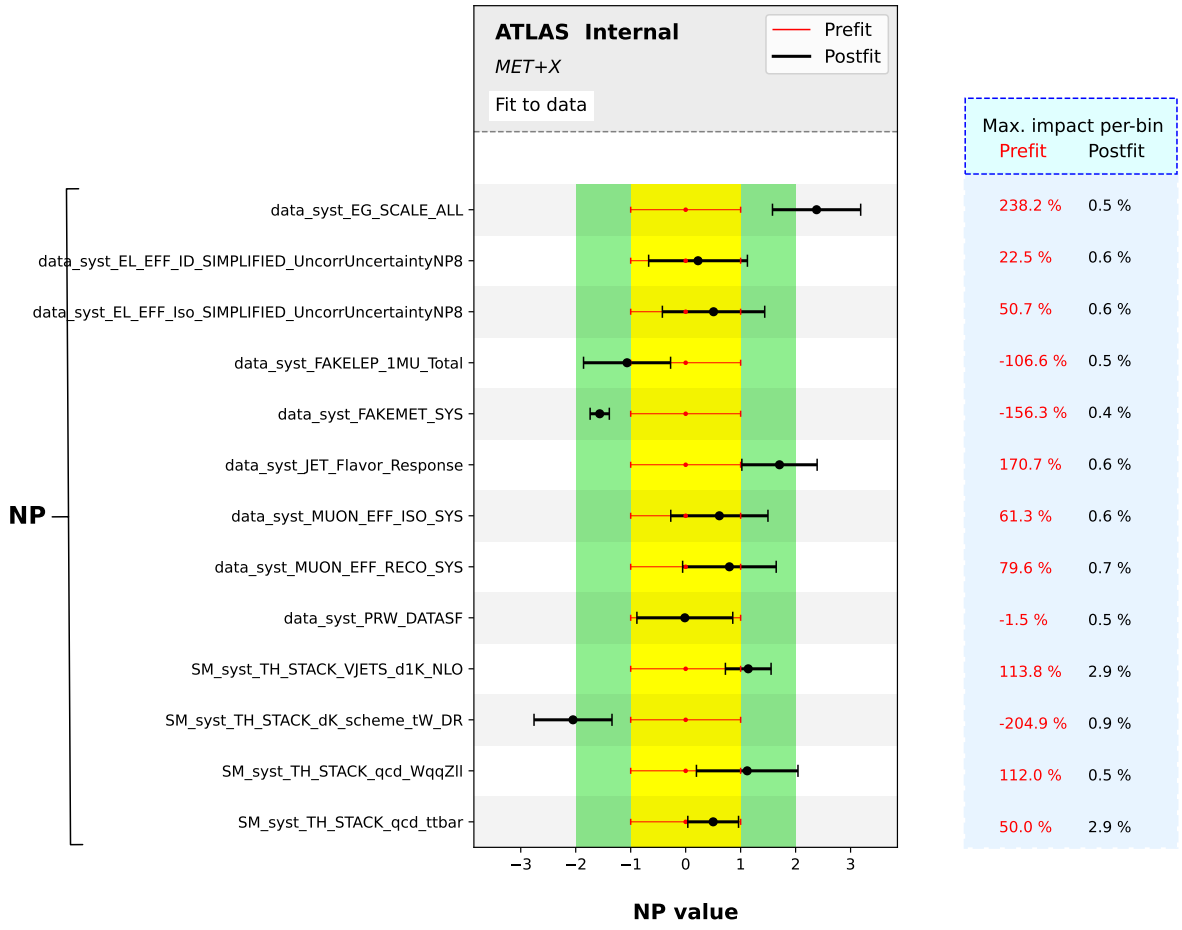

Figure 5.16.: The nuisance parameter ranking plot for the R^{miss} as a function of $\Delta\phi_{jj}$ in the $p_{\text{T}}^{\text{miss}}$ + jets region and auxiliary regions for the ≥ 2 jet phase-space. Only NPs with amplitude $> 0.5\%$ anywhere in the spectrum are plotted.

5.6. BSM Results

We will be excluding different BSM models using the CL_s method. For the CL_s method, one first calculates the likelihood function (see Equation 5.1) for both the SM hypothesis and the BSM + SM hypothesis as a function of the parameter of interest (e.g., m_{DM} and m_{Mediator}). The likelihood ratio test statistic is then calculated using Equation 5.3.

The distribution of the test statistic, t_μ, is obtained under the null hypothesis by generating many pseudo-experiments (i.e., throwing toys) with the same statistical and systematic uncertainties as the real data but with no signal contribution. This distribution is then used to compute the p-value as defined in Equation 5.7. The exact same procedure can be done for the alternate hypothesis, where there is now a signal contribution and we compute the p-value for the desired BSM model.

To set exclusion limits with the CL_s method, the ratio of these p-values can then be calculated which is equivalent to what is shown in Equation 5.9. The exclusion limit is then set at the parameter of interest (e.g., m_{DM}, m_{mediator}) value and this is repeated for the grid of values for the particular model (we generated 20,000 pseudo experiments per grid point to derive the t_μ distributions). Interpolation is then performed on the grid of PoI and the subsequent limits can be shown.

5.6.1. Dark Matter + Axial-Vector Mediator

It is possible to extend the SM with an additional U(1) gauge symmetry, in which a DM candidate has charges only under this gauge group. It is also assumed that some of these SM particles are also charged under this gauge group, and therefore are able to interact with the DM particle via a gauge boson mediator particle. In this analysis, a DM particle, χ, of mass m_χ is a Dirac fermion and the production proceeds with the exchange of a spin-1 mediator, Z_A, with axial-vector couplings in the s-channel. The minimal set of parameters under consideration for this model are g_q, g_χ, m_χ, m_{Z_A} along with the spin structure of the couplings. The quark coupling g_q should be universal in all cases and the decay width of the mediator should be set to the minimal width, meaning that it is assumed that the mediator has no couplings other than g_q and g_χ. The choice of $g_q = 0.25$ and $g_\chi = 1$ ensures that the mediator has $\Gamma_{\text{min}}/m_{\text{mediator}} \lesssim 0.06$ and that theory is far from the strong coupling regime.The usual choice of $g_q = g_\chi = 1$ used in literature [61] leads to $\Gamma_{\text{min}}/m_{\text{mediator}} \sim 0.5$, questioning

the applicability of the narrow width approximation.[4] The choice of $g_q = 1$ for spin-1 mediators is further motivated by the need to avoid the di-jet constraints from the LHC and earlier hadron colliders [203]. A choice of $g_q = 0.25$ and $g_\chi = 1$ is also reasonable because the kinematic distributions are resistant to changes in the coupling and this enables us to reduce the amount of parameter space that needs to be scanned for the coupling parameters [52].

Figure 5.17 (a) shows the expected and observed 95% CL exclusion contours in the $m_\chi - m_{Z_A}$ plane using the $p_{\mathrm{T}}^{\mathrm{miss}}$ distribution in the $p_{\mathrm{T}}^{\mathrm{miss}}$+jets and 2ℓ+jets regions in the ≥ 1 jet phase-space. In the region $m_{Z_A} > 2m_\chi$, mediator masses up to about 2.13 TeV for a DM mass of $m_\chi = 1$ GeV are excluded for a luminosity of 139 fb^{-1} in the expected limit. For the observed limit, mediator masses up to about 1.86 TeV for a DM mass of $m_\chi = 1$ GeV are excluded for a luminosity of 139 fb^{-1}.

Figure 5.17 (b) shows the expected and observed 95% CL exclusion contours using the $p_{\mathrm{T}}^{\mathrm{miss}}$ distribution in the $p_{\mathrm{T}}^{\mathrm{miss}}$+jets, 1ℓ+jets and 2ℓ+jets regions in the ≥ 1 jet phase-space. In the region $m_{Z_A} > 2m_\chi$, mediator masses up to about 2.20 TeV for a DM mass of $m_\chi = 1$ GeV are excluded for a luminosity of 139 fb^{-1} in the expected limit. For the observed limit, mediator masses up to about 1.55 TeV for a DM mass of $m_\chi = 1$ GeV are excluded for a luminosity of 139 fb^{-1}.

Figure 5.17 (a) and (b) shows a significant discrepancy between the expected and observed 95% CL exclusion contour. In Figure 5.17 (a), there is a discrepancy of $|\Delta m_{Z_A}| = 270$ GeV (this is still within the yellow 2 σ expected band) between the expected and observed for a DM mass of $m_\chi = 1$ GeV. In Figure 5.17 (b), there is a discrepancy of $|\Delta m_{Z_A}| = 650$ GeV (this is outside the yellow 2 σ expected band) between the expected and observed for a DM mass of $m_\chi = 1$ GeV. For this reason, a closer study of the axial-vector DM model is of interest and this is done by looking at the individual models for a DM mass of $m_\chi = 1$ GeV for mediator masses of $m_{Z_A} = 1750$ GeV, 2000 GeV and 2125 GeV. Figure 5.18 (a) shows the differential cross-section as a function of $p_{\mathrm{T}}^{\mathrm{miss}}$ for the $p_{\mathrm{T}}^{\mathrm{miss}}$+jets region and the 2ℓ+jets regions for the ≥ 1 jet phase-space with the axial-vector DM mediator models contributions. These contributions appear in the $p_{\mathrm{T}}^{\mathrm{miss}}$+jets region and mainly in the tail of the $p_{\mathrm{T}}^{\mathrm{miss}}$ distribution. As the mediator mass, m_{Z_A}, increases, the contribution gets smaller in

[4] The narrow width approximation is a simplification that can be made in particle physics calculations when a particle has a very narrow decay width compared to its mass. In this approximation, the propagator of the particle is replaced by a delta function, which effectively integrates out the energy dependence of the propagator. This simplification allows for much faster calculations and can be useful when considering the production and decay of resonant particles.

the tail. The ratio to SM shows that the data has some fluctuations near the tail of $p_{\mathrm{T}}^{\mathrm{miss}}$ as opposed to the Asimov case in Figure 5.19 (a). Figures 5.18 (b) and 5.19 (b) shows the observed exclusion limit. The reason for this discrepancy is that the contribution of the DM mediator model in the tails of the contribution mimics the fluctuation in data that is seen in the $p_{\mathrm{T}}^{\mathrm{miss}}$ tails and hence the observed constraints are weaker than the expected.

It is interesting to note that the observed limit is worse for Figure 5.17 (b) compared to Figure 5.17 (a) yet the opposite is true for the expected limit. The test statistic used quantifies which model (SM or BSM) agrees better with data. In the fit for the $p_{\mathrm{T}}^{\mathrm{miss}}$+jets and 2ℓ+jets, a combination of the systematic uncertainties is able to fit the SM to the data without any significant pulls as shown in Figure 5.6. When including all the regions as is done in Figure 5.17 (b), nearly all the systematic uncertainties have an influence on the four auxiliary regions.[5] In this case, the axial-vector DM contribution in the $p_{\mathrm{T}}^{\mathrm{miss}}$+jets region does help significantly in explaining the SM-Data discrepancy seen in Figure 5.1. The fact that the SM uncertainties are constrained as more auxiliary measurements are added is expected and indeed this results in a stronger expected limit. However with this, the observed limit gets weaker and these two results could be an indication that a signal process is present or that the uncertainties on the SM prediction are underestimated.

In Figure 5.17 (c) the exclusion contour from the 139 fb^{-1} reconstructed monojet search is shown [64] and the expected limits from this analysis are shown to be competitive. It is important to note that in [64], they use both the one lepton and two lepton regions to constrain their $p_{\mathrm{T}}^{\mathrm{miss}}$+jets region. Indeed, the interpretation of the measurement discussed in this note often gives similar constraints, and sometimes mildly better ones, compared to the dedicated search. The analysis strategies of this unfolded measurement and the reconstructed-level search are indeed comparable, with similar kinematic selections for the signal region, and a series of control regions which play a similar role to the auxiliary regions from this analysis in constraining backgrounds and uncertainties. The reconstructed-level search had a tighter selection on the distance between jets and missing energy, to reduce multi-jet backgrounds, but this gain has been more than compensated for by the fact that the current analysis uses particle flow jets, which have lower background contamination. The use of particle flow jets, and their more precise recommendations and uncertainties, explain

[5] In the two-lepton regions (see Figure 5.2), systematic uncertainties are somewhat similar to the $p_{\mathrm{T}}^{\mathrm{miss}}$+jets region due to both being dominated by Z processes.

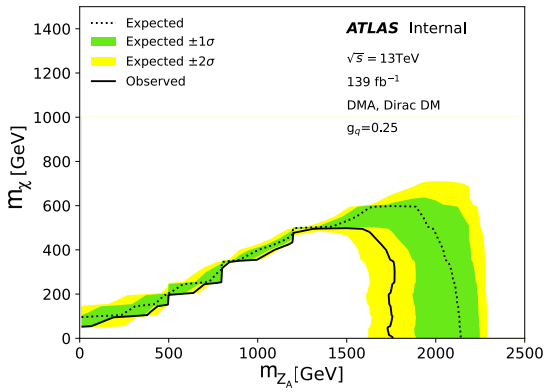

(a) Expected and observed exclusion for the axial-vector mediator model in the $m_\chi - m_{Z_A}$ for $p_{\mathrm{T}}^{\mathrm{miss}}$+jets and 2ℓ+jets regions.

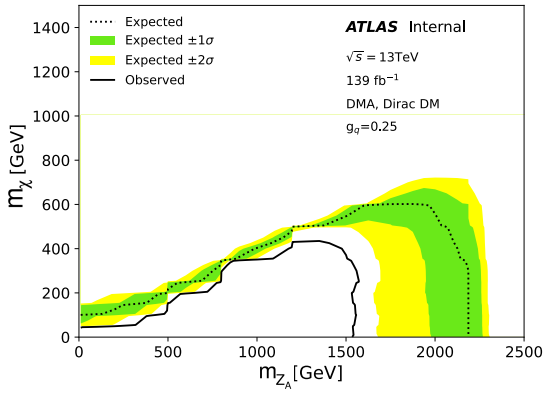

(b) Expected and observed exclusion for the axial-vector mediator model in the $m_\chi - m_{Z_A}$ for $p_{\mathrm{T}}^{\mathrm{miss}}$+jets and all auxiliary regions.

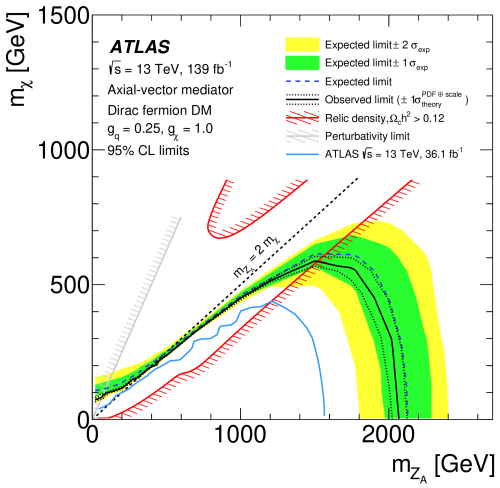

(c) Expected and observed exclusion for the axial-vector mediator model in the $m_\chi - m_{Z_A}$ plane of the recent ATLAS reconstructed monojet-like search [64]

Figure 5.17.

the competitive performance of this analysis with respect to the reconstructed-level search.

5.6.2. Dark Matter + Pseudoscalar Mediator

In parallel to excluding the axial-vector mediator, the pseudoscalar mediator DM model is also considered. This change of coupling leads to changes in the behaviour of the kinematics of the model. The minimal set of parameters for this model is $m_{\chi'}$

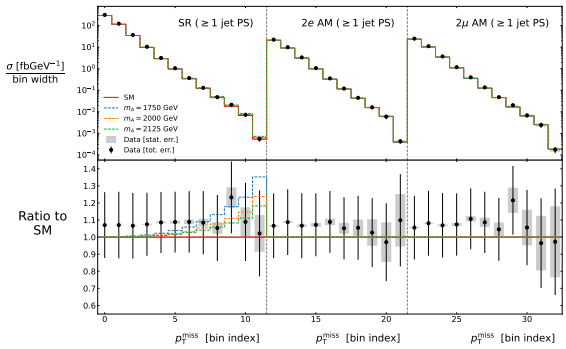

(a) The differential cross-section distribution as a function of $p_{\mathrm{T}}^{\mathrm{miss}}$ for the $p_{\mathrm{T}}^{\mathrm{miss}}$+jets region and the 2ℓ+jets region. A few axial-vector DM mediator models are shown in which the DM mass is always $m_{DM} = 1$ GeV with corresponding mediator masses of $m_{Z_A} = 1750$ GeV, 2000 GeV, 2125 GeV.

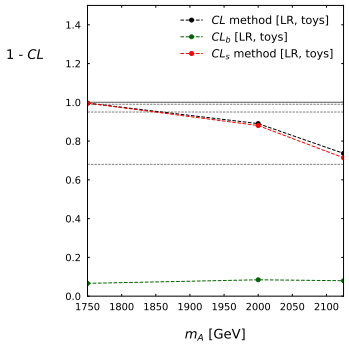

(b) The observed $1 - CL_s$ value is shown for these different mediator masses of $m_{Z_A} = 1750$ GeV, 2000 GeV, 2125 GeV for a $m_{DM} = 1$ GeV. The model is considered excluded when $1 - CL_s \geq 0.95$.

Figure 5.18.

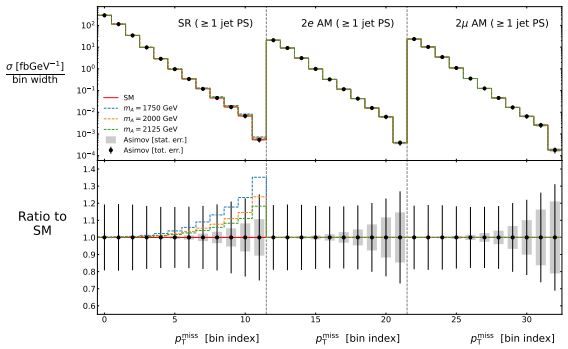

(a) The Asimov differential cross-section distribution as a function of $p_{\mathrm{T}}^{\mathrm{miss}}$ for the $p_{\mathrm{T}}^{\mathrm{miss}}$+jets region and the 2ℓ+jets region. A few axial-vector DM mediator models are shown in which the DM mass is always $m_{DM} = 1$ GeV with corresponding mediator masses of $m_{Z_A} = 1750$ GeV, 2000 GeV, 2125 GeV.

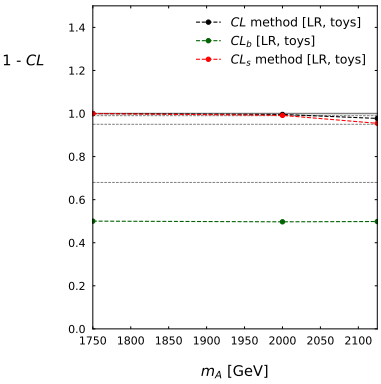

(b) The Asimov $1 - CL_s$ value is shown for these different mediator masses of $m_{Z_A} = 1750$ GeV, 2000 GeV, 2125 GeV for a $m_{DM} = 1$ GeV. The model is considered excluded when $1 - CL_s \geq 0.95$.

Figure 5.19.

m_{Z_p}, g_χ, g_q and coupling values of $g_q = g_\chi = 1$ are chosen. The difference in choice of g_q coupling is because the need to avoid the di-jet constraints from the LHC and earlier hadron colliders is not a concern for pseudo-scalar models. This is because the dijet signal emerges only at the 2-loop level through diagrams where the mediator is produced via gluon-gluon fusion and decays back into two gluons through a top loop. The strong loop suppression means such signals are unobservable at the LHC, hence the choice of $g_q = 1$ [52]. Figure 5.20 (a) shows the expected 95% CL_s exclusion contour in the $m_\chi - m_{Z_p}$ parameter plane. For very light DM particles, a mediator mass of around 395 GeV is excluded for the expected limits, and for the observed limit, a mediator mass of $\sim$400 GeV. At the moment, this exclusion contour is making use of the $p_{\mathrm{T}}^{\mathrm{miss}}$ distribution in the $p_{\mathrm{T}}^{\mathrm{miss}}$+jets and the 2ℓ+jets regions in the ≥ 1 jet phase-space. Figure 5.20 (b) shows the same exclusion contours except it includes all the auxiliary regions and it is shown to be very similar in terms of its exclusion power. Figure 5.20 (c) shows the expected 95% exclusion contours for the pseudoscalar mediator model in the dedicated ATLAS monojet-like search [64]. In this analysis [64], they use 1ℓ+jets and 2ℓ+jets regions as well as the $p_{\mathrm{T}}^{\mathrm{miss}}$+jets region in a phase-space similar to the ≥ 1 jet .

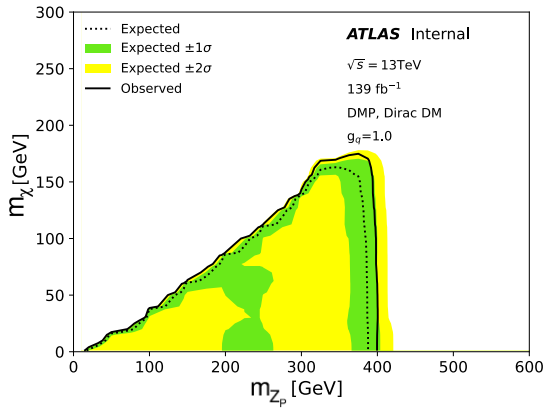

(a) Expected and observed exclusion for the pseudo-scalar mediator model in the $m_\chi - m_{Z_p}$ for $p_{\mathrm{T}}^{\mathrm{miss}}$+jets and 2ℓ+jets regions.

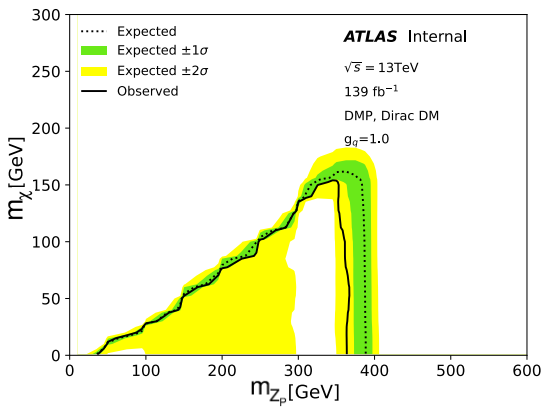

(b) Expected and observed exclusion for the pseudo-scalar mediator model in the $m_\chi - m_{Z_p}$ for $p_{\mathrm{T}}^{\mathrm{miss}}$+jets and all auxiliary regions.

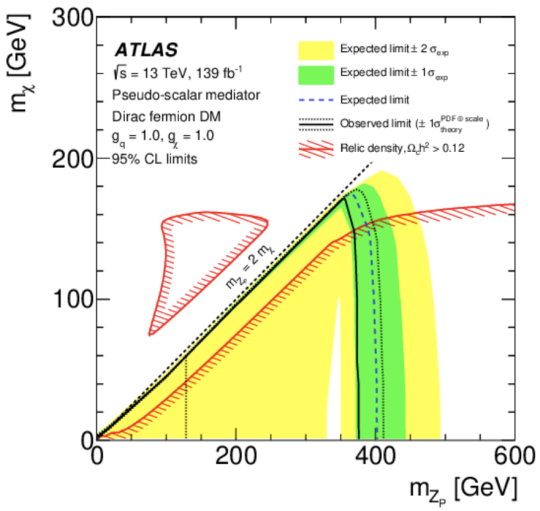

(c) Expected and observed exclusion for the pseudo-scalar mediator model in the $m_\chi - m_{Z_p}$ plane of the recent ATLAS reconstructed monojet-like search [64]

Figure 5.20.

Chapter 6.

Conclusion

This thesis presents the measurement of differential cross-sections along with their ratios for various different regions of phase-space which are largely populated by well-known SM processes but are also expected to be sensitive to dark matter particles as well as other beyond the Standard Model physics. The differential cross-section is measured in the $p_{\mathrm{T}}^{\mathrm{miss}}$+jets final state along with four other auxiliary regions which contain charged leptons: the one electron + jets, the one muon + jets, the two electron + jets and finally the two muon + jets. These lepton regions are primarily used to constrain the experimental and theoretical systematic uncertainties that are present in the $p_{\mathrm{T}}^{\mathrm{miss}}$+jets final state but they could also be sensitive to new physics produced in association with leptons.

The measurements are performed in three different phase-spaces: the ≥ 1 jet , the ≥ 2 jet and the VBF. These are defined in terms of the jet kinematics of the events with the primary aim to be sensitive to dark matter production mechanisms. The measurement is done differentially with respect to a number of observables because this allows us to gain insight into the structure and shape of the data. A ratio of the cross-sections is also presented as a function of different observables, with the primary benefit being the reduction of experimental and theoretical systematic uncertainties and any mismodelling. The measurements are corrected for detector effects and are presented in this thesis at the particle-level. This makes them readily available to be compared to updated particle-level predictions any time in the future without the need for computationally expensive detector simulation.

There are some inconsistencies found between the detector-corrected measured data and the SM particle-level predictions. The MC samples used in the comparisons between the data and the SM predictions are known to be mismodelled, specifically

the QCD V + jets process. More robust uncertainties or an updated decorrelation scheme is required to solve these issues.

A strong cancellation of the experimental and theoretical uncertainties is found for the R^{miss} ratio and this leads to a much more precise measurement, as is shown by the two lepton results. This also leads to an improved agreement between the detector-corrected measurement and the particle-level predictions which is quantified by the χ^2 and p-values that are seen.

Finally, the $p_{\text{T}}^{\text{miss}}$ observable is used in the $p_{\text{T}}^{\text{miss}}$+jets along with their auxiliary regions to set exclusion contours on the axial-vector and pseudo-scalar simplified DM models. The behaviour of the axial-vector model is explored, in which differences between the observed and expected limits are found and could potentially point to the underestimation of uncertainties or presence of signal. Both the observed and expected limits are found to be competitive with the recent results from the dedicated reconstructed monojet-like search [64].

Appendix A.

Data Quality Studies

A.1. $p_{\mathrm{T}}^{\mathrm{miss}}$ Distributions

Figures A.1–A.6 show the $\langle \mu_{\mathrm{med}} \rangle / \langle \mu_{\mathrm{low}} \rangle$ and $\langle \mu_{\mathrm{high}} \rangle / \langle \mu_{\mathrm{med}} \rangle$ ratios for the $p_{\mathrm{T}}^{\mathrm{miss}}$ distribution in the lepton regions for the ≥ 1 jet , VBF and ≥ 2 jet phase-spaces respectively. For all figures the MC is mostly in agreement with data (within the statistical errors).

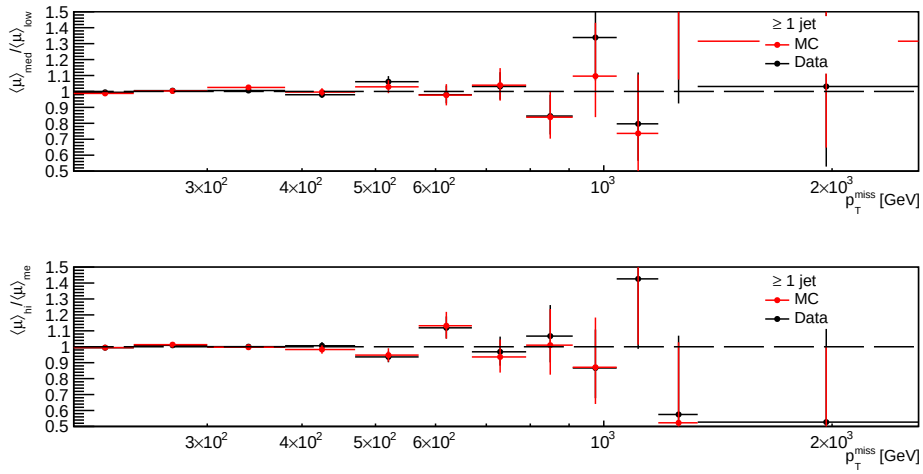

(a) One electron region.

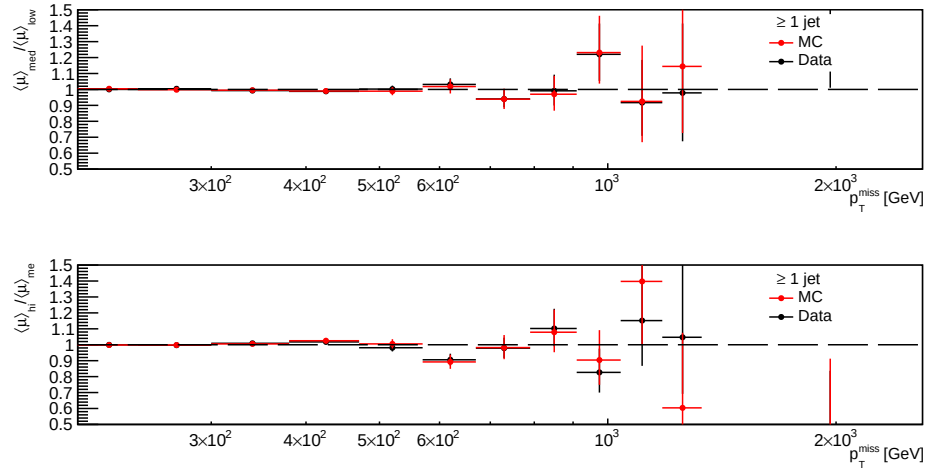

(b) One muon region.

Figure A.1.: The $\langle\mu\rangle$ dependence for the $p_{\mathrm{T}}^{\mathrm{miss}}$ in the one lepton regions for the ≥ 1 jet phase-space.

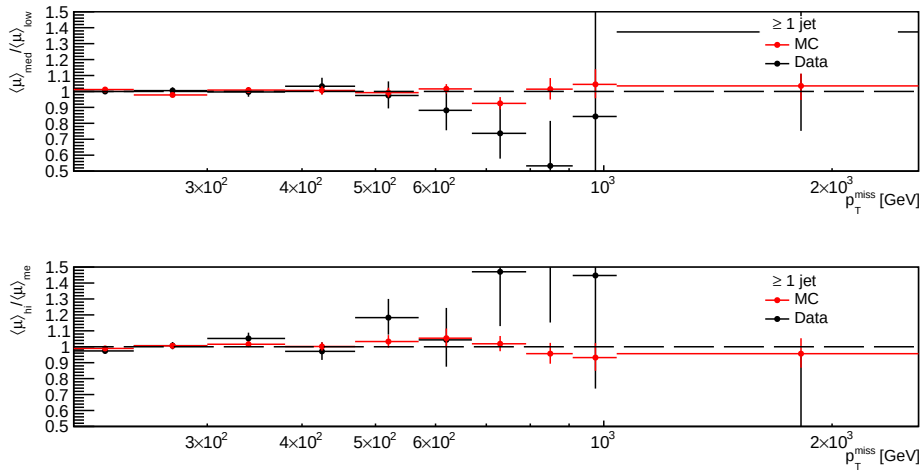

(a) Two electron region.

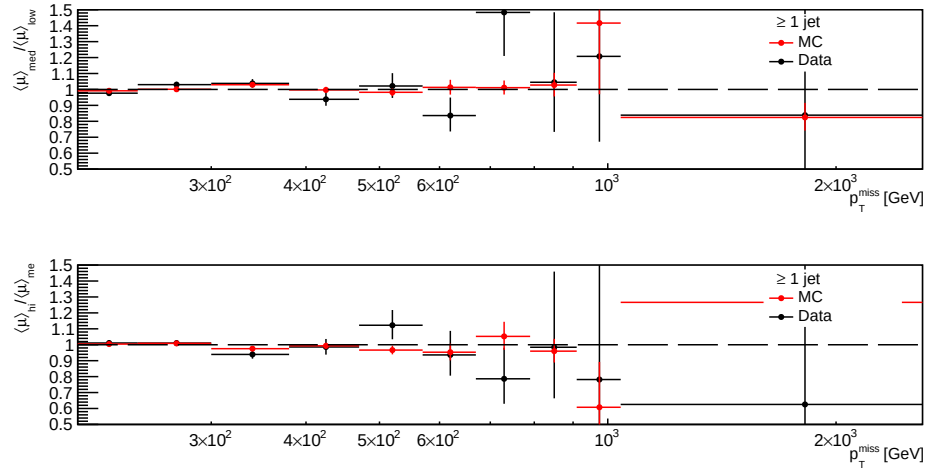

(b) Two muon region.

Figure A.2.: The $\langle\mu\rangle$ dependence for the $p_{\mathrm{T}}^{\mathrm{miss}}$ in the two lepton regions for the ≥ 1 jet phase-space.

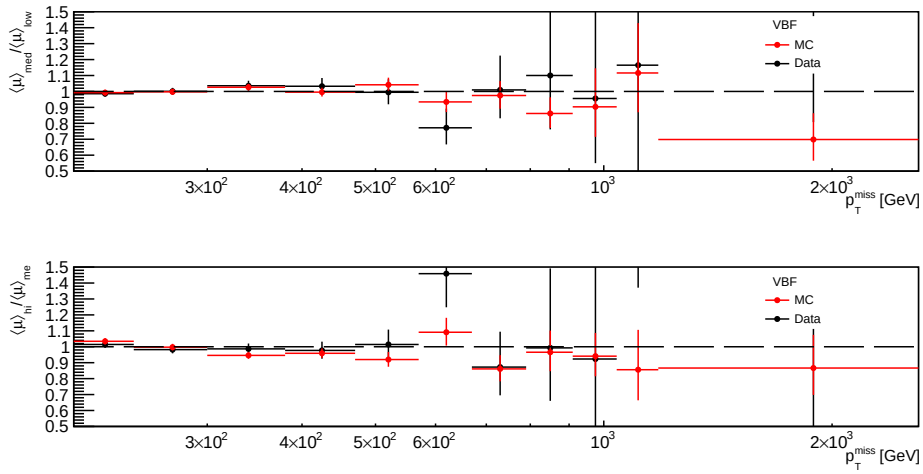

(a) One electron region.

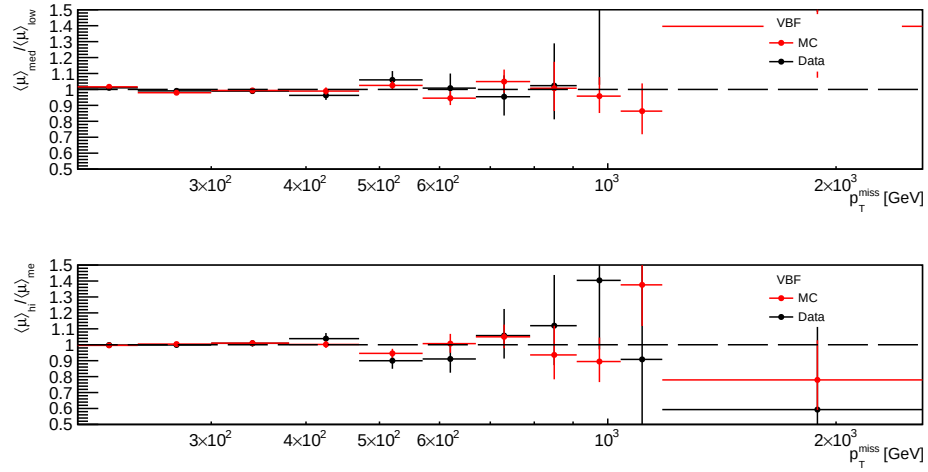

(b) One muon region.

Figure A.3.: The $\langle\mu\rangle$ dependence for the $p_{\mathrm{T}}^{\mathrm{miss}}$ in the one lepton regions for the VBF phase-space.

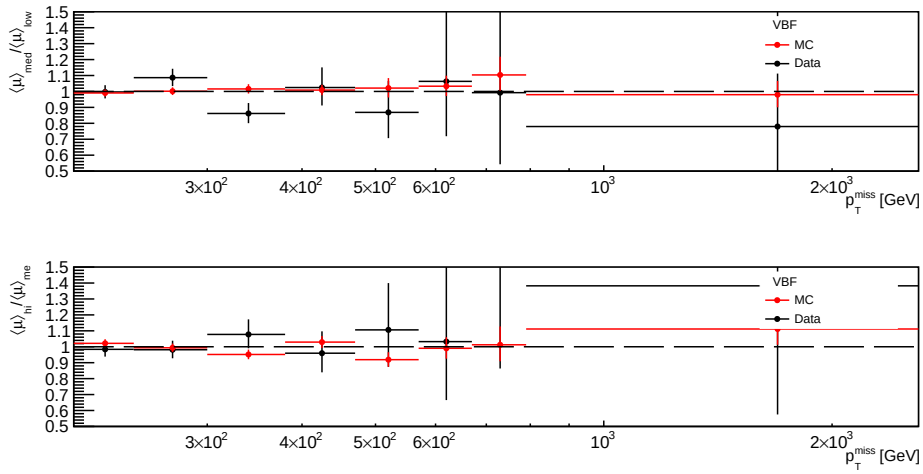

(a) Two electron region.

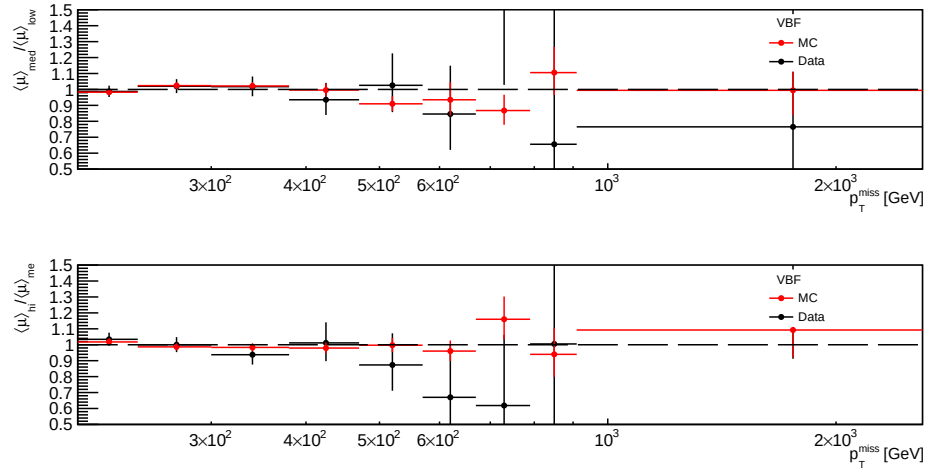

(b) Two muon region.

Figure A.4.: The $\langle\mu\rangle$ dependence for the $p_{\mathrm{T}}^{\mathrm{miss}}$ in the two lepton regions for the VBF phase-space.

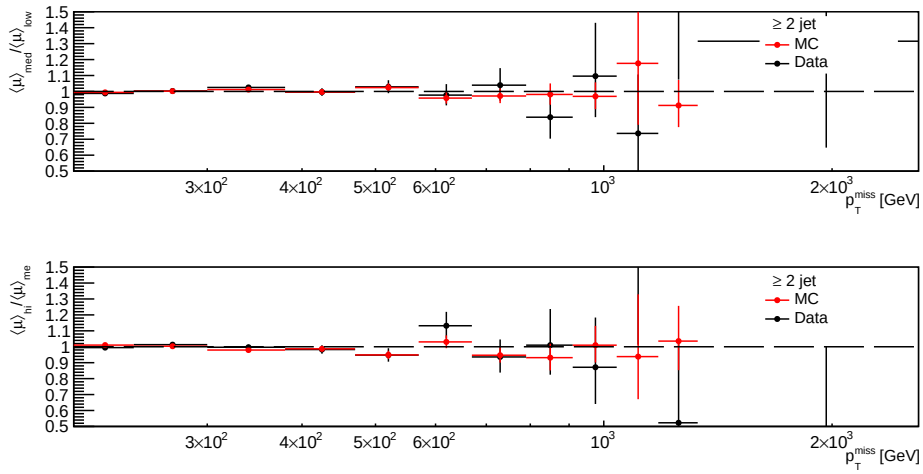

(a) One electron region.

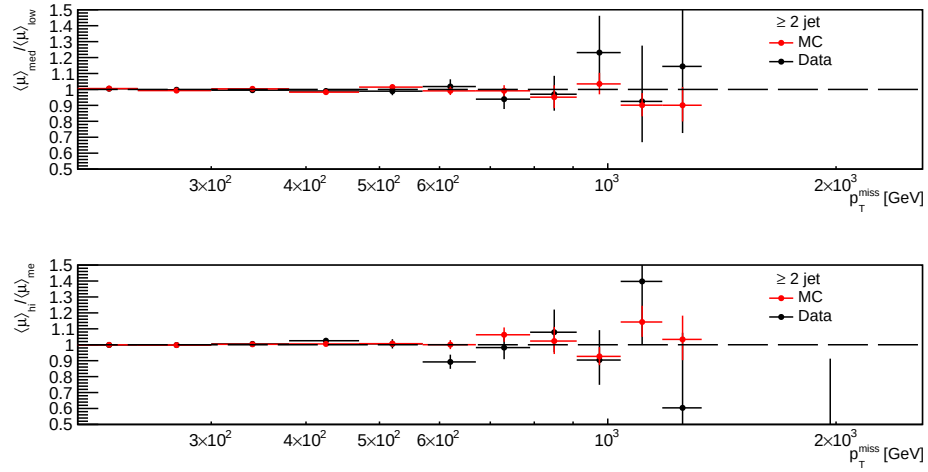

(b) One muon region.

Figure A.5.: The $\langle\mu\rangle$ dependence for the $p_{\mathrm{T}}^{\mathrm{miss}}$ in the one lepton regions for the ≥ 2 jet phase-space.

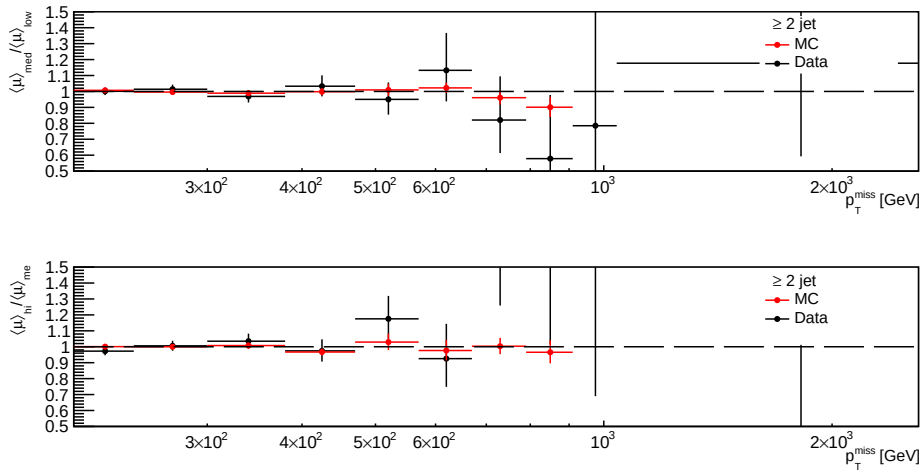

(a) Two electron region.

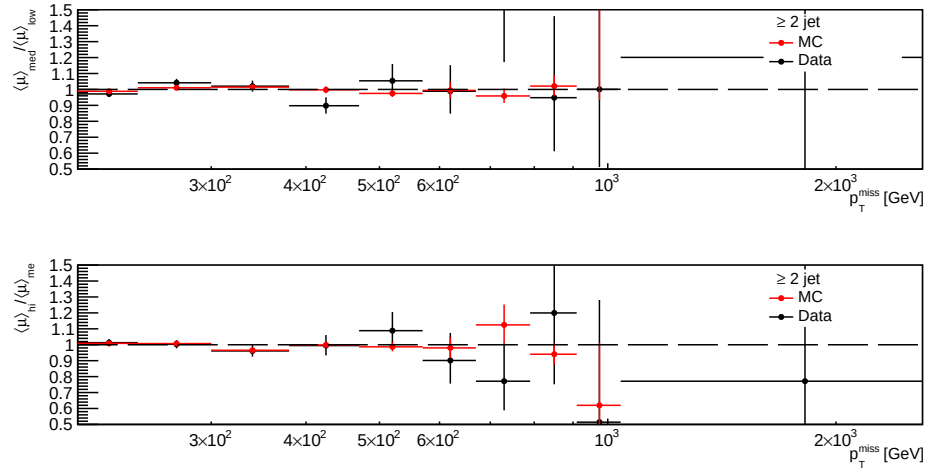

(b) Two muon region.

Figure A.6.: The $\langle\mu\rangle$ dependence for the $p_{\mathrm{T}}^{\mathrm{miss}}$ in the two lepton regions for the ≥ 2 jet phase-space.

A.2. m_{jj} Distributions

The invariant mass of the two leading jets, m_{jj}, is only determined for the VBF and ≥ 2 jet phase-space region as these phase-spaces require two jets, whereas in a ≥ 1 jet event only one energetic jet coming from the event of interest is required. Figures A.7, A.8, A.9 and A.10 show the ratios of $\langle\mu_{\text{med}}\rangle/\langle\mu_{\text{low}}\rangle$ and $\langle\mu_{\text{high}}\rangle/\langle\mu_{\text{med}}\rangle$ for the m_{jj} variable in the signal region for the VBF and ≥ 2 jet phase-space. The ratios for the MC and the data are mostly in agreement (within the statistical errors).

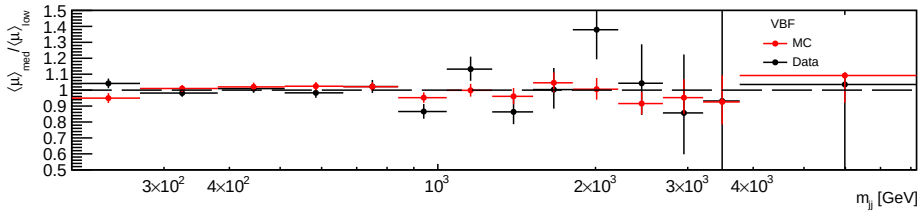

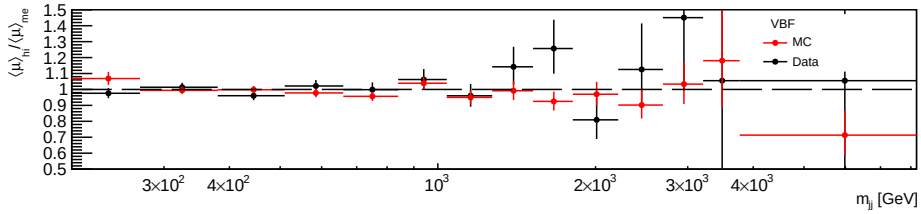

(a) One electron region.

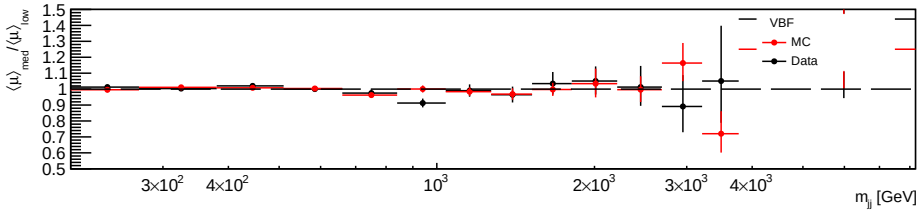

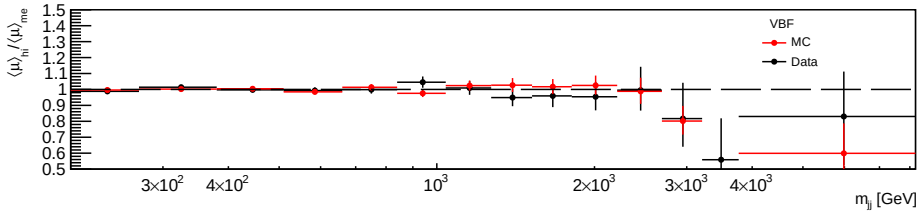

(b) One muon region.

Figure A.7.: The $\langle\mu\rangle$ dependence for the m_{jj} in the one lepton regions for the VBF phase-space.

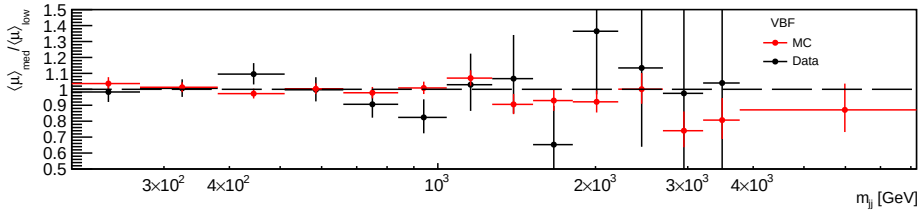

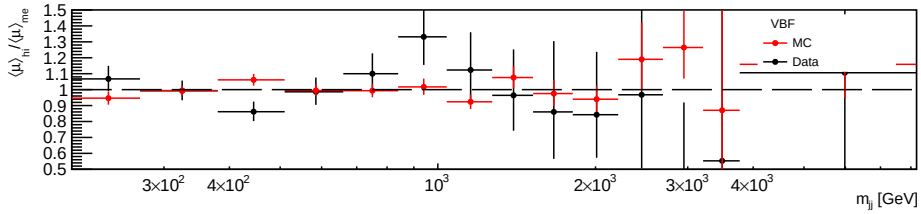

(a) Two electron region.

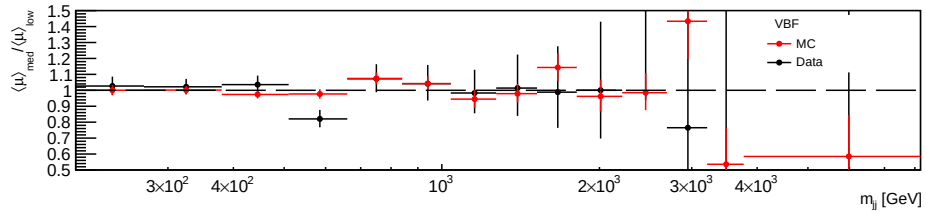

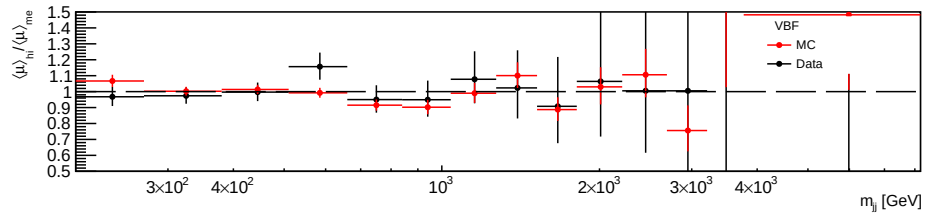

(b) Two muon region.

Figure A.8.: The $\langle\mu\rangle$ dependence for the m_{jj} in the two lepton regions for the VBF phase-space.

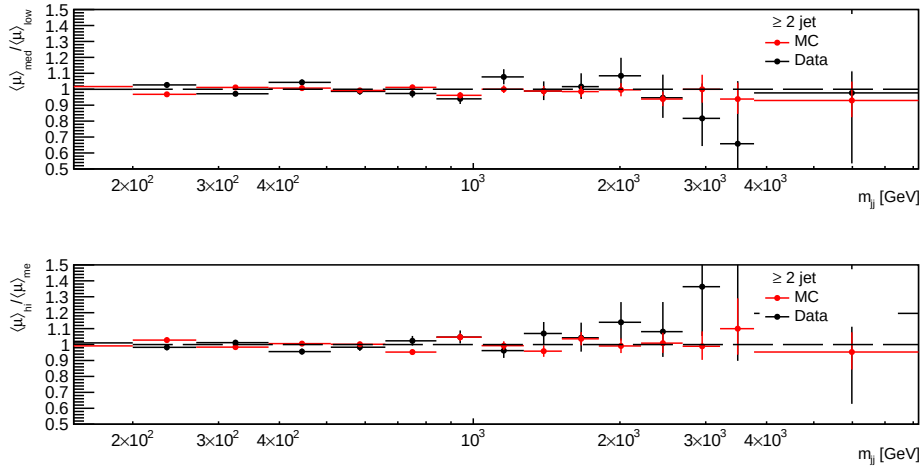

(a) One electron region.

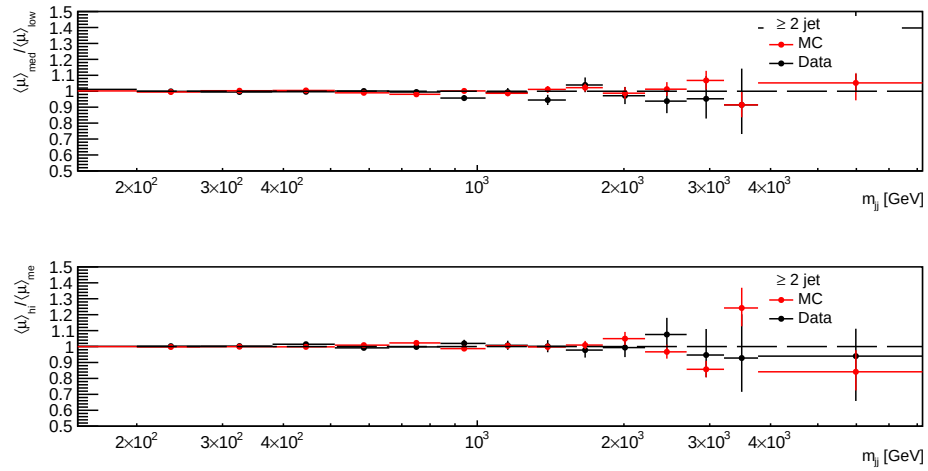

(b) One muon region.

Figure A.9.: The $\langle\mu\rangle$ dependence for the m_{jj} in the one lepton regions for the ≥ 2 jet phase-space.

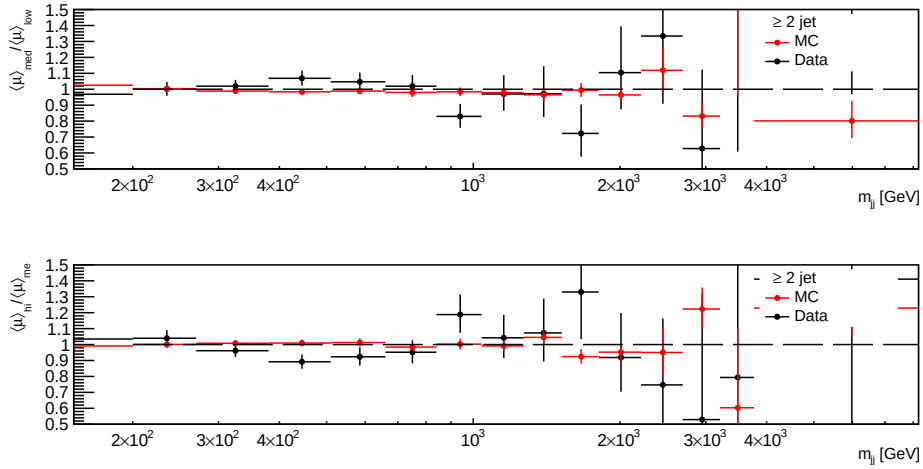

(a) Two electron region.

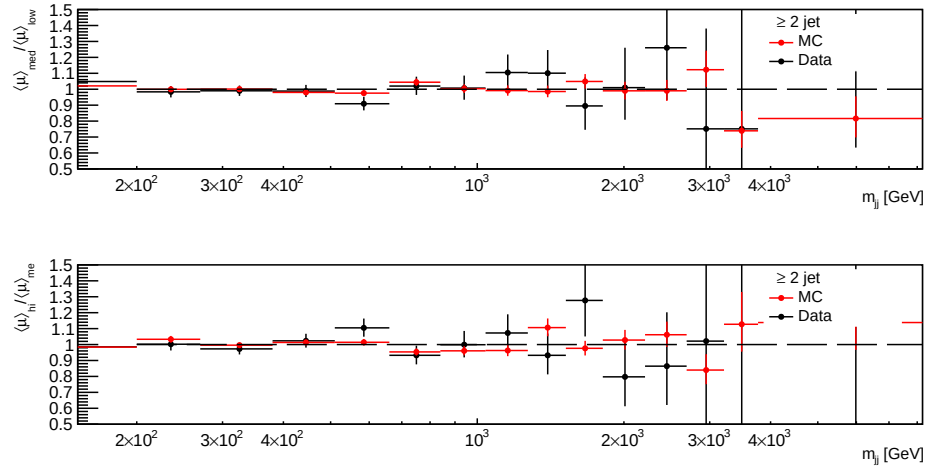

(b) Two muon region.

Figure A.10.: The $\langle\mu\rangle$ dependence for the m_{jj} in the two lepton regions for the ≥ 2 jet phase-space.

A.3. $\Delta\phi_{jj}$ Distributions

For the same reasoning as for the m_{jj} distributions we only consider the VBF and ≥ 2 jet phase-space for the $\Delta\phi_{jj}$ distribution. Figures A.11, A.12, A.13 and A.14 show the ratios of $\langle\mu_{\text{med}}\rangle/\langle\mu_{\text{low}}\rangle$ and $\langle\mu_{\text{high}}\rangle/\langle\mu_{\text{med}}\rangle$ for the $\Delta\phi_{jj}$ variable in the lepton regions. The ratios for the MC and the data are mostly in agreement (within the statistical errors).

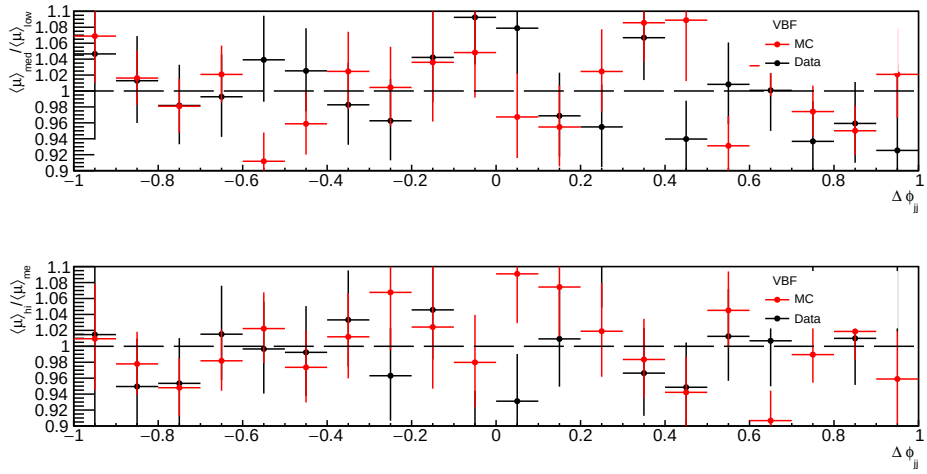

(a) One electron region.

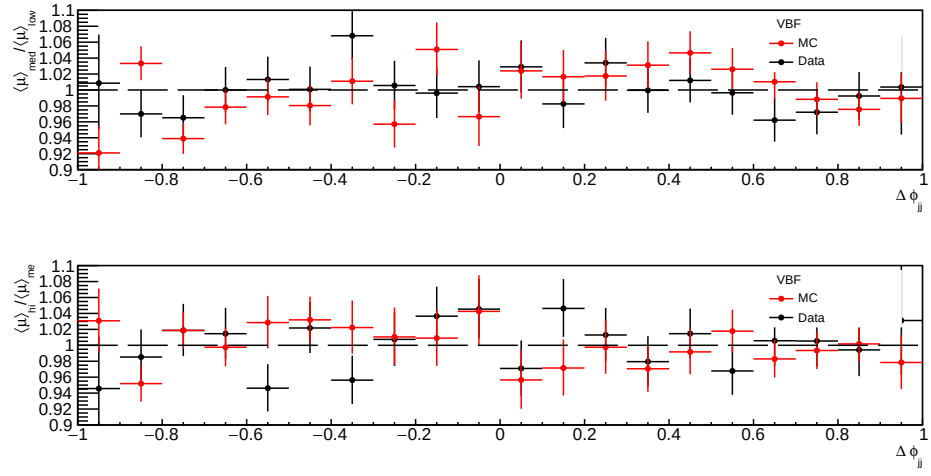

(b) One muon region.

Figure A.11.: The $\langle\mu\rangle$ dependence for the $\Delta\phi_{jj}$ in the one lepton regions for the VBF phase-space.

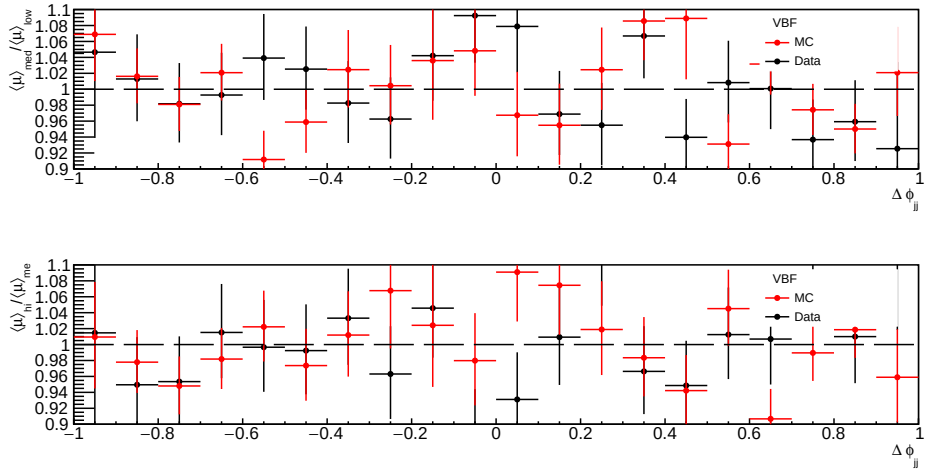

(a) Two electron region.

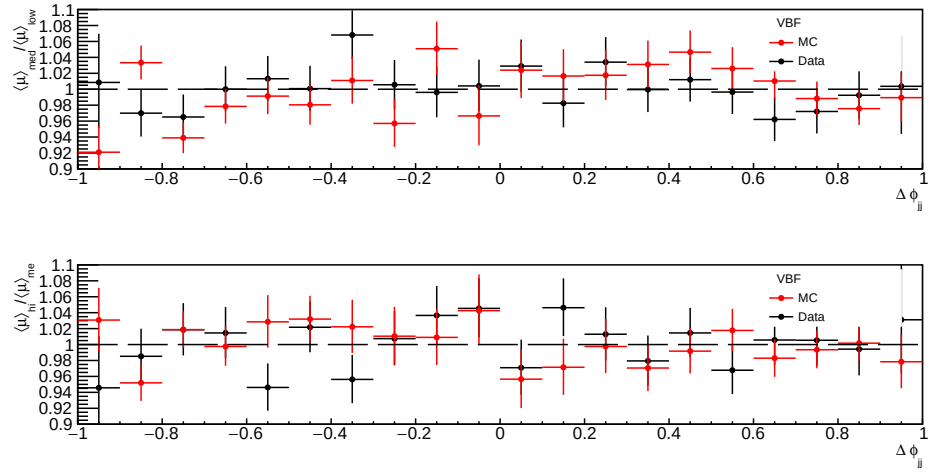

(b) Two muon region.

Figure A.12.: The $\langle\mu\rangle$ dependence for the $\Delta\phi_{jj}$ in the two lepton regions for the VBF phase-space.

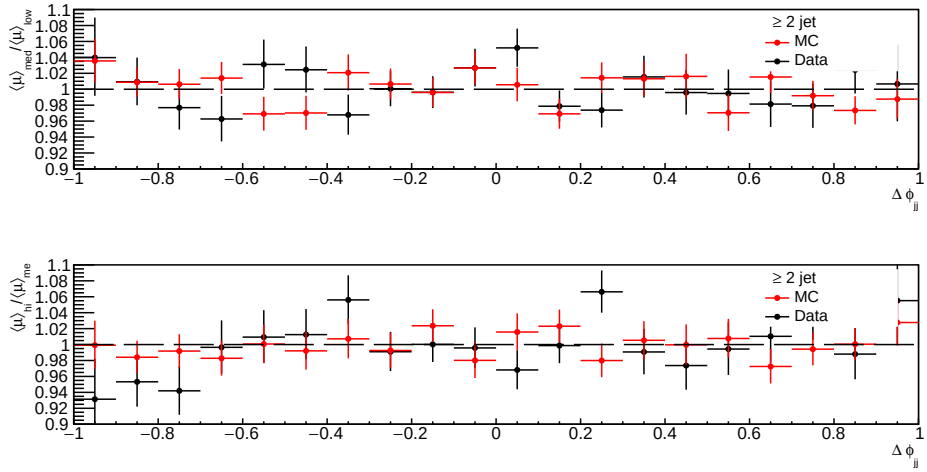

(a) One electron region.

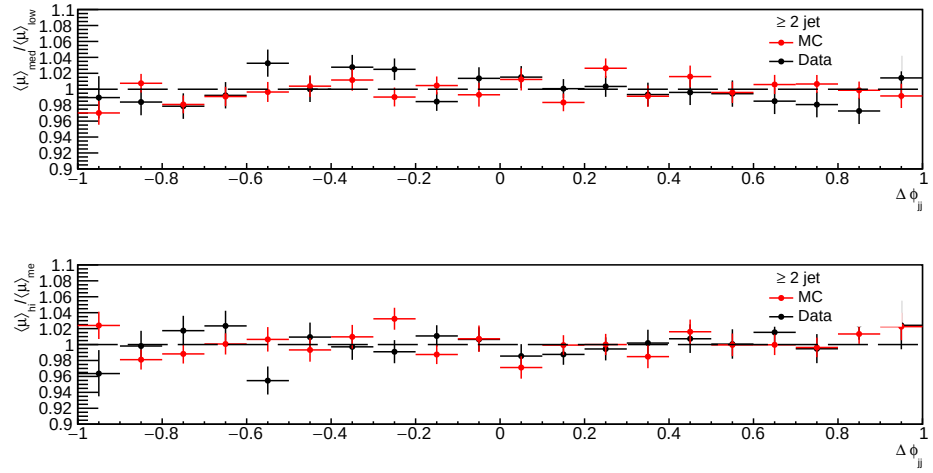

(b) One muon region.

Figure A.13.: The $\langle\mu\rangle$ dependence for the $\Delta\phi_{jj}$ in the one lepton regions for the ≥ 2 jet phase-space.

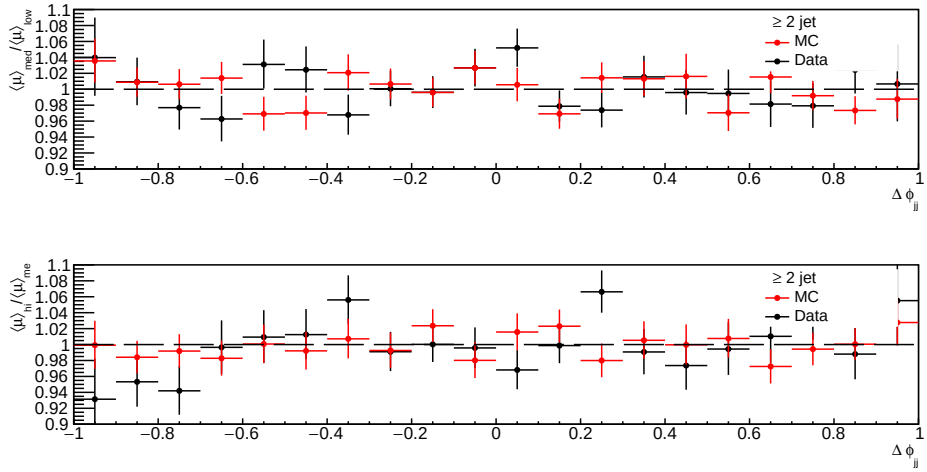

(a) Two electron region.

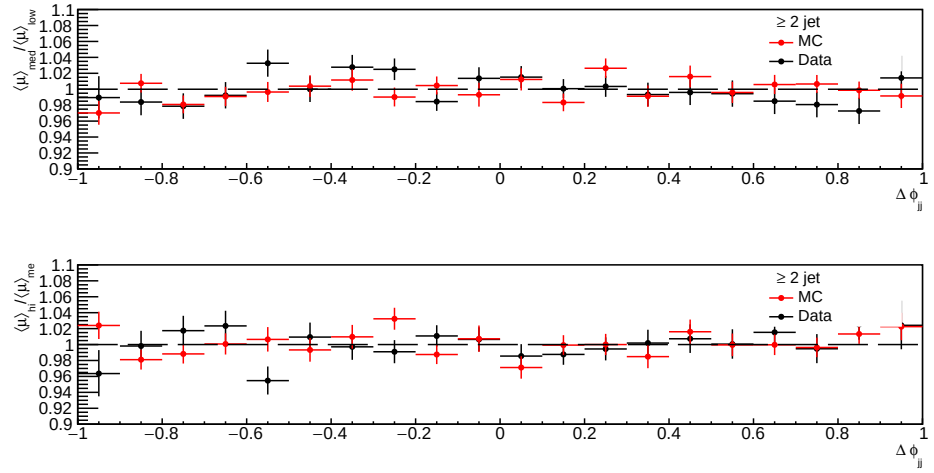

(b) Two muon region.

Figure A.14.: The $\langle\mu\rangle$ dependence for the $\Delta\phi_{jj}$ in the two lepton regions for the ≥ 2 jet phase-space.

Appendix B.

Updates to the RIVET–Athena interface and validation of Weak Boson samples

B.1. Introduction

For the ATLAS author qualification task we were tasked with updating the RIVET (Robust Independent Validation of Experiment and Theory)–Athena[1] interface and also validating some weak boson samples [204]. The aim of the qualification task was to make the RIVET-Athena interface compatible with the new major release version 3.0 and extend the Athena stream handling to "Analysis Object Data" (AOD) and TRUTH1 DAOD. RIVET is an analysis framework for generators and it is very useful for MC generator development, validation of an analysis and also tuning. It is often used within the high energy physics community to preserve analyses for comparison to future theoretical models. The first update was with regards to making the multiweight functionality available for ATLAS for the RIVET 3 [205] interface. With this update, we are now able to estimate the uncertainties in the event generator modelling (e.g. the scale uncertainty) with on-the-fly weight variations. The second update was extending this RIVET_I wrapper to be able to read in AOD and TRUTH1 DAOD files for RIVET 3. The ATLAS experiment uses an AOD file to store the event information which is as a result of a long chain of data-taking or simulation and reconstruction. There are always derivations from these AOD files, which typically contain different amount of the truth record, often denoted as DAOD files. The TRUTH1 DAOD files are reduced

[1] Athena is based on the common Gaudi framework that is used by ATLAS, LHCb and FCC. The Gaudi framework is a software package that is used to build data processing applications for High-Energy Physics experiments. It consists of all the components and interfaces to allow for event data processing frameworks for an experiment.

containers from TRUTH3[2] and complete collection of particles as well as links to truth jet constituents and truth charged particle jets.

We checked that this update was functioning correctly using a MC_JETS RIVET routine on POWHEG PYTHIA8 $t\bar{t}$ events and comparing this to the corresponding EVNT[3] output.

In addition, we produced a diboson sample decaying to four leptons, and compared this to a previous analysis Monte Carlo and data using the RIVET analysis framework. Diboson measurements are an important test of the SM and perturbative QCD at the TeV scale, and are also irreducible backgrounds for many of the Higgs analysis (WW, ZZ and $Z\gamma$) and BSM searches, such as the unfolded $p_{\mathrm{T}}^{\mathrm{miss}}$ analysis [119]. We can also indirectly search for new physics by measuring the anamolous triple and quartic gauge boson couplings in these diboson samples.

We also generated leptonically decaying single Z bosons in the low dilepton invariant mass, 10 GeV $< m_{\ell\ell} <$ 40 GeV, region with the Monte Carlo Generator SHERPA 2.2.11 [146]. This is needed to cover the full $m_{\ell\ell}$ phase space of the Z boson decay and is often an important background for BSM searches which may have a signature particle decaying to two leptons in that region of phase space. The single Z boson channel is an important process for an analysis which wants to measure the cross section of the Z boson or a BSM particle produced in association with a Z boson. The single Z boson in the low $m_{\ell\ell}$ phase space is also an important background for the Higgs channel, $H \to ZZ^* \to 4\ell$, where a virtual Z boson, Z^*, is more likely to occupy this low $m_{\ell\ell}$ phase space [11]. The low $m_{\ell\ell}$ single Z boson sample can also be an important background for a BSM particle whose signature is leptons, such as the search for supersymmetry in the four lepton final state [206]. This single Z boson sample was then validated using a RIVET routine and compared to the corresponding old SHERPA 2.2.1 low $m_{\ell\ell}$ single Z boson samples. The transition from the low $m_{\ell\ell}$ SHERPA 2.2.11 Z boson samples to the high ($m_{\ell\ell} > 40$ GeV) SHERPA 2.2.11 Z boson samples was checked with a RIVET routine to check the smoothness.

This section is laid out as follows, we begin with an introduction, followed by an explanation the multiweight functionality behind the new RIVET 3 release and also how we extend the RIVET_I wrapper around Athena to read in AOD and TRUTH1

[2] This consists of the containers with the main truth information that is needed for analyses purposes.

[3] This is the first part of the ATLAS MC chain which consists of providing different production steps, each with their corresponding output format: event generation (EVNT), the detector simulation (HITS), digitisation (RDO), reconstruction (AOD) and derivation (DAOD).

DAOD files in RIVET 3. This is then followed with an introduction to the SHERPA event generator and then briefly mention the diboson study we performed with the four lepton as the final state and then explain the motivation and steps behind generating the low $m_{\ell\ell}$ single Z boson samples.

B.2. RIVET Updates

RIVET

RIVET is a generator agnostic analysis framework for generators [204], i.e., it is a tool which produces physics plots from any generator that can produce events in HepMC format [207], and can be very useful for validating physics analyses. It is often used to archive LHC analyses which correspond to measurement papers and is useful for MC tuning[4], and also BSM analyses.[5]

In this part of the qualification task, we provided two updates to the area in which Athena interfaces to RIVET_I. The first update made the multiweight functionality available in the RIVET 3 Athena interface. With this update, we are able to model the theoretical uncertainties in an efficient way using on-the-fly variations weights in RIVET 3. The second update is allows the RIVET_I interface to read in AOD and TRUTH1 DAOD files, where before it was only able to read in EVNT files. This feature has been in demand and it is useful for validating the analysis logic against an independent analysis framework on an event by event basis. We validated this update using an MC_JETS RIVET routine on PowhegPythia8 $t\bar{t}$ events and compared to the corresponding output from EVNT files.

B.2.1. Multiweight Functionality

In order to estimate the generator uncertainty of a theory calculation, we can vary scales, parameters and parton density functions in the event generator. This was previously handled by generating many event samples corresponding to different setups. This meant that one would have to do this N times for N systematic variations. The same can be achieved for some of these variations by re-running the calculation N times for different sets of weights (e.g., for the different parton density functions). The modern event generators work out these on-the-fly reweighting factors on an event-by-event basis, this allows the event generator to store a weight for a given

[4] On the ability to check and tune our MC models with available data, a quote which succinctly summarises this is given by T.Sjoestrand in 1987: "The experience gained with the model, in failures as well as success could be used as a guideline in the evolution of yet more detailed models".

[5] For example we are able to run different BSM models using the analysis RIVET routine in an efficient way.

systematic variation, instead of having to produce and store to disk an entire new sample.

One of the challenges of the LHC is the huge number of events produced by it which correspondingly requires us to generate a huge number of events with our favourite MC generator. To try and speed this up, we often run these event generations in parallel and then combine afterwards in a statistically correct manner. To ensure that the weights are correctly treated, this handling is no longer exposed to the user but it is handled within the RIVET framework.

Update RIVET_I for RIVET 3

Standalone RIVET cannot deal with EVNT files, so that is why we need a RIVET_I interface with Athena. We updated this interface for the RIVET 3 release where the new main feature is the multiweight functionality [205]. This required removing previous features involved for the variation of weights from RIVET 2 and also some features that did not work at the time in RIVET 3, such as the conversion of YODA files to ROOT file format. We also updated some of the libraries, added and removed some job options related to the on-the-fly weight variations.

B.2.2. Reading in (D)AOD files with RIVET_I

Another part of the qualification task was extending RIVET_I to be able to read in AOD and TRUTH1 DAOD files and their corresponding xAOD::Truth format. It is possible to convert this format back to HepMC::GenEvent (corresponds to the EVNT format) which can be then passed onto RIVET. The nomenclature of EVNT, AODs and TRUTH1 DAOD files will be explained below. We validated this modification to RIVET_I by using the MC_JETS RIVET routine on the POWHEG PYTHIA8 $t\bar{t}$ events for both the AOD/TRUTH1 DAOD files and the EVNT files to see if the above conversion has worked. We would expect that the final output from both these types of files would be exactly the same. Before going further, we will briefly explain the difference between EVNT files and (D)AOD files.

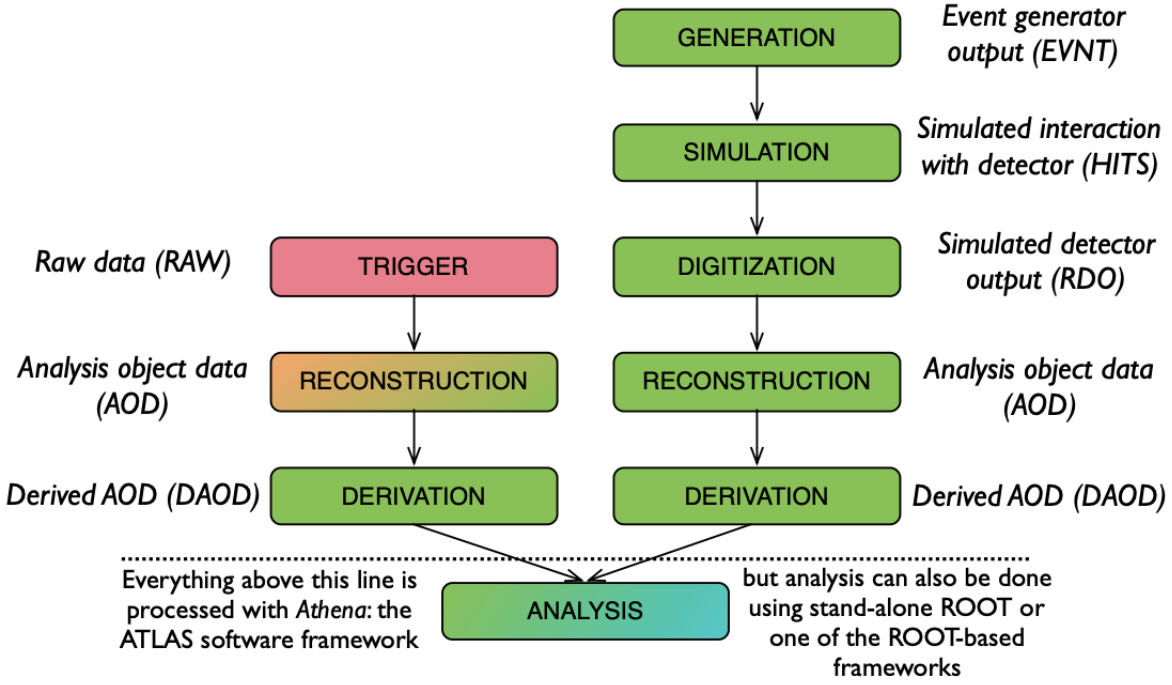

Figure B.1.: Flow diagram describing how data and MC are processed in ATLAS, RIVET_I was only able to read in EVNT files either locally or from the Grid. I have now updated so that it can read in AOD or TRUTH1 DAOD files. This figure is taken from [208].

(D)AOD and EVNT files

AOD files are a ROOT-readable data format and are in general produced at the reconstruction stage as indicated in Figure B.1. In general AODs are too big to analyse directly, so they are normally reduced according to the needs of the individual physics groups. These derived files, more commonly known as DAOD files, are made up of xAOD objects but they take up much less memory as we do not keep all the information from the objects. There are in fact close to ninety DAOD formats for all ATLAS activities. The AOD consists of information about the event itself (EventInfo) and also about reconstructed objects within each event such as tracks, muons, electrons and jets. The EVNT file is the event generator output produced by your favourite MC generator as indicated in Figure B.1. These files, which have the HepMC::GenEvent format can be used by RIVET.

Modification of RIVET_I to read in (D)AOD files

We extended RIVET_I to be able to read in AODs and TRUTH1 DAOD, where the AOD-type format is converted back to the EVNT-type format before being passed on to RIVET. This is easily done by modifying RIVET_I to recognise when what is been read is not an EVNT file but is instead in the AOD/DAOD format and then performing the conversion (from AOD format to EVNT format). Once the conversion has taken place, the RIVET framework then treats this event information as it would if it was coming from an EVNT file and proceeds as expected.

Validation of DAOD Truth 1 files

We validate our new extension to the RIVET_I by comparing the TRUTH1 DAOD events compared to the EVNT files for POWHEG PYTHIA8 8 $t\bar{t}$ events for the MC_JETS routine. The MC_JETS is a RIVET routine which contains MC validation observables for jet production. Jets with $p_{\mathrm{T}} > 20$ GeV are constructed with an anti-kt jet finder with $R = 0.4$ and are projected onto many observables. We see that for the leading jet p_{T} and η, there are no discernible differences, as can be seen in Figures B.2a and B.2b respectively.

However if we look at the leading and subleading jet masses in Figure B.3a and B.3b we see that at the beginning of the jet mass spectrum there are some differences between the DAOD Truth 1 events and the EVNT events. After some investigation, we found these differences were due to the fact that the constituents of the jets had slightly different masses. This is because we were converting from a double, produced by the generator, to a float, saved as this type in the AOD, and then back to a double type via the truth conversion.

AOD files

In some of the events contained in the AOD files, the incoming beam particles appear to be gluons instead of protons which is clearly incorrect. To fix this issue, when these incorrect beam particles are identified, we insert protons as the beam particles with the corresponding energy (this is calculated by totalling up the energy of the initial state

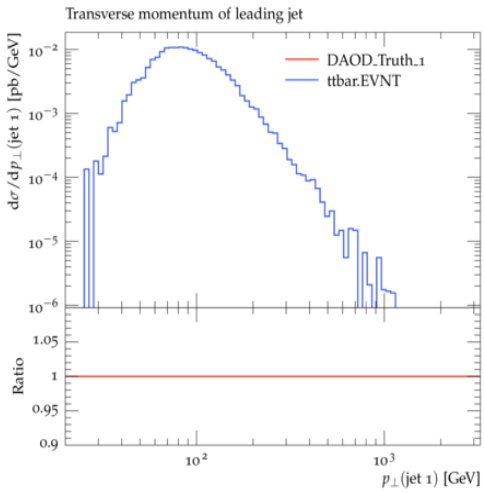

(a) A plot of the $t\bar{t}$ leading jet p_{T} for both the EVNT and DAOD_truth_1 files.

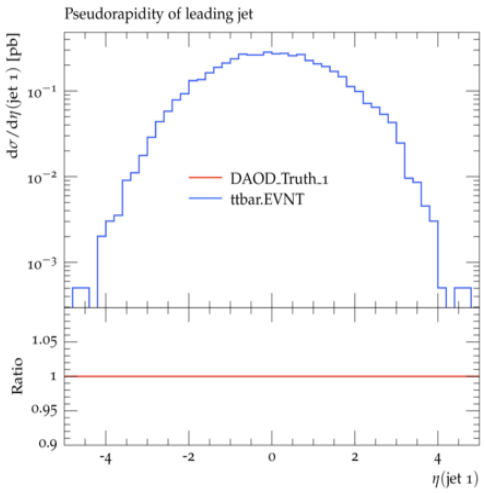

(b) A plot of the $t\bar{t}$ leading jet η for both the EVNT and DAOD_truth_1 files.

Figure B.2.

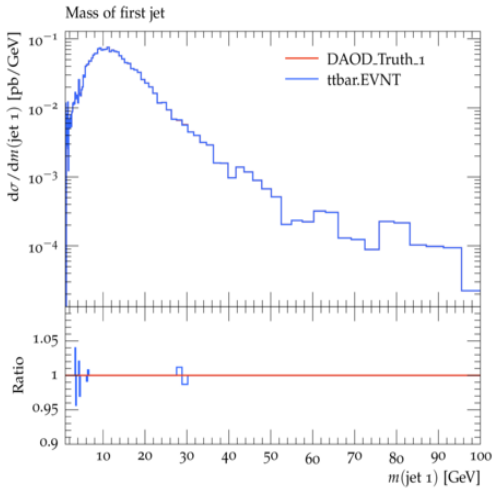

(a) A plot of the $t\bar{t}$ leading jet mass for both the EVNT and DAOD_truth_1 files, we can see some small differences at the beginning of the jet mass spectrum.

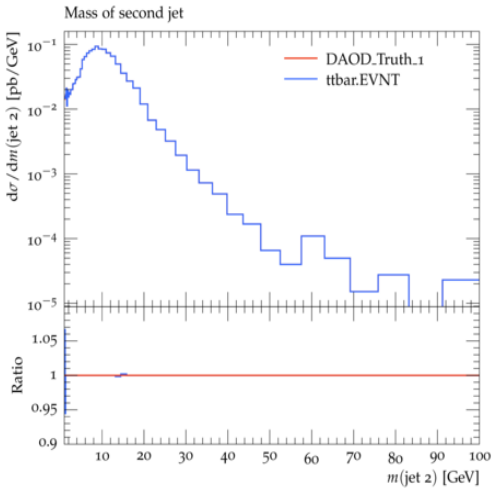

(b) A plot of the $t\bar{t}$ subleading jet mass for both the EVNT and DAOD_truth_1 files, we can see some small differences at the beginning of the jet mass spectrum.

Figure B.3.

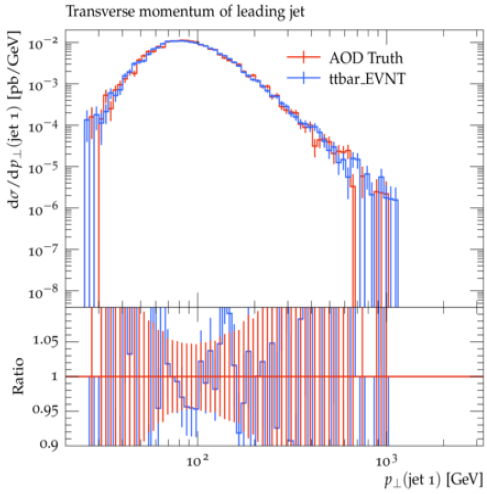

(a) A plot of the $t\bar{t}$ leading jet p_T for both the EVNT and AOD files.

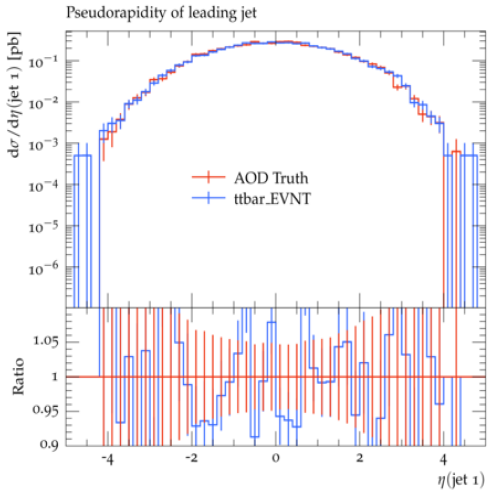

(b) A plot of the $t\bar{t}$ leading jet η for both the EVNT and AOD files.

Figure B.4.

particles) and this appear to work well for the AOD files.[6] In Figures B.4a, B.4b, B.5a and B.5b there is a comparison of AOD to EVNT for $t\bar{t}$ events for the leading jet p_T, η, mass and the subleading jet mass respectively. These are statistically independent events, so it is not a like for like comparison but it gives us an indication that the conversion is indeed working.

TRUTH3 DAOD

For TRUTH3 DAOD the file has a dictionary of containers that it retains. Crucially it does not have the generic TruthParticles container, but just the mini-containers like TruthMuons, TruthElectrons etc which typically have loose p_T and η cuts. This is a problem for RIVET routines as they construct their own jet collections which require all the particles. This means that we cannot use TRUTH3 DAOD in RIVET as we do not have the TruthParticles container. This may become problematic in the future for RIVET as more derived AOD files take on the TRUTH3 DAOD form.

[6] Unfortunately the above problem occurs for DAOD_STDM5 files except the totalled energy does not correspond to the beam energy, i.e., not all the initial state particles are kept in this derived class

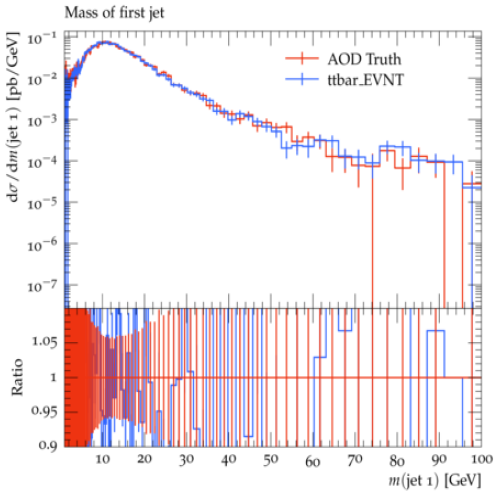

(a) A plot of the $t\bar{t}$ leading jet mass for both the EVNT and AOD files.

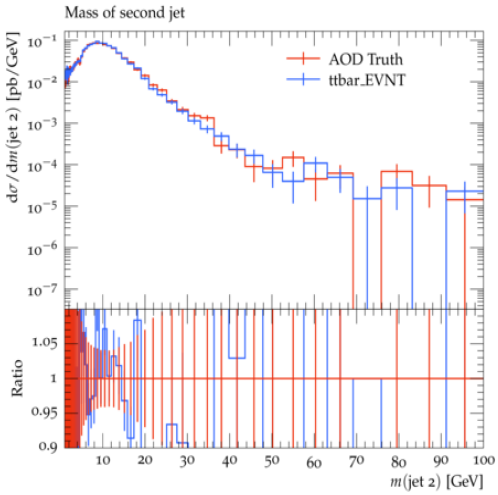

(b) A plot of the $t\bar{t}$ subleading jet mass for both the EVNT and DAOD_truth_1 files.

Figure B.5.

Instructions to run over (D)AOD files

The RIVET_I interface is now able to automatically detect whether we are dealing with AOD or an DAOD type file, however for AOD files specifically some of the events may be missing beam protons which will cause RIVET to complain. If you encounter this problem, you may instruct RIVET_I to add some dummy protons to the reconstructed GenEvent by setting the following flag in the JobOptions:

```
rivet.AddMissingBeamParticles = True
```

and this will inject the necessary protons in those events with the incorrect beam particles at the appropriate centre of mass energy.

B.3. Weak boson samples

B.3.1. The SHERPA Event Generator

SHERPA [146] is an MC event generator for the simulation of primarily high energy interactions of lepton-lepton, lepton-photon, photon-photon, lepton-hadron and the collisions we are interested in, hadron-hadron collisions. These produced events can

be passed through detector simulations used by various experiments, such as ATLAS. The SHERPA generator covers all SM processes and can enable BSM physics using UFO files [209] from programs such as FeynRules [210] [211]. The SHERPA program is able to do this as it has two inbuilt matrix-element generators called AMEGIC++ [212] and Comix [147]; in addition it has its phase-space generator called Phasic [212], which means it can calculate and integrate tree level amplitude for any of the desired models. These features allow SHERPA to integrate the process cross section, generate events at the parton-level using an in built parton shower[7] along with the ability to do consistent merging of NLO (+LO) emission multiplicities. We are using the SHERPA 2.2 release series for the diboson decaying to four leptons and a single Z boson decaying leptonically in the low $m_{\ell\ell}$ phase space. Both these versions include the ability to produce approximate electroweak NLO corrections [213] via OPENLOOPS [148,214,215] and parton shower variations [131,150] which are applicable for our diboson samples.

B.3.2. Event Simulation

The process $qq \to 4\ell$, for the diboson studies, was simulated with SHERPA 2.2.7 and the single low $m_{\ell\ell}$ Z boson, for the low $m_{\ell\ell}$ studies, was simulated with SHERPA 2.2.11. We started out with SHERPA 2.2.7 for the diboson studies, but this was put on hold while the V+jets R & D was ongoing. Once these studies were finalised we developed some low $m_{\ell\ell}$ complementary setups with the same version that the baseline V+jets settled on, SHERPA 2.2.11. For the $qq \to 4\ell$ process, the matrix elements were calculated with NLO accuracy in the strong coupling for up to one additional parton and are LO accurate for up to three additional parton emissions. For the low $m_{\ell\ell}$ single Z boson process, the matrix elements were calculated with NLO accuracy in the strong coupling for up to two additional partons and are LO accurate for up to five additional parton emissions. For both processes, the virtual QCD corrections at NLO were calculated using OPENLOOPS [148,214,215], and the relevant matrix elements were merged with the SHERPA parton shower [150] according to the ME+PS@NLO prescription [131]. These samples were generated using the NNLO PDFs from the PDF NNPDF3.0NNLO [216].

[7] Matrix element calculations are, by construction, at the parton level. The added feature that SHERPA has is that it can match its own matrix elements to its own showers thereby producing particle level events.

QCD scale uncertainties were also estimated using 7-point variations of the factorisation and renormalisation scales in the matrix element and parton shower, where the scales were varied by factors of 0.5 and 2. Approximate NLO electroweak corrections are provided for the $qq \to 4\ell$ and the low $m_{\ell\ell}$ samples as on-the-fly weight variations using OPENLOOPS and this is a new feature which avoids having to derive the corrections specifically for a given analysis.

B.3.3. Validation of Samples

Diboson Samples

To validate our diboson samples we use the RIVET routine created for the measurement of the four-lepton invariant mass spectrum with the ATLAS detector [217] which has a RIVET routine of ATLAS_2019_I1720442.

The focus of this study is to compare the MC particle-level simulation done by SHERPA 2.2.7, with its new features of virtual NLO EW corrections and parton shower variations, to the old SHERPA 2.2.2 and to its fixed order NLO EW.

In Figure B.6a we have the measured differential cross section (black dots) compared to the particle-level SM predictions (the coloured lines) as a function of the four lepton invariant mass, $m_{4\ell}$. The nominal description represents the shape of the distribution quite well without the approximate NLO electroweak corrections or scale variations. When we add the approximate NLO EW corrections to the nominal, we see that there is not a huge change in the values and that the approximate NLO EW corrections do not have a big effect on this observable in this phase space. However the diboson cross-sections in a different phase-space (e.g. VBF phase-space) may have NLO EW corrections which are much larger and this is where these corrections become vital.

In terms of the comparison between the diboson sample generated for Figure B.6a with SHERPA 2.2.7 and that generated for the original analysis in Figure B.6b with SHERPA 2.2.2, the SHERPA versions are different and this will come with some slight variations in terms of the central values. However the main difference is that with SHERPA 2.2.7 we can generate the virtual NLO EW corrections whereas with SHERPA 2.2.2 these corrections had to be explicitly derived for their specific phase space and the simulation was reweighted accordingly. We can see that Figure B.6a and Figure

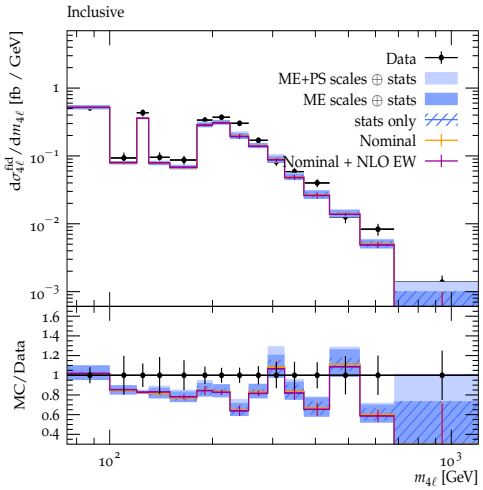

(a) The diboson samples are generated using SHERPA 2.2.7, the SM prediction that we are interested is the SHERPA + NLO EW corrections (magenta line).

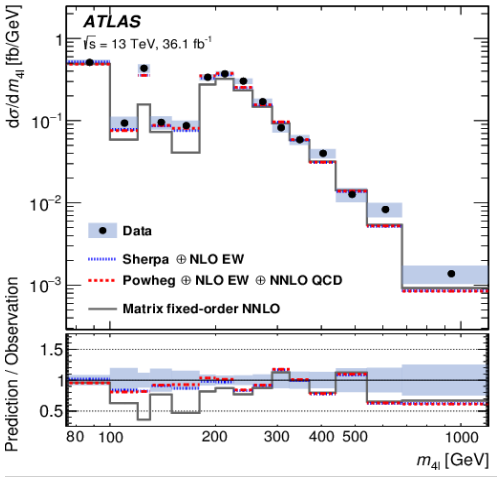

(b) The SM prediction we are interested in comparing with is that of the SHERPA + NLO EW corrections (blue line). This figure is taken from [217].

Figure B.6.: A comparison of the diboson sample that we have produced to that of the original analysis [217] for the $m_{4\ell}$ observable, where we are interested in the agreement between the SHERPA samples in (a) and (b) with their respective NLO EW corrections. The SHERPA samples are the coloured lines and the measured differential cross-section are the black dots for both (a) and (b). In both Figures, the nominal is the $q\bar{q} \to 4\ell$ process with the added Higgs and gluon induced corrections and the nominal plus NLO EW. In (a), the different shades of blue bands include the matrix element (ME) with QCD scale variations in combination with statistics, statistics only and ME plus parton showering with QCD scale uncertainties in combination with statistics. The ratio of the particle-level MC predictions to the unfolded data is shown in the lower panel.

B.6b ratios are quite similar with respect to the data and that our nominal + NLO EW prediction matches quite well with what was found in the analysis [217]. Another additional feature in SHERPA 2.2.7 are the scale variations of the factorisation and renormalisation scales which are consistent in the matrix elements and parton showers, which are represented by the light (matrix element scale variation only) and dark blue bands (matrix element and parton shower scale variation) in Figure B.6a; these could become more relevant in the high $p_{\mathrm{T}}^{4\ell}$ bins as extra emissions are more likely or it could equally be due to a low number of events (large statistical error bars). The QCD scale variations represented by the light and dark blue bands are uncertainties which indicate the size of the theory uncertainties of the SM prediction without taking into account all of the different theoretical systematic uncertainties.

We mentioned for Figure B.6a that the NLO EW effects might be larger in different regions of phase space, so it may be informative to look at higher $p_{\mathrm{T}}^{4\ell}$ phase space slices where the NLO EW effects may be more important. In Figure B.7 we have the measured differential cross section represented by the black dots again compared to the particle level MC SM predictions in different slices of the $p_{\mathrm{T}}^{4\ell}$ as a function of the $m_{4\ell}$ mass. The $p_{\mathrm{T}}^{4\ell}$ slices are 0 GeV $< p_{\mathrm{T}}^{4\ell} <$ 20 GeV, 20 GeV $< p_{\mathrm{T}}^{4\ell} <$ 50 GeV, 50 GeV $< p_{\mathrm{T}}^{4\ell} <$ 100 GeV, 100 GeV $< p_{\mathrm{T}}^{4\ell} <$ 600 GeV. In all the slices, the approximate NLO EW corrections do not have a large effect on the differential cross section, which is expected for the inclusive process and hence reassuring to see. The QCD scale variations in combination with statistical uncertainties are in agreement with the SM predictions.

Low $m_{\ell\ell}$ single Z boson samples

Single weak bosons, such as the Z boson, decaying leptonically can be an important background for many SM searches and BSM searches. The leptonically decaying single Z boson process can be the "signal" for a precision measurement of the Z boson or also an important background for a BSM particle which has a final state made up of leptons. As part of my qualification task I was charged with producing the low $m_{\ell\ell}$ single Z boson samples with SHERPA 2.2.11. The last samples of the low $m_{\ell\ell}$ Z boson were produced with SHERPA 2.2.1, where the phase space of interest is 10 GeV $< m_{\ell\ell} <$ 40 GeV. This low $m_{\ell\ell}$ phase space for the Z boson can be an important background for processes which produce a virtual weak boson such as the $\mathrm{H} \to \mathrm{ZZ}^* \to \ell\ell\ell\ell$ [11].

To validate the low $m_{\ell\ell}$ single Z boson samples that we have produced with SHERPA 2.2.11, we used the RIVET routines MC_ZINC_MU and MC_ZJETS_MU. In contrast to the diboson sample validation, we have validated the single Z boson samples only for the MC and not data. Initially we look at the low $m_{\ell\ell}$ samples where the Z boson decays to two muons and we compare that to the same sample but produced with SHERPA 2.2.1. The MC_ZINC_MU and MC_ZJETS_MU routines are validation RIVET routines for the $\mathrm{Z} \to \mu^+\mu^-$ + jets process with many different observables. The original routines have a mass cut on the muon pair of 66 GeV $< \mathrm{m}_{\mu\mu} <$ 116 GeV, which for the purpose of this study we have changed to 15 GeV $< \mathrm{m}_{\mu\mu} <$ 50 GeV. For both routines, there is a pseudorapidity cut on the muon of $|\eta| < 3.5$ and a transverse momentum cut of $\mathrm{p}_{\mathrm{T},\mu} >$ 25 GeV. The MC_ZJETS_MU routine has the following observables: the p_{T} of the first four leading jets, the $\Delta\eta(\mathrm{Z}, \text{jet 1})$, $\Delta\mathrm{R}(\text{jet 2}, \text{jet 3})$, the differential jet rates, the

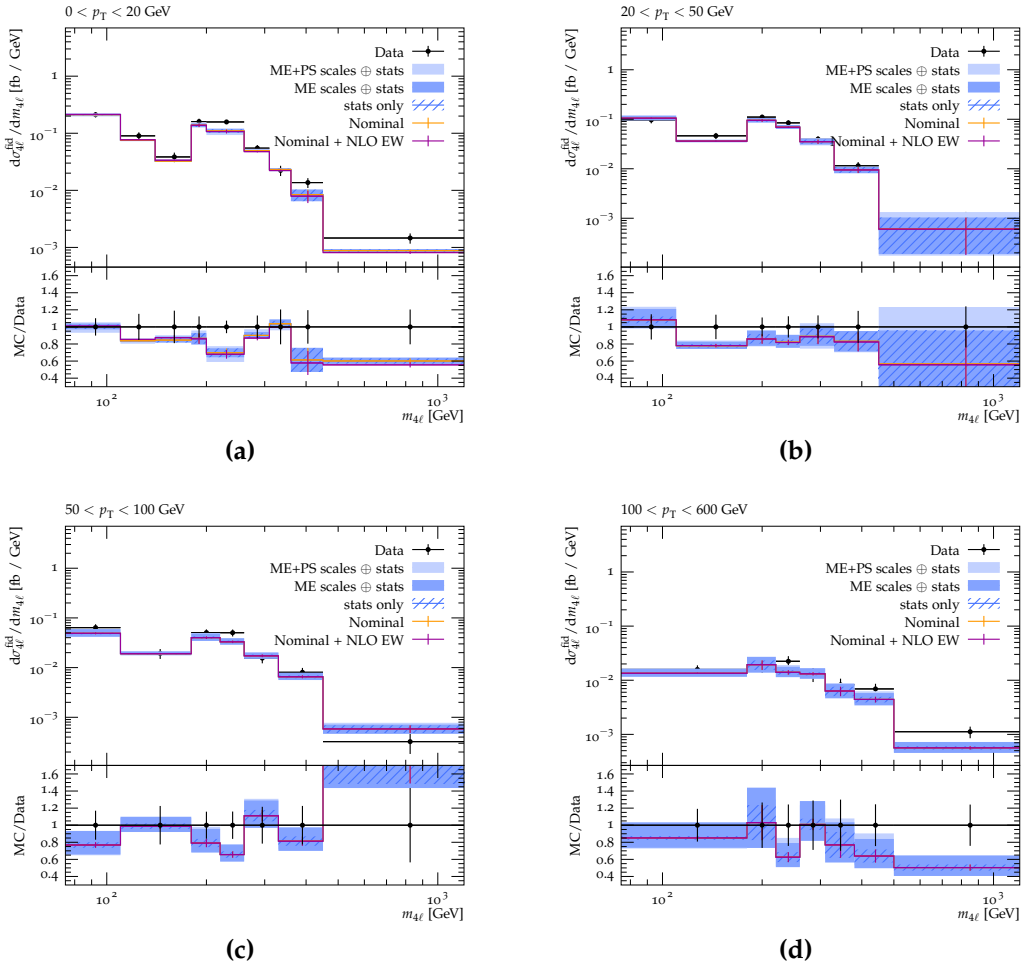

Figure B.7.: Measured differential cross section (black dots), which is unfolded, compared with the SHERPA MC simulation (coloured lines and bands) as a function of the $m_{4\ell}$ in slices of $p_T^{4\ell}$. The nominal is the $q\bar{q} \to 4\ell$ process plus the Higgs and gluon induced corrections and the nominal plus NLO virtual EW corrections include our OpenLoop generated corrections. The different shades of blue bands include statistics only, the matrix element (ME) with QCD scale variations in combination with statistics, and ME plus parton showering with QCD scale uncertainties in combination with statistics. The ratio of the particle-level MC predictions to the unfolded data is shown in the lower panels.

integrated jet rates and the invariant dimuon mass, $m_{\mu\mu}$. The MC_ZINC_MU routine has the following observables: p_{TZ}, the rapidity of the Z boson, y_Z, the azimuthal angle of Z, ϕ_Z, the lepton p_T, the lepton pseudorapidity, η, and the dimuon invariant mass, $m_{\mu\mu}$.

We see in Figures B.8a and B.8b that the dilepton invariant mass range is 30 GeV < $m_{\ell\ell}$ <50 GeV and 15 GeV $< m_{\ell\ell} <$ 35 GeV, where there is quite good agreement between SHERPA 2.2.1 and SHERPA 2.2.11 for the most part . There is also the markable drop off at 40 GeV which is what we expect, as the generator cut is at $m_{\ell\ell}$ =40 GeV. Despite this, the normalisation between the two samples appears to be slightly off (by $10\% - 15\%$) as the SHERPA 2.2.11 seems to be below that of SHERPA 2.2.1 for all bins.

In Figures B.9a and B.9b we show the leading lepton p_T and leading lepton pseudorapidity, η, for SHERPA 2.2.1 and SHERPA 2.2.11. Again, SHERPA 2.2.11 has quite a lot of statistical jitter due to the small number of events that were produced. We noticed that for the leading lepton pseudorapidity, η, it appears that SHERPA 2.2.11 has a larger contribution in the tails of the distribution but less of a contribution between $-3.2 < \eta < 3.2$ in comparison to SHERPA 2.2.1. In Figure B.9b, we see again in general that the SHERPA 2.2.11 sample has a smaller contribution than that of SHERPA 2.2.1 for the leading lepton p_T in $Z \to \mu^+\mu^-$ production.

The pattern we see throughout is that the new SHERPA 2.2.11 low $m_{\ell\ell}$ $Z \to \mu\mu$ samples have a smaller contribution to the differential cross section for these observables ($m_{\ell\ell}$, leading lepton η and p_T) than that of SHERPA 2.2.1 samples for the same process and phase space. This small offset that we see between SHERPA 2.2.1 and SHERPA 2.2.11 could be due to various reasons, however there is a large uncertainty of around 20% for low $m_{\ell\ell}$ samples. For example, SHERPA 2.2.11 has a lot of QCD improvements and the electroweak scheme is also different, so this may explain the difference.

Another way to validate the samples was to look at the transition from a low $m_{\ell\ell}$ region, 10 GeV $< m_{\ell\ell} <$ 40 GeV, to a high $m_{\ell\ell}$ region, $m_{\ell\ell} >$ 40 GeV which is shown in Figure B.10. To see the degree of smoothness of the transition, we have stacked the high $m_{\ell\ell}$ sample on top of the low $m_{\ell\ell}$ sample and we see that it is fairly smooth (within the statistical uncertainties). We did this same validation (transition from a low $m_{\ell\ell}$ region, 10 GeV $< m_{\ell\ell} <$ 40 GeV, to a high $m_{\ell\ell}$ region, $m_{\ell\ell} >$ 40 GeV) for the $Z \to ee$ process for the SHERPA 2.2.11 samples. This is shown in Figure B.11.

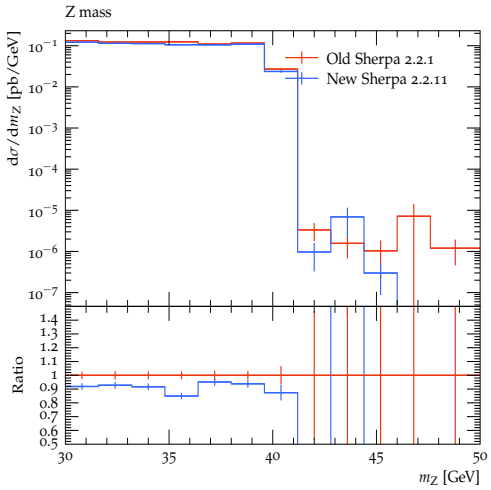

(a) The dilepton invariant mass spectrum from 30 GeV $< m_{\ell\ell} <$ 50 GeV for $Z \to \mu^+\mu^-$ production.

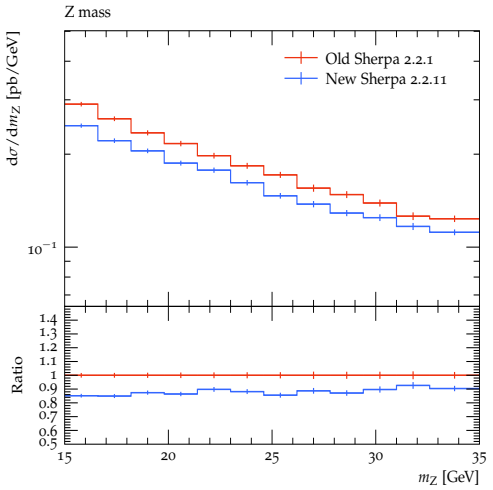

(b) The dilepton invariant mass spectrum from 15 GeV $< m_{\ell\ell} <$ 35 GeV for $Z \to \mu^+\mu^-$ production.

Figure B.8.

As well as validating the sample itself, we want to see if the uncertainty bands which we calculate appear reasonable. As in SHERPA 2.2.7 a feature of SHERPA 2.2.11 is that we are able to produce some QCD scale variations. These can be seen by the light blue band (matrix element scale variation only) and the dark blue band (matrix element and parton shower scale variation) in Figures B.12a, B.12b, B.13a and B.13b. At high p_T in the leading jet distribution of this sample, shown in Figure B.13b, we see that there are larger error bands and this could be due to extra emissions from the jets. We can take the QCD scale variations represented here by the light and dark blue bands as an approximation of the theory uncertainties of the SM without taking into account all of the systematic uncertainties.

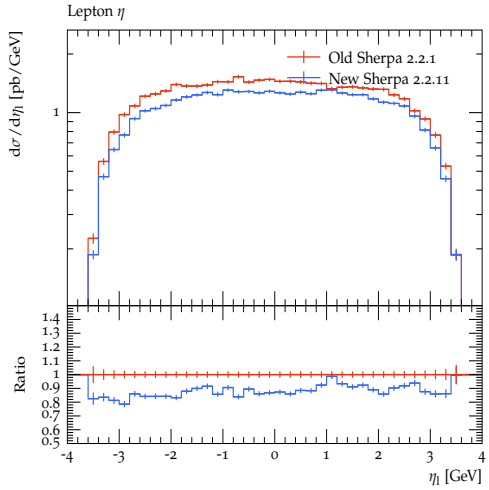

(a) The leading lepton η for $Z \to \mu^+\mu^-$ production

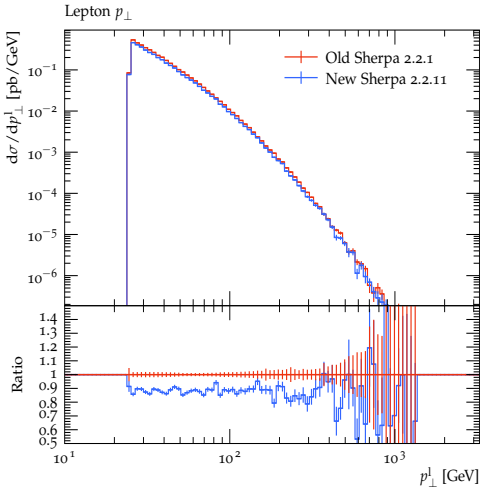

(b) The leading lepton p_T for $Z \to \mu^+\mu^-$ production

Figure B.9.

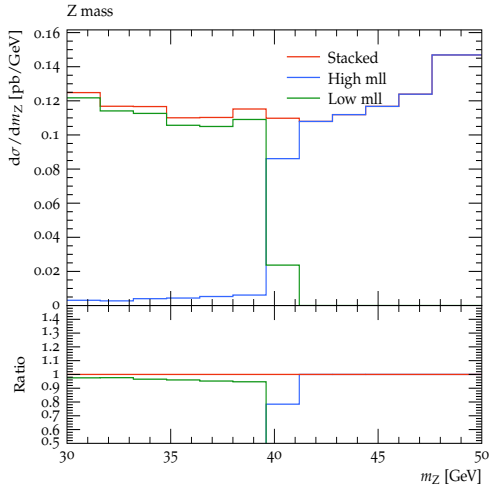

Figure B.10.: The dilepton invariant mass spectrum from 30 GeV $< m_{\ell\ell} <$ 50 GeV for $Z \to \mu^+\mu^-$ production. This is showing the transition between the low $m_{\ell\ell}$ samples to the high $m_{\ell\ell}$ samples ($m_{\ell\ell} >$ 40 GeV), with the stacked version of both showing that the transition is smooth.

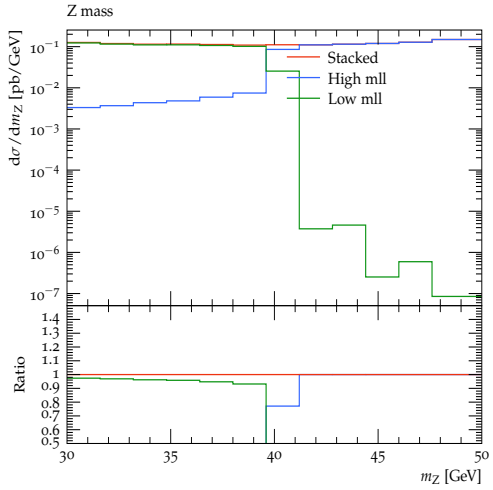

Figure B.11.: The dilepton invariant mass spectrum from 30 GeV $< m_{\ell\ell} <$ 50 GeV for $Z \to e^+e^-$ production. This is showing the transition between the low $m_{\ell\ell}$ samples to the high $m_{\ell\ell}$ samples ($m_{\ell\ell} >$ 40 GeV), with the stacked version of both showing that the transition is smooth.

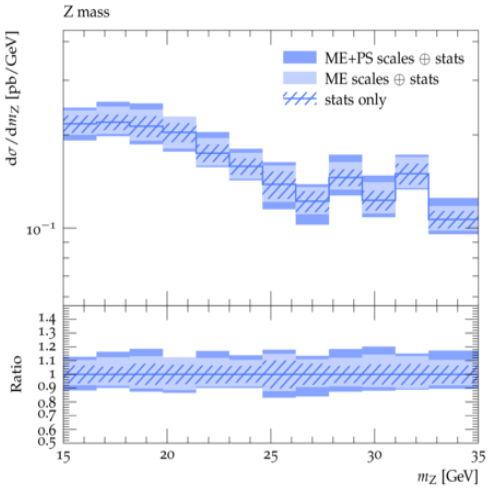

(a) The dilepton invariant mass spectrum from 15 GeV $< m_{\ell\ell} <$ 35 GeV for $Z \to \mu^+\mu^-$ production with their matrix element scale uncertainties (light blue band) and also the matrix element + parton shower scale variations (dark blue band).

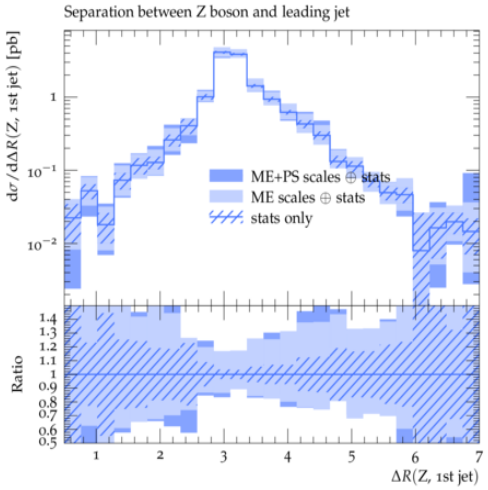

(b) The separation, ΔR, between the leading jet and the Z boson for the low $m_{\ell\ell}$ $Z \to \mu^+\mu^-$ sample with their matrix element scale uncertainties (light blue band) and also the matrix element + parton shower scale variations (dark blue band).

Figure B.12.

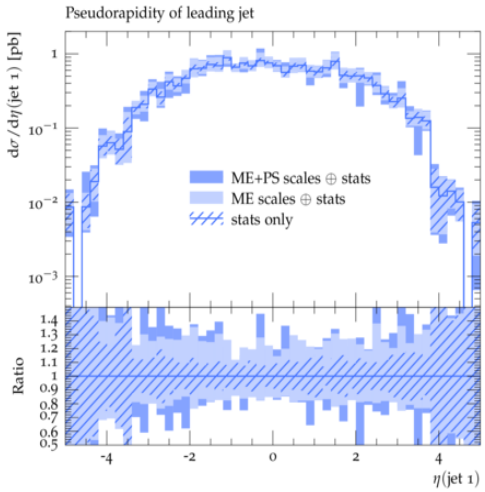

(a) The leading jet η for $Z \to \mu^+\mu^-$ production with their matrix element scale uncertainties (light blue band) and also the matrix element + parton shower scale variations (dark blue band).

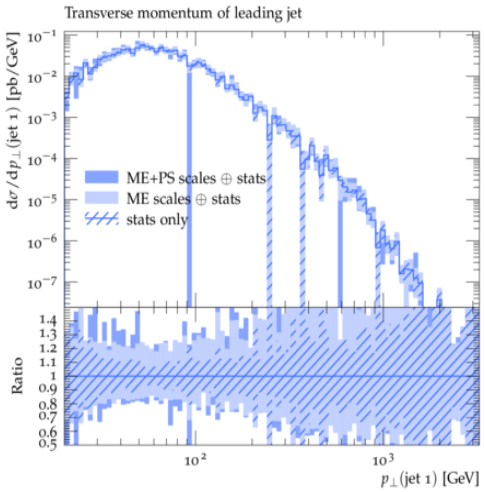

(b) The leading jet p_T for the low $m_{\ell\ell}$ $Z \to \mu^+\mu^-$ sample with their matrix element scale uncertainties (light blue band) and also the matrix element + parton shower scale variations (dark blue band).

Figure B.13.

Appendix C.

Details on the likelihood function

If we measure a random variable x that is Gaussian distributed with mean μ and a standard deviation σ, the likelihood, $\mathcal{L}$, is made up of probability density functions (pdfs) and is given by:

$$\mathcal{L}(x|\mu) = \frac{1}{\sqrt{2\pi}\sigma} e^{-\frac{1}{2}(\frac{x-\mu}{\sigma})^2} \tag{C.1}$$

If we instead conduct a number of k independent measurements, their likelihood is simply the product of all individual pdfs:

$$\begin{aligned}
\mathcal{L}(\vec{x}|\vec{\mu}) &= \prod_i \frac{1}{\sqrt{2\pi}\sigma_i} e^{-\frac{1}{2}(\frac{x_i-\mu_i}{\sigma_i})^2}, && \text{(C.2)}\\
&= \frac{1}{(\sqrt{2\pi})^k \prod_i \sigma_i} e^{-\frac{1}{2}\sum_i(\frac{x_i-\mu_i}{\sigma_i})^2}, && \text{(C.3)}\\
&= \frac{1}{(\sqrt{2\pi})^k \prod_i \sqrt{\sigma_i^2}} e^{-\frac{1}{2}\sum_i(\frac{x_i-\mu_i}{\sigma_i})^2}, && \text{(C.4)}\\
&= \frac{1}{(\sqrt{2\pi})^k \sqrt{\prod_i \sigma_i^2}} e^{-\frac{1}{2}\sum_i(\frac{x_i-\mu_i}{\sigma_i})^2}. && \text{(C.5)}
\end{aligned}$$

Defining σ as a matrix of variances that is diagonal because all measurements are uncorrelated we can obtain:

$$\mathcal{L}(\vec{x}|\vec{\mu}) = \frac{1}{(\sqrt{2\pi})^k \sqrt{\det\left(\sigma_i^2\right)}} e^{-\frac{1}{2}(\vec{x}-\vec{\mu})^\dagger (\sigma^2)^{-1}(\vec{x}-\vec{\mu})} \tag{C.6}$$

However in normal circumstances, not all measurements will be uncorrelated. As a consequence, a change of basis is needed according the transformation:

$$\vec{x} \to \vec{x}^{'} := \mathbf{U}\vec{x}, \tag{C.7}$$
$$\vec{x}^{\mathrm{T}} \to \vec{x}^{'\mathrm{T}} := \vec{x}^{\mathrm{T}}\mathbf{U}^{\mathrm{T}}, \tag{C.8}$$
$$\vec{\mu} \to \vec{\mu}^{'T} := \mathbf{U}\vec{\mu}, \tag{C.9}$$
$$\vec{\mu}^{T} \to \vec{\mu}^{'\mathrm{T}} := \vec{\mu}^{\mathrm{T}}\mathbf{U}^{\mathrm{T}}, \tag{C.10}$$
$$\sigma^2 \to \mathbf{U}\sigma^2\mathbf{U}^{\mathrm{T}} := \mathrm{Cov} \tag{C.11}$$

with the transformation matrix $\mathbf{U}$. Therefore σ^2 is transformed into a matrix with off-diagonal elements which reflects both the degree of variance and also the degree of correlation. This is known as the covariance matrix.

The likelihood therefore looks like:

$$\mathcal{L}(\vec{x}^{'}|\vec{\mu}^{'}) = \frac{1}{(\sqrt{2\pi})^k \sqrt{\det\left(\mathrm{Cov}\right)}} \cdot e^{-\frac{1}{2}(\vec{x}^{'}-\vec{\mu}^{'})^{\mathrm{T}}(\mathrm{Cov}^{-1})(\vec{x}^{'}-\vec{\mu}^{'})}. \tag{C.12}$$

Theoretically speaking, we are modelling a multi-dimensional normal distribution which is stretched and rotated by a linear transformation. The likelihood of our measurements is evaluated by undoing this transformation and comparing to normal distributions. The appearance of the determinant can be understood intuitively: if the measurement is performed in a basis where all individual components are independent and normally distributed, the pdfs is simply a product of k normal pdfs. The covariance matrix instructs how to change the basis, stretching and rotating the space. To ensures that the total pdf integrates to unity, a factor is required which reflects that the space is now denser or sparser. This is the function of the determinant: taking a shape with area A and transforming it linearly with matrix M will result in an area of the transformed shape of $\det \mathrm{M} \cdot \mathrm{A}$. In the last step, we can add systematic

uncertainties, θ, to the likelihood with a Gaussian constraint:

$$\mathcal{L}(\vec{x}^{\,\prime}|\vec{\mu}^{\,\prime},\vec{\theta}) = \frac{1}{(\sqrt{2\pi})^k\sqrt{\det\left(\mathrm{Cov}\right)}} \cdot e^{-\frac{1}{2}(\vec{x}^{\,\prime}-\vec{\mu}^{\,\prime})^{\mathrm{T}}(\mathrm{Cov}^{-1})(\vec{x}^{\,\prime}-\vec{\mu}^{\,\prime})} \cdot \prod_i \mathcal{G}(\theta^{(i)}). \quad \text{(C.13)}$$

Appendix D.

Correlation Matrices

In this Chapter, the correlation matrices for the data and SM predictions from Section 5.5 are studied. The correlations between different regions are calculated using the Pearson correlation coefficient which is commonly represented by r_{xy}. Given paired data $\{(x_1, y_1), ..., (x_n, y_n)\}$ which consists of n pairs, r_{xy}, is defined as:

$$r_{xy} = \frac{\sum_{i=1}^{n}(x_i - \overline{x})(y_i - \overline{y})}{\sqrt{\sum_{i=1}^{n}(x_i - \overline{x})^2}\sqrt{\sum_{i=1}^{n}(y_i - \overline{y})^2}}, \tag{D.1}$$

where n is the number of bins, x_i and y_i are the individual bin contents indexed with i, and $\overline{x} = \frac{1}{n}\sum_{i=1}^{n} x_i$ is the mean (analogously for $\overline{y}$).

In Figures D.1a and D.1b the correlation matrices are shown for the differential cross-section as a function of $p_{\mathrm{T}}^{\mathrm{miss}}$ in the ≥ 1 jet phase-space for all regions ($p_{\mathrm{T}}^{\mathrm{miss}}$ + jets + auxiliary regions). As is shown, the different regions for the differential cross-section are highly correlated to each other for both the SM prediction and the data, with the lowest correlation coefficient being $r_{xy,SM} = 0.9959$ and $r_{xy,data} = 0.9954$ for the $p_{\mathrm{T}}^{\mathrm{miss}}$ + jets region and the one electron region.

In Figures D.2a and D.2b the correlation matrices are shown for the R^{miss} as a function of $p_{\mathrm{T}}^{\mathrm{miss}}$ in the ≥ 1 jet phase-space for all regions ($p_{\mathrm{T}}^{\mathrm{miss}}$ + jets + auxiliary regions). As is shown, the different regions for the R^{miss} are highly correlated to each other for both the SM prediction and the data. The lowest correlation coefficient for the SM prediction is $r_{xy,SM} = 0.9937$ for the one electron and two electron region, whereas the lowest correlation coefficient for the data is for the one muon and two electron region with a value of $r_{xy,data} = 0.9552$.

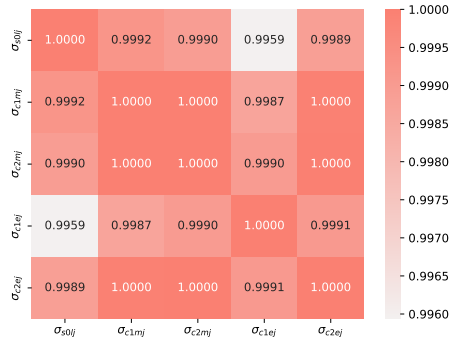

(a) The correlation matrix of the differential cross-section for $p_{\mathrm{T}}^{\mathrm{miss}}$ for the SM prediction, in all regions of the ≥ 1 jet phase-space. The correlations between different regions are calculated using the Pearson correlation coefficient.

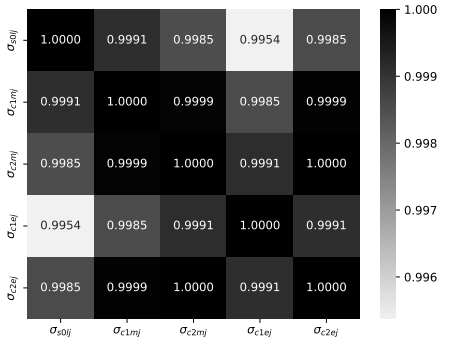

(b) The correlation matrix of the differential cross-section for $p_{\mathrm{T}}^{\mathrm{miss}}$ for data, in all regions of the ≥ 1 jet phase-space. The correlations between different regions are calculated using the Pearson correlation coefficient.

Figure D.1.

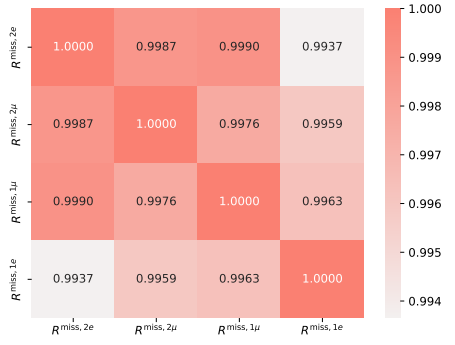

(a) The correlation matrix of the R^{miss} for $p_{\mathrm{T}}^{\mathrm{miss}}$ for the SM prediction, in all regions of the ≥ 1 jet phase-space.

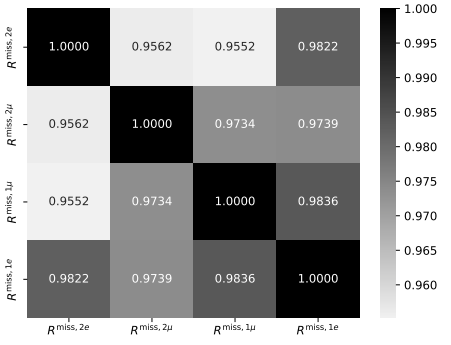

(b) The correlation matrix of the R^{miss} for $p_{\mathrm{T}}^{\mathrm{miss}}$ for data, in all regions of the ≥ 1 jet phase-space.

Figure D.2.

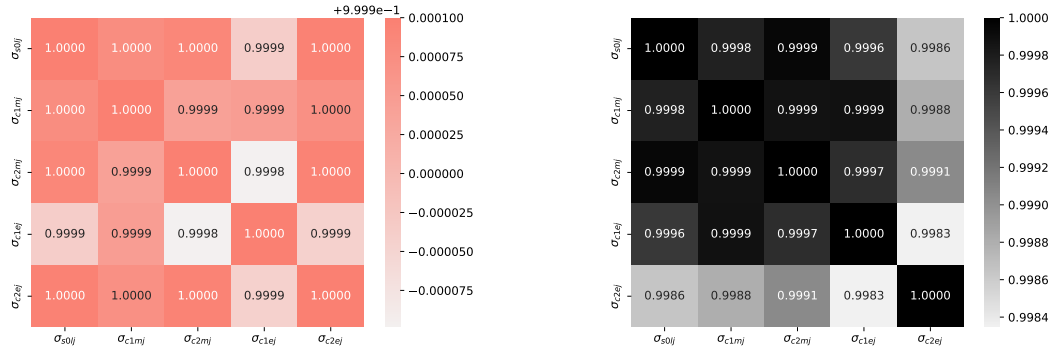

(a) The correlation matrix of the differential cross-section for m_{jj} for the SM prediction, in all regions of the VBF phase-space.

(b) The correlation matrix of the differential cross-section for m_{jj} for data, in all regions of the VBF phase-space.

Figure D.3.

In Figures D.3a and D.3b the correlation matrices are shown for the differential cross-sections as a function of m_{jj} in the VBF phase-space for all regions ($p_{\mathrm{T}}^{\mathrm{miss}}$ + jets + auxiliary regions). As is shown, the different regions for the m_{jj} differential cross-sections are highly correlated to each other for both the SM prediction and the data. The lowest correlation coefficient for SM is $r_{xy,SM} = 0.9998$ for the one electron and two muon region, whereas the lowest correlation coefficient for the data is for the one electron and two electron region with a value of $r_{xy,data} = 0.9983$.

In Figures D.4a and D.4b the correlation matrices are shown for the R^{miss} as a function of m_{jj} in the VBF phase-space for all regions ($p_{\mathrm{T}}^{\mathrm{miss}}$ + jets + auxiliary regions). As is shown, the different regions for the R^{miss} are highly correlated to each other for the SM prediction but this is not the case for the data. The lowest correlation coefficient for SM is $r_{xy,SM} = 0.9514$ for the one electron and two muon region, whereas the lowest correlation coefficient for the data is for the one muon and two electron region with a value of $r_{xy,data} = -0.4463$, meaning in fact these two regions are anti-correlated. This is likely due to the fact that the one muon region in $R^{\mathrm{miss}}(m_{jj})$ for data and SM has a flat shape and good agreement, whereas the two muon region has some variation, as well as some disagreement between the data and the SM prediction.

In Figures D.5a and D.5b the correlation matrices are shown for the differential cross-sections as a function of $\Delta\phi_{jj}$ in the ≥ 2 jet phase-space for all regions ($p_{\mathrm{T}}^{\mathrm{miss}}$ + jets + auxiliary regions). As is shown, the different regions for the $\Delta\phi_{jj}$ differential cross-sections are highly correlated to each other for both the SM prediction and the data,

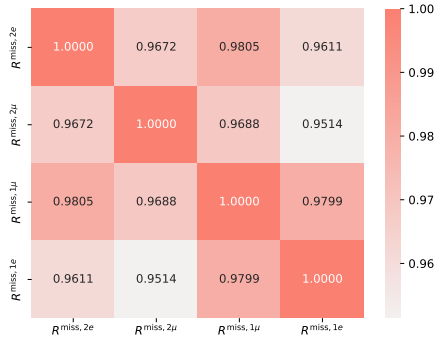

(a) The correlation matrix of the R^{miss} for m_{jj} for the SM prediction, in all regions of the VBF phase-space.

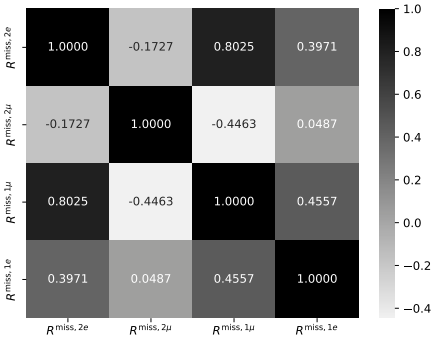

(b) The correlation matrix of the R^{miss} for m_{jj} for data, in all regions of the VBF phase-space.

Figure D.4.

with the lowest correlation coefficients being $r_{xy,SM} = 0.9280$ and $r_{xy,data} = 0.9358$ for the one electron region and the two muon regions.

In Figures D.6a and D.6b the correlation matrices are shown for the R^{miss} as a function of $\Delta\phi_{jj}$ in the ≥ 2 jet phase-space for all regions ($p_{\text{T}}^{\text{miss}}$ + jets + auxiliary regions). As the Figures show, the one lepton regions are highly correlated with each other and the same goes for the two lepton regions, however the one lepton region has an anti-correlation with the two lepton region. This has a clear pattern in the Figures, with the top left and bottom right quadrant being highly correlated (darker red) whereas the top right and bottom left quadrant have a negative correlation (indicated with much lighter red). It is obvious why when looking at the R^{miss} distributions in Section 5.5, where for the two lepton regions the tail of the distribution has a distinct upward trend which is not present in the one lepton regions. As this pattern is present for both the SM prediction and the data, it suggests that this may be due to some kinematic differences between the $p_{\text{T}}^{\text{miss}}$ + jets / one lepton regions and the two lepton regions caused by the different behaviour of the W+jets and Z+jets processes. In Z+jets events with exactly two leptons and large $p_{\text{T}}^{\text{miss}}$, the $\Delta\phi_{jj}$ distribution between the two leading jets tends to exhibit a back-to-back configuration due to the conservation of momentum. This leads to a $\Delta\phi_{jj}$ distribution that is expected to peak around π radians as is shown in Section 5.5, whereas the W+jets events tend to have a more isotropic distribution due to the fact that some of the $p_{\text{T}}^{\text{miss}}$ is carried away by the neutrino.

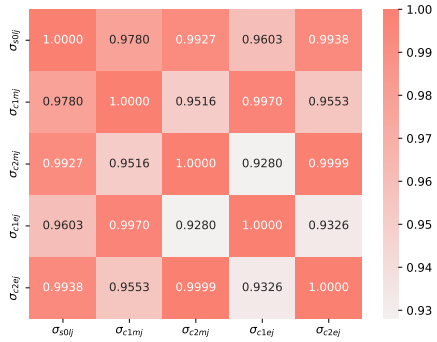

(a) The correlation matrix of the differential cross-section for $\Delta\phi_{jj}$ for the SM prediction, in all regions of the ≥ 2 jet phase-space.

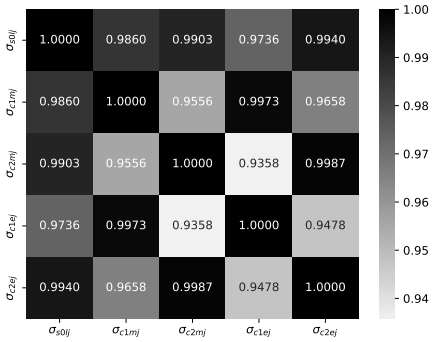

(b) The correlation matrix of the differential cross-section for $\Delta\phi_{jj}$ for data, in all regions of the ≥ 2 jet phase-space.

Figure D.5.

(a) The correlation matrix of the R^{miss} for $\Delta\phi_{jj}$ for the SM prediction, in all regions of the ≥ 2 jet phase-space.

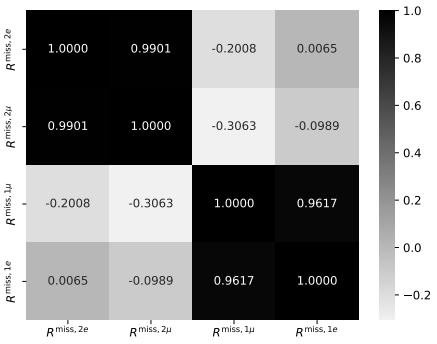

(b) The correlation matrix of the R^{miss} for $\Delta\phi_{jj}$ for data, in all regions of the ≥ 2 jet phase-space.

Figure D.6.

Colophon

This thesis was made in LaTeX 2_ε using the "hepthesis" class [218].

Bibliography

[1] E. D. Bloom *et al.*, Phys. Rev. Lett. **2**3, 930 (1969).

[2] M. Breidenbach *et al.*, Phys. Rev. Lett. **2**3, 935 (1969).

[3] F. J. Hasert *et al.*, Phys. Lett. B **4**6, 121 (1973).

[4] Gargamelle Neutrino, F. J. Hasert *et al.*, Phys. Lett. B **4**6, 138 (1973).

[5] Gargamelle Neutrino, F. J. Hasert *et al.*, Nucl. Phys. B **7**3, 1 (1974).

[6] M. K. Gaillard, P. D. Grannis, and F. J. Sciulli, Rev. Mod. Phys. **7**1, S96 (1999), hep-ph/9812285.

[7] B. R. Stella and H.-J. Meyer, Eur. Phys. J. H **3**6, 203 (2011), 1008.1869.

[8] CDF Collaboration, F. Abe *et al.*, Phys. Rev. Lett. **7**4, 2626 (1995).

[9] D0 Collaboration, S. Abachi *et al.*, Phys. Rev. Lett. **7**4, 2632 (1995).

[10] DONUT, K. Kodama *et al.*, Phys. Lett. B **5**04, 218 (2001), hep-ex/0012035.

[11] ATLAS, G. Aad *et al.*, Phys. Lett. B **7**16, 1 (2012), 1207.7214.

[12] CMS, S. Chatrchyan *et al.*, Phys. Lett. B **7**16, 30 (2012), 1207.7235.

[13] E. Sather, SLAC Beam Line **2**6N1, 31 (1996).

[14] A. Einstein and J. J. e. a. Stachel, *The collected papers of Albert Einstein: English translation supplement* (Princeton Univ. Press, Princeton, NJ, 1987), Every document in The Collected Papers of Albert Einstein appears in the language in which it was written, and the supplementary paperback volumes present the English translations of all non-English materials. This translation does not include notes or annotation of the documentary volume and is not intended for use without the original language documentary edition which provides the extensive editorial commentary necessary for a full historical and scientific understanding

of the documents.

[15] P. J. E. Peebles and B. Ratra, Rev. Mod. Phys. **7**5, 559 (2003).

[16] ALEPH, DELPHI, L3, OPAL, SLD, LEP Electroweak Working Group, SLD Electroweak Group, SLD Heavy Flavour Group, S. Schael *et al.*, Phys. Rept. **4**27, 257 (2006), hep-ex/0509008.

[17] Q. L. He *et al.*, Science **3**57, 294 (2017), 1606.05712.

[18] C. Amsler *et al.*, Physics Letters B **6**67, 1 (2008), Review of Particle Physics.

[19] J. Ellis, Higgs Physics, in *2013 European School of High-Energy Physics*, pp. 117–168, 2015, 1312.5672.

[20] K. C. Freeman, Astrophys. J. **1**60, 811 (1970).

[21] V. C. Rubin and W. K. Ford, Jr., Astrophys. J. **1**59, 379 (1970).

[22] V. Springel, C. S. Frenk, and S. D. M. White, Nature **4**40, 1137 (2006), astro-ph/0604561.

[23] WMAP, G. Hinshaw *et al.*, Astrophys. J. Suppl. **1**80, 225 (2009), 0803.0732.

[24] D. Walsh, R. F. Carswell, and R. J. Weymann, Nature **2**79, 381 (1979).

[25] A. S. Bolton *et al.*, Astrophys. J. **6**82, 964 (2008), 0805.1931.

[26] F. De Paolis, G. Ingrosso, P. Jetzer, and M. Roncadelli, (1998), astro-ph/9803200.

[27] F. De Paolis, G. Ingrosso, P. Jetzer, and M. Roncadelli, Astrophys. J. **5**00, 59 (1998), astro-ph/9801126.

[28] T. Nakamura, M. Sasaki, T. Tanaka, and K. S. Thorne, Astrophys. J. Lett. **4**87, L139 (1997), astro-ph/9708060.

[29] Macho, R. A. Allsman *et al.*, Astrophys. J. Lett. **5**50, L169 (2001), astro-ph/0011506.

[30] K. Jedamzik, Phys. Rept. **3**07, 155 (1998), astro-ph/9805147.

[31] J. Yokoyama, Astron. Astrophys. **3**18, 673 (1997), astro-ph/9509027.

[32] A. Venkatesan, A. V. Olinto, and J. W. Truran, Astrophys. J. **5**16, 863 (1999), astro-ph/9705091.

[33] M. Milgrom, Astrophys. J. **270**, 365 (1983).

[34] S. S. McGaugh, Can. J. Phys. **93**, 250 (2015), 1404.7525.

[35] P. Kroupa, M. Pawlowski, and M. Milgrom, Int. J. Mod. Phys. D **21**, 1230003 (2012), 1301.3907.

[36] U. Seljak, A. Makarov, P. McDonald, and H. Trac, Phys. Rev. Lett. **97**, 191303 (2006), astro-ph/0602430.

[37] A. Boyarsky, M. Drewes, T. Lasserre, S. Mertens, and O. Ruchayskiy, Prog. Part. Nucl. Phys. **104**, 1 (2019), 1807.07938.

[38] EROS, C. Renault *et al.*, (1996), astro-ph/9612102.

[39] M. A. Monroy-Rodríguez and C. Allen, Astrophys. J. **790**, 159 (2014), 1406.5169.

[40] S. Dodelson, Int. J. Mod. Phys. D **20**, 2749 (2011), 1112.1320.

[41] Super-Kamiokande, K. Abe *et al.*, Phys. Rev. D **91**, 052019 (2015), 1410.2008.

[42] MINOS, P. Adamson *et al.*, Phys. Rev. Lett. **107**, 011802 (2011), 1104.3922.

[43] A. Salam and J. A. Strathdee, Phys. Lett. B **51**, 353 (1974).

[44] J. Wess and B. Zumino, Nucl. Phys. B **70**, 39 (1974).

[45] J.-L. Gervais and B. Sakita, Nucl. Phys. B **34**, 632 (1971).

[46] D. V. Volkov and V. P. Akulov, JETP Lett. **16**, 438 (1972).

[47] S. Dimopoulos, S. Raby, and F. Wilczek, Phys. Rev. D **24**, 1681 (1981).

[48] S. Dimopoulos and H. Georgi, Nucl. Phys. B **193**, 150 (1981).

[49] C. Csaki, Mod. Phys. Lett. A **11**, 599 (1996), hep-ph/9606414.

[50] B. S. Acharya, G. Kane, S. Watson, and P. Kumar, Phys. Rev. D **80**, 083529 (2009), 0908.2430.

[51] G. Jungman, M. Kamionkowski, and K. Griest, Phys. Rept. **267**, 195 (1996), hep-ph/9506380.

[52] D. Abercrombie *et al.*, Physics of the Dark Universe **27**, 100371 (2020).

[53] K. Agashe, R. Contino, and A. Pomarol, Nucl. Phys. B **719**, 165 (2005), hep-

ph/0412089.

[54] H. Georgi and D. B. Kaplan, Phys. Lett. B **1**45, 216 (1984).

[55] O. Buchmueller, M. J. Dolan, S. A. Malik, and C. McCabe, JHEP **0**1, 037 (2015), 1407.8257.

[56] M. R. Buckley, D. Feld, and D. Goncalves, Phys. Rev. D **9**1, 015017 (2015), 1410.6497.

[57] P. Harris, V. V. Khoze, M. Spannowsky, and C. Williams, Phys. Rev. D **9**1, 055009 (2015), 1411.0535.

[58] U. Haisch and E. Re, JHEP **0**6, 078 (2015), 1503.00691.

[59] M. Papucci, A. Vichi, and K. M. Zurek, JHEP **1**1, 024 (2014), 1402.2285.

[60] Y. Bai and J. Berger, JHEP **1**1, 171 (2013), 1308.0612.

[61] A. Boveia *et al.*, Phys. Dark Univ. **2**7, 100365 (2020), 1603.04156.

[62] Planck, N. Aghanim *et al.*, Astron. Astrophys. **6**41, A6 (2020), 1807.06209, [Erratum: Astron.Astrophys. 652, C4 (2021)].

[63] WMAP, C. L. Bennett *et al.*, Astrophys. J. Suppl. **2**08, 20 (2013), 1212.5225.

[64] ATLAS, G. Aad *et al.*, Phys. Rev. D **1**03, 112006 (2021), 2102.10874.

[65] G. Arcadi, A. Djouadi, and M. Raidal, Phys. Rept. **8**42, 1 (2020), 1903.03616.

[66] C. P. Burgess, M. Pospelov, and T. ter Veldhuis, Nucl. Phys. B **6**19, 709 (2001), hep-ph/0011335.

[67] Y. G. Kim and K. Y. Lee, Phys. Rev. D **7**5, 115012 (2007).

[68] J. McDonald, Phys. Rev. D **5**0, 3637 (1994), hep-ph/0702143.

[69] M. Zaazoua, L. Truong, K. A. Assamagan, and F. Fassi, LHEP **2**022, 270 (2022), 2107.01252.

[70] CRESST, A. H. Abdelhameed *et al.*, Phys. Rev. D **1**00, 102002 (2019), 1904.00498.

[71] DarkSide, P. Agnes *et al.*, Phys. Rev. Lett. **1**21, 081307 (2018), 1802.06994.

[72] PandaX-4T, Y. Meng *et al.*, Phys. Rev. Lett. **1**27, 261802 (2021), 2107.13438.

[73] J. Billard, L. Strigari, and E. Figueroa-Feliciano, Phys. Rev. D **89**, 023524 (2014), 1307.5458.

[74] F. Ruppin, J. Billard, E. Figueroa-Feliciano, and L. Strigari, Phys. Rev. D **90**, 083510 (2014), 1408.3581.

[75] CERN, LHC, https://home.cern/science/accelerators/large-hadron-collider, 2022, Accessed: 2022-04-13.

[76] R. Assmann, M. Lamont, and S. Myers, Nucl. Phys. B Proc. Suppl. **109**, 17 (2002).

[77] A. Schaeffer, Waltz of the LHC magnets has begun, https://home.cern/news/news/accelerators/waltz-lhc-magnets-has-begun, Accessed: 2023-05-01.

[78] CERN, Pulling together: Superconducting electromagnets, https://home.cern/science/engineering/pulling-together-superconducting-electromagnets, Accessed: 2023-05-01.

[79] UCL HEP, The LHC supermagnets and cooling system, https://www.hep.ucl.ac.uk/undergrad-projects/3rdyear/PPguide/cool.htm, Accessed: 2023-05-01.

[80] CERN, Cryogenics: Low temperatures, high performance, https://home.cern/science/engineering/cryogenics-low-temperatures-high-performance, Accessed: 2023-05-01.

[81] CERN, Time for lead collisions in the LHC, https://home.cern/news/news/accelerators/time-lead-collisions-lhc, 2023, Accessed: 2023-05-01.

[82] LHC report: full house for the LHC, https://home.cern/news/news/accelerators/lhc-report-full-house-lhc, Accessed: 2023-05-01.

[83] Linear accelerator 4, https://home.cern/science/accelerators/linear-accelerator-4, Accessed: 2023-05-01.

[84] The Proton Synchrotron Booster, https://home.cern/science/accelerators/proton-synchrotron-booster, Accessed: 2023-05-01.

[85] The Proton Synchrotron, https://home.cern/science/accelerators/proton-synchrotron, Accessed: 2023-05-01.

[86] The Super Proton Synchrotron, https://home.cern/science/accelerators/

super-proton-synchrotron, Accessed: 2023-05-01.

[87] R. Vanden Broeck, THE CERN ACCELERATOR COMPLEX. Complexe des accelerateurs du CERN, 2019.

[88] G. Apollinari, O. Brüning, T. Nakamoto, and L. Rossi, CERN Yellow Rep. , 1 (2015), 1705.08830.

[89] I. Zurbano Fernandez *et al.*, High-Luminosity Large Hadron Collider (HL-LHC): Technical design report, https://cds.cern.ch/record/2749422?ln=en, 2020.

[90] ATLAS, G. Aad *et al.*, JINST **15**, P04003 (2020), 1911.04632.

[91] ATLAS, G. Aad *et al.*, JINST **3**, S08003 (2008).

[92] Detector & Technology, https://atlas.cern/Discover/Detector.

[93] C. AC, Layout of ATLAS. Dessin representant le detecteur ATLAS, https://cds.cern.ch/record/39038, 1998, Accessed: 2023-05-01.

[94] The inner detector, https://atlas.cern/Discover/Detector/Inner-Detector#:~:text=The%20Inner%20Detector%20measures%20the,Transition%20Radiation%20Tracker%20(TRT)., Accessed: 2023-05-01.

[95] ATLAS Collaboration, The inner detector, https://atlas.cern/Discover/Detector/Inner-Detector, n.d., Accessed: 2023-05-01.

[96] ATLAS Collaboration, ATLAS inner detector: Technical design report. Vol. 1, https://cds.cern.ch/record/331063?ln=en, 1997.

[97] ATLAS IBL, B. Abbott *et al.*, JINST **13**, T05008 (2018), 1803.00844.

[98] ATLAS, G. Aad *et al.*, JINST **9**, P08009 (2014), 1404.7473.

[99] ATLAS TRT, V. A. Mitsou, The ATLAS transition radiation tracker, in *8th International Conference on Advanced Technology and Particle Physics (ICATPP 2003): Astroparticle, Particle, Space Physics, Detectors and Medical Physics Applications*, pp. 497–501, 2003, hep-ex/0311058.

[100] Calorimeter, https://atlas.cern/Discover/Detector/Calorimeter.

[101] ATLAS, G. Aad *et al.*, JINST **3**, S08003 (2008).

[102] J. Pequenao, Computer Generated image of the ATLAS calorimeter, https:

//cds.cern.ch/record/1095927, 2008.

[103] A. Artamonov *et al.*, JINST **3**, P02010 (2008).

[104] Muon Spectrometer, https://atlas.cern/Discover/Detector/Muon-Spectrometer.

[105] J. Pequenao, Computer generated image of the ATLAS Muons subsystem, https://cds.cern.ch/record/1095929, 2008.

[106] ATLAS Collaboration, C. Bernius and A. Collaboration, JINST **15**, C09009 (2020), 2007.03460.

[107] Trigger and Data Acquisition System, https://atlas.cern/Discover/Detector/Trigger-DAQ.

[108] ATLAS, W. Panduro Vazquez, J. Phys. Conf. Ser. **898**, 032017 (2017).

[109] M. Cacciari, G. P. Salam, and G. Soyez, JHEP **04**, 063 (2008), 0802.1189.

[110] J. Pequenao and P. Schaffner, How ATLAS detects particles: diagram of particle paths in the detector, https://cds.cern.ch/record/1505342, 2013.

[111] ATLAS, G. Aad *et al.*, Eur. Phys. J. C **77**, 490 (2017), 1603.02934.

[112] ATLAS, G. Aad *et al.*, Eur. Phys. J. C **81**, 689 (2021), 2007.02645.

[113] ATLAS, M. Aaboud *et al.*, Eur. Phys. J. C **80**, 1104 (2020), 1910.04482.

[114] ATLAS, M. Aaboud *et al.*, Eur. Phys. J. C **77**, 466 (2017), 1703.10485.

[115] ATLAS, G. Aad *et al.*, Eur. Phys. J. C **72**, 1844 (2012), 1108.5602.

[116] ATLAS, G. Aad *et al.*, Eur. Phys. J. C **77**, 241 (2017), 1609.09324.

[117] ATLAS, M. Aaboud *et al.*, Eur. Phys. J. C **78**, 903 (2018), 1802.08168.

[118] Tomiwa, KG and Mellado, Xifeng Ruan Bruce, Mitigating the effect of fake missing energy using Machine learning technique in the ATLAS experiment, https://events.saip.org.za/event/100/papers/223/files/201-Tomiwa_ID_126_SAIP2018.pdf.

[119] ATLAS, M. Aaboud *et al.*, Eur. Phys. J. C **77**, 765 (2017), 1707.03263.

[120] F. U. Bernlochner *et al.*, Phys. Lett. B **790**, 372 (2019), 1808.06577.

[121] R. Atkin, J. Phys. Conf. Ser. **6**45, 012008 (2015).

[122] ATLAS, G. Aad *et al.*, JINST **1**4, P12006 (2019), 1908.00005.

[123] ATLAS, G. Aad *et al.*, Eur. Phys. J. C **8**1, 578 (2021), 2012.00578.

[124] ATLAS, S. Rettie, PoS **D**IS2018, 097 (2018).

[125] ATLAS, G. Aad *et al.*, Eur. Phys. J. C **7**6, 581 (2016), 1510.03823.

[126] E. Nurse *et al.*, Detector-corrected cross-sections in events with large missing transverse momentum in association with jets, https://cds.cern.ch/record/2702246, 2019.

[127] ATLAS Collaboration, Tools for estimating fake/non-prompt lepton backgrounds with the ATLAS detector at the LHC, https://inspirehep.net/literature/2605175, 2022, CERN-EP-2022-214.

[128] ATLAS Collaboration, Luminosity determination in pp collisions at $\sqrt{s} = 13$ TeV using the ATLAS detector at the LHC, https://cds.cern.ch/record/2677054, 2019, ATLAS-CONF-2019-021.

[129] T. A. Collaboration, Annual plots on the number of interactions per crossing (mu) and the integrated luminosity delivered by atlas, https://twiki.cern.ch/twiki/bin/view/AtlasPublic/LuminosityPublicResultsRun2, 2021.

[130] R. Frederix and S. Frixione, JHEP **1**2, 061 (2012), 1209.6215.

[131] S. Hoeche, F. Krauss, M. Schonherr, and F. Siegert, JHEP **0**4, 027 (2013), 1207.5030.

[132] L. Lönnblad and S. Prestel, JHEP **0**3, 166 (2013), 1211.7278.

[133] S. Plätzer, JHEP **0**8, 114 (2013), 1211.5467.

[134] B. R. Webber, Nucl. Phys. B **2**38, 492 (1984).

[135] B. Andersson, G. Gustafson, G. Ingelman, and T. Sjostrand, Phys. Rept. **9**7, 31 (1983).

[136] M. Cacciari, G. P. Salam, and G. Soyez, JHEP **0**4, 063 (2008), 0802.1189.

[137] S. Catani, Y. L. Dokshitzer, M. H. Seymour, and B. R. Webber, Nucl. Phys. B **4**06, 187 (1993).

[138] S. Bentvelsen and I. Meyer, Eur. Phys. J. C **4**, 623 (1998), hep-ph/9803322.

[139] J. C. Collins, D. E. Soper, and G. F. Sterman, Nucl. Phys. B **3**08, 833 (1988).

[140] J. C. Collins, D. E. Soper, and G. F. Sterman, Adv. Ser. Direct. High Energy Phys. **5**, 1 (1989), hep-ph/0409313.

[141] GEANT4, S. Agostinelli *et al.*, Nucl. Instrum. Meth. **A**506, 250 (2003).

[142] Geant4 collaboration, J. Allison *et al.*, IEEE Trans.Nucl.Sci. **5**3, 270 (2006).

[143] T. Sjostrand, S. Mrenna, and P. Z. Skands, Comput. Phys. Commun. **1**78, 852 (2008), 0710.3820.

[144] R. D. Ball *et al.*, Nucl. Phys. B **8**67, 244 (2013), 1207.1303.

[145] ATLAS, The Pythia 8 A3 tune description of ATLAS minimum bias and inelastic measurements incorporating the Donnachie-Landshoff diffractive model, https://cds.cern.ch/record/2206965?ln=en, 2016.

[146] T. Gleisberg *et al.*, JHEP **0**2, 007 (2009), 0811.4622.

[147] T. Gleisberg and S. Hoeche, JHEP **1**2, 039 (2008), 0808.3674.

[148] F. Cascioli, P. Maierhofer, and S. Pozzorini, Phys. Rev. Lett. **1**08, 111601 (2012), 1111.5206.

[149] A. Denner, S. Dittmaier, and L. Hofer, Comput. Phys. Commun. **2**12, 220 (2017), 1604.06792.

[150] S. Schumann and F. Krauss, JHEP **0**3, 038 (2008), 0709.1027.

[151] J.-C. Winter, F. Krauss, and G. Soff, Eur. Phys. J. C **3**6, 381 (2004), hep-ph/0311085.

[152] NNPDF, R. D. Ball *et al.*, JHEP **0**4, 040 (2015), 1410.8849.

[153] S. Hoeche, F. Krauss, M. Schonherr, and F. Siegert, JHEP **0**9, 049 (2012), 1111.1220.

[154] S. Catani, F. Krauss, R. Kuhn, and B. R. Webber, JHEP **1**1, 063 (2001), hep-ph/0109231.

[155] C. Anastasiou, L. J. Dixon, K. Melnikov, and F. Petriello, Phys. Rev. D **6**9, 094008 (2004), hep-ph/0312266.

[156] ATLAS Collaboration, CERN Report No. ATL-PHYS-PUB-2017-006, 2017 (unpublished).

[157] S. Frixione, P. Nason, and G. Ridolfi, JHEP **0**9, 126 (2007), 0707.3088.

[158] P. Nason, JHEP **0**411, 040 (2004), hep-ph/0409146.

[159] S. Frixione, P. Nason, and C. Oleari, JHEP **0**711, 070 (2007), 0709.2092.

[160] S. Alioli, P. Nason, C. Oleari, and E. Re, JHEP **1**006, 043 (2010), 1002.2581.

[161] ATLAS Collaboration, Studies on top-quark Monte Carlo modelling for Top2016, https://inspirehep.net/literature/1795329, 2016.

[162] T. Sjöstrand *et al.*, Comput. Phys. Commun. **1**91, 159 (2015), 1410.3012.

[163] ATLAS, CERN Report No. ATL-PHYS-PUB-2014-021, 2014 (unpublished).

[164] M. Beneke, P. Falgari, S. Klein, and C. Schwinn, Nucl. Phys. B **8**55, 695 (2012), 1109.1536.

[165] M. Cacciari, M. Czakon, M. Mangano, A. Mitov, and P. Nason, Phys. Lett. B **7**10, 612 (2012), 1111.5869.

[166] P. Bärnreuther, M. Czakon, and A. Mitov, Phys. Rev. Lett. **1**09, 132001 (2012), 1204.5201.

[167] M. Czakon and A. Mitov, JHEP **1**2, 054 (2012), 1207.0236.

[168] M. Czakon and A. Mitov, JHEP **0**1, 080 (2013), 1210.6832.

[169] M. Czakon, P. Fiedler, and A. Mitov, Phys. Rev. Lett. **1**10, 252004 (2013), 1303.6254.

[170] M. Czakon and A. Mitov, Comput. Phys. Commun. **1**85, 2930 (2014), 1112.5675.

[171] E. Re, Eur. Phys. J. C **7**1, 1547 (2011), 1009.2450.

[172] S. Frixione, E. Laenen, P. Motylinski, B. R. Webber, and C. D. White, JHEP **0**7, 029 (2008), 0805.3067.

[173] M. Aliev *et al.*, Comput. Phys. Commun. **1**82, 1034 (2011), 1007.1327.

[174] P. Kant *et al.*, Comput. Phys. Commun. **1**91, 74 (2015), 1406.4403.

[175] R. Frederix, E. Re, and P. Torrielli, JHEP **0**9, 130 (2012), 1207.5391.

[176] S. Alioli, P. Nason, C. Oleari, and E. Re, JHEP **0**9, 111 (2009), 0907.4076.

[177] J. M. Lindert *et al.*, Eur. Phys. J. C **7**7, 829 (2017), 1705.04664.

[178] U. Haisch, F. Kahlhoefer, and E. Re, JHEP **1**2, 007 (2013), 1310.4491.

[179] P. Nason and C. Oleari, JHEP **0**2, 037 (2010), 0911.5299.

[180] ATLAS, G. Aad *et al.*, JHEP **0**9, 145 (2014), 1406.3660.

[181] G. Cullen *et al.*, Eur. Phys. J. C **7**2, 1889 (2012), 1111.2034.

[182] K. Hamilton, P. Nason, and G. Zanderighi, JHEP **1**0, 155 (2012), 1206.3572.

[183] G. Luisoni, P. Nason, C. Oleari, and F. Tramontano, JHEP **1**0, 083 (2013), 1306.2542.

[184] ATLAS, M. Aaboud *et al.*, Phys. Rev. D **9**6, 072002 (2017), 1703.09665.

[185] ATLAS, M. Aaboud *et al.*, Eur. Phys. J. C **7**7, 195 (2017), 1612.01456.

[186] ATLAS, G. Aad *et al.*, Eur. Phys. J. C **8**1, 578 (2021), 2012.00578.

[187] ATLAS Collaboration, CERN Report No. ATLAS-CONF-2017-029, 2017 (unpublished).

[188] ATLAS, M. Aaboud *et al.*, Eur. Phys. J. C **7**9, 205 (2019), 1810.05087.

[189] S. Dulat *et al.*, Phys. Rev. D **9**3, 033006 (2016), 1506.07443.

[190] L. A. Harland-Lang, A. D. Martin, P. Motylinski, and R. S. Thorne, Eur. Phys. J. C **7**5, 204 (2015), 1412.3989.

[191] ATLAS Collaboration, CERN Report No. ATL-PHYS-PUB-2017-007, 2017 (unpublished).

[192] ATLAS, M. Aaboud *et al.*, Phys. Lett. B **7**75, 206 (2017), 1709.10264.

[193] G. D'Agostini, Nucl. Instrum. Meth. A **3**62, 487 (1995).

[194] G. D'Agostini, Improved iterative Bayesian unfolding, in *Alliance Workshop on Unfolding and Data Correction*, 2010, 1010.0632.

[195] S. Schmitt, EPJ Web Conf. **1**37, 11008 (2017), 1611.01927.

[196] B. Efron, Annals Statist. **7**, 1 (1979).

[197] K. G. Hayes, M. L. Perl, and B. Efron, Phys. Rev. D **3**9, 274 (1989).

[198] S. S. Wilks, Annals Math. Statist. **9**, 60 (1938).

[199] A. Wald, *Sequential Analysis*Wiley Publications in Statistics (J. Wiley & Sons, 1959).

[200] G. L. Fogli, E. Lisi, A. Marrone, D. Montanino, and A. Palazzo, Phys. Rev. D **6**6, 053010 (2002), hep-ph/0206162.

[201] U. Haisch and G. Polesello, JHEP **0**2, 128 (2019), 1812.08129.

[202] ATLAS, G. Aad *et al.*, Eur. Phys. J. C **8**1, 163 (2021), 2006.15458.

[203] M. Chala, F. Kahlhoefer, M. McCullough, G. Nardini, and K. Schmidt-Hoberg, JHEP **0**7, 089 (2015), 1503.05916.

[204] A. Buckley *et al.*, Comput. Phys. Commun. **1**84, 2803 (2013), 1003.0694.

[205] C. Bierlich *et al.*, SciPost Phys. **8**, 026 (2020), 1912.05451.

[206] ATLAS, M. Goblirsch-Kolb, Search for Supersymmetry in the 4-lepton final state with the ATLAS detector, in *2nd Large Hadron Collider Physics Conference*, 2014, 1408.6832.

[207] A. Buckley *et al.*, Comput. Phys. Commun. **2**60, 107310 (2021), 1912.08005.

[208] J. Catmore, The atlas data processing chain: from collisions to papers, https://indico.cern.ch/event/472469/contributions/1982677/attachments/1220934/1785823/intro_slides.pdf, 2016.

[209] C. Degrande *et al.*, Comput. Phys. Commun. **1**83, 1201 (2012), 1108.2040.

[210] N. D. Christensen and C. Duhr, Comput. Phys. Commun. **1**80, 1614 (2009), 0806.4194.

[211] N. D. Christensen *et al.*, Eur. Phys. J. **C**71, 1541 (2011), 0906.2474.

[212] F. Krauss, R. Kuhn, and G. Soff, JHEP **0**2, 044 (2002), hep-ph/0109036.

[213] C. Gütschow, J. M. Lindert, and M. Schönherr, Eur. Phys. J. **C**78, 317 (2018), 1803.00950.

[214] S. Kallweit, J. M. Lindert, P. Maierhöfer, S. Pozzorini, and M. Schönherr, JHEP **0**4, 012 (2015), 1412.5157.

[215] F. Buccioni *et al.*, Eur. Phys. J. C **7**9, 866 (2019), 1907.13071.

[216] S. Alekhin, J. Bluemlein, and S.-O. Moch, PoS **LL**2018, 049 (2018), 1808.08404.

[217] ATLAS, M. Aaboud *et al.*, JHEP **0**4, 048 (2019), 1902.05892.

[218] A. Buckley, The hepthesis LaTeX class.

List of figures

List of tables